



## City Research Online

### City, University of London Institutional Repository

---

**Citation:** Uthman, Muhammad (2013). Finite element characterisation of photonic crystal fibres. (Unpublished Doctoral thesis, City University London)

This is the unspecified version of the paper.

This version of the publication may differ from the final published version.

---

**Permanent repository link:** <https://openaccess.city.ac.uk/id/eprint/3012/>

**Link to published version:**

**Copyright:** City Research Online aims to make research outputs of City, University of London available to a wider audience. Copyright and Moral Rights remain with the author(s) and/or copyright holders. URLs from City Research Online may be freely distributed and linked to.

**Reuse:** Copies of full items can be used for personal research or study, educational, or not-for-profit purposes without prior permission or charge. Provided that the authors, title and full bibliographic details are credited, a hyperlink and/or URL is given for the original metadata page and the content is not changed in any way.

# **Finite Element Characterisation of Photonic Crystal Fibres**

by

**Muhammad Uthman**

A thesis submitted to the City University London in partial  
fulfilment of the requirement for the degree of PhD

Photonics Research Group  
School of Engineering and Mathematical Sciences  
City University, London

August, 2013

## TABLE OF CONTENTS

TABLE OF CONTENTS.....	2
TABLE OF ILLUSTRATIONS.....	7
ACKNOWLEDGEMENT.....	15
DECLARATION .....	16
ABSTRACT.....	17
LIST OF ABBREVIATIONS .....	18
LIST OF SYMBOLS .....	20
CHAPTER ONE: Introduction .....	22
1.1 Historical Background .....	22
1.1.1 Optical Fibre Communications Systems .....	25
1.2 The Optical Fibre.....	27
1.2.1 Index of Refraction.....	27
1.2.2 Critical Angle .....	28
1.2.3 Total Internal Reflection .....	28
1.2.4 Principle of Wave Guidance in a Fibre .....	30
1.3 Multimode Fibre .....	31
1.4 Single Mode Fibre .....	32
1.5 Special Purpose Fibre.....	33
1.6 Optical Fibre Manufacture.....	33
1.7 Practical Issues with Optical Fibres.....	35
1.7.1 Attenuation in Optical Fibres.....	35
1.7.2 Dispersion in Optical Fibres .....	36
1.7.3 Terminating and Splicing of Optical Fibres .....	36
1.7.4 Coupling Optical Fibres in Free Space.....	38
1.7.5 Optical Fibre Fuse .....	38

1.8 Advantages of Optical Fibres .....	39
1.9 Applications of Optical Fibres .....	40
1.10 Aims and Objectives of the Thesis .....	41
1.11 Structure of the Thesis.....	42
CHAPTER TWO: Photonic Crystal Fibre .....	45
2.0 Abstract.....	45
2.1 Photonic Crystal Fibre (PCF).....	45
2.2 Structure of PCF .....	49
2.3 Light-Guiding Mechanism .....	49
2.3.1 Index Guiding Photonic Crystal Fibre.....	50
2.3.2 Photonic Bandgap (PBG) Effect.....	50
2.4 Properties of Photonic Crystal Fibres.....	51
2.5 Advantages of Photonic Crystal Fibres over Optical Fibres .....	51
2.6 Applications of Photonic Crystal Fibre .....	52
2.7 Analysing Photonic Crystal Fibres .....	52
2.8 Confinement Losses .....	53
2.9 Bending Loss .....	53
2.9.1 Conformal Transformation .....	54
2.9.2 Types of Bending Loss.....	55
2.10 Summary .....	55
CHAPTER THREE: Numerical Methods.....	56
3.0 Abstract.....	56
3.1 Basic Equations .....	56
3.1.1 Maxwell's Equations .....	56
3.1.2 Boundary Conditions.....	57
3.1.3 Wave Equations .....	59
3.2 Analysis of Optical Waveguides .....	60

3.2.1 Marcatili's Method.....	61
3.2.2 The Effective Index Method.....	62
3.3 Numerical Solution Methods .....	62
3.3.1 The Boundary Element Method.....	64
3.3.2 The Point Matching Method .....	64
3.3.4 The Mode Matching Method.....	65
3.3.5 The Spectral Index Method.....	66
3.3.6 The Beam Propagation Method.....	66
3.3.7 The Finite Difference Method.....	67
3.3.8 The Finite Element Method .....	68
3.4 Fundamentals of the Finite Element Method.....	69
3.4.1 Theoretical Background .....	70
3.4.2 Variational Formulation .....	72
3.4.3 Scalar Approximation.....	72
3.4.4 Vector Formulation .....	73
3.4.5 Natural Boundary Conditions.....	75
3.4.6 FEM Formulation.....	75
3.4.7 Domain Discretisation.....	76
3.4.8 Shape Functions .....	78
3.4.9 Global and Element Matrices.....	83
3.4.10 Spurious Solution .....	87
3.5 The Perfectly Matched Layer (PML) Boundary Condition .....	88
3.6 The Least Squares Boundary Residual Method .....	92
3.6.1 Analysis of Discontinuity in Dielectric Waveguides .....	94
3.6.2 Numerical Analysis Using Finite Element Output .....	96
3.6.3 Losses in Optical Waveguides .....	98
3.7 Summary .....	99

CHAPTER FOUR: Mode Degeneration .....	100
4.0 Abstract .....	100
4.1 Introduction .....	100
4.2 Results for PCF with Identical Air-holes .....	101
4.3 Mesh Refinement and Perfectly Matched Layer Optimisation .....	101
4.4 Results of Numerical Experiments .....	105
4.5 Summary .....	131
CHAPTER FIVE: Polarization Maintaining Fibre .....	133
5.0 Abstract .....	133
5.1 Polarization Maintaining Optical Fibres .....	133
5.2 Photonic Crystal Fibre as a Polarization Maintaining Optical Fibre .....	134
5.3 Straight Single Mode Single Polarization Asymmetric PCF .....	137
5.4 Results for Bent Asymmetric PCF, $d \neq d_2$ (Non-Identical Air-holes) .....	140
5.6 Summary .....	158
CHAPTER SIX: Mode Coupling .....	160
6.0 Abstract .....	160
6.1 Introduction .....	160
6.2 Mode Field Study of a Single Mode Fibre .....	162
6.3 Analysis of a Tapered PCF .....	166
6.4 Coupling between Photonic Crystal Fibre and Optical Fibre .....	172
6.5 Summary .....	178
CHAPTER SEVEN: Photonic Crystal Fibre for Terahertz .....	180
7.0 Abstract .....	180
7.1 Introduction .....	180
7.2 Equiangular Spiral Photonic Crystal Fibre .....	182
7.3 Bending Loss Calculation in Teflon .....	202
7.4 Low-Loss Porous Core Photonic Crystal Fibre .....	204

7.4.1 Numerical Solution for Porous-Core PCF .....	206
7.5 Summary .....	224
CHAPTER EIGHT: Conclusion and Further Work .....	226
8.0 Review of the Aims and Objectives of the Work .....	226
8.1 General Conclusions and Directions for Further Work.....	230
LIST OF PUBLICATIONS BY THE AUTHOR.....	232
APPENDIX.....	234
REFERENCES.....	245

## TABLE OF ILLUSTRATIONS

Fig. 1. 1: John Tyndall's Experiment (Goff 2002) .....	22
Fig. 1. 2: IP traffic growth between 2011 and 2016 (projected) (After Cisco 2012).....	25
Fig. 1. 3: The propagation of light through a multi-mode optical fibre .....	27
Fig. 1. 4: The larger the angle to the normal, the smaller is the fraction of light transmitted, until the angle when total internal reflection occurs (Goure and Verrier 2002).....	29
Fig. 1. 5: Optical fibre types (a) step index fibre (b) graded index fibre (Goure and Verrier 2002). .....	31
 Fig. 2. 1: SEM micrographs of a photonic-crystal fibre produced at US Naval Research Laboratory. (a) The diameter of the solid core at the centre of the fibre is 5 $\mu\text{m}$ , while (b) the diameter of the holes is 4 $\mu\text{m}$ (Image of Photonic Crystal Fibre from NRL 2006). .....	47
Fig. 2. 2: Fabrication of Photonic Crystal Fibre (Fabrication of Photonic Crystal Fibre NKT photonics 2008) .....	48
Fig. 2. 3: Photonic Crystal Fibre (Photonic crystal fibre NKT photonics 2008). .....	49
Fig. 2. 4: Fibre Optic Cable .....	52
Fig. 2. 5: A bent optical fibre .....	53
Fig. 2. 6: Refractive index profile of bent PCF. (a) straight fibre; (b) a bent fibre with the centre located at the side of 'inside' (Xiangru <i>et al.</i> 2010) .....	55
 Fig. 3. 1: Boundary between two media of refractive indices $n_1$ and $n_2$ , where $\mathbf{n}$ , is the unit vector normal to the interface.....	58
Fig. 3. 2: Arbitrary shaped optical waveguide, divided into arbitrary sub-domains, each having different type of material .....	71
Fig. 3. 3: Finite elements in two dimensions .....	76
Fig. 3. 4: Finite element discretisation of a waveguide with triangular elements.....	77
Fig. 3. 5: Pascal's triangle for complete polynomials in two dimensions. ....	78
Fig. 3. 6: Representation of a first order triangular element.....	79
Fig. 3. 7: The structure of a PCF showing transverse section of the PCF surrounded by PML (Saitoh and Koshiba 2002). ....	90



Fig. 3. 8: Discontinuity junction of two dielectric waveguide (a) vertical section of the discontinuity between side I and II (b) Transverse cross section of the discontinuity at the junction of two sides.....	95
Fig. 4. 1: A graph depicting the cross-section of a 3 ring PCF with half symmetry.....	101
Fig. 4. 2: The variation of effective index of $H_{11}^x$ mode with bending radius for mesh divisions 128 x 65 and mesh 133 x 70.....	102
Fig. 4. 3: The variation of spot sizes with the bending radius, R for mesh divisions 128 x 65 and 133 x 70.....	103
Fig. 4. 4: Variation of modal loss with the bending radius, R, for mesh divisions 128 and 133. ....	104
Fig. 4. 5: $H_x$ field profile of the $H_{11}^x$ mode $R = \infty$ , $\Lambda = 1.0\mu\text{m}$ , $d/\Lambda = 0.5$ .....	105
Fig. 4. 6: $H_x$ field profile of the $H_{11}^x$ mode at $R = 200\mu\text{m}$ , with $\Lambda = 1.0\mu\text{m}$ and $d/\Lambda = 0.5$ . ....	106
Fig. 4. 7: $H_x$ field contours for the $H_{11}^x$ mode at $R = 100\mu\text{m}$ , with $\Lambda = 1.0\mu\text{m}$ , $d/\Lambda = 0.5$ . ....	107
Fig. 4. 8: The variation of effective index with the bending radius for $\Lambda = 1.6\mu\text{m}$ , $1.7\mu\text{m}$ , $1.8\mu\text{m}$ and $1.9\mu\text{m}$ . ....	108
Fig. 4. 9: The variation of bending losses with the bending radius, R for $\Lambda = 1.6\mu\text{m}$ , $1.7\mu\text{m}$ , $1.8\mu\text{m}$ and $1.9\mu\text{m}$ .....	109
Fig. 4. 10: $H_x$ field contours for the $H_{11}^x$ mode $R = \infty$ , $\Lambda = 1.9\mu\text{m}$ , $d/\Lambda = 0.5$ .....	110
Fig. 4. 11: Variation loss with the pitch lengths for $R = 5000\mu\text{m}$ , $10000\mu\text{m}$ and $50000\mu\text{m}$ ....	111
Fig. 4. 12: The variation of effective index with bending radius, R for $d/\Lambda = 0.5$ and $d/\Lambda = 0.45$ . ....	112
Fig. 4. 13: $H_x$ field profile of the $H_{11}^x$ mode $R = \infty$ , $\Lambda = 1.0\mu\text{m}$ , $d/\Lambda = 0.45$ .....	113
Fig. 4. 14: $H_x$ field profile of the $H_{11}^x$ mode $R = 350\mu\text{m}$ , $\Lambda = 1.0\mu\text{m}$ , $d/\Lambda = 0.45$ .....	114
Fig. 4. 15: The variation of spot size with bending radius, R for $\Lambda = 1.0\mu\text{m}$ $d/\Lambda = 0.5$ and $d/\Lambda = 0.45$ . ....	115
Fig. 4. 16: $H_x$ field contours for the $H_{11}^x$ mode $R = 170\mu\text{m}$ , $\Lambda = 1.9\mu\text{m}$ , $d/\Lambda = 0.5$ .....	116
Fig. 4. 17: Variation of bending loss against bending radius, R, for $\Lambda = 1.6\mu\text{m}$ , $2.6\mu\text{m}$ and $5.0\mu\text{m}$ for $H_{11}^x$ mode and $d/\Lambda = 0.5$ .....	117
Fig. 4. 18: The variation of bending loss against bending radius, R, for values of R between $700\mu\text{m}$ to $900\mu\text{m}$ , when $\Lambda = 5.0\mu\text{m}$ , $d/\Lambda = 0.5$ . ....	118

Fig. 4. 19: The variation of effective index against bending radius, $R$ , for values of $R$ between $700\mu\text{m}$ to $900\mu\text{m}$ , $\Lambda = 5.0\mu\text{m}$ , $d/\Lambda = 0.5$ . .....	119
Fig. 4. 20: The variation of spot size against bending radius, $R$ , for values of $R$ between $700\mu\text{m}$ to $900\mu\text{m}$ , $\Lambda = 5.0\mu\text{m}$ , $d/\Lambda = 0.5$ .....	120
Fig. 4. 21: Variation of the effective indices with the bending radius for the quasi-TE modes. ....	121
Fig. 4. 22: Variation of the total losses with the bending radius $R$ . ....	122
Fig. 4. 23: Variation of the $H_y$ field along the x-axis for $R = 840\mu\text{m}$ , $\Lambda = 5.0\mu\text{m}$ , $d/\Lambda = 0.5$ . ....	123
Fig. 4. 24: $H_y$ field profile along the X axis for the $H_{11}^y$ core when $R = 830\mu\text{m}$ below the degeneration point. ....	124
Fig. 4. 25: Variation of the $H_x$ field along the x-axis $R = 825\mu\text{m}$ , $\Lambda = 5.0\mu\text{m}$ , $d/\Lambda = 0.5$ .....	124
Fig. 4. 26: $H_y$ contour of the higher order cladding mode when $R = 833\mu\text{m}$ . ....	125
Fig. 4. 27: $H_x$ 3-D field for the $H_{11}^x$ mode $R = 825\mu\text{m}$ , $\Lambda = 5.0\mu\text{m}$ , $d/\Lambda = 0.5$ . ....	126
Fig. 4. 28: Variation of the effective indices with the bending radius $R$ . ....	127
Fig. 4. 29: Variation of the total losses with the bending radius $R$ . ....	127
Fig. 4. 30: $H_x$ field profile of the $H_{11}^x$ core mode along the x axis through the centre of the core when $R = 1460\mu\text{m}$ . ....	128
Fig. 4. 31: $H_x$ field contour for $H_{c1}^x$ cladding mode when $R = 1460\mu\text{m}$ . ....	129
Fig. 4. 32: The variation of effective index with bending radius, $R$ for $\Lambda = 2.6\mu\text{m}$ , for both the quasi-TE and quasi-TM modes. ....	130
Fig. 4. 33: The variation of loss with bending radius, $R$ for $\Lambda = 2.6\mu\text{m}$ , for both quasi-TE and quasi-TM modes. ....	131
Fig. 5. 1: The panda type (b) the bow-tie and (c) the elliptical clad type polarization maintaining optical fibres (Liu <i>et al.</i> 1994) .....	134
Fig. 5. 2: The core and the first ring of air-holes in a PCF (a) with all the air-holes of the same diameter thus the core is circular (b) two larger air-holes on the side of the core making the core elliptical, height > width (c) two larger air-holes above the core and two larger air-holes below the core makes the core elliptical, width > height.....	135
Fig. 5. 3: A graph depicting half of the cross-section of a PCF; $d \neq d_2$ .....	135
Fig. 5. 4: A graph depicting half of the cross-section of a PCF; $d \neq d_2$ , same as shown in Fig. 5.3 but with a 90 degree rotation.....	136

Fig. 5. 5: Variation of effective index and birefringence with $d_2/\Lambda$ . ....	138
Fig. 5. 6: Variation of the TE and TM modal losses with $d_2/\Lambda$ .....	138
Fig. 5. 7: Variation of the differential LR with $d_2/\Lambda$ for pitches 1.6 and 1.8 $\mu\text{m}$ . ....	139
Fig. 5. 8: Variation of effective index with bending radius, R for $\Lambda = 1.8\mu\text{m}$ , $d/\Lambda = 0.5$ , $d_2/\Lambda = 0.8$ for both quasi-TE and quasi-TM modes.....	140
Fig. 5. 9: $H_x$ field profile of the $H_x^{11}$ mode at $R = \infty$ , $\Lambda = 1.8$ , $d_2/\Lambda = 0.8$ .....	141
Fig. 5. 10: $H_x$ field profile of the $H_x^{11}$ mode at $R = 500\mu\text{m}$ , $\Lambda = 1.8$ , $d_2/\Lambda = 0.8$ .....	142
Fig. 5. 11: Variation of spot size with the bending radius, R for $\Lambda = 1.8\mu\text{m}$ , $d/\Lambda = 0.5$ , $d_2/\Lambda = 0.8$ for both quasi-TE and quasi-TM modes.....	143
Fig. 5. 12: Variation of loss with the bending radius, R for $\Lambda = 1.8\mu\text{m}$ , $d/\Lambda = 0.5$ , $d_2/\Lambda = 0.8$ for both quasi-TE and quasi-TM modes. ....	144
Fig. 5. 13: Variation of birefringence with bending radius, R for $\Lambda = 1.8\mu\text{m}$ , $d/\Lambda = 0.5$ , $d_2/\Lambda = 0.8$ . ....	145
Fig. 5. 14: Variation of loss ratio with bending radius, R for $\Lambda = 1.8\mu\text{m}$ , $d/\Lambda = 0.5$ , $d_2/\Lambda = 0.8$ . ....	146
Fig. 5. 15: Variation of the bending losses with the bending radius, R, of the TM modes for different $d_2/\Lambda$ ratios. ....	147
Fig. 5. 16: Variation of loss ratio with bending radius, R for $\Lambda = 1.8\mu\text{m}$ , $d/\Lambda = 0.5$ , $d_2/\Lambda = 0.8$ , 0.85 and 0.9. ....	148
Fig. 5. 17: Variation of birefringence with bending radius, R for $\Lambda = 1.8\mu\text{m}$ , $d/\Lambda = 0.5$ , $d_2/\Lambda = 0.8$ , 0.85 and 0.9. ....	149
Fig. 5. 18: Variation of loss ratio with $d_2/\Lambda$ , $\Lambda = 1.8\mu\text{m}$ for $R = \infty$ and $600\mu\text{m}$ .....	150
Fig. 5. 19: Variation of loss with bending radius, R for $\Lambda = 1.6\mu\text{m}$ , $d/\Lambda = 0.5$ , $d_2/\Lambda = 0.85$ for both quasi-TE and quasi-TM modes. ....	151
Fig. 5. 20: Variation of loss ratio with bending radius, R for $\Lambda = 1.6\mu\text{m}$ and $\Lambda = 1.8\mu\text{m}$ , $d/\Lambda = 0.5$ , $d_2/\Lambda = 0.85$ . ....	152
Fig. 5. 21: Variation of birefringence with bending radius, R for $\Lambda = 1.6\mu\text{m}$ and $\Lambda = 1.8\mu\text{m}$ with $d/\Lambda = 0.5$ , $d_2/\Lambda = 0.85$ .....	153
Fig. 5. 22: Variation of the LRs with the bending radius for different N values.....	154
Fig. 5. 23: Variation of $L_{20\text{dB}}$ length with the bending radius for different N values.....	155
Fig. 5. 24: Variation of $L_{20\text{dB}}$ length with respect to the TE loss for different N values. ....	156

Fig. 5. 25: Variation of the loss with the bending radius for two different asymmetric orientations.....	157
Fig. 5. 26: Variation of loss with the operating wavelength for two different asymmetry orientations.....	158
Fig. 6. 1: Variation of mode field area and effective index of a SMF against core radius, R. ...	163
Fig. 6. 2: 2-D $H_x$ field profile for a Single Mode Fibre exploiting 2-fold symmetry with only quarter of the structure simulated. ....	164
Fig. 6. 3: Comparing Gaussian field profile and the obtained profile for $R = 5.0\mu\text{m}$ .....	165
Fig. 6. 4: Comparing Gaussian field profile and the obtained profile for $R = 7.0\mu\text{m}$ .....	165
Fig. 6. 5: Comparing Gaussian field profile and the obtained profile for $R = 3.0\mu\text{m}$ .....	166
Fig. 6. 6: Variation of mode field areas of a PCF against the pitch, $\Lambda$ .....	166
Fig. 6. 7: $H_x$ field profile of the $H_{11}^x$ mode for $N = 7$ , $\Lambda = 1.0$ , $d/\Lambda = 0.4$ , and $d_7/\Lambda=0.8$ . ....	167
Fig. 6. 8: Variation of $H_x$ field profile along $x$ $N = 7$ , $\Lambda = 1.0$ , $d/\Lambda = 0.4$ , and $d_7/\Lambda=0.8$ . ....	168
Fig. 6. 9: Variations of the $A_{\text{eff}}$ with the pitch length for PCF having $d/\Lambda = 0.4$ and $0.5$ for $N = 5$ with all air-holes equal.....	170
Fig. 6. 10: Variations of the $A_{\text{eff}}$ with the pitch length for PCF having $d/\Lambda = 0.5$ for $N = 5$ with the outermost ring having larger air-holes. ....	170
Fig. 6. 11: Variations of the $A_{\text{eff}}$ with the pitch length for PCF having $d/\Lambda = 0.4$ and $0.5$ for $N = 5$ . ....	171
Fig. 6. 12: Variations of the $A_{\text{eff}}$ with the pitch length for PCF having $d/\Lambda = 0.4$ for $N = 5$ and $N = 7$ . ....	172
Fig. 6. 13: Variations of the coupled power to a EDFA with the tapered pitch, $\Lambda$ , of a PCF....	174
Fig. 6. 14: Variations of the $A_{\text{eff}}$ with the pitch length for PCFs having $d/\Lambda = 0.4$ and outermost $d/\Lambda = 0.8$ for $N = 7, 8$ and $10$ . ....	174
Fig. 6. 15: Variation of $A_{\text{eff}}$ and core refractive index difference, $n_g$ of a SMF against fibre radius, $a$ . ....	176
Fig. 6. 16: Variation of Coupling Efficiency to PCF with tapered pitch, $\Lambda$ and SMF, $a = 3.5\mu\text{m}$ . ....	177
Fig. 7. 1: Schematic of the Hexagonal Photonic Crystal Fibre structure .....	182

Fig. 7. 2: Graph of effective index against pitch and spot size against pitch in hexagonal TOPAS.	183
Fig. 7. 3: Graph comparing effective index for Teflon and TOPAS PCFs with respect to pitch.	184
Fig. 7. 4: Variations of spot sizes for Teflon and TOPAS PCFs with the pitch.	185
Fig. 7. 5: Variations of the leakage loss in Teflon and TOPAS PCFs with the pitch.	186
Fig. 7. 6: Graph comparing effective index in Teflon and TOPAS with respect to bending radius.	187
Fig. 7. 7: Graph of loss against bending radius in TOPAS for hexagonal arrangement with $d/\Lambda = 0.45$ and $0.5$ .	188
Fig. 7. 8: Graph comparing loss Hexagonal TOPAS with respect to pitch for bending radius of 5m, 10m and 100m.	189
Fig. 7. 9: Field profile in the bent Hexagonal PCF in Teflon, where bend radius = 60mm.	190
Fig. 7. 10: Schematic of the Equiangular Spiral Photonic Crystal Fibre.	191
Fig. 7. 11: Schematic of the ES-PCF structure	191
Fig. 7. 12: Graph comparing the effective index verses frequency for Hexagonal TOPAS, equiangular spiral TOPAS and Hexagonal Teflon.	193
Fig. 7. 13: Graph of spot size against frequency for hexagonal TOPAS, equiangular spiral TOPAS and Hexagonal Teflon.	194
Fig. 7. 14: Graph of loss against frequency in hexagonal PCF, equiangular spiral PCF in TOPAS and hexagonal PCF in Teflon.	195
Fig. 7. 15: Graph of bending loss against bending radius in equiangular spiral PCF with $d/\Lambda = 0.45$ and $0.5$ .	196
Fig. 7. 16: Field profile in the bent Equiangular Spiral Photonic Crystal Fibre, where bend radius = 60mm.	197
Fig. 7. 17: Graph of loss against bending radius in Teflon for equiangular spiral arrangement with $\Lambda = 0.55, 0.56$ and $0.57$ with $n_{arm} = 7$ , $n_{ring} = 5$ and $\theta = 27^\circ$ .	198
Fig. 7. 18: Graph of bending loss against bending radius using various configurations of spiral TOPAS PCF arrangement.	199
Fig. 7. 19: Variation of bending loss against bending radius and normalised spotsize against bending radius for hexagonal PCF and equiangular spiral PCF in TOPAS.	199
Fig. 7. 20: Graph of loss against frequency in hexagonal PCF and equiangular spiral PCF in Teflon with inclusion of material loss.	201

Fig. 7. 21: Graph comparing loss (without material loss) of Equiangular spiral Teflon with respect to pitch for bending radius of 5,000mm, 10,000mm and infinity. ....	202
Fig. 7. 22: Modal loss (including material loss) variation with bend radius at 1THz for the Hexagonal PCF and equiangular spiral PCF.....	203
Fig. 7. 23: Field profile of the fundamental mode in the bent Hexagonal PCF (mode leaking into cladding region) and the equiangular spiral PCF with bend radius 40mm.....	204
Fig. 7. 24: Representation of the porous core PCF cross-section with $N_{\text{core}} = 4$ , $N_{\text{clad}} = 4$ . $\Lambda_o =$ outer pitch and $d_o =$ outer radius. Inset shows $\Lambda_i =$ inner pitch and $d_i =$ inner radius. ....	207
Fig. 7. 25: Variations of the mode field areas and effective index with the pitch, $\Lambda_o$ for $d_o/\Lambda_o = 0.8$ and $d_i/\Lambda_i = 0.5$ for $H_{11}^x$ Mode. ....	209
Fig. 7. 26: Variation of the confinement factors with the outer pitch, $\Lambda_o$ , for $d_o/\Lambda_o = 0.8$ and $d_i/\Lambda_i = 0.5$ .....	210
Fig. 7. 27: Variation of the confinement factors with the outer pitch, $\Lambda_o$ , for $d_o/\Lambda_o = 0.8$ and $d_i/\Lambda_i = 0.6$ .....	211
Fig. 7. 28: Variations of the $H_x$ field of the $H_{11}^x$ mode along the x-axis for $\Lambda_o = 0.7\text{mm}$ . ....	212
Fig. 7. 29: Variations of the $H_x$ field of the $H_{11}^x$ mode along the x-axis for $\Lambda_o = 0.35\text{mm}$ , when $d_o/\Lambda_o = 0.8$ , and $d_i/\Lambda_i = 0.50$ . ....	213
Fig. 7. 30: Variation of the confinement factor in the core air-holes, $\Gamma_{\text{aircore}}^a$ , with the outer pitch $\Lambda_o$ for $d_o/\Lambda_o = 0.8$ but with different $d_i/\Lambda_i$ values. ....	214
Fig. 7. 31: Variation of the confinement factor in the core air-holes, $\Gamma_{\text{airclad}}^a$ , with the outer pitch $\Lambda_o$ for $d_o/\Lambda_o = 0.8$ but with different $d_i/\Lambda_i$ values. ....	215
Fig. 7. 32: Variation of the confinement factor in the core air-holes, $\Gamma_{\text{solidclad}}^a$ , with the outer pitch $\Lambda_o$ for $d_o/\Lambda_o = 0.8$ but with different $d_i/\Lambda_i$ values. ....	216
Fig. 7. 33: Variation of the confinement factor in the core air-holes, $\Gamma_{\text{solidclad}}^a$ , with the outer pitch $\Lambda_o$ for $d_o/\Lambda_o = 0.8$ but with different $d_i/\Lambda_i$ values. ....	217
Fig. 7. 34: Variation of the maximum confinement factor in the air core with the $d_i/\Lambda_i$ for some fixed $d_o/\Lambda_o$ values.....	218
Fig. 7. 35: Variation of the maximum confinement factor in the air cladding with the $d_i/\Lambda_i$ for some fixed $d_o/\Lambda_o$ values. ....	219
Fig. 7. 36: Variation of the total maximum confinement factor in the air core and air cladding with the $d_i/\Lambda_i$ for some fixed $d_o/\Lambda_o$ values. ....	220
Fig. 7. 37: Variation of the $H_x$ field along the x-axis for the $H_{11}^x$ mode when $\Lambda_o = 0.35\text{mm}$ , $d_o/\Lambda_o = 0.95$ and $d_i/\Lambda_i = 0.85$ . ....	221

Fig. 7. 38: Variation of bending loss with bending radius, R at $\Lambda_o = 0.35\text{mm}$ and $\Lambda_i = 0.039\text{mm}$ . .....	222
Fig. 7. 39: $H_x$ field profile of the bent PCF for the fundamental $H_{11}^x$ mode for bending radius, 1.5 cm.....	223

## **ACKNOWLEDGEMENT**

I would like to express my sincere and utmost gratitude to my first supervisor Professor B. M. A. Rahman for giving me the opportunity to study under his tutelage in the first place and for patiently enduring all my obnoxious shortcomings throughout the years.

I would like to extend my gratitude to my second supervisor Professor K. T. V. Grattan for always finding the time to help my research despite his incredibly busy schedule.

I would like to thank Dr Kejalakshmy Namassivayane and Dr Arti Agrawal for mentoring and guiding me in the research work and for all the research collaborations.

I would like to give my special thanks to all current and former students of the Photonics Research group and all my other colleagues for all the help and contributions they have provided me through my time at the group.

I would especially want to thank my parents for their support and understanding over this long period of time I was involved with studies.



## **DECLARATION**

I grant powers of discretion to the University Librarian to allow this thesis to be copied in whole or in part without further reference to me. This permission covers only single copies made for study purposes, subject to normal conditions of acknowledgment.

## ABSTRACT

Rigorous numerical simulations have been carried out by using the Finite Element Method (FEM) in order to calculate bending and leakage losses of Photonic Crystal Fibres (PCF). A modal solution approach including the implementations of the conformal transformation and the Perfectly Matched Layer (PML) were undertaken to determine the bending and leakage losses of several designs of Photonic Crystal Fibres. This was carried out by varying key parameters such as the pitch ( $\Lambda$ ), diameter ( $d$ ) and air-filling fraction ( $d/\Lambda$ ). Output modal parameters including the effective indices, spot sizes, leakage and bending losses as well as the mode field profiles were obtained. These output parameters were obtained by varying the bending radius ( $R$ ) from very large values to very low values for different dimensions of the PCF, with results being obtained for Transverse Magnetic and Transverse Electric (quasi-TM and quasi-TE) polarizations. These parameters were calculated by solving the Maxwell's equations using the  $\mathbf{H}$ -field vector formulation and with the inclusion of PML to solve complex eigenvalue equations. Generally, it was observed that for all  $\Lambda$ ,  $d/\Lambda$  and the polarization considered, as  $R$  is reduced from a very high value to lower values, the bending losses increase and there is a sharp increase at some lower values of  $R$ . At some very low values of  $R$ , some oscillatory behaviour was observed in the curves obtained for the fibre losses, where further investigations were carried out. These oscillations appeared due to degeneration of the fundamental mode with the cladding modes. In most of the cases investigated, there was a correlation in the variation of effective indices the loss values and also in the variation of spot sizes. PCFs with non-identical air-holes were also investigated in which case the  $d \neq d_2$  (diameter of 4 larger air-holes in the first ring) and knowing the values for TM and TE polarizations, it was possible to determine the birefringence, which is the difference between the effective indices for the TM and TE modes and also the loss ratio, which is the ratio of TM loss to that of the TE loss. All the input and output parameters that were considered with the symmetric air-holes were also considered in the case with fibre with asymmetric air-holes study. The results obtained are very important in the design of Single Mode Single Polarization PCF. Results have also been obtained from the studies done of asymmetric arrangement of air-holes which lead to the design of Single Mode Single Polarization PCF. Work was carried out on the design of a tapered PCF that could be efficiently coupled to a single mode fibre, SMF. This was achieved by increasing the number rings up to 10 rings of air-holes in the cladding and having the outermost ring with larger air-holes, the inner rings were near cutoff. This fibre was coupled to a conventional SMF to allow for better tolerance to fabrication errors. There has also been work carried out in polymer fibre namely Teflon and TOPAS in the terahertz regime. The conventional hexagonal arrangement of PCF was simulated and compared to spiral PCF in THz. An improved PCF design having a porous core with hexagonal arrangement and cladding was designed and analysed and low-loss guidance in THz was achieved. Thus overall a number of different PCF designs were considered and their properties evaluated and detailed knowledge has been obtained on potential performance of such fibres.

## **LIST OF ABBREVIATIONS**

ABC	Absorbing Boundary Condition
BEM	Boundary Element Method
BPM	Beam Propagation Method
ES-PCF	Equiangular Spiral PCF
FDTD	Finite Difference Time Domain
FEM	Finite Element Method
LR	Loss Ratio
LSBR	Least Squares Boundary Residual
MFA	Mode Field Area
MMF	Multimode Fibre
MMM	Mode Matching Method
M-TIR	Modified Total Internal Reflection
PBG	Photonic Bandgap Fibre
PCF	Photonic Crystal Fibre
PML	Perfectly Matched Layer
PMM	Point Matching Method
POF	Plastic Optical Fibre
SMF	Single Mode Fibre
SSC	Spot Size Converter
TBC	Transparent Boundary Condition
TE	Transverse Electric

TM Transverse Magnetic

WDM Wavelength Division Multiplexing

## LIST OF SYMBOLS

$\mu_o$	Permeability of the vacuum ( $4\pi \times 10^{-7}$ Henry/metre)
$\mu_r$	Relative permeability
<b>B</b>	Magnetic flux density (Tesla)
$c$	Velocity of light in vacuum
<b>D</b>	Electric flux density (coulomb/metre <sup>2</sup> )
$d$	diameter of air-holes
<b>E</b>	Electric field intensity (volts/metre)
<b>H</b>	Magnetic field intensity (amperes/metre)
<b>J</b>	Electric current density
$k$	Wavenumber
$n$	Refractive index
<b>n</b>	Unit vector perpendicular to the surface
$p$	Penalty factor
$w$	Weighting factor
$\alpha$	Attenuation constant
$\beta$	Propagation constant
$\gamma$	Complex propagation constant
$\Gamma$	Confinement factor
$\epsilon$	Permittivity
$\epsilon_o$	Permittivity of the vacuum ( $8.854 \times 10^{-12}$ Farad/metre)
$\epsilon_r$	Relative permittivity of the medium

$\Lambda$	Pitch
$\lambda$	Wavelength
$\rho$	Dielectric charge density (coulomb/metre <sup>3</sup> )
$\omega$	Angular frequency

## CHAPTER ONE: Introduction

### 1.1 Historical Background

The concept of being able to communicate using light has been in existence since the early history of man. As examples, in ancient Americas and in ancient China, smoke signals were used to warn of impending enemy attacks or of other dangers. But the concept of light guiding in optical fibres dates back two centuries to the optical telegraph invented by French engineer Claude Chappe in 1790. He invented a system which comprised a series of semaphores mounted on towers whereby human operators would relay messages from one tower to another tower. These were later replaced by the electric telegraph in the mid-19<sup>th</sup> century thus leaving a scattering of telegraph hills as the most visible legacy (Hecht 1999). Further work continued on the modification, improvement and application of optical fibre, which still had so much attenuation associated with it.

In 1870, John Tyndall demonstrated that light used internal reflection and follows a specific path. He demonstrated this with sunlight and used a jet of water that flowed from one container to another. The light followed a zigzag path inside the curved path of the water. The simple experiment, illustrated in Fig. 1.1, marked early research into the guided transmission of light (Goff 2002) that has implications for modern fibre optics.



Fig. 1. 1: John Tyndall's Experiment (Goff 2002)

Alexander Graham Bell patented an optical telephone system named Photophone in 1880 (Hecht 1999) which used free-space light to carry the human voice 200 metres. Alexander Graham Bell believed this invention was superior to the telephone which was an earlier invention of his because the Photophone did not need wires to connect the transmitter and receiver (Goff 2002).

The need for reliable long distance communication systems has existed since antiquity. Over time, the sophistication of these systems has gradually improved leading to the development of the telegraph and to the first coaxial cable put into service in 1940. As these communication systems improved, certain fundamental limitations presented themselves. Electrical systems were limited by their small repeater spacing (the distance a signal can propagate before attenuation requires the signal to be amplified) and the bit rate of microwave systems was limited by their carrier frequency. In the second half of the twentieth century, it was realized that an optical carrier of information would have a significant advantage over the existing electrical and microwave carrier signals.

Narinder Kapany from Imperial College of Science and Technology, London, first coined the term “fibre optics” in 1956 (Goff 2002) and the development of fibre bundles for image transmission, which had as the primary application as a medical endoscope, was patented by Basil Hirschowitz, C. Wilbur Peters and Lawrence E. Curtiss who were then researchers at the University of Michigan in 1956. While developing the endoscope, Curtiss produced the first glass-clad fibres.

The next important step in the development of fibre optics has to be the development of the laser technology. In 1957, Gordon Gould as a graduate student at Columbia University described the laser conceptually as an intense light source (Goff 2002) and it was developed experimentally by Theodore Maiman in 1960 using ruby as the laser medium.

In 1965, Charles K. Kao (Nobel Laureate) and George A. Hockman of British company the Standard Telecommunication Laboratory were the first to recognize that attenuation of contemporary fibres was caused by impurities, which could be removed, rather than fundamental physical effects such as scattering (Kao and Hockman 1966). They suggested that optical fibre could be used for telecommunications if the attenuation could be reduced to 20 dB/km or lower.



Inspired by Charles K. Kao and George A. Hockman's proposal, glass researchers began to work on the problem of purifying glass. In 1970, the first practical optical fibre (with a loss of 17 dB/km by doping silica glass with titanium) for communications was developed by researchers Robert D. Maurer, Donald Keck, Peter Schultz and Frank Zimar of American based glass maker Corning. It was the purest glass ever made (Goff 2002). On 22 April, 1977, General Telephone and Electronics sent the first live telephone traffic through fibre optics at 6 Mbit/s in Long Beach, California. Further work continued on improving the optical fibre by researchers in University of Southampton, Bell Laboratories and others which produced lots of improvements and also new applications such as the erbium-doped fibre amplifiers which eliminated the need for optical-electrical-optical regeneration.

In 1986, David Payne of the University of Southampton and Emmanuel Desurvire at Bell Laboratories developed the erbium-doped fibre amplifier (Desurvire *et al.* 1987), which has reduced the cost of long-distance fibre systems by eliminating the need for optical-electrical-optical repeaters. The first transatlantic telephone cable to use optical fibre was TAT-8, based on Desurvire optimized laser amplification technology which went into operation in 1988.

In 1991, the emerging field of photonic crystals led to the development of photonic crystal fibre (Russell 2003). In 1995, Prof Phillip Russell and his research team created the world's first working photonic crystal fibre (Knight *et al.* 1996b) which became commercially available in subsequent years from various suppliers. One way the photonic crystal fibre may guide light is by means of diffraction from a periodic structure; but it also guides light by means of total internal reflection. Photonic crystal fibres can be designed to carry higher power than conventional fibre and their wavelength dependent properties can be manipulated to improve their performance in certain applications. Photonic crystal fibres now find applications in fibre optic communications (Russell 2003), fibre lasers (Agrawal 2008), nonlinear devices (Agrawal 2008), high-power transmission (Poli *et al.* 2007; Agrawal 2008), highly sensitive gas sensor (Jacobsen *et al.* 1996), and other areas.

As the demand for data bandwidth increases (as shown in Fig. 1.2) driven by the phenomenal growth of the Internet, the move to optical networking is the focus of new technologies.

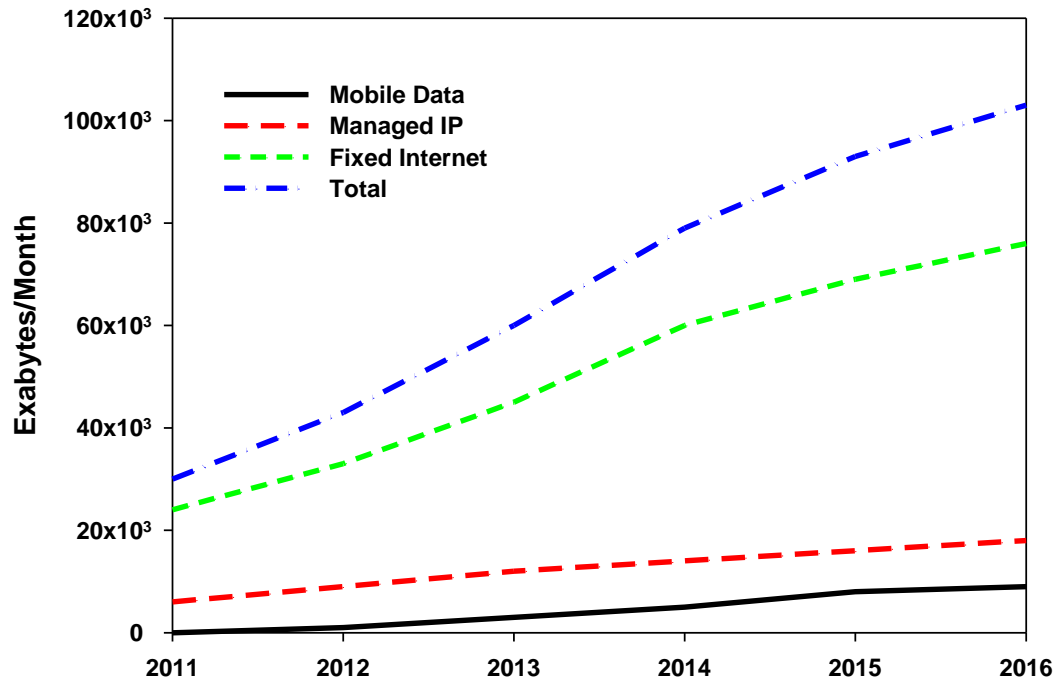


Fig. 1. 2: IP traffic growth between 2011 and 2016 (projected) (After Cisco 2012).

The immense potential of internet traffic, which is projected to be 90,000 Exabytes or greater per month in 2016, implies that there are extraordinary possibilities for future fibre optic applications. Today optical fibre cables are the backbone of the telecommunication system, which has led to high speed broadband Internet and affordable long distance telephone calls. Broadband service available to a mass market opens up a wide variety of interactive communications for both consumers and businesses bringing to reality interactive video networks, interactive banking and shopping from home and interactive distance learning (Goff 2002).

### 1.1.1 Optical Fibre Communications Systems

After a period of intensive research from 1975 to 1980 the first commercial optical fibre communication system was developed. This system operated at a wavelength around  $0.8 \mu\text{m}$  and it used GaAs semiconductor lasers. This first generation system operated at

a bit rate of 45 Mbit/s with repeater spacing of up to 10 km (Agrawal 2002). The second generation optical fibre communication system was then developed for commercial use in the early 1980s and this system operated at 1.3  $\mu\text{m}$  using the InGaAsP semiconductor lasers. These systems were initially limited by dispersion but in 1981 the single mode fibre was revealed which greatly improve system performance. By 1987 these systems were operating at bit rates of up to 1.7 Gb/s with repeater spacing up to 50 km (Agrawal 2002). TAT-8 was developed as the first undersea fibre optic link between the United States and Europe and this cable is more than 5,600 km in length and was the first transatlantic cable to use optical fibres. It was designed to handle a mix of information formats. At its inauguration it had an estimated lifetime in excess of 20 years. TAT-8 was the first of a new class of cables even though it had already been used in long distance land and short distance undersea operations. Its installation was preceded by extensive deep water experiments and trials conducted in the early 1980s to demonstrate the project's feasibility (Agrawal 2002). The third generation of optical fibre systems operated at 1.55 $\mu\text{m}$  and had the lowest loss of about 0.2dB/km. They achieved this despite earlier difficulties with pulse spreading at that wavelength using conventional InGaAsP semiconductor lasers this is because scientists overcame this difficulty by using dispersion shifted fibres designed to have minimal dispersion at 1.55 $\mu\text{m}$  or by limiting the laser spectrum to a single longitudinal mode. These developments eventually allowed third generation systems to operate commercially at 2.5 Gbit/s with repeater spacing in excess of 100 km (Agrawal 2002). The fourth generation of optical fibre communication systems is the one to use optical amplification rather than electrical amplification to reduce the need for repeaters and it also employed wavelength division multiplexing to increase fibre capacity. These two improvements caused a revolution that resulted in the doubling of system capacity every 6 months starting in 1992 until a bit rate of 10 Tb/s was reached by 2001. By the year 2006, bit rates of up to 14 Tbit/s have been reached over a single 160 km line using optical amplifiers (Agrawal 2002) but over 90,000 Exabytes/month data rates is projected by 2016. The fifth generation of fibre optic communications is all about the extension of the wavelength range over which a WDM system can operate. The conventional wavelength window, known as the C band, covers the wavelength range 1.53-1.57 $\mu\text{m}$ , and the new dry fibre has a low loss window promising an extension of that range to 1.30-1.65 $\mu\text{m}$ . Other developments with this generation of optical fibre system include

the concept of optical solitons, pulses that preserve their shape by counteracting the effects of dispersion with the nonlinear effects of the fibre by using pulses of a specific shape (Agrawal 2002).

## 1.2 The Optical Fibre

An optical fibre is an optical waveguide made usually of glass (silica) or plastic and it is used to guide light along its length. It achieves this by exploiting the principle of total internal reflection whereby the light is confined within the core of the optical fibre as light travels along its length. The core has a refractive index slightly higher than that of the cladding and this enables the light to be trapped within the core as it travels along the length of the fibre as can be seen in Fig. 1.3. Today, optical fibre has largely replaced metal wires in telecommunications because of their higher data rates, low loss, immunity to electromagnetic interference, better security amongst others. Optical fibres which support a single propagation path or a single mode along the guide are called Single Mode Fibres (SMF), likewise, an optical fibre which supports multiple modes is known as Multimode Fibres (MMF). Single mode fibres are used in applications requiring very high data rates and longer distances whereas low-cost multimode fibres are used for shorter distances with lower data rates.

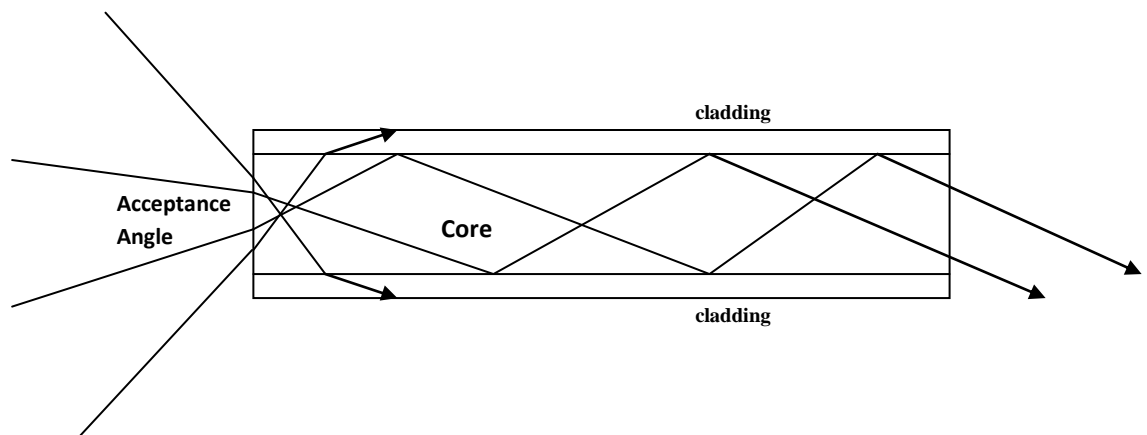


Fig. 1. 3: The propagation of light through a multi-mode optical fibre

### 1.2.1 Index of Refraction

The index of refraction is a way of measuring the speed of light in a material. Light travels fastest in vacuum such as outer space. The actual speed of light in a vacuum is

given as  $c = 299,792$  kilometres per second or 186,282 miles per second. Index of refraction is calculated by dividing the speed of light in a vacuum by the speed of light in some other medium. The index of refraction of a vacuum is therefore 1 by definition. The typical value of refractive index of silica is 1.445 (Agrawal 2002). The greater the refractive index, the more slowly light travels in that medium.

### 1.2.2 Critical Angle

Snell's law gives the relationship between the incident and refracted rays at a boundary between two different media with different refractive indices. It is expressed as

$$n_1 \sin \theta_1 = n_2 \sin \theta_2 \quad (1.2)$$

Where  $n_1$  and  $n_2$  are the refractive indices of the materials and  $\theta_1$  and  $\theta_2$  are the angles of incidence and refraction. The critical angle is the angle of incidence above which total internal reflection occurs. The angle of incidence is measured with respect to the normal at the refractive boundary. The critical angle  $\theta_c$  is given by:

$$\theta_c = \sin^{-1} \left( \frac{n_2}{n_1} \right) \quad (1.3)$$

Where  $n_2$  is the refractive index of the less dense medium and  $n_1$  is the refractive index of the denser medium.

If the incident ray is precisely at the critical angle, the refracted ray is tangent to the boundary at the point of incidence.

### 1.2.3 Total Internal Reflection

When light crosses a boundary between materials with different refractive indices, the light beam will be partially refracted at the boundary surface and partially reflected. However, if the angle of incidence is larger; that is the ray is closer to being parallel to the boundary than the critical angle, the angle of incidence at which light is refracted such that it travels along the boundary, then the light will stop crossing the boundary altogether and instead be totally reflected back internally. This can only occur where light travels from a medium with a higher refractive index to one with a lower refractive

index as shown in Fig. 1.4. For example, it will occur when passing from glass to air, but not when passing from air to glass (Goure and Verrier 2002).

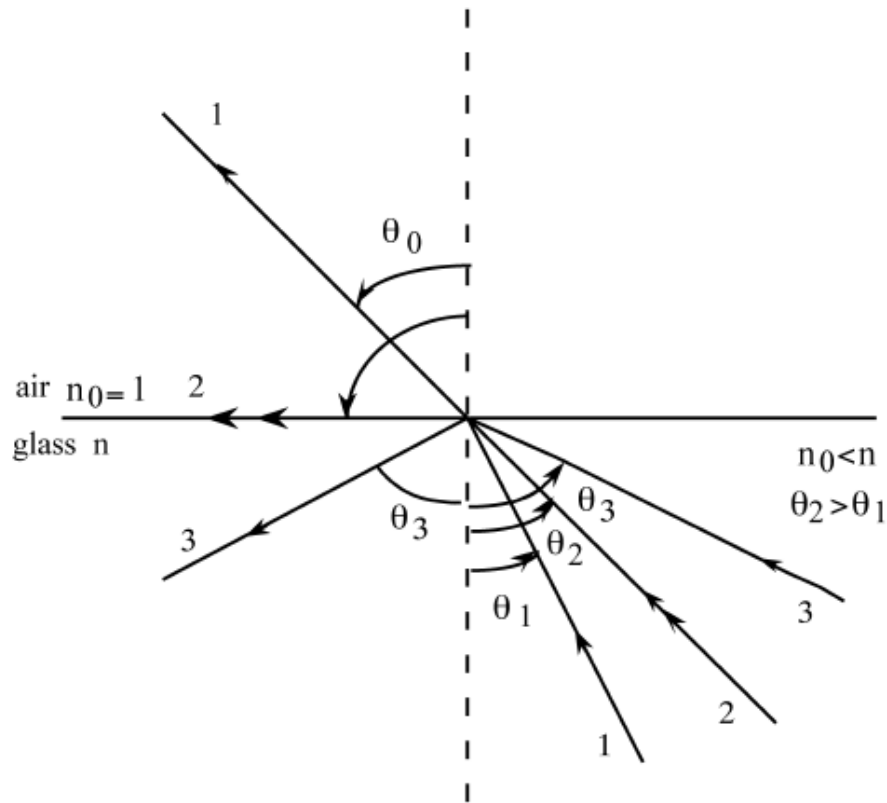


Fig. 1. 4: The larger the angle to the normal, the smaller is the fraction of light transmitted, until the angle when total internal reflection occurs (Goure and Verrier 2002)

As an example, consider light coming from a dense medium like glass into a less dense medium like air. When the light coming from the glass strikes the surface, part will be reflected and part will be refracted. Measured with respect to the normal line perpendicular to the surface, the reflected light comes off at an angle equal to that at which it entered at as shown by path 1 with angle  $\theta_1$ , while that for the refracted light, that is angle  $\theta_0$ , is larger than the incident angle. In fact the greater the incident angle, the more the refracted light bends away from the normal. As can be seen from Fig. 1.4 above, increasing the angle of incidence from path “1” to “2” with angle  $\theta_2$  will eventually reach a point where the refracted angle is  $90^\circ$ , at which point the light appears to emerge along the surface between the glass and air. This angle,  $\theta_2$  is also known as the critical angle. If the angle of incidence is increased further to path “3”

with angle  $\theta_3$  the refracted light cannot leave the glass and gets completely reflected. The interesting thing about total internal reflection is that it really is total. That is 100% of the light gets reflected back into the more dense medium, as long as the angle at which it is incident to the surface is equal or larger than the critical angle (Goure and Verrier 2002).

The light must strike the boundary with an angle greater than the critical angle and because of this only light that enters the fibre within a certain range of angles can travel down the fibre without leaking out. This range of angles is called the acceptance cone of the fibre as shown in Fig. 1.3. The size of this acceptance cone is a function of the refractive index difference between the fibre's core and cladding (Goure and Verrier 2002).

In simpler terms there is a maximum angle from the fibre axis at which light may enter the fibre so that it will propagate or travel in the core of the fibre. The size of this maximum angle of incidence is the numerical aperture (NA) of the fibre and  $\theta_c$  is the critical angle (Fig. 1.5) cone,  $n_1$  and  $n_2$  is the refractive indices of the core and cladding respectively. The numerical aperture can be expressed as

$$NA = \sqrt{n_2^2 - n_1^2} \quad (1.4)$$

Fibre with a larger NA requires less precision to splice and work with than fibre with a smaller NA (Goure and Verrier 2002).

#### 1.2.4 Principle of Wave Guidance in a Fibre

An optical fibre is a cylindrical dielectric waveguide that transmits light along its axis by the process of total internal reflection. The fibre consists of a core surrounded by a cladding layer. To confine the optical signal in the core, the refractive index of the core must be greater than that of the cladding. The boundary between the core and cladding may be abrupt, which is referred to as step index fibre as in Fig. 1.5(a) or it could be gradual and it is referred to as graded index fibre as can be seen in Fig. 1.5(b).

### 1.3 Multimode Fibre

Optical fibres with large core diameters, that are greater than  $10\mu\text{m}$ , may be analyzed by geometric optics. Such optical fibres are more likely to be multimode fibres from the electromagnetic analysis. This is because the  $V$  parameter (which is the normalised optical frequency) is likely above 2.405 (as discussed in more detail in Chapter 6). In a step index multimode fibre, rays of light are guided along the fibre core by total internal reflection. Rays that meet the core-cladding boundary at an angle (measured relative to a line normal to the boundary), greater than the critical angle for this boundary, are completely reflected. The critical angle (minimum angle for total internal reflection) is determined by the difference in index of refraction between the core and cladding materials. Rays that meet the boundary at a low angle are refracted from the core into the cladding and do not confine light and hence information along the fibre. The critical angle also determines the acceptance angle of the fibre, often related to the numerical aperture. A high numerical aperture allows light to propagate down the fibre in rays both close to the axis and at various angles, allowing efficient coupling of light into the fibre. However, this high numerical aperture increases the amount of dispersion as rays at different angles have different path lengths and therefore take different times to traverse along the fibre. A low numerical aperture may therefore be desirable (Poli *et al.* 2007).

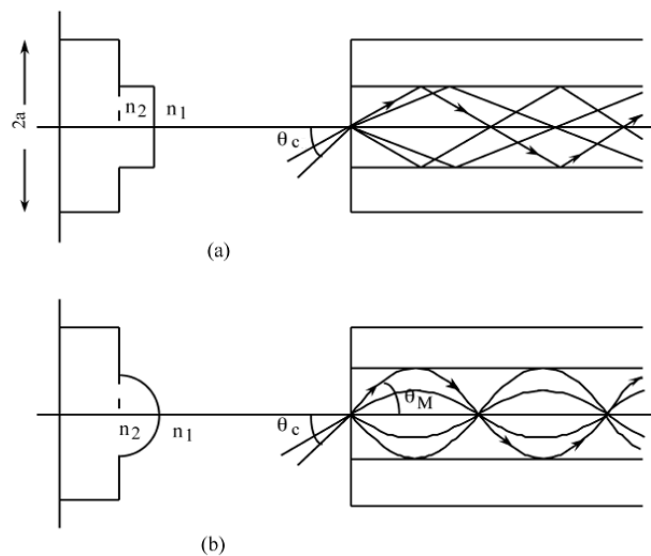


Fig. 1. 5: Optical fibre types (a) step index fibre (b) graded index fibre (Goure and Verrier 2002).



In a graded index fibre, the refractive index in the core decreases continuously between the axis and the cladding. This causes light rays to bend smoothly as they approach the cladding rather than reflecting abruptly from the core-cladding boundary. The resulting curved paths reduce multipath dispersion because high angle rays pass more through the lower index periphery of the core rather than the high index centre. The index profile is chosen to minimize the difference in axial propagation speeds of the various rays in the fibre. This ideal index profile is very close to a parabolic relationship between the index and the distance from the axis (Poli *et al.* 2007).

## 1.4 Single Mode Fibre

Fibre with a core diameter less than about ten times the wavelength of the propagating light cannot be modelled using geometric optics. Instead, it must be analyzed as an electromagnetic structure, by solution of Maxwell's equations as reduced to the electromagnetic wave equation. As an optical waveguide, the fibre may support one or more confined transverse modes by which light can propagate along the fibre. Fibre supporting only one mode is called single mode or mono mode fibre. The behaviour of larger core multimode fibre can also be modelled using the wave equation which shows that such fibre supports more than one mode of propagation. The results of such modelling of multi-mode fibre approximately agree with the predictions of geometric optics if the fibre core is large enough to support more than a few modes (Poli *et al.* 2007).

The waveguide analysis shows that the light energy in the fibre is not completely confined in the core. Instead, especially in single mode fibres a significant fraction of the energy in the bound mode travels in the cladding as an evanescent wave.

The most common type of single mode fibre has a core diameter of 8 to 10  $\mu\text{m}$ , with refractive index difference between core and cladding around 0.36% and is designed for use in the near infrared. Multimode fibre by comparison, is manufactured with core diameters as small as 50 micrometres and as large as hundreds of micrometres (Goure and Verrier 2002).

## 1.5 Special Purpose Fibre

Some special purpose optical fibre is constructed with a non-cylindrical core and/or cladding layer, usually with an elliptical or rectangular cross section. These include polarization maintaining fibre and fibre designed to suppress whispering gallery mode propagation like the suspended core micro-structured fibre.

Photonic crystal fibre is made with a regular pattern of index variation, in the form of air-holes that run along the length of the fibre. Such fibre uses diffraction effects instead of or in addition to total internal reflection to confine light to the fibre's core. The properties of the fibre can be tailored to a wide variety of applications and it is the focus of this thesis.

## 1.6 Optical Fibre Manufacture

Glass optical fibres are almost always made from silica but some other materials, such as fluoroaluminates, fluoroaluminate, and chalcogenide glasses are also used for longer wavelength infrared applications. Typically the difference between core and cladding is less than one percent (Goure and Verrier 2002).

Plastic optical fibres (POF) are commonly step index multimode fibres with a core diameter of 0.5mm or larger. POF typically have higher attenuation coefficients than glass fibres, 1 dB/m or higher and this high attenuation limits the range of POF based systems (Poli *et al.* 2007). Plastic optical fibres are low cost and used for short distance links.

Standard optical fibres are made by first constructing a large diameter preform with a carefully controlled refractive index profile and then pulling the preform to form the long, thin optical fibre. The preform is commonly made by one of the three chemical vapour deposition methods: inside vapour deposition, outside vapour deposition and vapour axial deposition (Poli *et al.* 2007).

With inside vapour deposition, a hollow glass tube approximately 40 cm in length known as a "preform" is placed horizontally and rotated slowly on a lathe and gases such as silicon tetrachloride ( $\text{SiCl}_4$ ) or germanium tetrachloride ( $\text{GeCl}_4$ ) are injected

with oxygen at the end of the tube. The gases are then heated by means of an external hydrogen burner, bringing the temperature of the gas up to 1900 Kelvin, where the tetrachlorides react with oxygen to produce silica or germania (germanium oxide) particles. When the reaction conditions are chosen to allow this reaction to occur in the gas phase throughout the tube volume, in contrast to earlier techniques where the reaction occurred only on the glass surface, this technique is called modified chemical vapour deposition (Goure and Verrier 2002).

The oxide particles then agglomerate to form large particle chains which subsequently deposit on the walls of the tube as soot. The deposition is due to the large difference in temperature between the gas core and the wall causing the gas to push the particles outwards; termed thermophoresis. The torch is then traversed up and down the length of the tube to deposit the material evenly. After the torch has reached the end of the tube, it is then brought back to the beginning of the tube and the deposited particles are then melted to form a solid layer. This process is repeated until a sufficient amount of material has been deposited. For each layer the composition can be modified by varying the gas composition, resulting in precise control of the finished fibre's optical properties (Goure and Verrier 2002).

In outside vapour deposition or vapour axial deposition, the glass is formed by flame hydrolysis, a reaction in which silicon tetrachloride and germanium tetrachloride are oxidized by reaction with water ( $H_2O$ ) in an oxyhydrogen flame. In outside vapour deposition the glass is deposited onto a solid rod, which is removed before further processing. In vapour axial deposition, a short seed rod is used, and a porous preform, whose length is not limited by the size of the source rod, is built up on its end. The porous preform is consolidated into a transparent, solid preform by heating to about 1800 Kelvin.

The preform, however it may have been constructed, is then placed in a device known as a drawing tower, where the preform tip is heated and the optic fibre is pulled out as a string. By measuring the resultant fibre diameter, the tension on the fibre can be controlled to maintain the fibre thickness (Goure and Verrier 2002).

## 1.7 Practical Issues with Optical Fibres

In practical applications of optical fibres, the cladding is usually coated with a tough resin buffer layer. This layer might still be surrounded by a jacket layer made of plastic which helps to add strength to the fibre but without affecting its guidance properties. Rigid fibre assemblies sometimes put light absorbing dark glass between the fibres to prevent light that leaks out of a fibre from entering into another fibre. This reduces cross talk between the fibres or reduces flare in fibre bundle imaging applications. Modern cables come in a wide variety of sheathings and armour designed for applications such as direct burial in trenches, dual use as power lines and installation in conduit, lashing to aerial telephone poles, submarine installation or insertion in paved streets. In recent years the cost of small fibre count pole mounted cables has greatly decreased due to the high Japanese and South Korean demand for fibre to the home installations (Agrawal 2002).

Fibre cable can be very flexible but traditional fibre loss increases greatly if the fibre is bent with a radius smaller than around 30 mm. This creates a problem when the cable is bent around corners or wound around a spool, making FTTH installations more complicated. "Bendable fibres", targeted towards easier installation in home environments, have been standardized as ITU-T G.657. This type of fibre can be bent with a radius as low as 7.5 mm without adverse impact. Even more bendable fibres have been developed. Bendable fibre may also be resistant to fibre hacking, in which the signal in a fibre is surreptitiously monitored by bending the fibre and detecting the leakage (Agrawal 2008).

### 1.7.1 Attenuation in Optical Fibres

Fibre attenuation, which necessitates the use of amplification systems, is caused by a combination of material absorption, Rayleigh scattering, Mie scattering, and connection losses. Although material absorption for pure silica is only around 0.03 dB/km (modern fibre has attenuation around 0.2 dB/km) (Agrawal 2002), impurities in the original optical fibres caused attenuation of about 1000 dB/km. Other forms of attenuation are caused by physical stresses to the fibre, microscopic fluctuations in density and imperfect splicing techniques (Goure and Verrier 2002; Poli *et al.* 2007).

### 1.7.2 Dispersion in Optical Fibres

For modern glass optical fibre, the maximum transmission distance is limited not by attenuation but by dispersion or spreading of optical pulses as they travel along the fibre. Dispersion in optical fibres is caused by a variety of factors. Intermodal dispersion caused by the different axial speeds of different transverse modes, limits the performance of multimode fibre. Because single mode fibre supports only one transverse mode, intermodal dispersion is eliminated (Goure and Verrier 2002).

In single mode fibre performance is primarily limited by chromatic dispersion (also called group velocity dispersion), which occurs because the index of the glass varies slightly with the wavelength of the light and light from real optical transmitters necessarily has nonzero spectral width (due to modulation). Polarization mode dispersion, another source of limitation, occurs because although the single mode fibre can sustain only one transverse mode, it can carry this mode with two different polarizations and slight imperfections or distortions in a fibre can alter the propagation velocities for the two polarizations. This phenomenon is called fibre birefringence and can be counteracted by polarization maintaining optical fibre. Dispersion limits the bandwidth of the fibre because the spreading optical pulse limits the rate that pulses can follow one another on the fibre and still be distinguishable at the receiver.

Some dispersion, notably chromatic dispersion, can be removed by a dispersion compensator. This works by using a specially prepared length of fibre that has the opposite dispersion to that induced by the transmission fibre and this sharpens the pulse so that it can be correctly decoded by the electronics (Poli *et al.* 2007).

### 1.7.3 Terminating and Splicing of Optical Fibres

Optical fibres are connected to terminal equipment by optical fibre connectors. These connectors are usually of a standard type such as FC, SC, ST, LC or MTRJ.

Optical fibres may be connected to each other by connectors or by splicing, which mean joining two fibres together to form a continuous optical waveguide. The generally accepted splicing method is arc fusion splicing, which melts the fibre ends together with an electric arc (Goure and Verrier 2002).

Fusion splicing is done with a specialized instrument that typically operates as follows: The two cable ends are fastened inside a splice enclosure that will protect the splices and the fibre ends are stripped of their protective polymer coating (as well as the sturdier outer jacket, if present). The ends are cleaved (cut) with a precision cleaver to make them perpendicular and are placed into special holders in the splicer. The splice is usually inspected via a magnified viewing screen to check for cleaves before and after the splice. The splicer uses small motors to align the end faces together and emits a small spark between electrodes at the gap to burn off dust and moisture. Then the splicer generates a larger spark that raises the temperature above the melting point of the glass, fusing the ends together permanently. The location and energy of the spark is carefully controlled so that the molten core and cladding don't mix and this minimizes optical loss. A splice loss estimate is measured by the splicer, by directing light through the cladding on one side and measuring the light leaking from the cladding on the other side. A splice loss under 0.1 dB is typical. The complexity of this process makes fibre splicing much more difficult than splicing copper wire (Goure and Verrier 2002).

Mechanical fibre splices are designed to be quicker and easier to install but there is still the need for stripping, careful cleaning and precision cleaving. The fibre ends are aligned and held together by a precision made sleeve, often using a clear index matching gel that enhances the transmission of light across the joint. Such joints typically have higher optical loss and are less robust than fusion splices, especially if the gel is used. All splicing techniques involve the use of an enclosure into which the splice is placed for protection afterward (Goure and Verrier 2002).

Fibres are terminated in connectors so that the fibre end is held at the end face precisely and securely. A fibre optic connector is basically a rigid cylindrical barrel surrounded by a sleeve that holds the barrel in its mating socket. The mating mechanism can be "push and click", "turn and latch" ("bayonet"), or screw-in (threaded). A typical connector is installed by preparing the fibre end and inserting it into the rear of the connector body. Quickset adhesive is usually used so the fibre is held securely and a strain relief is secured to the rear. Once the adhesive has set, the fibre's end is polished to a mirror finish. Various polish profiles are used depending on the type of fibre and the application. For single mode fibre, the fibre ends are typically polished with a slight curvature such that when the connectors are mated the fibres touch only at their cores.

This is known as a physical contact (PC) polish. The curved surface may be polished at an angle to make an angled physical contact (APC) connection. Such connections have higher loss than PC connections but greatly reduced back reflection, because light that reflects from the angled surface leaks out of the fibre core; the resulting loss in signal strength is known as gap loss. APC fibre ends have low back reflection even when disconnected (Goure and Verrier 2002).

#### **1.7.4 Coupling Optical Fibres in Free Space**

It often becomes necessary to align an optical fibre with another optical fibre or an optical device such as a light emitting diode, a laser diode or an optoelectronic device such as a modulator. This can involve both carefully aligning the fibre and placing it in contact with the device to which it is to couple or can use a lens to allow coupling over an air gap. In some cases the end of the fibre is polished into a curved form that is designed to allow it to act as a lens called lensed fibre.

In a laboratory environment, the fibre end is usually aligned to the device or other fibre with a fibre launch system that uses a microscope objective lens to focus the light down to a fine point. A precision translation stage (micro-positioning table) is used to move the lens, fibre or device to allow the coupling efficiency to be optimized (Goure and Verrier 2002).

#### **1.7.5 Optical Fibre Fuse**

At high optical intensities, above 2 Megawatts per square centimetre, when a fibre is subjected to a shock or is otherwise suddenly damaged, a fibre fuse can occur. The reflection from the damage vaporizes the fibre immediately before the break and this new defect remains reflective so that the damage propagates back toward the transmitter. The open fibre control system, which ensures laser eye safety in the event of a broken fibre, can also effectively halt propagation of the fibre fuse. In situations, such as undersea cables, where high power levels might be used without the need for open fibre control, a fibre fuse protection device at the transmitter can break the circuit to prevent any damage.

## 1.8 Advantages of Optical Fibres

Fibre optic transmission systems offer a wide range of benefits not offered by traditional copper wires or coaxial cables. The small size and the fact that no electrical power is needed at the remote location give fibre optic sensor advantages to conventional electric sensor in certain applications.

Optical fibre offers enormous bandwidth and it takes a lot less room. A copper bundle can be replaced with one single fibre strand.

Fibre optics has several advantages over traditional metal communication lines such as:

- **High data rates:** fibre optic networks operate at high speeds – up into the gigabits and more recently into the terabits region as well.
- **Thinner diameters:** optical fibres can be drawn to smaller diameters than copper wire.
- **High bandwidth:** fibre optic cables have a much greater bandwidth than metal cables. Because optical fibres are thinner than copper wires, more fibres can be bundled into a given diameter cable than copper wire. This allows more phone lines to go over the same cable. This means that fibre cables can carry more data over greater distances and with greater fidelity than either copper wire or coaxial cable.
- **Easier maintenance:** fibre optic cables cost much less to maintain.
- **Invulnerability:** optic fibre is totally immune to virtually all kinds of interference, including lighting, electromagnetic noise such as radios, motors or other nearby cables and will not conduct electricity. It can therefore come in direct contact with high voltage electrical equipment and power lines.
- **Less expensive:** several miles of optical cable can be made cheaper than equivalent lengths of copper wire.
- **Less signal degradation:** the loss of signal in optical fibre is less than in copper wire.
- **No light interference between fibres:** electrical signals in copper wires can interfere with each other; however, light signals from one fibre do not interfere



with those of other fibres in the same cable. This means clearer phone conversations or TV reception.

- **Lower power consumption:** because signals in optical fibres degrade less, lower-power transmitters can be used instead of the high-voltage electrical transmitters needed for copper wires. Again, this saves the provider and its client's money.
- **Digital signals:** data can be transmitted digitally (the natural form for computer data, useful in computer networks) rather than analogically.
- **Non-flammable:** because no electricity is passed through optical fibres, there is no fire hazard. Since the only carrier in the fibre is light, there is no possibility of a spark from a broken fibre. Even in the most explosive of atmosphere, there is no fire hazard and no danger of electrical shock to personnel repairing broken fibres.
- **Lightweight:** an optical cable weighs less than a comparable copper wire cable. A fibre cable even one that contains many fibres is usually much smaller and lighter in weight than a wire or coaxial cable with similar information carrying capacity. It is easier to handle and install and uses less channel space.
- **Flexibility:** fibre optics is very flexible to transmit and receive light.
- **Secure communication:** fibre optic cable is ideal for secure communications systems because it is very difficult to tap but very easy to monitor. In addition, there is absolutely no electrical radiation from a fibre.
- **Immunity to chemical reactions:** as the basic fibre is made of glass, it will not corrode and is unaffected by most chemicals. It can be buried directly in most kinds of soil or exposed to most corrosive atmospheres in chemical plants without significant concern. Fibre optic cables are virtually unaffected by outdoor atmospheric conditions, allowing them to be lashed directly to telephone poles or existing electrical cables without concern for extraneous signal pickup (Keiser 2000; Myabae and Scheiner 2002).

## 1.9 Applications of Optical Fibres

Optical fibre is used by many telecommunications companies to transmit telephone signals, internet communication and cable television signals (Poli *et al.* 2007). Due to

much lower attenuation and interference, optical fibre has large advantages over existing copper wire in long-distance and high-demand applications. However, infrastructure development within cities was relatively difficult and time-consuming and fibre-optic systems were complex and expensive to install and operate. Due to these difficulties, fibre optic communication systems have primarily been installed in long distance applications where they can be used to their full transmission capacity, offsetting the increased cost (Goure and Verrier 2002). Since the year 2000, the prices for fibre-optic communications have dropped considerably. The price for rolling out fibre to the home has currently become more cost effective than that of rolling out a copper based network.

Since 1990, when optical amplification systems became commercially available, the telecommunications industry has laid a vast network of intercity and transoceanic fibre communication line. By 2002, an intercontinental network of 250,000 km of submarine communications cable with a capacity of 2.56 Tb/s was completed and although specific network capacities are privileged information, telecommunications investment reports indicate that network capacity has increased dramatically since 2002.

## **1.10 Aims and Objectives of the Thesis**

The broad aim of the work undertaken in this thesis is the design, characterization and optimization of certain Photonic Crystal Fibres (PCFs) for potential uses in several practical applications and showing an improvement in performance over that seen with current optical systems. The analysis required for such work was undertaken by implementing the rigorous full vectorial Finite Element (FEM) **H**-field formulation together with the conformal transformation and the Perfectly Matched Layer (PML) boundary. PCF designs have unique characteristics and offer several advantages over conventional optical fibre as well as other optical waveguides. PCF is typically made from a single material which allows a lot of flexibility and has a very high index contrast between the core and the cladding and the fibre can remain single moded over a wide range of wavelengths.

In light of these unique characteristics offered by PCF designs, the research work set out in this thesis had the following specific objectives:

1. To calculate the leakage and bending losses associated with the PCF, for several different designs, by varying the pitch ( $\Lambda$ ) and diameter of air-holes ( $d$ ) and thereby optimising those designs that would provide the lowest loss and that would be less susceptible to bending for telecommunications applications at wavelength of  $1.55\mu\text{m}$ .
2. Having established the optimal PCF designs and bending radii for low loss transmission, next, the changing of the design where the first ring of air-holes were altered to increase the birefringence of the PCF for single mode single polarization guidance was done. This was also enhanced by increasing the bending radius of the PCF.
3. An important issue that needed to be addressed is how to couple the PCF to a conventional single mode fibre or to other waveguides like the erbium doped fibre amplifier. This was investigated using the Least Squares Boundary Residual (LSBR) method in conjunction with the FEM and the power transmission at the discontinuity boundary of the butt coupling between the PCF and conventional fibre were obtained.
4. The application of PCF designs to the Terahertz (THz) region in the development of a low loss waveguide was also investigated. Several polymer materials were analysed for this purpose and the conventional PCF was compared to an equiangular spiral PCF arrangement.
5. A novel design of porous core PCF was considered, aimed at further reducing the leakage and bending losses in the THz regime was also investigated which provided some very unique guiding properties.
6. To disseminate the results of the work to the wider international community through high quality Journal and Conference papers.

### **1.11 Structure of the Thesis**

The thesis has been structured as follows to present the key elements in the most coherent and logical way:

Chapter One discusses optical communications in general starting with looking back at the history of the development over the years and reflects on the applications and advantages of optical communications. The guidance principles of optical fibres and

the types of guidance for the different types of optical fibre were also discussed. The procedures for manufacturing optical fibres as well as the practical issues associated optical fibres were also included. The aims and objectives of the thesis are set out systematically as is the structure of the thesis.

Chapter Two focuses the discussion on Photonic Crystal Fibres (PCF) which are the main waveguides analysed in this thesis. It also discussed the history of its development over the years and the major applications and advantages of PCF. The guidance principle and the manufacturing process of the PCF were also discussed. The uniqueness of the PCF as a waveguide and issues that affect the PCF were presented. The method for calculating the bending of the PCF with conformal transformation which is used in conjunction with the Finite Element Method was also presented.

Chapter Three discusses the various techniques used in the analysis of optical waveguides but with a focus on the Finite Element Method (FEM) which was the predominant method used in this work. Some other methods that are used by other research groups were presented very briefly. However, in this thesis, the Finite Element Method together with the conformal transformation was used for the analyses. The Perfectly Matched Layer (PML) is used as the boundary of the computational domain and the method of suppressing spurious solutions by implementing the penalty factor was also presented.

Chapter Four presents the results of mode degeneration in PCF which was observed by simulations to calculate the bending losses associated with the PCFs studied. As the bending radius is increased there is a steady increase in the bending loss. However, at some very low bending radii there is a more rapid increase in the bending radius and some oscillatory behaviour was observed when the bending radius is lowered even further which is as a result of the mode degeneration. This effect is seen at different bending radii for different PCF designs considered.

Chapter Five presents the results of a design of polarization maintaining PCF obtained by designing and simulating highly birefringent PCF. By increasing the size of some of the air-holes in the first ring of the cladding, the round symmetry of the core is destroyed thereby leading to the core being more elliptical. This ensures the guidance of

a single polarization at a time in the PCF. Also, by bending the PCF, the birefringence can be further enhanced.

Chapter Six concerns the method of butt coupling a PCF to a Single Mode Fibre (SMF) with reduced losses. This numerical simulation was carried out using the FEM and the Least Squares Boundary Residual (LSBR) method. By operating the PCF close to cutoff the mode area expands more into the cladding region making a larger mode area. Also by introducing larger air-hole diameters in the outermost ring of the cladding, this expansion can be stabilized over a range of tapered PCF cross-section hence ensuring good butt coupling even with manufacturing deviations.

Chapter Seven introduces the terahertz (THz) regime and design of Equiangular Spiral PCF (ES-PCF) arrangement in polymer materials; Teflon and TOPAS. The bending and leakage losses were calculated. There are few waveguides available in this frequency range and the PCF made of these polymer materials aims to fill in that gap. The waveguides were designed using the ES-PCF and then an attempt was made to compare them to the conventional hexagonal PCF. Also, a new design is considered, that of a hexagonal PCF with a porous core whereby the core is made up of tiny air-holes similar to the relatively larger air-holes found in the cladding. The aim is to reduce the transmission losses by having some fraction of the power in the air-holes in the core. The results of the numerical experiments carried out are presented.

In Chapters Three to Seven, a review of the relevant literature is presented at the start of each Chapter to enable the background to the research issues for that Chapter to be considered and the key research questions to be developed and then discussed in the work reported subsequently in the Chapter. Chapter Eight then provides an overview of the responses to these research issues and key conclusions of the research done which lead to suggestions for new directions and further research work to continue in this field.

## CHAPTER TWO: Photonic Crystal Fibre

### 2.0 Abstract

The fundamental issues relating to the Photonic Crystal Fibres (PCF) are discussed in this chapter starting with its history and its development. The stack-and-draw fabrication technique used in manufacturing of PCF is presented. The guidance principle involved with PCF as well as the advantages and applications of the PCF are discussed. The confinement and bending losses and the conformal transformation used in conjunction with the Finite Element Method is introduced.

### 2.1 Photonic Crystal Fibre (PCF)

Photonic crystals have been the focus of increasing scientific and technological interests since the pioneering works of Eli Yablonovitch (Yablonovitch 1987) and Sajeev John (John 1987) because of their unique properties and numerous potential applications. Research in the field of photonic crystals was stimulated by the prediction of Photonic Bandgap (Yablonovitch 1987) which was the only guiding mechanism considered for this new class of optical fibres. Later, researchers discovered that by microstructuring and including air-holes in the fibre, these devices could provide revolutionary features using the simpler and more conventional principle of total internal reflection (Broeng *et al.* 1998).

The photonic crystal fibre was first demonstrated by Professor Philip Russell in 1995 at the University of Bath (Knight *et al.* 1996b). Back in the 1920s, John Logie Baird had the idea of using hollow tubes to transmit images in an early incarnation of television. Recently, the idea of transmitting light through hollow waveguides has become cutting edge technology once again in the form of “Holey Fibres” (Williamson 2002) which has brought about revolutionary changes in the fibre optics world. Professor Philip Russell has spent the years designing the so called holey fibre and some years later at the University of Bath, he and a team of fellow researchers built a prototype that proved that holey fibre could transmit light through a hollow, air-filled core (Lindstrom 2001).

The beginning of research on PCF can be traced back over past decade that has seen PCF cut a large swath across a variety of disciplines. Many exciting phenomena have

been reported since the first results on photonic crystal fibres (Knight *et al.* 1996a; Knight *et al.* 1996b). The most common type of PCF, which was first fabricated in 1996 by Prof. Philip Russell and his research group, consists of pure silica core with an array of air-holes running along the entire fibre length (Knight *et al.* 1996a; Knight *et al.* 1996b).

Over the past few years, photonic crystal fibres technology has evolved from a strong research-oriented field to a commercial technology providing characteristics such as single-mode operation from UV to IR spectral regions, large mode areas with core diameters larger than 20 $\mu$ m and highly nonlinear performance with optimized dispersion properties (Kristiansen 2002).

In general, such fibres have a cross-section (normally uniform along the fibre length) microstructured from two or more materials, most commonly arranged periodically over much of the cross-section, usually as a "cladding" surrounding a core (or several cores) where light is confined (Agrawal 2008). For example, the fibres first demonstrated by Russell consisted of a hexagonal lattice of air-holes in a silica fibre, with a solid (1996) or hollow (1998) core at the centre where light is guided. Other arrangements include concentric rings of two or more materials, first proposed as "Bragg fibres" by Yeh and Yariv (Yeh *et al.* 1978), a variant of which was recently fabricated by Temelkuran *et al.* (Temelkuran *et al.* 2002).

Photonic crystal fibre can also be classified in different categories, like photonic band gap fibre (PCFs that confine light by band gap effects), holey fibre (PCFs using air-holes in their cross-sections), hole-assisted fibre (PCFs guiding light by a conventional higher index core modified by the presence of air-holes), and the Bragg fibre (photonic band gap fibre formed by concentric rings of multilayer film). Photonic crystal fibres can be designed to carry higher power than conventional fibres. Their wavelength dependent properties can be manipulated to improve their performance in certain applications and they have the ability to be continuously single moded amongst others (Saitoh and Koshiba 2003). Band gap fibres with hollow cores can potentially circumvent limits imposed by available materials, for example to create fibres that guide light at wavelengths for which transparent materials are not available because the light is primarily in the air, not in the solid materials. Another potential advantage of a

hollow core is that one can dynamically introduce materials into the core such as a gas that is to be analyzed for the presence of some substance (Poli *et al.* 2007; Agrawal 2008). Figure 2.1 shows a typical 2-D cross-sectional structure of a PCF in which the solid pure silica core region is surrounded by a cladding region containing air-holes.

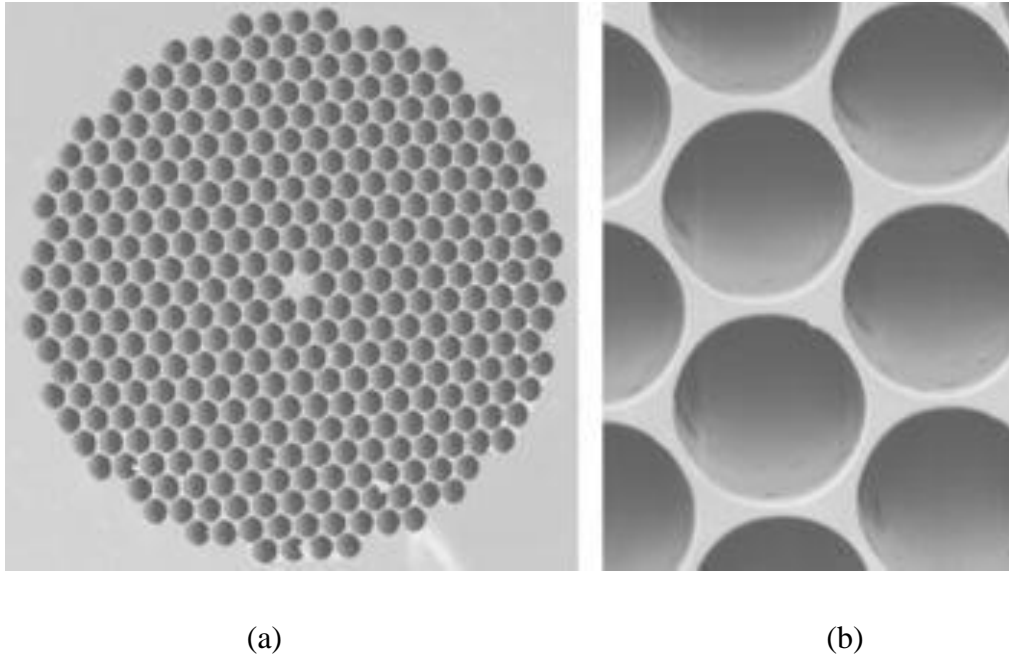


Fig. 2. 1: SEM micrographs of a photonic-crystal fibre produced at US Naval Research Laboratory. (a) The diameter of the solid core at the centre of the fibre is  $5\text{ }\mu\text{m}$ , while (b) the diameter of the holes is  $4\text{ }\mu\text{m}$  (Image of Photonic Crystal Fibre from NRL 2006).

Generally, such fibres are constructed by the same methods as other optical fibres: A preform on the scale of centimetres in size is constructed and then it is heated and drawn down to a much smaller diameter (often nearly as small as a human hair), shrinking the preform cross section but (usually) maintaining the same features. In this way, kilometres of fibre can be produced from a single preform. This is illustrated in Fig. 2.2. Other methods used in the fabrication of PCF include drilling and also extrusion. The method of extrusion is applied to glasses other than silica which may not be readily available in tube form. In this method, molten glass is forced through a die containing a suitably designed pattern of holes. Extrusion allows fibre to be drawn directly from bulk glass, using a fibre drawing tower and almost any structure, crystalline or amorphous, can be produced. It works for many materials, including chalcogenides, polymers, and compound glasses. However, selective doping of specified regions, in order to introduce



rare earth ions or render the glass photosensitive, is much more difficult (Poli *et al.* 2007).

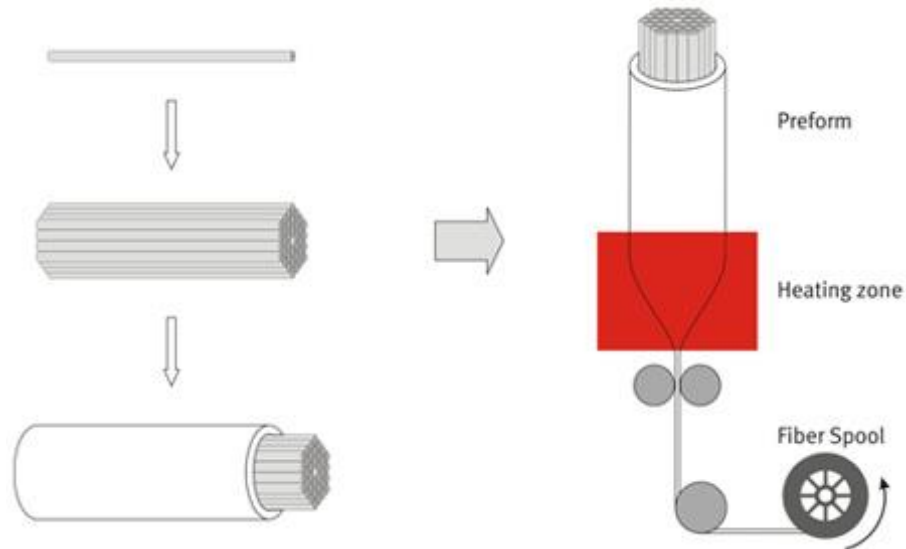


Fig. 2. 2: Fabrication of Photonic Crystal Fibre (Fabrication of Photonic Crystal Fibre NKT photonics 2008)

Most photonic crystal fibre has been fabricated in silica glass, but other glasses have also been used to obtain particular optical properties (such as high optical non-linearity). There is also a growing interest in making them from polymer, where a wide variety of structures have been explored, including graded index structures, ring structured fibres and hollow core fibres (Poli *et al.* 2007; Agrawal 2008). These polymer fibres have been termed "MPOF", short for microstructured polymer optical fibres (Eijkelenborg *et al.* 2001). A combination of a polymer and a chalcogenide glass was used by Temelkuran *et al.* (Temelkuran *et al.* 2002) for 10.6  $\mu\text{m}$  wavelengths (where silica is not transparent).

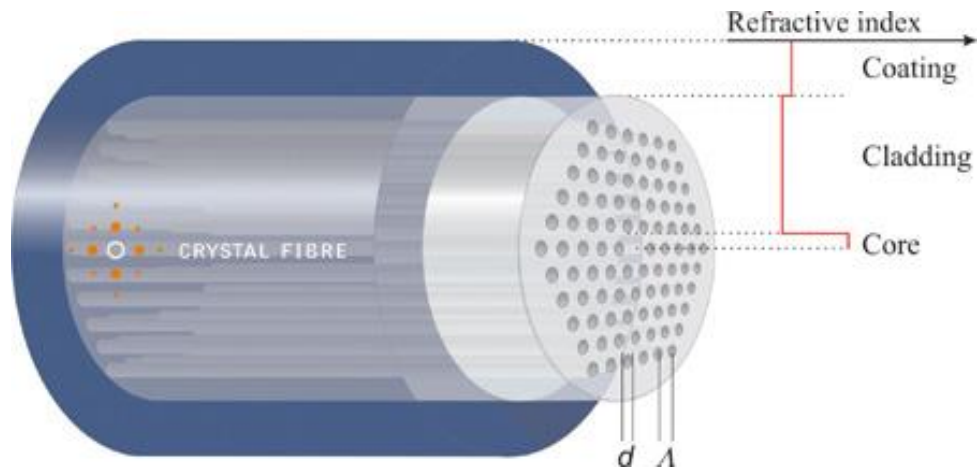


Fig. 2. 3: Photonic Crystal Fibre (Photonic crystal fibre NKT photonics 2008).

## 2.2 Structure of PCF

The transverse section of a photonic crystal fibre (PCF) consists basically of a two-dimensional (2D) photonic crystal, which for some specific geometries shows photonic bandgaps. By making a suitable geometry of the periodic dielectric medium, a photonic crystal can be used as an optical fibre. The existence of a defect in the regular structure produces the transverse localization of light in its vicinity with the consequent generation of axial guiding modes (Poli *et al.* 2007; Agrawal 2008).

A typical PCF has a 2-D cross-sectional structure in which the solid pure silica core region is surrounded by a cladding region that contains air-holes, as shown in Fig. 2.1. These holes effectively lower the index of refraction in the cladding region creating a step-index optical fibre as demonstrated by Fig. 2.3.

PCF structures can vary according to their applications; the design flexibility is very large and designers can use many different, fascinating and odd air-holes patterns to achieve specific PCF parameters. The triangular arrangement of round air-holes in the cladding is typically used to create single-mode fibres. Increasing the air-filling fraction in the cladding typically leads to multimode behaviour. An elliptical core can create a highly birefringent fibre that is polarization maintaining (Poli *et al.* 2007; Agrawal 2008).

## 2.3 Light-Guiding Mechanism

Generally, two different kinds of PCF exist, classified by their light-guiding mechanism, depending on its structure:

- (i) waveguiding by total internal reflection (index guiding PCF)
- (ii) waveguiding by photonic band gap effect.

### 2.3.1 Index Guiding Photonic Crystal Fibre

If the cladding which is full of holes has a lower average refractive index than the core, then light is guided by the modified total internal reflection (M-TIR) principle which is similar to conventional fibres. It is possible to use a two-dimensional photonic crystal as a fibre cladding, by choosing a core material with a higher refractive index than the cladding effective index. This kind of structures is the PCF with a silica solid core surrounded by a photonic crystal cladding with a triangular lattice of air-holes. These fibres also known as index-guiding PCFs, guide light through a form of total internal reflection (TIR), called modified TIR (M-TIR) and they have many different properties with respect to conventional optical fibres (Poli *et al.* 2007).

### 2.3.2 Photonic Bandgap (PBG) Effect

The second type of fibre provides guidance by the photonic band gap effect. In this case, the index of the core is uncritical, although the air-holes need to follow a strict periodicity, it can be hollow or filled with material (Russell 2003) such as liquids, gasses or particles. A holey fibre can guide light even when the refractive index of the core is lower than that of the cladding ( $n_{\text{core}} < n_{\text{cladding}}$ ) – if, for example, the core of the fibre comprises an air-hole. This phenomenon is known as the photonic bandgap (PBG) effect.

A photonic band gap is a region in the optical frequency spectrum where propagating modes do not exist. This allows for novel features such as light confinement to low-index core. There is no material with a refractive index less than air, so this structure would not support total internal reflection; instead the light would be contained within the hollow core by the barrier of the two-dimensional photonic bandgap formed by the periodic array of air-holes encircling of the core (Poli *et al.* 2007; Agrawal 2008).

Light can be controlled and transformed in these fibres with unprecedented freedom, allowing for example the guiding of light in a hollow core, the creation of highly nonlinear solid cores with anomalous dispersion in the visible and the design of fibres that support only one transverse spatial mode at all wavelengths (Russell 2003). In

PBG, the air-holes that surround the light almost entirely eliminate dispersion, optical nonlinearities and reflections on the fibre (Poli *et al.* 2007; Agrawal 2008).

Typical applications for these fibres are high power delivery with reduced nonlinear effects and material damage, short pulse delivery and low loss guidance in vacuum.

This thesis will focus on index-guiding PCFs as these fibres are presently most common and have less stringent requirements on structural uniformity.

## 2.4 Properties of Photonic Crystal Fibres

Photonic crystal fibres (PCF) offer a wide variety of possibilities as a result of the variety air-holes arrangements possible. This means it is easier to control the index contrast between the core and cladding unlike in the conventional optical fibres which leads to some unique optical properties as listed below:

- High birefringence
- Dispersion tailoring
- Very high nonlinearities
- Large mode areas
- Can also have very small mode areas

## 2.5 Advantages of Photonic Crystal Fibres over Optical Fibres

- Due to high effective index contrast between silica and air a much broader range of dispersive behaviour is accessible with Photonic Crystal Fibres than with standard fibres.
- Existence of two different light guiding mechanisms is one of the reasons for the versatile nature of the Photonic Crystal Fibre.
- The design flexibility for tailoring a specific property in the Photonic Crystal Fibre makes it more controllable to fabricate parameters than in single mode fibres.
- Exceptional characteristics like insensitivity to bending, reduced fibre loss, zero dispersion, non-linearity, polarization stability, highly adjustable effective mode area and the engineerable dispersion at visible and near-

infrared wavelength, high-power density and so forth give it a superior improvement than the standard optical fibre.

- Additional degree of freedom because of number of holes, shapes, orientation and placement also make it better than the standard optical fibre.
- The Photonic Crystal Fibre achieves single mode operation over a wide range of wavelengths.

## 2.6 Applications of Photonic Crystal Fibre

- Its zero dispersion can be applied to eliminate dispersion compensation for long haul transmission links.
- It's extremely negative dispersion can be used in the area of dispersion compensation.
- It could have a large mode area which can be used to avoid non-linearity for high power delivery.
- It could have a small mode area for improved non-linearity interaction.
- It could be designed to have high birefringence.
- Photonic Crystal Fibres with higher numerical aperture (NA) are better for collection and high performance in sensors, etc.

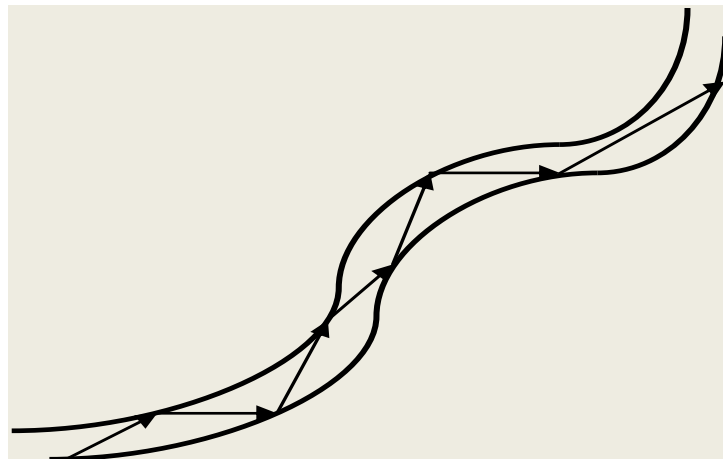


Fig. 2. 4: Fibre Optic Cable

## 2.7 Analysing Photonic Crystal Fibres

In this project, the analysis of PCF was carried out using the Finite Element Method (FEM) as explained in Chapter 3. The simulations using the FEM, which was developed

by City University London's Photonics Group, were run in FORTRAN on a Linux operating system. The simulations were carried out using a real program and a complex program. For every design considered, initial testing was carried out then results obtained to compare to other results to ensure accuracy. To conserve computer resources, the symmetry of the design is taken advantage of; therefore half structure or a quarter structure is used when it is practical instead of using the full structure.

## 2.8 Confinement Losses

Confinement losses or leakage losses are present in PCFs due to the fact that there are a finite number of air-holes that can be made in the cross-section of the cladding which results in the PCF guided modes to be leaky (Poli *et al.* 2007). The diameter to pitch ratio ( $d/\Lambda$ ) in a particular design of PCF determines how much light leaks from the core into the cladding. The lower the ratio, the more leakage is expected into the cladding.

## 2.9 Bending Loss

This is caused by bending of the fibre as shown in Fig. 2.4. This is because internal light paths exceeding the critical angle for total internal reflection, TIR. Theoretically, when the fibre is bent, light propagates outside the bend faster than the inner radius, as is represented in Fig. 2.5. This is not possible practically and the light is radiated away (Goure and Verrier 2002; Poli *et al.* 2007; Agrawal 2008).

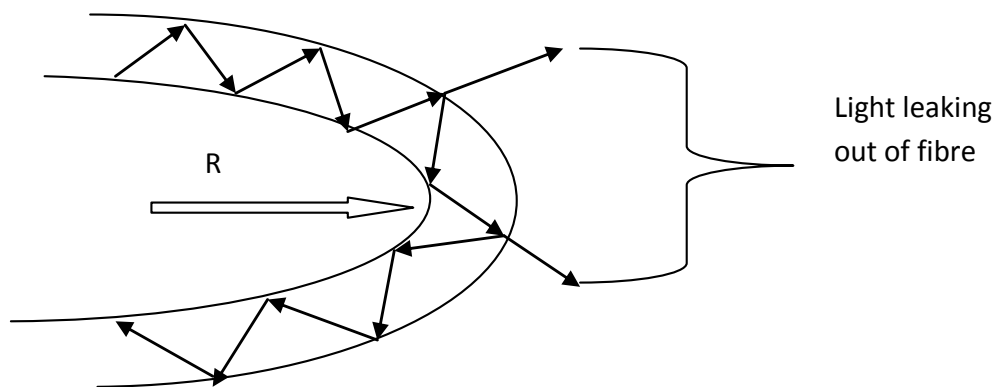


Fig. 2. 5: A bent optical fibre

### 2.9.1 Conformal Transformation

It is also known that a bent PCF suffers from the bending that can also influence the cutoff condition of a PCF as is seen in Fig. 2.5. This can be exploited further in the optimization of the birefringence value. To study the effects of arbitrary bends, various numerical methods have been developed and used to simulate the light propagation in bent waveguides with the aim of characterizing the bending, the transition, and the polarization losses. The conformal transformation (Heiblum and Harris 1975) has been most widely used to represent such bent waveguides by converting a curved dielectric waveguide to its equivalent straight waveguide with a modified index profile. The coordinate transformation allows a bent optical waveguide in the  $x$  plane to be represented by an equivalent straight waveguide with a modified refractive index distribution,  $n_{eq}(x,y)$  (Heiblum and Harris 1975):

$$n_{eq}(x,y) = n(x,y)(1+x/R) \quad (2.2)$$

where  $n(x,y)$  is the original refractive index profile of the bent waveguide as shown in Fig. 2.6(a),  $n_{eq}(x,y)$  is the equivalent index profile of a straight guide as shown in Fig. 2.6(b),  $R$  is the radius of curvature and  $x$  is the distance from the centre of the waveguide. With a reduction in the bending radius, the cladding in the outer side (away from bending centre) encounters a higher equivalent index compared to the inner side cladding and hence, the fundamental mode shifts farther outward, with a slight increase in the modal effective index value. The shift of the modal field toward the raised equivalent cladding index increases the leakage loss due to this bending, which increases further for a lower bending radius.

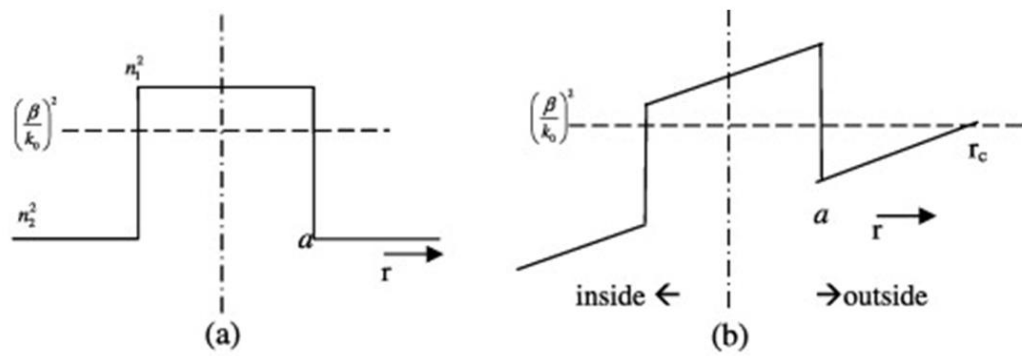


Fig. 2. 6: Refractive index profile of bent PCF. (a) straight fibre; (b) a bent fibre with the centre located at the side of 'inside' (Xiangru *et al.* 2010)

### 2.9.2 Types of Bending Loss

- Macro bending: Large scale bending that is visible in which the bend is imposed on optical fibre. The bend region strain affects the refractive index and acceptance angle of the light ray.
- Micro bending: This is a small scale bend that is not visible which occurs due to the pressure on the fibre that can be as a result of temperature, tensile stress of force and so forth. It affects refractive index and refracts out the ray of light; thus loss occurs.

### 2.10 Summary

In this chapter the fundamental issues related to photonic crystal fibres are discussed. The history and development of the PCF including the fabrication technique has been discussed. The guidance principle and the structure of the PCF were shown. This project is based on the design and characterisation of the PCF by simulations using the finite element method. This was carried out through the calculation of the confinement and bending losses associated with these particular types of special fibres. This was achieved with a view to minimising these losses as well as applying these losses to applications in engineering these particular fibres for novel applications. The finite element method is described in the next Chapter.



## CHAPTER THREE: Numerical Methods

### 3.0 Abstract

In this chapter, the theoretical background of the **H**-field Finite Element Method (FEM) used in the analysis of waveguides is presented starting with the presentation of Maxwell's equations. The method of suppressing spurious solutions by including the penalty factor in the FEM formulation is also discussed. The properties of the various numerical methods used in waveguide analysis are discussed briefly. The Least Squares Boundary Residual (LSBR) method used in the discontinuity analyses when butt coupling waveguides is also presented.

### 3.1 Basic Equations

#### 3.1.1 Maxwell's Equations

Maxwell's equations comprise a set of four electromagnetic field vectors, which represent the governing laws of the electromagnetic wave phenomena. The four vectors are: the electric field intensity **E** (volts/meter), magnetic field intensity **H** (amperes/meter), the electric flux density **D** (Coulomb/metre<sup>2</sup>) and the magnetic flux density **B** (Tesla). The Maxwell's equations can be written in differential or integral form. Since, the FEM is boundary-value problem which is defined by differential equations; Maxwell's equations are presented in differential form as follows:

$$\nabla \times \mathbf{E} + \frac{\partial \mathbf{B}}{\partial t} = 0 \quad (3.1)$$

$$\nabla \times \mathbf{H} - \frac{\partial \mathbf{D}}{\partial t} = \mathbf{J} \quad (3.2)$$

$$\nabla \cdot \mathbf{D} = \rho \quad (3.3)$$

$$\nabla \cdot \mathbf{B} = 0 \quad (3.4)$$

Where  $\rho$ , is the dielectric charge density (coulomb/metre<sup>3</sup>);  $\mathbf{J}$ , is the electric current density (ampere/metre<sup>2</sup>)

The associated constitutive equations for the medium can be written as:

$$\mathbf{D} = \epsilon \mathbf{E} \quad (3.5)$$

$$\mathbf{B} = \mu \mathbf{H} \quad (3.6)$$

Where  $\epsilon$  is the permittivity and  $\mu$  is the permeability of the medium which can be defined by:

$$\epsilon = \epsilon_o \epsilon_r \quad (3.7)$$

$$\mu = \mu_o \mu_r \quad (3.8)$$

Where  $\epsilon_o$ ,  $\epsilon_r$ ,  $\mu_o$  and  $\mu_r$  are the permittivity of the vacuum ( $8.854 \times 10^{-12}$  Farad/meter), the relative permittivity of the medium, the permeability of the vacuum ( $4\pi \times 10^{-7}$  Henry/meter) and the relative permeability of the medium, respectively.

### 3.1.2 Boundary Conditions

Boundary conditions are the conditions that must be met at the boundary surface when two different media 1 and 2 come in contact. If the unit normal vector  $\mathbf{n}$ , is directed from medium 1 to medium 2 as shown in Fig. 3.1 in the absence of any surface currents ( $\mathbf{J} = 0$ ) and surface charges ( $\rho = 0$ ), the following boundary conditions apply:

1. the tangential component of the electric field must be continuous

$$\mathbf{n} \times (\mathbf{E}_1 - \mathbf{E}_2) = 0 \quad (3.9)$$

2. the tangential component of the magnetic field must be continuous

$$\mathbf{n} \times (\mathbf{H}_1 - \mathbf{H}_2) = 0 \quad (3.10)$$

3. The normal component of the electric flux density must be continuous

$$\mathbf{n} \cdot (\mathbf{D}_1 - \mathbf{D}_2) = 0 \quad (3.11)$$

4. The normal component of the magnetic flux density must be continuous

$$\mathbf{n} \cdot (\mathbf{B}_1 - \mathbf{B}_2) = 0 \quad (3.12)$$

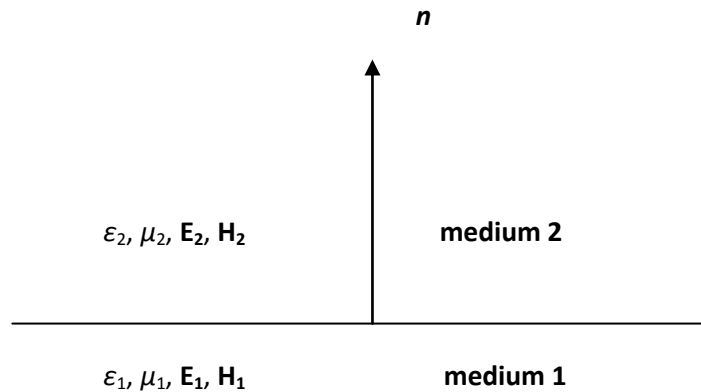


Fig. 3. 1: Boundary between two media of refractive indices  $n_1$  and  $n_2$ , where  $\mathbf{n}$ , is the unit vector normal to the interface.

In certain cases, one of the two media can be considered, either as a perfect electric conductor or a perfect magnetic conductor. When one of the two media becomes a perfect electric conductor, an electric wall boundary condition is imposed as:

$$\mathbf{n} \times \mathbf{E} = 0 \quad \mathbf{n} \cdot \mathbf{H} = 0 \quad (3.13)$$

such conditions ensures the continuity of the electric field vector,  $\mathbf{E}$  and that of the magnetic field vector,  $\mathbf{H}$  vanishes at the boundary. When one of the two media becomes a perfect magnetic conductor, a magnetic wall boundary condition is imposed as:

$$n \times \mathbf{H} = 0 \quad n \cdot \mathbf{E} = 0 \quad (3.14)$$

The above condition vanishes the electric field vector,  $\mathbf{E}$  and ensures the continuity of the magnetic field at the boundary.

In the case of a closed surface, such as the boundary of an optical waveguide, additional boundary conditions are considered. These boundary conditions can be natural, in case where the field decays at the boundary, therefore they can be left free. In some other cases they can be forced, in order to take advantage of the symmetry of the waveguide, to reduce the number of elements in FEM (and the order of the matrices) or to impose complementary symmetry to the waveguide, in order to obtain a particular polarized mode. The above boundary conditions can be classified as follows (Davies 1989):

$$\Phi = 0 \quad \text{homogenous Dirichlet} \quad (3.15)$$

$$\Phi = k \quad \text{Inhomogenous Dirichlet} \quad (3.16)$$

$$\frac{\partial \Phi}{\partial \mathbf{n}} = 0 \quad \text{homogenous Neumann} \quad (3.17)$$

Where  $\Phi$  can be the electric or magnetic field,  $k$  is a prescribed constant value and  $\mathbf{n}$  is the unit vector normal to the surface.

The Neumann boundary conditions represents the rate of change of the field when it is directed out of the surface and it can be used in the FEM to impose the field decay along finite elements, adjacent to the boundary elements of a waveguide structure.

### 3.1.3 Wave Equations

In an isotropic lossless medium with no wave source ( $\mathbf{J} = 0$ ,  $\rho = 0$ ), with constant permeability  $\mu = \mu_0$  by eliminating the magnetic flux density in and the electric flux density components for Maxwell's equation (3.1) and (3.2) these can be written as:

$$\nabla^2 \mathbf{E} + k^2 \mathbf{E} = 0 \quad (3.18)$$

$$\nabla^2 \mathbf{H} + k^2 \mathbf{H} = 0 \quad (3.19)$$

Where the wavenumber,  $k$  (rad/m) is given as:

$$k = \omega \sqrt{\epsilon \mu_o} \quad (3.20)$$

If  $\epsilon = \epsilon_o$  then the wavenumber,  $k_o$  is called free space wavenumber and is defined by:

$$k_o = \omega \sqrt{\epsilon_o \mu_o} \quad (3.21)$$

Equations (3.18) and (3.19) are known as the vector Helmholtz wave equations (Mearz 1995) for homogenous media and in addition to the physical solutions, they may also support non-physical or spurious solutions, since the conditions  $\nabla \cdot \mathbf{H} = 0$ , may not be satisfied. In a rectangular coordinate system, if only one component of the electric or magnetic field is considered, for example  $E_x$ , the vector Helmholtz wave equation can lead to the scalar Helmholtz wave equation as (Koshiha 1990):

$$\nabla^2 E_x + k^2 E_x = 0 \quad (3.22)$$

### 3.2 Analysis of Optical Waveguides

Optical waveguides analyses imply the process of finding the propagation constants and the field profiles of all the modes that a waveguide can support. To be able to calculate these propagation characteristics, solutions of the well-known Maxwell's equations are obtained along with the satisfaction of the necessary boundary conditions. Applying the Maxwell's equations may not be an easy task and precise analyses of optical waveguides is generally considered to be a difficult task because of some major reasons such as the optical waveguides may have complex structures, arbitrary refractive index distribution (graded optical waveguides or photonic crystal fibres) anisotropic and non-linear optical materials as well as materials with complex refractive index such as semiconductors and metals. These difficulties are surmounted using various methods of optical waveguide analyses developed. These methods can be broadly classified into two groups, namely the analytical approximation solutions and the numerical solutions. An exact analytical solution can be obtained for stepped 2-D optical waveguides (i.e. slab waveguides) and stepped optical fibre. However, if the waveguide has an arbitrary refractive index distribution, then the exact solutions may not be possible. Therefore various types of analytical approximation solutions have been developed for 2-D stepped optical waveguides which have their refractive index distribution gradually

changing along the thickness of the waveguide. Some typical analytical approximation solution techniques for such optical waveguides are the Ray Approximation Method (RAM) (Qiao and Wang 1992) and the Wentzel, Kramers and Brillouin (WKB) method (Srivastava *et al.* 1987). For 3-D optical waveguides, hybrid mode analysis is required in order to satisfy the boundary conditions. However, the analytical approximation solutions developed for these guides do not treat them as hybrid modes and therefore they are not suitable for accurately analysing the practically used 3-D optical waveguides. Approximation solutions used typically for 3-D optical waveguides are the Marcatili's Method and subsequently the Effective Index Method (Okamoto 2006).

The numerical solutions can also be grouped into two categories and these are the domain solution also called a differential solution and the boundary solution also known as an integral solution. The domain solution includes the whole domain of the optical waveguide structure as the operational area whereas the boundary solution includes only the boundaries as the operational area. Some examples of the domain solutions include the Finite Element Method (FEM), Finite Difference Method (FDM), Variational Method (VM) and Multilayer Approximation Method (MAM). The boundary solutions include the Boundary Element Method (BEM), Point Matching Method (PMM) and Mode Matching Method (MMM).

A brief description of the most commonly used analytical and numerical solution techniques for modelling in opto-electronics will be presented in subsequent sections.

### 3.2.1 Marcatili's Method

Marcatili's Method (MM) was one of the first analytical approximation methods to be developed for the analysis of buried waveguides and couplers (Marcatili 1969). The method was developed for guiding structures with large dimensions and a small refractive index difference (less than 5%) between the guiding (core) and cladding materials. The field is assumed to exist in the rectangular waveguide core region and also in the four neighbouring cladding regions which are obtained by extending the width and the height of the waveguide to infinity. The field is also assumed to vary sinusoidally in the core region and exponentially in the four cladding regions, thus the field is approximated to the field in two slab waveguides; one vertical and the other horizontal. Two transcendental or eigenvalue equations for each slab waveguide are

solved simultaneously to give the axial propagation constant. Marcatili's method works well in the regions far from cut-off but does not provide a satisfactory solution close to cut-off region (Chiang 1994).

### 3.2.2 The Effective Index Method

The Effective Index method was first proposed by Knox and Toullos in 1970 (Knox and Toullos 1970) as an extension to the Marcatili's method (Marcatili 1969) for the fundamental mode of a simple rectangular core waveguide. This resulted in the effective index method becoming one of the most popular methods in the 1970s for the analysis of optical waveguides whereby the rectangular structure is replaced by an equivalent slab with an effective refractive index obtained from another slab. The rectangular dielectric waveguide is divided into two slab waveguides in each transverse direction. The initial step solves the transcendental equation for a vertical slab waveguide by applying the appropriate boundary conditions. The effective index calculated in this step is then used as the refractive index of the horizontal slab waveguide and by solving the eigenvalue equation gives a good approximation to the effective index of the original waveguide structure. This method is significantly more efficient than those methods that solve the rectangular structure directly since only the solutions for slab waveguides are required. The advantage of the effective index method is that it can be applied to a wide variety of structures including channel waveguides, strip waveguides and arrays of such waveguides (Chiang *et al.* 1996) and also for various types of optical fibres and fibre devices (Chiang 1986b; Van de Velde *et al.* 1988). The disadvantage of this method is that it does not give good results when the structure operates near cut-off region. However, the simplicity and speed of the method have encouraged many engineers to search for different approaches that will improve the accuracy of the effective index method which subsequently lead to many different variants of the effective index method to be developed including the effective index method based on linear combinations of solutions (Chiang 1986a; Van Der Tol and Baken 1988) or the effective index method with perturbation correction (Chiang *et al.* 1996).

### 3.3 Numerical Solution Methods

The rapid growth in the millimetre-wave, optical fibre and integrated optics fields has included the use of arbitrarily shaped dielectric waveguides, which in many cases also happened to be arbitrary inhomogeneous and/or arbitrarily anisotropic which do not

easily lend themselves to analytical solutions. Therefore many scientists have given their attention to the development of numerical methods to solve such waveguides. Numerical methods may be used to solve Maxwell's equations exactly and the results they provide are accurate enough for the characterisation of most of the devices. Since the advent of computers with large memories, considerable attention has been paid to methods of obtaining numerical solutions of the boundary and initial value problems. These methods are usually evaluated in terms of their generality, accuracy, efficiency and complexity. It is evident from the review articles (Chiang 1994; Vassalo 1997) that every method represents some sort of compromise between these aspects, implying that no method is superior to the others in all aspects. The optimal method should be the one that can solve the problem with acceptable accuracy but requires the minimum effort to implement and run in terms of manpower and computer capacity. Also, the continuing improvement in computer power has made computational efficiency less of an issue over the years. Some factors with regards to the selection of methods for analysing optical waveguide problems, based on reviews (Davies 1972; Ng 1974; Saad 1985) are:

- Whether the shape of the cross section of the structure is curved or polygonal or whether it is convex or non-convex.
- Whether a method that can be realised as a computer program suitable for the automatic solution of a wide range of structures is needed.
- Whether a computer program requiring human intervention of some exploratory work with the computer is required.
- Whether the method could be programmable and/or if it has to be written specially for each region of the structure separately.
- Whether it is just the dominant mode only or a number of higher order modes that are required as well.
- Whether the field distribution and/or the cut-off frequency are needed.
- Whether the requirements for the accuracy needed are for the eigenvalues and/or eigenfunctions.



- Whether the method would accurately model the dielectric boundaries and regions.
- Whether the method would accurately give solution in specific frequency ranges as well as near cut-off frequency.
- Whether the method has a mechanism of generating spurious numerical solutions and if so whether the method can identify and/or eliminate them.
- Whether the method is computationally efficient as well as its computer storage requirements.

A short overview of these commonly used numerical solution techniques is given next.

### **3.3.1 The Boundary Element Method**

The Boundary Element Method (BEM) is interpreted as a combination technique of the conventional boundary integral equation method and a discretisation techniques (Kagami and Fukai 1984). The BEM is a boundary solution method and therefore the fields would be required only at the nodes which are on the boundaries of the region. The derivation of the integral equations with respect to the unknown fields at boundaries is obtained by the method of weighted residuals or the Green's formula. These integral equations are then discretised to a set of linear equations to be solved for the numerical solutions. The BEM can be used for the analysis of arbitrarily shaped discontinuities as is with the finite element method, but the boundary element method can be performed using far fewer nodes than by the finite element method. Moreover, the BEM can handle unbounded field problems easily and therefore has the possibility of modelling domains extending to infinity without an infinite element analysis which is often performed in the finite element method. However, the boundary element method can only be applied to homogenous structures (Hirayama and Koshiba 1989) and also it has been known that the matrices involved are dense matrices unlike those used with the finite element method which are sparse. Therefore, the finite element method can be treated as more numerically efficient than the boundary element method.

### **3.3.2 The Point Matching Method**

The Point Matching Method (PMM) is one of the oldest and simplest 'boundary solution' techniques for the analysis of isotropic homogenous dielectric waveguides. Its

application was first shown by J. E. Goell (Goell and Standley 1969) to investigate the propagation characteristics in rectangular cross section dielectric waveguides. The numerical analysis used in the technique by Goell is based on expressing the internal and external fields in terms of circular harmonics. The fields inside the dielectric and outside the dielectric are expressed by a sum of Bessel functions and modified Bessel functions multiplied by trigonometric functions, respectively and their derivatives. By matching the tangential fields at optimally selected points around the boundary called ‘matching points’, a system of linear equations is obtained. By applying the condition of nontrivial solution, a characteristic equation including the propagation constant is obtained and solved for each mode eigenfunction by standard matrix techniques. The point matching method is capable of analysing dielectric waveguides with arbitrary cross sections and composite structures and also computing coupling coefficients between two rectangular rods. Improved results for the point matching method were reported (Cullen *et al.* 1971) by rotating the grid of equiangularly spaced matching points in order to place a matching point at the corner of a rectangular dielectric waveguide. However, the point matching method is not suitable for the analysis of a 3-D waveguide structures with inhomogeneous index distribution such as graded index fibres.

### 3.3.4 The Mode Matching Method

The Mode Matching Method (MMM) which is also known as the Equivalent Network Method is an approximate solution method for the analysis of open dielectric waveguides (Peng and Oliner 1981). In this approach the structure is artificially bounded and the waveguide cross section is viewed in terms of constituent parts or building blocks, which are usually portions of uniform dielectric layered structures interfaced by the dielectric step discontinuities. Then each constituent is analysed separately and all the parts are put together to comprise the final structure of interest. A transverse equivalent network for the structure is obtained by representing the uniform dielectric regions as uniform transmission lines and by characterising the step discontinuities as transformers. From this, the dispersion relation can be derived to obtain the waveguide propagation characteristics. In the earlier analysis of the mode matching method due to the artificial bounding of the structure, the continuous spectrum (Peng and Oliner 1981) and TE and TM coupling at the sides of the waveguide are

neglected. Dagli and Fonstad (Dagli and Fonstad 1986) reported a modified approach, which takes into account the continuous spectra. Rather than artificially bounding the structure to discretise the continuous modal spectrum, here, they are discretised by converting integrals into summations using suitable basis function expansions. Koshiba and Suzuki (Koshiba and Suzuki 1985; Koshiba and Suzuki 1986) reported a vectorial wave analysis of rectangular optical waveguide using equivalent network method by taking the TE-TM coupling and the discrete-continuous spectrum coupling into account.

### 3.3.5 The Spectral Index Method

The Spectral Index (SI) method may be used to find quickly and easily the guided modes and propagation constants of semiconductor rib waveguides (Kendall *et al.* 1989; Stern *et al.* 1990). Here the true open structure is replaced by slightly larger, partially closed one, which is simpler to analyse, in order to model the penetration of the optical field into the cladding. The spectral index method can be expressed using steps in the region below the rib. First of all, the Fourier transform is applied in order to reduce the dimensionality of the problem to a one-dimensional structure and the field is expressed in spectral space using Fourier transform. Next, in the rib region the wave equation is exactly expressed using Fourier series in terms of cosine and sine functions then the two solutions are linked by employing a transfer relationship and consequently, giving a transcendental equation which can be solved for the propagation constant of the original rib structure. The presence of the strong discontinuities at the dielectric interfaces is dealt with by using an effective rib width and an effective outer slab depth. The spectral index method has been extended to include rib coupler problems (Burke 1989; Burke 1990) cases with loss and gain (Burke 1994) and also it has been used to analyse multiple rib waveguides (Pola *et al.* 1996).

### 3.3.6 The Beam Propagation Method

The Beam Propagation Method (BPM) describes the evolution of the total field propagating along a waveguide and it is the most widely used tool in the study of light propagation in longitudinally varying waveguides such as tapers, Y-junctions, bends and gratings. The beam propagation method was first applied to optoelectronics in 1980 (Feit and Fleck 1980) and the solutions for the optical waveguides can be made to generate mode-related properties such as propagation constants, relative mode powers and group delays with high precision and considerable flexibility. The initial BPM is

based on the Fast Fourier Transform (FFT) and only solves the scalar wave equations under paraxial approximation. Therefore the FFT-BPM was only developed for the case of weakly guiding structures, neglecting the vectorial properties of the field. Several numerical algorithms to treat the vectorial wave propagation (vector BPM) using the finite difference method, have been reported (Chung *et al.* 1991; Huang *et al.* 1992a; Huang *et al.* 1992b). The VBPMs are capable of simulating polarized or even hybrid wave propagation in strongly guiding structures. Recently, the finite element method has been utilised to develop BPM approaches. A unified finite element beam propagation method has been reported (Tsuji and Koshiba 1996) for both TE and TM waves propagating in strongly guiding longitudinally varying optical waveguides. Obayya *et al.* (Obayya *et al.* 2000) has reported a full-vectorial BPM algorithm based on the finite element method to characterise 3-D optical guided wave devices.

### 3.3.7 The Finite Difference Method

The Finite Difference Method (FDM) is one of the oldest and perhaps the most commonly used numerical techniques in analysing dielectric waveguide problems. Its application to the modelling of optical waveguides dates from the early eighties, originally evolving from previous finite difference models for metal waveguides (Davies and Muilwyk 1966). The finite difference method discretises the cross section of the device that is being analysed and it is therefore suitable for modelling inhomogeneous media and complicated boundaries. In FDM, it is necessary to define the a finite cross section by enclosing the dielectric guide in a rectangular box; such as Transparent Boundary Conditions, TBC (Okamoto 2006), with the side walls as either electric or magnetic walls and the field at these boundaries are assumed to be very small. However, if leakage losses need to be calculated, these hard boundaries can be replaced by Perfectly Matched Layer (PML) (Berenger 1994). The enclosed cross section is divided into a rectangular mesh allowing for the material discontinuities only along mesh lines (Bierwirth *et al.* 1986). The nodes are placed on mesh points so that each node can be associated to a maximum of four or eight neighbouring nodes and each node can be of one or more field variables depending on vector, semi-polarized or scalar wave equations that can be approximated in terms of the fields at the neighbouring nodes of the mesh. Taking into account the continuity and discontinuity conditions of the electric and magnetic components at the field interfaces an eigenvalue

problem is generated which can be solved in order to obtain the modal propagation constants and their modal field profiles. The accuracy of the method depends on the mesh size, the assumed nature of the electromagnetic field (scalar, polarized or vector) and the order of the finite difference scheme used. If a uniform mesh is used then it can result in a very large number of nodes and large matrices and therefore the disadvantages like long run times and high memory requirements may become apparent.

### 3.3.8 The Finite Element Method

The Finite Element Method (FEM) is a well-established numerical method for the solution of a wide range of guided wave problems. It can be very easily applied not only to optical waveguides of any shape but also to optical waveguides with any refractive index distribution and to those with any anisotropic materials or nonlinear materials. This method is based upon dividing the problem region into a non-overlapping patchwork of polygons, usually triangular elements. The field over each element is then expressed in terms of polynomials weighted by the fields over each element. By applying the variational principle to the system functional, and thereby differentiating the functional with respect to each nodal value, the problem reduces to a standard eigenvalue matrix equation. This is solved using iterative techniques to obtain the propagation constants and the field profiles (Rahman and Davies 1984b; Koshiba and Inoue 1992). The accuracy of the finite element method can be increased by using finer mesh. A number of formulations have been proposed, however, the full vectorial  $\mathbf{H}$ -field formulation is the most commonly used and versatile method in modelling optical waveguides due to much easier treatment of the boundary conditions. This method can accurately solve the open type waveguide problems near cut-off region and much better results were obtained by introducing infinite elements to extend the region of explicit field representation to infinity (Rahman and Davies 1984a). One drawback associated with this powerful vector formulation is the appearance of spurious or non-physical solutions. Suppression of these spurious solutions can be achieved by introducing a penalty term into the variational expression (Rahman and Davies 1984c). In order to eliminate the spurious solutions completely, another approach is employed using the edge elements (Bossavit and Mayergoyz 1989; Koshiba and Inoue 1992). In modelling more complex structures, the finite element method is considered to be more flexible

than the finite difference method due to the ability of employing irregular mesh. Since this method is used in this work, a more detailed description of the finite element method will be presented next.

### 3.4 Fundamentals of the Finite Element Method

The Finite Element Method (FEM) has emerged as one of the most successful numerical methods for the analysis of waveguides from low frequency to microwave to optical region. It is indeed capable of solving waveguides of arbitrary refractive index distribution. In this thesis a full-vectorial  $\mathbf{H}$ -field based FEM has been used to characterise waveguides operating at optical and terahertz frequencies. Such methods are capable of handling a wide range of inhomogeneous problems with greater ease. It is also capable of solving anisotropic problems.

In this approach, any waveguide cross-section can be divided in a patchwork of triangular elements, where the appropriate field components are approximated by polynomial expressions over these elements. Each element can have a different dielectric material, which may be anisotropic, non-linear or lossy. The FEM, which is based on the Ritz-Galerkin approach, converts a continuous system into a discretized model. By applying the variational principle (Davies 1989) to the functional of the system, the problem reduces to a standard eigenvalue matrix equation  $[A]x - \lambda[B]x = 0$ , which can then be solved by using standard matrix solver algorithms. The FEM can be used effectively for the analysis of various optical waveguides, with any shape, including 2D and 3D optical waveguides, axisymmetrical and non-axisymmetrical optical fibre and non-linear optical waveguides.

The FEM is based on the similar principles as the FDM; therefore a comparison of the two methods can be attempted. Although in the FDM simpler matrix eigenvalue equations are formed, which are formulated with less computer programming, less computer memory storage and execution time and the clarity solution is free of spurious modes ( $\mathbf{H}_x - \mathbf{H}_y$  formulation), the above approach cannot be easily applied to structures with odd-shaped boundaries. The triangular elements used in the FEM can give a better fit to such structures and also the change of the density or the order of the elements in regions where there is more rapid field variation is performed more easily with the FEM. Additionally, in the FEM, the field is defined explicitly everywhere and this

makes it easier for manipulation, such as when evaluating spatial derivatives to give related fields (Davies 1989).

### 3.4.1 Theoretical Background

Mathematically, the FEM is a numerical technique for obtaining approximate solutions to boundary-value problems and it is the extension of the two classical methods, the Raleigh-Ritz variational methods and the Galerkin method of weighted residuals. A boundary value problem can be defined by a governing differential equation in a domain, together with the boundary conditions on the boundary that encloses the domain. In the variational approach the boundary-problem is formulated in terms of variational expressions, referred to as functionals, whose minimum corresponds to the governing differential equations. The approximate solution is obtained by minimising the functional with respect to its variables (Jin 1993). The Galerkin method is based on the method of weighted residuals (Davies 1989) in which the domain of the differential equation is discretized and the solution is approximated by the summation of the unknown solutions of each subdomain weighted by known functionals, relating them to the domain. The overall solution is obtained by minimising the error residual of the differential equation.

Research on the application of the FEM to electromagnetic-wave engineering began towards the end of the 1960s and since then, with the availability of larger and faster computers, it has been established as a very powerful tool dealing with the analysis of optical waveguides, particularly structures with arbitrary shapes, index profiles, nonlinearities and anisotropies.

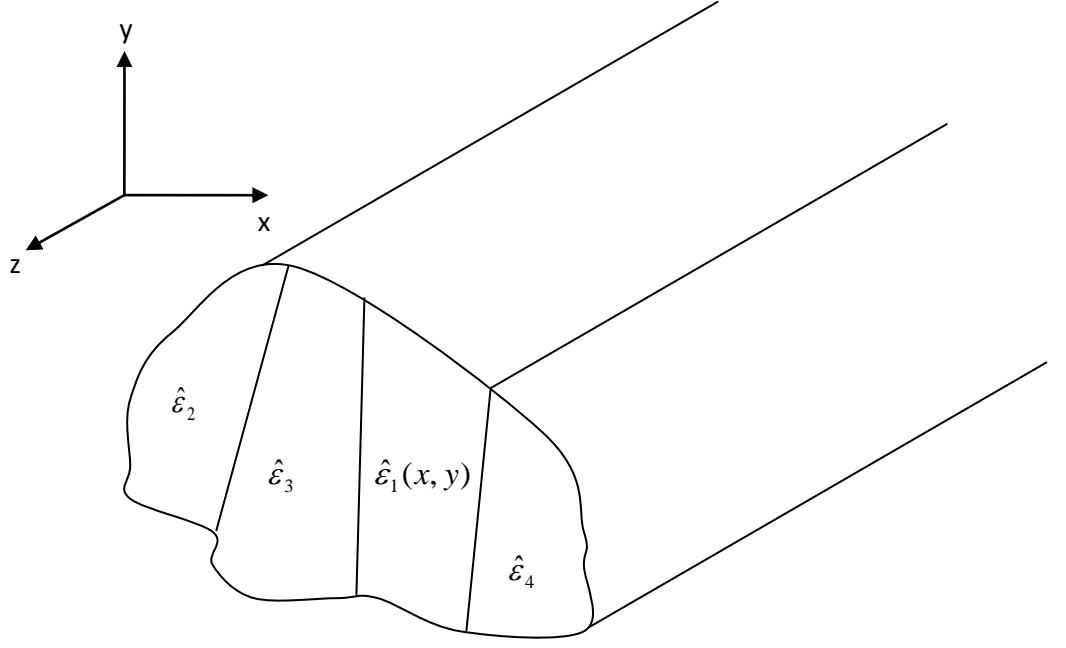


Fig. 3. 2: Arbitrary shaped optical waveguide, divided into arbitrary sub-domains, each having different type of material

A cross-section of an arbitrary shaped optical waveguide in the  $x - y$  transverse plane as shown in Fig. 3.2 is considered, divided into a number of sub-domains, which may be composed of several different materials, each of which can be described by arbitrary permittivity and permeability tensors,  $\hat{\epsilon}_1(x, y)$  and  $\hat{\mu}_1(x, y)$  respectively. A uniform shape of the waveguide along the longitudinal  $z$ -axis is assumed and time and axial dependencies are given by  $e^{j\omega t}$  and  $e^{-\gamma z}$  where  $\omega$  is the angular frequency and the complex propagation constants,  $\gamma$ , given by:

$$\gamma = \alpha + j\beta \quad (3.23)$$

Where  $\alpha$  (Np/m) is the attenuation constant and  $\beta$  (rad/m) is the phase constant. For a loss less case, the propagation constant is considered to be equal to the phase constant  $j\beta$ . The electric,  $\mathbf{E}(x, y, z, t)$  and the magnetic  $\mathbf{H}(x, y, z, t)$  fields over the region of the waveguide can be expressed by

$$\mathbf{E}(x, y, z, t) = \mathbf{E}(x, y)e^{j(\alpha x - \beta z)} \quad (3.24)$$

$$\mathbf{H}(x, y, z, t) = \mathbf{H}(x, y)e^{j(\alpha x - \beta z)} \quad (3.25)$$



where  $\mathbf{H}(x,y)$  and  $\mathbf{E}(x,y)$  are the spatial time-domain-independent magnetic and electric fields respectively.

For optical waveguides with 2-dimensional confinement, the modes are not purely of TE or TM type, but they are hybrid in nature, with all the 6 components being present. The quasi-TE modes with  $H_y$  being dominant can also be identified as  $H_{mn}^y$  mode, where  $m$  and  $n$  indicates spatial variation order in the  $x$  and  $y$  directions. Similarly, quasi-TM modes with their  $H_x$  field being dominant can also be identified as  $H_{mn}^x$  mode. These notations are used throughout this thesis.

### 3.4.2 Variational Formulation

The finite element formulation is based on the variational or Raleigh-Ritz approach, therefore, several variational formulations have been proposed for the analysis of the optical waveguide problem. These can be a scalar form (Mabaya *et al.* 1981), where the electric or magnetic field is expressed only in terms of one component, according to the predominant field component or can be in the vector form, where the electric or magnetic field is expressed in terms of at least two of the constituent field components.

It should be noted that most of the formulations applied in the FEM, yield to a standard eigenvalue problem:

$$[A]\{x\} - \lambda[B]\{x\} = 0 \quad (3.26)$$

where  $[A]$  and  $[B]$  are real symmetric sparse and  $B$  is also positive definite. The eigenvalue,  $\lambda$ , can be chosen as  $\beta^2$  or  $k^2$ , depending on the formulation and the eigenvalues represent the nodal field values of the finite elements. It is desirable for the above matrix equation to be of this canonical form to allow an efficient solution.

### 3.4.3 Scalar Approximation

The scalar approximation can be applied in situations where the field can be described as predominantly TE or TM and it can be expressed in terms of the longitudinal components of the above modes. It has been used for the solution of homogenous waveguide problems (Daly 1984), open boundary problems (Wu and Chen 1986) and for the analysis of the anisotropic waveguides (Koshiha *et al.* 1984). For the quasi-TE modes over a region where the dominant field component is  $E_x$ , the formulation can be written as

$$L = \iint_{\Omega} \left[ \left( \frac{\partial E_x}{\partial x} \right)^2 + \left( \frac{\partial E_x}{\partial y} \right)^2 - k_o n^2 E_x^2 + \beta^2 E_x^2 \right] d\Omega \quad (3.27)$$

Where  $\beta$  is the propagation constant and  $n$  is the refractive index. For the quasi-TM modes, where  $H_x$  is the dominant field, the formulation can be written as (Mabaya *et al.* 1981):

$$L = \iint_{\Omega} \frac{1}{n^2} \left[ \left( \frac{\partial H_x}{\partial x} \right)^2 + \left( \frac{\partial H_x}{\partial y} \right)^2 - k_o H_x^2 + \frac{1}{n^2} \beta^2 H_x^2 \right] d\Omega \quad (3.28)$$

### 3.4.4 Vector Formulation

The scalar formulation is inadequate to handle general anisotropic or inhomogeneous problems and it can be used only as an approximation in such cases. For a more accurate representation of general waveguide fields, a vector formulation, with at least two components is essential. This is particularly true for the analysis of photonic crystal fibres. Several vector formulations dealing with optical waveguide problems have been proposed by many authors. However, some of them are affected by non-physical spurious solutions, which appear mixed with the correct ones in the computations and therefore several methods have also been proposed to overcome such problems.

The  $\mathbf{E}_z$ - $\mathbf{H}_z$  formulation which is one of the first formulations used in finite element analysis (Csendes and Silvester 1970; Mabaya *et al.* 1981) cannot treat general anisotropic problems without destroying the canonical form of the eigenvalue equation (3.26). In addition to that some problems also arise whilst enforcing boundary conditions for a waveguide with an arbitrary dielectric distribution. Additionally, this approach is based on the axial field components which are the least important of the  $\mathbf{E}$  and  $\mathbf{H}$  fields for optical waveguide.

A vector  $\mathbf{E}$ -field formulation (English and Young 1971; Hano 1984; Koshiba *et al.* 1985a) which can handle general anisotropy but loss-less problems, has also been applied to the solution of several types of optical waveguides. For such a formulation, the natural boundary conditions correspond to a magnetic wall and therefore it is essential to enforce the electric wall ( $\mathbf{n} \times \mathbf{E} = 0$ ) as a boundary condition, which is difficult to implement for irregular shaped structures.

The vector **H**-field formulation is more suitable for dielectric waveguide problems because the magnetic field is continuous everywhere and the natural boundary conditions correspond to those of the electrical wall therefore no forced boundary conditions at the boundaries are required. This formulation can be written as (Berk 1956; Rahman and Davies 1984a):

$$\omega^2 = \frac{\int (\nabla \times \mathbf{H})^* \cdot \hat{\epsilon}^{-1} \cdot (\nabla \times \mathbf{H}) d\Omega}{\int \mathbf{H}^* \cdot \hat{\mu} \cdot \mathbf{H} d\Omega} \quad (3.29)$$

Where  $\omega$ , is the angular frequency,  $\Omega$  is the waveguide cross-section  $\hat{\epsilon}$  and  $\hat{\mu}$  are the permittivity and permeability tensors respectively. To obtain the stationary solution of the functional (3.29) this is minimised with respect to each of the variables, which are the unknown nodal field components  $H_x$ ,  $H_y$  and  $H_z$ . This minimisation leads to a matrix eigenvalue equation as stated in equation (3.26), where  $[A]$  is a complex Hermitian matrix and  $[B]$  is a real symmetric and positive-definite matrix. Because of the general  $90^\circ$  phase difference between the axial and transverse components of **H**-field (Konrad 1977), the Hermitian matrix  $[A]$  can be transformed to a real symmetric matrix for a loss-less problem. In general, the matrices  $[A]$  and  $[B]$  are quite sparse. The eigenvectors  $\{x\}$  represents the unknown field components at the nodal points for different modes with  $\lambda$  as their corresponding eigenvalues and also  $\lambda$  is proportional to  $\omega^2$ . In order to obtain a solution for a given wavelength, the propagation constant,  $\beta$  value has to be changed iteratively until the output eigenvalue corresponds to that wavelength. By varying  $\beta$  over the range of interest, it is possible to calculate the dispersion characteristics for the various modes.

However, the above formulation (as well as the **E**-field) yields spurious solutions because the divergence condition,  $\nabla \cdot \mathbf{H} = 0$  is not satisfied automatically, therefore alternative approaches, such as the penalty coefficient method (Rahman and Davies 1984a; Koshiba *et al.* 1985b) have been proposed to eliminate those non-physical solutions. This method will be discussed in a later section of this Chapter.

### 3.4.5 Natural Boundary Conditions

The term “natural boundary condition” arises in the calculus of variations and since the finite element method is fundamentally one minimisation of an error functional, the term arises also in this context. The boundary condition, which is automatically satisfied in the variational procedure is called the ‘natural boundary condition’. In variational formulations these can be automatically satisfied, if left free. The scalar functional defined earlier in equation (3.27) has the continuity of  $\frac{\partial E_x}{\partial \mathbf{n}}$  as the natural boundary

condition and the functional defined in equation (3.28) has the continuity  $\left(\frac{1}{n}\right)\left(\frac{\partial H_x}{\partial \mathbf{n}}\right)$  as

the natural boundary condition, where  $\mathbf{n}$  is the outward normal unit vector. The vector  $\mathbf{H}$ -field formulation described in equation (3.29) has the natural boundary condition of an electric wall, i.e.  $\mathbf{n} \cdot \mathbf{H} = 0$ . Therefore there is no need to force any boundary condition on conducting guide walls. But for regular shaped waveguides and at the symmetric walls (if applicable) the natural boundary condition can be imposed to reduce the matrix problem size. However, it may be necessary to analyse the structure with complementary symmetry conditions to obtain all the modes, although the exploitation of the symmetry greatly reduces the computational cost.

### 3.4.6 FEM Formulation

The key objective of using the finite element method is to find the solution of a complicated problem by replacing it with a simpler one. The differential operator equations which describe the physical problem are replaced by an appropriate extremum functional  $J$ , which is the variational for the desired quantity. The problem can be regarded as obtaining the solution  $\mathbf{H}$  over a specified region in the transverse plane so that the boundary conditions and also the extremum requirement are satisfied. The axial dependence is assumed in the form  $e^{-j\beta z}$  and the transverse plane is used for the discretisation.

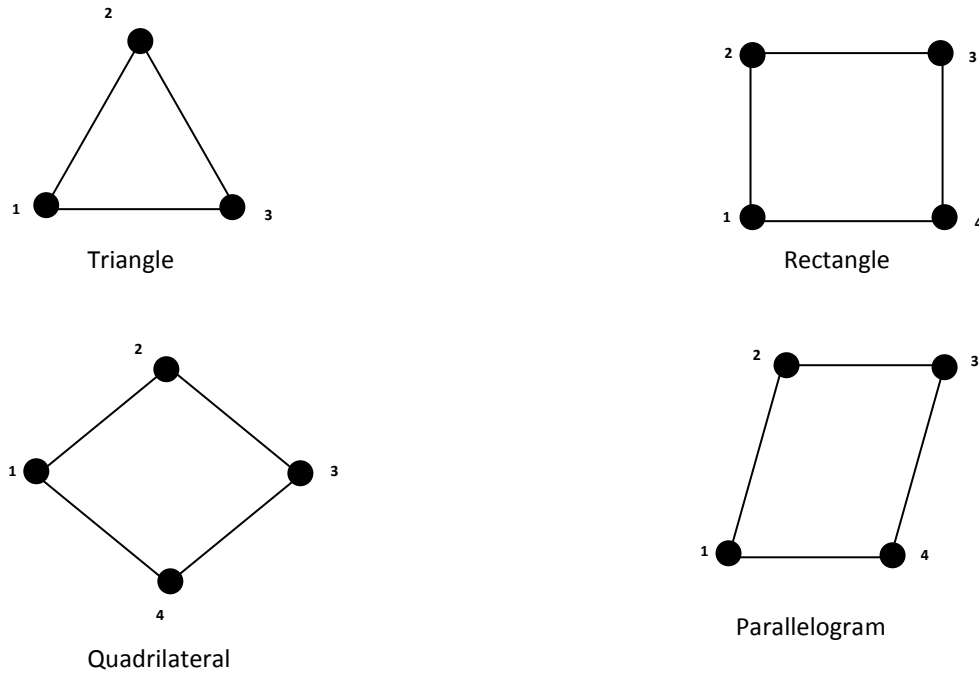


Fig. 3. 3: Finite elements in two dimensions

### 3.4.7 Domain Discretisation

The discretisation of the domain into sub-regions (finite elements) is considered as the initial step in the finite element method. The shapes, sizes, number and configurations of the elements have to be chosen carefully such that the original body or domain is simulated as closely as possible without increasing the computational effort needed for the solution. Each element is essentially a simple unit within which the unknown can be described in a simpler manner. There are various types of elements available for use in finite element formulations. These elements can be satisfied as one, two and three dimensional elements. When the geometry and material properties can be described in terms of two independent spatial coordinates, the two-dimensional elements shown in Fig. 3.3 can be used. The simplest and indeed the most basic element typically considered for two-dimensional analysis is the triangular element. The size of the element also dictates the accuracy of the final solution as higher order elements tend to provide more accurate solutions. A typical representation of an arbitrary waveguide structure using triangular elements is shown in Fig. 3.4.

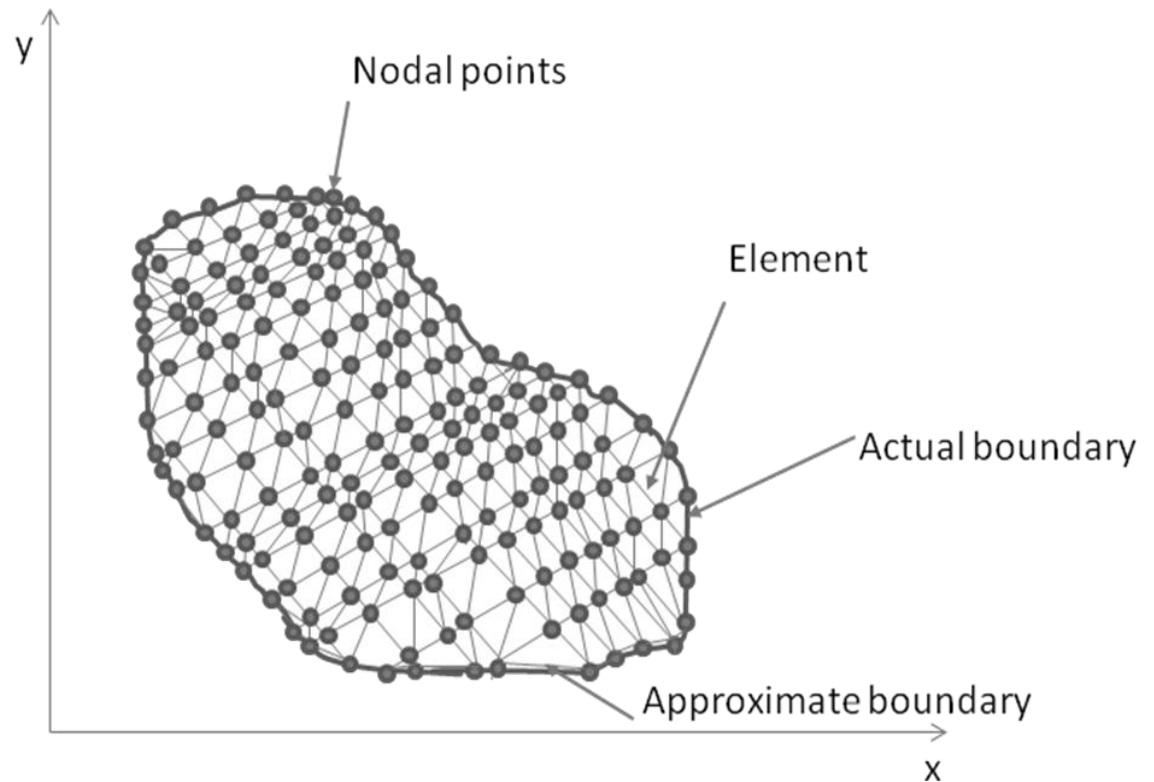


Fig. 3. 4: Finite element discretisation of a waveguide with triangular elements

By dividing the waveguide cross section into triangular elements, the unknown  $\mathbf{H}$  is also considered as to be discretised into corresponding sub-regions. These elements are easier to analyse rather than analysing the distribution over the whole cross section. As shown in Fig. 3.4, the transverse plane is covered with a grid of discrete nodes which are the vertices of each triangular element. The values of  $\mathbf{H}$  at these nodal points are the basic unknowns. The intersections of the sides of the triangular elements are called the nodal lines.

After running the simulations for the numerical experiments, the following parameters are noted down from the program after the simulations concludes:

- Wavelength
- Real propagation constant
- Imaginary propagation constant
- Effective index
- Loss
- $H_x$  field

- $H_y$  field
- $H_z$  field
- Spot size
- Effective area

To be sure the output is correct, the 1-D, 2-D or even 3-D field profiles of the output result of the  $H_x$  and/or  $H_y$  fields is plotted using MATLAB or Sigma plot. The dominant field would yield a field profile showing the field within the core.

### 3.4.8 Shape Functions

In two-dimensional problems, the element assumes a linear interpolation between the field values at the vertices of the triangle. Within each element the unknown field  $\mathbf{H}$ , is approximated by means of suitably chosen set of polynomials. These functions are called ‘shape functions’. For a simple triangular element the interpolation polynomial should include a constant term and both the  $x$  and  $y$  terms rather than only one of them. The field variable representation within an element should not alter the local co-ordinate system. In order to achieve this ‘geometric isotropy’ the polynomial should be complete according to Pascal’s triangle as shown in Fig. 3.5.

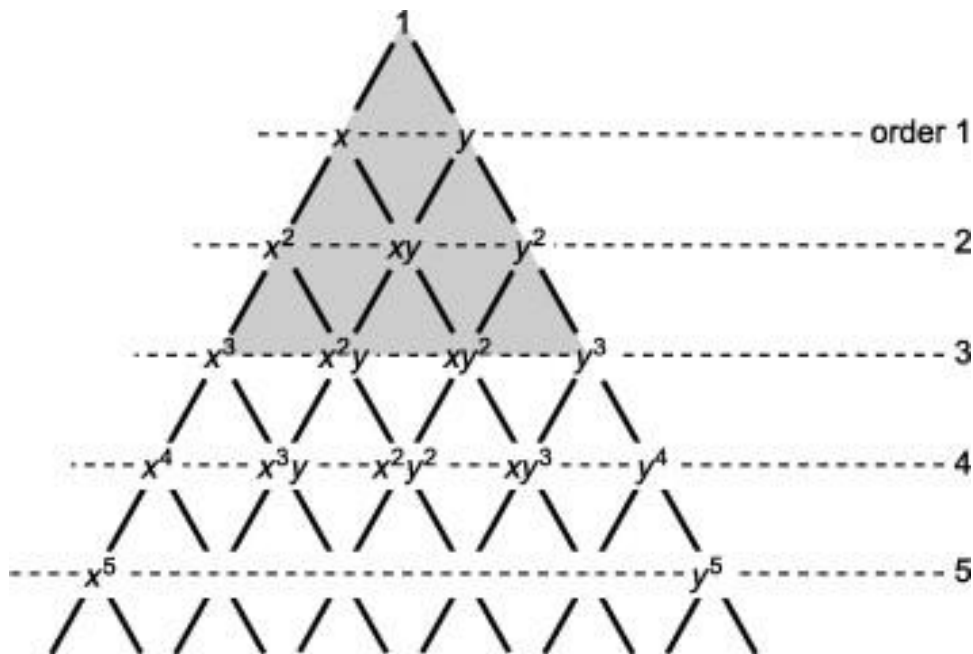


Fig. 3. 5: Pascal’s triangle for complete polynomials in two dimensions.

The final consideration in selecting the order of the interpolation polynomial is to make the total number of terms in the polynomial equal to the number of nodal degrees of freedom of the element. For example, the first degree polynomial involves three coefficients and so can be expressed in terms of three nodal values at the triangle vertices as shown in Fig. 3.6. The second degree polynomial needs six coefficients and can similarly be expressed in terms of values of six nodes.

The continuous field function  $\phi(x,y)$  in the problem domain may be replaced by a set of discrete values ( $\phi_i = 1, 2, 3, \dots, m$ ) where  $m$  is the total number of nodes. This function will be continuous across the triangles. To be admissible functions, they must satisfy some specific conditions between the elements; usually the continuity of the field across the boundaries is preferred.

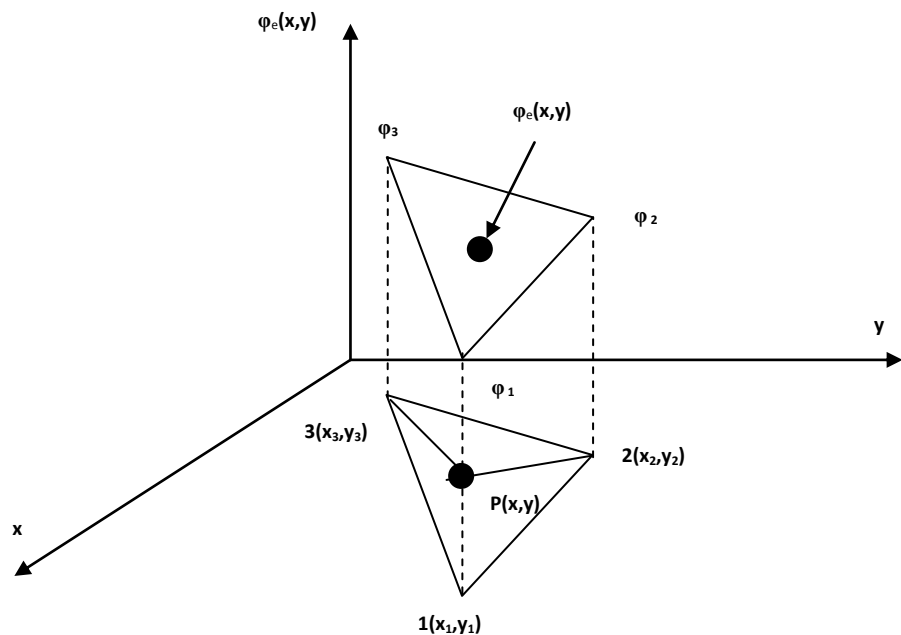


Fig. 3. 6: Representation of a first order triangular element.

A typical first order triangular element used in finite element discretisation is shown in Fig. 3.6. Inside each first order element, the nodal field values  $\phi$  are interpolated



continuously. This can be achieved by introducing the interpolation functions,  $N_i(x,y)$ . Thus, using the interpolation function the element field can be written as:

$$\phi_e(x, y) = \sum_{i=1}^3 N_i(x, y) \cdot \phi_i \quad (3.30)$$

where  $\phi_i$  are the nodal field values. The functions  $N_i(x,y)$  are called 'shape functions'. Equation (3.30) can also be written in matrix form as:

$$\phi_e(x, y) = [N_1 \ N_2 \ N_3] \begin{Bmatrix} \phi_1 \\ \phi_2 \\ \phi_3 \end{Bmatrix} \quad (3.31)$$

$$\phi_e(x, y) = [N] \{\phi_e\} \quad (3.32)$$

where  $[N]$  is the shape function matrix and the column vector  $\{\phi_e\}$  is a vector corresponding to the field values at the 3 vertices of the triangular element. In order to obtain the shape functions,  $N_i(x,y)$ ,  $i = 1,2,3,\dots$ , a linear approximation of the field inside the elements must be performed:

$$\phi_e(x, y) = \alpha_1 + \alpha_2 x + \alpha_3 y \quad (3.33)$$

for which  $\alpha_1$ ,  $\alpha_2$ , and  $\alpha_3$  are constants. By re-writing the above relation, such that the following conditions are satisfied:

$$\phi_e(x_i, y_i) = \phi_i \quad i = 1,2,3 \quad (3.34)$$

$$\phi_e(x, y) = \sum_{i=1}^3 N_i(x, y) \cdot \phi_i$$

where  $(x_i, y_i)$  ( $i = 1,2,3$ ) are the global co-ordinates of the three vertices of the triangle. Hence the nodal field values  $\phi_i$  can be written as:

$$\begin{aligned} \phi_1 &\equiv \phi_e(x_1, y_1) = \alpha_1 + \alpha_2 x_1 + \alpha_3 y_1 \\ \phi_2 &\equiv \phi_e(x_2, y_2) = \alpha_1 + \alpha_2 x_2 + \alpha_3 y_2 \end{aligned} \quad (3.35)$$

$$\phi_3 \equiv \phi_e(x_3, y_3) = \alpha_1 + \alpha_2 x_3 + \alpha_3 y_3$$

This can also be written in the matrix form as:

$$\begin{Bmatrix} \phi_1 \\ \phi_2 \\ \phi_3 \end{Bmatrix} = \begin{bmatrix} 1 & x_1 & y_1 \\ 1 & x_2 & y_2 \\ 1 & x_3 & y_3 \end{bmatrix} \begin{Bmatrix} \alpha_1 \\ \alpha_2 \\ \alpha_3 \end{Bmatrix} \quad (3.36)$$

By solving the above matrix equation, the constants  $\alpha_1$ ,  $\alpha_2$  and  $\alpha_3$  can be determined in terms of  $\phi_i$ ,  $i=1, 2, 3$ :

$$\begin{aligned} \alpha_1 &= \frac{1}{2A_e} [\phi_1(x_2 y_3 - x_3 y_2) + \phi_2(x_3 y_1 - x_1 y_3) + \phi_3(x_1 y_2 - x_2 y_1)] \\ \alpha_2 &= \frac{1}{2A_e} [\phi_1(y_2 - y_3) + \phi_2(y_3 - y_1) + \phi_3(y_1 - y_2)] \\ \alpha_3 &= \frac{1}{2A_e} [\phi_1(x_3 - x_2) + \phi_2(x_1 - x_3) + \phi_3(x_2 - x_1)] \end{aligned} \quad (3.37)$$

where  $A_e$  is the area of the triangular element given by:

$$A_e = \frac{1}{2} \begin{vmatrix} 1 & x_1 & y_1 \\ 1 & x_2 & y_2 \\ 1 & x_3 & y_3 \end{vmatrix} = \frac{1}{2} (x_2 y_3 - x_3 y_2) + (x_3 y_1 - x_1 y_3) + (x_1 y_2 - x_2 y_1) \quad (3.38)$$

Substituting the values of  $\alpha_i$  from equation (3.37) into equation (3.33) results in the formation of the following equation:

$$\phi_e(x, y) = N_1(x, y) \cdot \phi_1 + N_2(x, y) \cdot \phi_2 + N_3(x, y) \cdot \phi_3$$

$$\phi_e(x, y) = [N] \{\phi_e\} \quad (3.39)$$

The above relation has close resemblance to the matrix relation given earlier in equation (3.32) and  $N_i(x, y)$   $i = 1, 2, 3$  are shape functions given by the matrix notation (Davies 1989):

$$[N]^T = \begin{bmatrix} N_1 \\ N_2 \\ N_3 \end{bmatrix} = \frac{1}{2A_e} \begin{bmatrix} x_2 y_3 - x_3 y_2 & y_2 - y_3 & x_3 - x_2 \\ x_3 y_1 - x_1 y_3 & y_3 - y_1 & x_1 - x_3 \\ x_1 y_2 - x_2 y_1 & y_1 - y_2 & x_2 - x_1 \end{bmatrix} \begin{bmatrix} 1 \\ x \\ y \end{bmatrix} \quad (3.40)$$

Where T denotes a transpose of the N matrix. The shape function matrix can also be re-written as:

$$[N]^T = \begin{bmatrix} N_1 \\ N_2 \\ N_3 \end{bmatrix} = \begin{bmatrix} a_1 + b_1 x + c_1 y \\ a_2 + b_2 x + c_2 y \\ a_3 + b_3 x + c_3 y \end{bmatrix} \quad (3.41)$$

And  $a_i, b_i, c_i$  ( $i = 1, 2, 3$ ) are the constants for a given element and calculated as:

$$a_1 = \frac{x_2 y_3 - x_3 y_2}{2A_e}$$

$$b_1 = \frac{y_2 - y_3}{2A_e} \quad (3.42)$$

$$c_1 = \frac{x_3 - x_2}{2A_e}$$

Similarly  $a_2, b_2, c_2, a_3, b_3,$  and  $c_3$  can be calculated by cyclic exchange of  $1 \rightarrow 2 \rightarrow 3$  in equation (3.42). The shape functions  $N_i$  can also be expressed in terms of the areas of the triangle shown earlier in Fig. 3.6 as:

$$N_i = \frac{\text{area of sub triangle P23}}{\text{area of triangle 123}} \quad (3.43)$$

Similarly  $N_2$  and  $N_3$  can be defined in the same way. Hence,  $N_i$  has the following property:

$$\sum_{i=1}^3 N_i = 1 \quad (3.44)$$

Thus evaluating the shape function  $N_i$  gives a value of 1 at the node  $1(x_1, y_1)$  whereas at nodes 2 and 3 a value of 0 is obtained. Hence it is unique first-degree interpolation

function for node 1. Similarly the shape functions  $N_2$  and  $N_3$  gives a value of 1 at nodes 2 and 3 respectively and 0 at other nodes.

### 3.4.9 Global and Element Matrices

The solution of the optical waveguide problem by the FEM can be transformed to a standard eigenvalue problem as in equation (3.26) where matrices  $[A]$  and  $[B]$  are known as global matrices and consist of the summation of the element matrices for each triangular element of the discretised cross-section of the optical waveguide. In this section, the assembly of the element and global matrices is shown, with respect to the shape functions and the nodal field values of each triangular element, based on the variational formulation. Throughout the procedure, the full  $\mathbf{H}$ -field formulation in terms of the three components is assumed and first-order triangular elements are being used. Within each of the triangular elements the three unknown field  $\mathbf{H}$ -components  $H_x$ ,  $H_y$  and  $H_z$  of the magnetic field can be represented as follows:

$$H_x(x, y) = [N_1 \ N_2 \ N_3] \begin{bmatrix} H_{x1} \\ H_{x2} \\ H_{x3} \end{bmatrix}$$

$$H_y(x, y) = [N_1 \ N_2 \ N_3] \begin{bmatrix} H_{y1} \\ H_{y2} \\ H_{y3} \end{bmatrix} \quad (3.45)$$

$$H_z(x, y) = [N_1 \ N_2 \ N_3] \begin{bmatrix} H_{z1} \\ H_{z2} \\ H_{z3} \end{bmatrix}$$

Where  $H_{xi}$ ,  $H_{yi}$  and  $H_{zi}$  for  $i=1,2,3$  are the x,y and z components of the magnetic fields. Hence the magnetic field over the element  $[\mathbf{H}]_e$  can be described as:

$$[\mathbf{H}]_e = \begin{bmatrix} H_x(x, y) \\ H_y(x, y) \\ H_z(x, y) \end{bmatrix} = \begin{bmatrix} N_1 & N_2 & N_3 & 0 & 0 & 0 & 0 & 0 & 0 \\ 0 & 0 & 0 & N_1 & N_2 & N_3 & 0 & 0 & 0 \\ 0 & 0 & 0 & 0 & 0 & 0 & N_1 & N_2 & N_3 \end{bmatrix} \begin{bmatrix} H_{x1} \\ H_{x2} \\ H_{x3} \\ H_{y1} \\ H_{y2} \\ H_{y3} \\ H_{z1} \\ H_{z2} \\ H_{z3} \end{bmatrix} \quad (3.46)$$

In more compact form, the above equation (3.46) can be written as:

$$[\mathbf{H}]_e = [\mathbf{N}]\{\mathbf{H}\}_e \quad (3.47)$$

where  $\{\mathbf{H}\}_e$  is the column vector representing the three components of the nodal field values in the elements and  $[\mathbf{N}]$  is the shape function matrix. Also using equation (3.47), the curl of  $\mathbf{H}$  equation (3.29) can be written as:

$$(\nabla \times \mathbf{H})_e = \nabla \times [\mathbf{N}]\{\mathbf{H}\}_e = \begin{bmatrix} 0 & -\frac{\partial}{\partial z} & \frac{\partial}{\partial y} \\ \frac{\partial}{\partial z} & 0 & -\frac{\partial}{\partial x} \\ -\frac{\partial}{\partial y} & \frac{\partial}{\partial x} & 0 \end{bmatrix} [\mathbf{N}]\{\mathbf{H}\}_e = [\mathbf{Q}]\{\mathbf{H}\}_e \quad (3.48)$$

Where the matrix  $[\mathbf{Q}]$  can be written as:

$$[\mathbf{Q}] = \begin{bmatrix} [0] & -\frac{\partial}{\partial z} & \frac{\partial}{\partial y} \\ \frac{\partial}{\partial z} & [0] & -\frac{\partial}{\partial x} \\ -\frac{\partial}{\partial y} & \frac{\partial}{\partial x} & [0] \end{bmatrix} \quad (3.49)$$

Where  $[0] = [0 \ 0 \ 0]$  and  $[\mathbf{N}] = [N_1 \ N_2 \ N_3]$  and some of the shape function derivatives are assumed substituted using equation (3.41) as shown:

$$\begin{aligned}\frac{\partial N_1}{\partial x} &= b_1, \quad \frac{\partial N_2}{\partial x} = b_2, \quad \frac{\partial N_3}{\partial x} = b_3 \\ \frac{\partial N_1}{\partial y} &= c_1, \quad \frac{\partial N_2}{\partial y} = c_2, \quad \frac{\partial N_3}{\partial y} = c_3\end{aligned}\tag{3.50}$$

The solutions of the constants  $b_1, b_2, b_3, c_1, c_2$  and  $c_3$  were shown earlier in equation (3.42). By substituting the expressions shown in equations (3.47) and (3.48) in to the variational formulation of equation (3.29), the vector  $\mathbf{H}$ -field formulation functional for an element can be obtained as:

$$\begin{aligned}\omega^2 &= \frac{\int (\nabla \times \mathbf{H})^* \cdot \hat{\varepsilon}^{-1} \cdot (\nabla \times \mathbf{H}) d\Omega}{\int (\mathbf{H}^* \cdot \hat{\mu} \cdot \mathbf{H}) d\Omega} \\ \Rightarrow \omega^2 &= \frac{\int_{\Delta} ([Q]\{\mathbf{H}\}_e)^* \cdot \hat{\varepsilon}^{-1} \cdot [Q]\{\mathbf{H}\}_e d\Omega}{\int_{\Delta} ([N]\{\mathbf{H}\}_e)^* \cdot \hat{\mu} \cdot ([N]\{\mathbf{H}\}_e) d\Omega} \\ \Rightarrow \omega^2 &= \frac{\int_{\Delta} \{\mathbf{H}\}_e^T [Q]^* \cdot \hat{\varepsilon}^{-1} [Q]\{\mathbf{H}\}_e d\Omega}{\int_{\Delta} \{\mathbf{H}\}_e^T [N]^T \cdot \hat{\mu} ([N]\{\mathbf{H}\}_e) d\Omega}\end{aligned}\tag{3.51}$$

Re-arranging the last part of the above equation (3.51), the following can be obtained:

$$J_e = \int_{\Delta} \{\mathbf{H}\}_e^T [Q]^* \cdot \hat{\varepsilon}^{-1} \cdot [Q]\{\mathbf{H}\}_e d\Omega - \omega^2 \int_{\Delta} \{\mathbf{H}\}_e^T [N]^T \cdot \hat{\mu} [N]\{\mathbf{H}\}_e d\Omega\tag{3.52}$$

Where  $\Delta$  represents the integration over the triangular element domain. T and \* denote the transpose of a matrix and the complex conjugate transpose, respectively. The [Q] matrix was defined earlier in equation (3.49). A transpose operation on this matrix would define the [Q]\* matrix. For isotropic material, the relative permittivity  $\varepsilon_r$  is a scalar quantity. For waveguides consisting of anisotropic material the relative permittivity  $\varepsilon$  can be taken as a tensor represented by a 3 x 3 matrix and the inverse of the matrix should be implemented. The total function, J associated with the whole cross-

section of the waveguide can be obtained by summing  $J_e$  of all the individual elements as:

$$J = \sum_{e=1}^N J_e \quad (3.53)$$

Where  $N$  is the number of elements.

The minimisation of the functional given in equation (3.53) can be performed by differentiating with respect to the field nodal values and equating it to vary as below:

$$\frac{\partial J}{\partial \{\mathbf{H}\}_e} = 0 \quad (3.54)$$

Thus the following relation can be obtained:

$$\frac{\partial J}{\partial \{\mathbf{H}\}_e} = 2 \int_{\Delta} \{\mathbf{H}\}_e [\mathbf{Q}]^* \cdot \hat{\varepsilon}^{-1} [\mathbf{Q}] d\Omega - 2\omega^2 \int_{\Delta} [\mathbf{N}]^T \hat{\mu} [\mathbf{N}] \{\mathbf{H}\}_e d\Omega = 0 \quad (3.55)$$

$$\therefore \int_{\Delta} [\mathbf{Q}]^* \cdot \hat{\varepsilon}^{-1} [\mathbf{Q}] d\Omega \cdot \{\mathbf{H}\}_e - \omega^2 \int_{\Delta} \mu [\mathbf{N}]^T [\mathbf{N}] d\Omega \cdot \{\mathbf{H}\}_e = 0$$

Thus the following eigenvalue equation can be obtained:

$$[\mathbf{A}] \{\mathbf{H}\} - \omega^2 [\mathbf{B}] \{\mathbf{H}\} = 0 \quad (3.56)$$

Where the matrices  $[\mathbf{A}]$  and  $[\mathbf{B}]$  can be defined as:

$$[\mathbf{A}] = \sum_{e=1}^N [\mathbf{A}]_e = \sum_{e=1}^N \int_{\Delta} [\mathbf{Q}]^* \hat{\varepsilon}^{-1} [\mathbf{Q}] d\Omega$$

$$[\mathbf{B}] = \sum_{e=1}^n [\mathbf{B}]_e = \sum_{e=1}^n \hat{\mu} \int_{\Delta} [\mathbf{N}]^T [\mathbf{N}] d\Omega \quad (3.57)$$

Matrix  $\{\mathbf{H}\}$  contains all the  $\mathbf{H}$ -field nodal values over the whole cross-section of the waveguide considered.  $[\mathbf{A}]_e$  and  $[\mathbf{B}]_e$  represent the element matrices whose assemblage over the whole cross-section result in formation of the so called global matrices of the eigenvalue equation, given by  $[\mathbf{A}]$  and  $[\mathbf{B}]$ , respectively. The calculation of the element matrices,  $[\mathbf{A}]_e$  and  $[\mathbf{B}]_e$  are shown in Appendix.

When solving waveguide problems by using finite elements, the key factor affecting storage requirements and computational effort is the choice of algorithm to solve the matrix equation. The global matrices  $[A]$  and  $[B]$  shown in equation (3.57) are highly sparse. The sparsity increases with the order of the matrices and decreases with the polynomial order of the shape functions. It is obvious that using higher order basis functions, one may obtain a more accurate solution of the problem under consideration. However, the added disadvantage to that is that the process involves increasing the programming effort, particularly when considering waveguide problems with material anisotropy, infinite elements and penalty functions. In addition to that higher order polynomials for a given matrix order increases the density of the matrix although this can be handled with reasonable effort by using a sophisticated matrix solver.

### 3.4.10 Spurious Solution

The usage of vector formulations in analysing waveguide problems results in generating some non-physical, spurious solutions along with the physical solutions of the system. Spurious solutions may evolve due to several reasons such as:

- (i) enforcement of boundary condition
- (ii) positive definiteness of the operator
- (iii) non-zero divergence of the trial fields

In the  $\mathbf{H}$ -field formulation, the associated Euler equation is consistent with the two curl Maxwell's equations (3.1), (3.2) but does not satisfy the  $\nabla \cdot \mathbf{B} = 0$  condition which may be the reason behind the appearance of spurious modes (Rahman and Davies 1984a).

The identification of the spurious modes amongst the physical modes can be difficult, when a set of eigenmodes is computed. Sometimes spurious modes can be spotted from their dispersion curves or by their eigenvectors, where the field varies in an unreasonable, sometimes in a random way along the cross-section of the waveguide. Rahman and Davies (Rahman and Davies 1984c) have developed a procedure which gives a reasonable identification of the spurious modes. In the above approach, the divergence of the magnetic field,  $\nabla \cdot \mathbf{H} = 0$  is calculated for each eigenvector and when the value obtained is high, it is assumed that the eigenmode does not satisfy the divergence condition and therefore it is a spurious mode.



Several approaches have been used, most of them aiming to force the condition  $\nabla \cdot \mathbf{H} = 0$ , which is considered the main cause of spurious modes. In the method developed by Rahman and Davies (Rahman and Davies 1984c) an integral is added to the  $\mathbf{H}$ -field formulation so that the resulting Euler equation is the Helmholtz equation plus the  $\nabla \cdot \mathbf{B} = 0$  condition. The variational formulation then becomes as (Rahman and Davies 1984a; Rahman and Davies 1984c):

$$\omega^2 = \frac{\int (\nabla \times \mathbf{H})^* \frac{1}{\varepsilon} \cdot (\nabla \times \mathbf{H}) d\Omega + \frac{p}{\varepsilon_o} \int (\nabla \cdot \mathbf{H})^* (\nabla \cdot \mathbf{H}) d\Omega}{\int (\mathbf{H}^* \cdot \mu \mathbf{H}) d\Omega} \quad (3.58)$$

Where  $p$  is the dimensionless penalty factor. The value of  $p$  is often taken to be around  $1/\varepsilon_n$ , where  $\varepsilon_n$  is the dielectric constant of the core of the waveguide. In this method the divergence free constraint is imposed in a least-squares sense and the larger the penalty factor the more heavily the constraint is implemented giving a further reduction of the spurious modes from the spectrum. The penalty function also improves the quality of the eigenvectors without increasing the order of the matrix in the eigenvalue problem.

There are some associated methods besides the mode solver methods discussed in section 3.2 which are used. These techniques are used with the mode solvers and are discussed below.

### 3.5 The Perfectly Matched Layer (PML) Boundary Condition

The Perfectly Matched Layer (PML) is the latest version of boundary conditions that have shown their high efficiency and has proved to be more robust compared to the previous approaches such as the Absorbing Boundary Conditions (ABC) and Transparent Boundary Conditions (TBC). Using an imaginary electrical layer enables the PML to absorb and attenuate the output wave at different angles and frequencies (Berenger 1994).

Through the adjusting of the PML parameters so as to have a wave impedance of exactly the same as inside the computational domain, the PML can offer a reflectionless boundary to the outgoing radiation whatever its strength or angle it hits the PML-computational domain interface. The PML boundary condition effectively absorbs the unwanted radiation waves without reflection. The concept of the Perfectly Matched

Layer (PML) was first introduced by Berenger (Berenger 1994) as an alternative to the Absorbing Boundary Conditions (ABC) and Transparent Boundary Conditions (TBC), in order to synthesise an absorbing layer for the Finite Difference Time Domain (FDTD) method. The PML concept has been successfully applied in one-dimensional and three-dimensional FD-BPM (Huang *et al.* 1996) and needs the splitting of field components into two equations, which is not the desired form for the application of finite elements. Pekel and Mittra (Pekel and Mittra 1995a; Pekel and Mittra 1995b) had introduced a new form of the PML, for treating free space scattering problems, which does not involve the field splitting, maintaining the desired form of the Maxwell's equation for the finite element application.

Obayya, Rahman and El-Mikati (Obayya *et al.* 2000), incorporated the robust perfectly matched layer boundary condition into the finite element –based BPM formulations, which considers all the three field components. In this project, the PML is applied to our FEM formulation. The main advantage of the present formulation is that the sparsity of the global matrices is retained. Therefore a numerically efficient sparse matrix solver can be used.

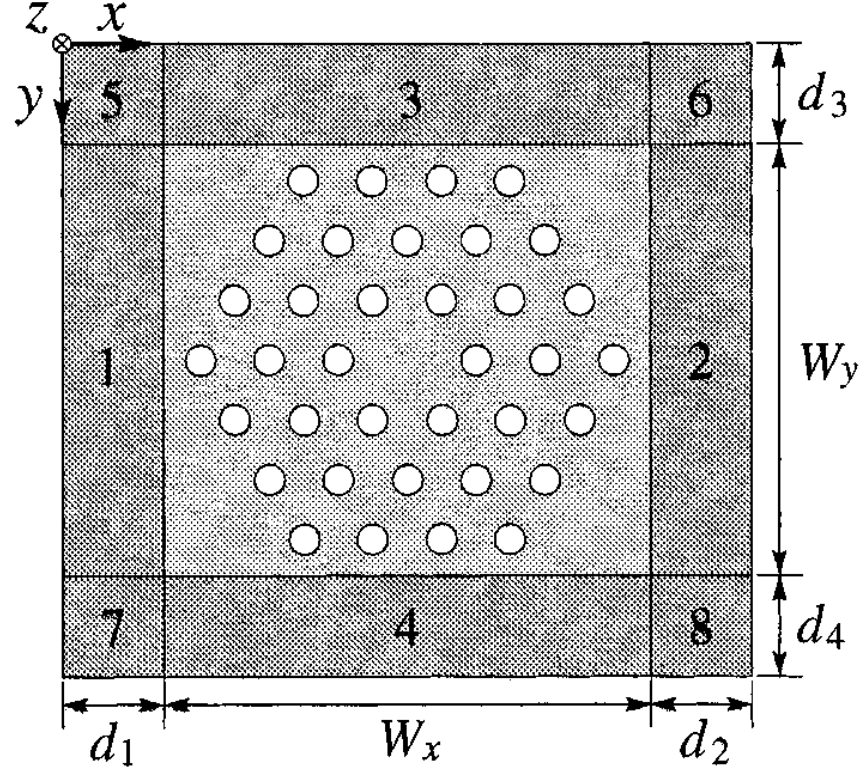


Fig. 3. 7: The structure of a PCF showing transverse section of the PCF surrounded by PML (Saitoh and Koshiba 2002).

Figure 3.7 shows the optical waveguide cross-section with different PML regions, where  $x$  and  $y$  are the transverse directions,  $z$  is the direction of the propagation, the regions 1, 2, 3 and 4 are the PML regions normally faced with  $x$  and  $y$  directions, respectively, regions 5, 6, 7 and 8 corresponds to the four corners of the PML, the middle region corresponds to the computational domain region;  $d_1, d_2, d_3$  and  $d_4$  are the width or height of the PML and  $W_x$  and  $W_y$  are the width and height of the computational domain in the  $x$  and  $y$  directions, respectively

Starting with new PML form, Maxwell's equations can be taken the form:

$$\nabla \times \mathbf{H} = \varepsilon \frac{\partial \mathbf{E}}{\partial t} + \mathbf{J} \quad (3.59)$$

$$\nabla \times \mathbf{E} = -\mu \frac{\partial \mathbf{H}}{\partial t} \quad (3.60)$$

Where  $\mathbf{E}$  and  $\mathbf{H}$  are the electric and magnetic field vectors respectively.

Assuming the time dependence to be  $e^{j\omega t}$  where  $t$  is the time and  $\omega$  is the radian or angular frequency and  $j$  is the imaginary part for convenience purposes. Thus the differential form of Maxwell's equations can be written as:

$$\nabla \times \mathbf{H} = j\omega\epsilon_o n^2 \mathbf{E} \quad (3.61)$$

$$\nabla \times \mathbf{E} = -j\omega\mu_o \mathbf{H} \quad (3.62)$$

Where,  $n$  is the refractive index and  $\nabla$  is the modified differential operator defined as:

$$\nabla = \mathbf{x}a_x \frac{\partial}{\partial x} + \mathbf{y}a_y \frac{\partial}{\partial y} + \mathbf{z}a_z \frac{\partial}{\partial z} \quad (3.63)$$

Where  $\mathbf{x}$ ,  $\mathbf{y}$  and  $\mathbf{z}$  are the unit vectors in the  $x$ ,  $y$  and  $z$  directions respectively and  $a_x$ ,  $a_y$  and  $a_z$  are the parameters associated with the PML boundary conditions imposed at the edge of the computational window. Since the wave propagation is assumed to be along  $z$  direction,  $a_z$  will be set unity. On the other hand,  $a_x$  and  $a_y$  has to be set in such a way that the radiating waves can freely leave the computational window with almost no reflection by taking the following profile (Obayya *et al.* 2000):

$$\alpha_i (t = x \text{ or } y) = \frac{1}{1 - j \frac{\sigma_e}{\omega\epsilon_o n^2}} = \frac{1}{1 - j \frac{\sigma_m}{\omega\mu_o}} \quad (3.64)$$

In the case  $\sigma_e$ , and  $\sigma_m$  are the electric and magnetic conductivities of the PML respectively. The equation (3.64) shows that the PML satisfies the impedance matching condition with an adjacent medium in the computational domain with refractive index  $n$

and wave impedance  $\sqrt{\frac{\mu_o}{\epsilon_o n^2}}$ .

The values of the parameters  $\alpha_x$  and  $\alpha_y$  are defined in the different regions as:

- (i) Central region (computational domain):  $\alpha_x = 1$  and  $\alpha_y = 1$
- (ii) regions 1 and 2 :  $\alpha_x = \alpha_t$  and  $\alpha_y = 1$
- (iii) regions 3 and 4 :  $\alpha_x = 1$  and  $\alpha_y = \alpha_t$
- (iv) regions 5, 6, 7, 8 :  $\alpha_x = \alpha_t$  and  $\alpha_y = \alpha_t$

in the PML regions, the electric conductivity profile can be assumed as

$$\sigma_e(\rho) = \sigma_{\max} \left[ \frac{\rho}{W_{(x,y)}} \right]^m \quad (3.65)$$

where  $\sigma_{\max}$  is the maximum value of the electric conductivity,  $\rho$  is the distance inside the PML which is measured from the interface of the computational domain and the PML and  $m$  is the power of the conductivity profile and be taken as 2. For this conductivity profile, the theoretical reflection coefficient,  $R$ , at the interface between the PML and the computational domain is given as (Berenger 1994):

$$R = \exp \left[ -2 \frac{\sigma_{\max}}{cn\epsilon_o} \int_0^W \left( \frac{\rho}{W_{(x,y)}} \right)^2 \partial \rho \right] \quad (3.66)$$

Where  $c$  is the velocity of light in free space. Performing the integrating in equation (3.66)  $\alpha_{\max}$  can be shown as:

$$\sigma_{\max} = \frac{3cn\epsilon_o}{2d} \ln \left( \frac{1}{R} \right) \quad (3.67)$$

Where  $R$  is the value of the theoretical reflection coefficient.

In the case when  $R$  is set to a very small value, the maximum electric conductivity ( $\sigma_{\max}$ ) is calculated using the equation (3.67). Therefore, the PML parameters  $\alpha_x$  and  $\alpha_y$  and the electric conductivity profile  $\sigma(\rho)$  will be determined for the different PML areas. Such PML arrangements will force any non-physical radiating wave to leave freely the computational domain whatever the angle and/or the strength it hits the boundary of the computational domain.

### 3.6 The Least Squares Boundary Residual Method

There has been a considerable interest in the analysis and design of integrated optical devices in which waveguide parameters vary along the axial direction. They play an important role in designing practical devices such as an isolated step discontinuity as in the simple butt-joining of two waveguides of different dimensions or materials or as finite cascades of discontinuities as in the bending of an optical waveguide in an integrated optical directional coupler circuit, the tapering of a channel waveguide for

efficient coupling to an optical fibre, gratings on the dielectric waveguides on certain components like Bragg reflectors or Y-junctions. Various methods for the analysis of the discontinuity problems in a dielectric waveguide have been developed by a number of authors (Clarricoats and Sharpe 1972; Hockman and Sharpe 1972; Mahmoud and Beal 1975; Morishita *et al.* 1979; Shigesawa and Tsuji 1986). However, most of the theoretical analyses reported earlier have restricted limitations of practical application, since the radiated and reflected waves have been ignored and also used under the assumption of slight discontinuity.

The problem considered here is an abrupt discontinuity in the transverse plane  $z = 0$ , between two arbitrarily shaped uniform waveguides. Each waveguide can have scalar or tensor permittivity that varies arbitrarily with the two transverse directions. The incoming wave incident upon the discontinuity plane is presumed of one mode. In this thesis, the discontinuities in the dielectric waveguides are accurately analysed using the Least Squares Boundary Residual (LSBR) method (Rahman and Davies 1988). Consequently, the LSBR method has been used along with the versatile vector finite element method (Rahman and Davies 1984b) in order to calculate the power transfer from a waveguide section to another.

The least squares boundary residual method was introduced as an alternative to the point matching (and Galerkin) methods of numerically solving problems. The LSBR method satisfies the boundary conditions in the useful least-squares sense over the discontinuity interface. In contrast to the point matching method, the LSBR method is a rigorously convergent procedure, free from the phenomenon of relative convergence. The LSBR method has the flexibility of introducing an electric/magnetic weighting factor and unlike the point matching the errors being minimised are global rather than sampled just at discrete points. The method has been widely used to study discontinuity parameters in microwave and optical waveguides (Davies 1973; Brooke and Kharadly 1976; Matsumoto *et al.* 1986; Cullen and Yeo 1987; Fernandez and Davies 1988). The LSBR method matches the continuity of the tangential fields in the least squares sense considering many modes at the discontinuity plane to provide the generalised scattering matrix. In this study, it has been shown that LSBR method is an accurate and versatile numerical tool to obtain the power transfer between coupled waveguides.

### 3.6.1 Analysis of Discontinuity in Dielectric Waveguides

Consider the abrupt junction of two dielectric waveguides as illustrated in Fig. 3.8. It is assumed that the discontinuity junction is excited by an incident wave of one mode from side I. This incoming wave is partly reflected, partly transmitted and radiated at the junction interface. Let  $E_t^{\text{in}}$  and  $H_t^{\text{in}}$  be the transverse components of the electric and magnetic fields of the incident wave respectively. Some of the incident wave is reflected back into the side I. On the other hand, many modes will be generated at the discontinuity plane to satisfy the boundary conditions. These can be guided or radiated modes in both sides of the discontinuity. The total transverse electric and magnetic fields  $E_t^{\text{I}}$  and  $H_t^{\text{I}}$  in side I and  $E_t^{\text{II}}$  and  $H_t^{\text{II}}$  in side II at the discontinuity plane ( $z = 0$ ), can be expressed in terms of the eigenmodes in side I and side II, respectively as follows:

$$E_t^{\text{I}} = E_t^{\text{in}} + \sum_{i=0}^{\infty} a_i E_{ti}^{\text{I}} \quad (3.68)$$

$$H_t^{\text{I}} = H_t^{\text{in}} - \sum_{i=0}^{\infty} a_i H_{ti}^{\text{I}} \quad (3.69)$$

$$E_t^{\text{II}} = \sum_{i=0}^{\infty} b_i E_{ti}^{\text{II}} \quad (3.70)$$

$$H_t^{\text{II}} = \sum_{i=0}^{\infty} b_i H_{ti}^{\text{II}} \quad (3.71)$$

The modes which are generated at the discontinuity plane may be propagating, radiating or evanescent. Therefore  $E_{ti}^{\text{I}}$  and  $H_{ti}^{\text{I}}$  represent the transverse field components of the  $i^{\text{th}}$  mode reflected from the junction in side I and  $a_i$  are the corresponding modal amplitudes of these reflected modes. Similarly,  $E_{ti}^{\text{II}}$  and  $H_{ti}^{\text{II}}$  are the transverse field components of the  $i^{\text{th}}$  mode transmitted in side II and  $b_i$  are the modal amplitudes of those transmitted modes. These scattering coefficients  $a_i$  and  $b_i$  have to be determined.

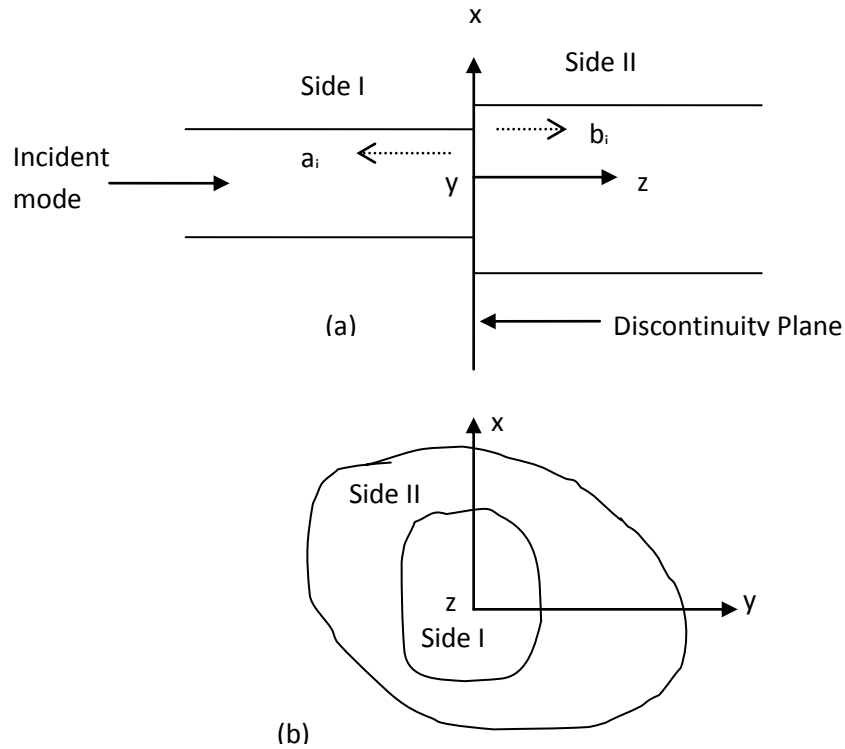


Fig. 3. 8: Discontinuity junction of two dielectric waveguide (a) vertical section of the discontinuity between side I and II (b) Transverse cross section of the discontinuity at the junction of two sides.

Considering the fields in either side of the discontinuity the mean-squares error to the boundary condition in that plane can be defined as the functional:

$$J = \int \left| E_t^I - E_t^{II} \right|^2 + w Z_0^2 \left| H_t^I - H_t^{II} \right|^2 d\Omega \quad (3.72)$$

Where  $w$  is a convenient, positive and dimensionless weighting factor  $Z_0$  is the free-space wave impedance and the integral is calculated over the discontinuity plane.

In the LSBR method, the aim is to look for a stationary solution to satisfy the continuity conditions of the tangential fields in a least squares sense by minimising the functional (3.72) to obtain the approximate numerical solution to the problem. The infinite series expansion of 3.68 to 3.71 are truncated including all relevant propagating modes plus as many radiating and/or evanescent modes as convenient. In this analysis, all the



reflection, transmission and radiation fields are determined in such a way the  $J$  becomes a minimum. The electromagnetic fields thus obtained are the best approximate fields in the sense of least square error. The condition for eq. (3.72) being minimised is

$$\frac{\partial J}{\partial a_i} = 0, \quad \frac{\partial J}{\partial b_i} = 0 \quad \text{for } i = 1, \dots, \text{infinity} \quad (3.73)$$

this results in a set of linear equations:

$$Cx = v \quad (3.74)$$

The solution of this equation gives (Yeh *et al.* 1978), the required approximate modal coefficient of  $a_i$  and  $b_i$ . These constitute one column of the scattering matrix, corresponding to the chosen incident mode.  $C$  is a square matrix generated from the eigenvectors and  $v$  is an array due to the incident mode. The elements of  $C$  and  $v$  are given by:

$$C_{ij} = \langle E_{ii}, E_{ij} \rangle + wZ^2 \langle H_{ii}, H_{ij} \rangle \quad (3.75a)$$

$$v_i = \langle E_t^{in}, E_{ii} \rangle + wZ^2 \langle H_t^{in}, H_{ii} \rangle \quad (3.75b)$$

where  $i, j = 1, \dots, N$ , and  $N$  is the total number of modes in side I and side II and the vectors  $E_t$  and  $H_t$  are made up of all the corresponding modal fields in both sides.

The inner products involved in the above expressions are defined as:

$$\langle x_1, x_2 \rangle = \int x_1 \cdot x_2^* ds \quad (3.76)$$

Where  $x_1$  and  $x_2$  are two field vectors,  $x_2^*$  is the complex conjugate of  $x_2$  and integration is carried out over the waveguide cross section.

### 3.6.2 Numerical Analysis Using Finite Element Output

The vector **H**-field finite element has become a powerful tool for the solution of microwave and optical waveguides as described previously. One of the main advantages of **H**-field formulation is that the continuity of **H**-field component is automatically satisfied even with permittivity discontinuities. In this thesis, to analyse the power transfer characteristics of coupled waveguides, the rigorously convergent LSBR method

is used along with **H**-field Finite Element program. The elimination of spurious solutions by using the penalty method particularly improves the eigenvector quality, which is a very important fact for the analysis of discontinuity problems.

By employing the Finite Element program the nodal values of the complete **H**-field for each mode are obtained for both the waveguides (side I and side II). The **E**-field over each element is calculated using these nodal **H**-field values by means of Maxwell's equation. Modal eigenvalues and eigenvectors of all the modes in both sides of the discontinuities are used as the input data to the LSBR method. All these eigenvalues and eigenvectors are easily generated by employing the vector FEM program. The LSBR program reads all the input data and calculates the integral  $J$  and minimises the error criterion of equation 3.72 with respect to each value of  $a_i$  and  $b_i$  for any given incidence by solving a homogenous linear equation 3.74. There is no need to generate the **E**-fields as the nodal **H**-fields can be directly used to calculate the electric field part of the functional,  $J$ . The solution of the equation 3.74 gives the unknown vector  $\{x\}$  consisting of the reflected and transmitted coefficients of all the modes considered in the analysis. The singular value decomposition algorithm has been used to solve the linear equation 3.74. For numerical efficiency, the Finite Element nodal points of side I are matched with the nodal points of side II across the transverse plane at the discontinuity. The LSBR method can be applied to a wide range of discontinuity problems, involving abrupt changes at the transverse plane between arbitrary guiding structures of uniform cross section. These include vertical shifts, horizontal misalignments, sudden changes of width or height change in guide dimensions or materials or combinations of all these varieties. The method can also be used to guiding structures, such as optical fibres or titanium diffused  $\text{LiNbO}_3$  channel waveguides with anisotropic or electro-optic refractive indices. On the other hand the LSBR method can be used to find the optimum matching of the two side waveguides by controlling the geometries and material properties of the guides. In addition, by choosing the optimum guide parameters, the radiation losses resulting from random fluctuations in the waveguide geometry and refractive index can also be minimised. The resulting reflection matrix and the transmission matrix give a complete understanding of the discontinuity problem which facilitates better designs of optical and microwave devices.

### 3.6.3 Losses in Optical Waveguides

The sources of losses in waveguide devices include coupling losses, propagation loss, electrode loading loss and if considered, the waveguide bending loss. The propagation loss is generally attributable to three different mechanisms: scattering, absorption and radiation. The scattering loss usually predominates in glass or dielectric waveguides while absorption loss is most important in semiconductors and other crystalline materials. Radiation losses become significant when waveguides are bent through a curve. Photons can be scattered, absorbed or radiated as the optical beam progresses through the waveguide, thus reducing the total power transmitted. To describe quantitatively the magnitude of the scattering loss, the exponential attenuation coefficient is generally used and the intensity (power per unit area) at any point along the length of the waveguide is given by:

$$I(z) = I_0 e^{-2\alpha z} \quad (3.77)$$

Where  $I_0$  is the initial intensity at  $z = 0$  and  $\alpha$  is the power attenuation coefficient, as this is given as  $P = E^* \times H$ .

In the applications described in this thesis, the light is coupled in and out of one optical waveguide to another through a butt joint. The LSBR method analyses the waveguide junction efficiently in order to calculate the power transfer from the input guide to the other. When a guided TE or TM mode is incident on the discontinuity plane between two waveguides, some of the incident light energy is lost, called the insertion loss. The method can also be used to calculate this power loss suffered by the TE or TM mode, by utilising the scattering coefficients. If an incident mode of unit power is assumed then the insertion loss in decibels is given by:

$$L = 10 \log_{10} \left( \sum_{i=1}^N |b_i|^2 \right) \quad (3.78)$$

Where,  $b_i$  is the transmission coefficients of the  $i^{\text{th}}$  mode and  $N$  is the total number of modes considered.

### 3.7 Summary

The aim of this chapter was to present a theoretical background of the finite element method based on the variational principle to perform modal analysis of various waveguide structures. The properties of various numerical methods often used in analysing waveguide problems have been examined. An elaborate mathematical description is given for the vector  $\mathbf{H}$ -field based FEM formulation. Several aspects of the method such as the boundary conditions, shape functions and methods aimed at eliminating spurious solutions have been extensively analysed. Also, a rigorously convergent least squares boundary residual method is described for use to analyse the discontinuities in optical waveguides. The method is also capable of calculating the power transfer between two waveguides using the scattering coefficients. The role of the finite element program in utilising the LSBR technique is also presented followed by the calculation of the insertion loss. Having established these formulations, the results of their applications will be presented in the subsequent Chapters.

## CHAPTER FOUR: Mode Degeneration

### 4.0 Abstract

In this chapter the leakage and bending losses of various PCF designs are calculated and presented. Some mode degeneration which is as a result of the coupling between the core and cladding modes were discovered and analysed. As the bending radius is increased the bending losses increase steadily and at some low bending radii there were oscillatory behaviours observed which are as a result of the localised cladding modes in the silica bridging regions (solid areas in between air-holes) coupling with the core mode.

### 4.1 Introduction

Photonic Crystal Fibres (PCFs) are seen as potentially important specialized optical waveguides due to their inherent advantages arising from their modal properties, such as controllable spot size, birefringence and their dispersion properties which are achieved through tailoring their structural parameters. In many practical applications, such PCFs will encounter bends, twists and stress. It is also well known that when a fibre is bent, the modal field shifts in the outward direction and suffers from radiation loss. One of the main disadvantages suffered by standard silica fibre has been that significant bending loss arises due to the low index contrast between the core and the cladding when compared to that of a PCF. This chapter shows the studies on the variation of the key modal parameters in such fibres that arises from the change in the coupling between the fundamental core mode and the localized cladding mode across the air-holes. This analysis was done by using a rigorous full-vectorial finite element method with the conformal transformation.

## 4.2 Results for PCF with Identical Air-holes

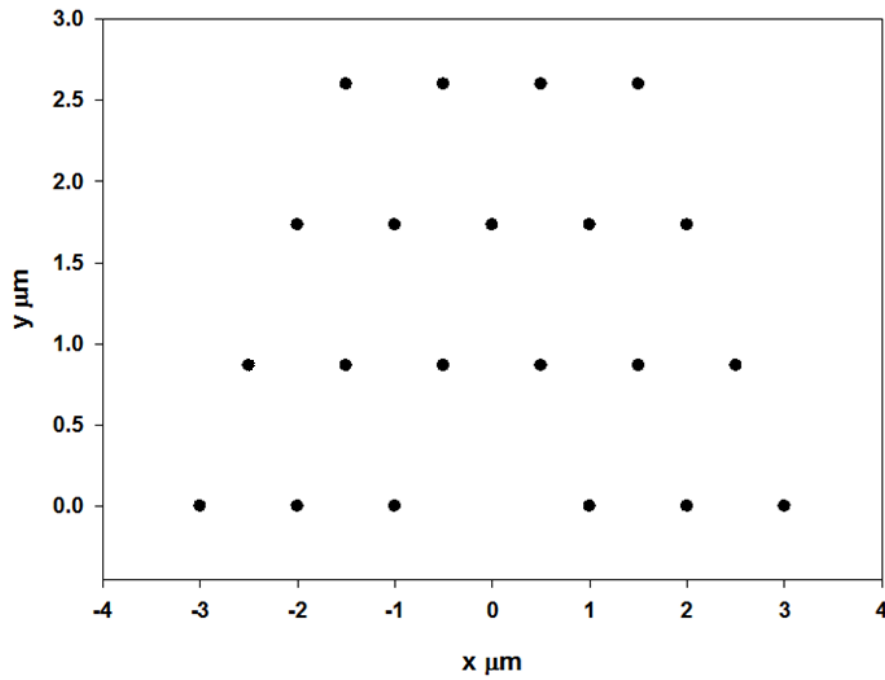


Fig. 4. 1: A graph depicting the cross-section of a 3 ring PCF with half symmetry.

Figure 4.1 shows the structure of a photonic crystal fibre with 3 air-hole rings. It was generated by using a graphics software package. The solid circles show the position of the air-holes in the PCF. The centre of the PCF is taken as the origin of the Cartesian coordinates. The scaling used in Fig. 4.1 should be viewed as a general representation of the cross-section of a half-structure PCF. The scales on results obtained subsequently would vary.

## 4.3 Mesh Refinement and Perfectly Matched Layer Optimisation

For the modal solutions of straight PCF, only a quarter of its cross-section is considered by exploiting the available 2-fold of symmetry. However, to analyze modal properties of a bent PCF, it is required to apply the conformal transformation, which will destroy its symmetry along the vertical axis. So, in this case the available one-fold symmetry is exploited and only upper half of the PCF is simulated as shown in Fig. 4.1.

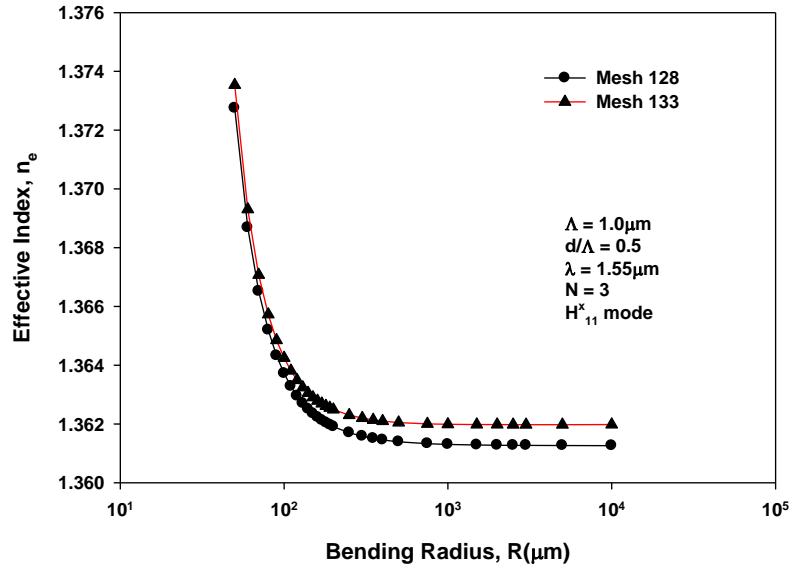


Fig. 4. 2: The variation of effective index of  $H^x_{11}$  mode with bending radius for mesh divisions 128 x 65 and mesh 133 x 70.

The accuracy of all numerically simulated results are known to depend on the accuracy of their representation. Initially, stability of the mesh refinement was studied. Figure 4.2 shows a comparison between two mesh divisions used, 128 x 65 and 133 x 70, on effective index values as the bending radius,  $R$  is varied. The full width of the PCF is discretized but only half of its height, so mesh division used in the  $x$  and  $y$  directions are different. For this particular bench marking work a photonic crystal fibre with three rings of air-holes is considered. The refractive index of the background material, in this case silica, is taken as 1.445 and the air-holes are filled up with air with its refractive index value of 1. The wavelength,  $\lambda$ , considered here is  $1.55\mu\text{m}$  and initially, the air filling fraction,  $d/\Lambda = 0.5$  and pitch,  $\Lambda = 1.0\mu\text{m}$ .

It can be observed from the curves that as the bending radius is reduced, the effective index of the  $H^x_{11}$  mode increases and the increase is sharper for the lower values of bending radius. It can be observed that the effective index value obtained for mesh of 133 x 70 is slightly higher than that of mesh 128 x 65 for all the bending radii. It agrees with the results obtained from research previously carried out within the Photonics Group at City University London that a finer mesh gives more accurate results and for finer mesh refinement the effective index values increase slightly.

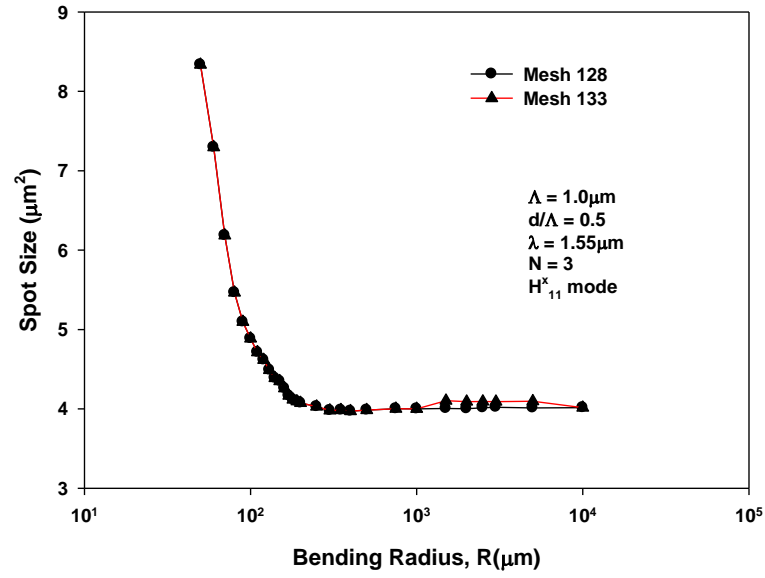


Fig. 4. 3: The variation of spot sizes with the bending radius,  $R$  for mesh divisions  $128 \times 65$  and  $133 \times 70$ .

Figure 4.3 shows the variation of the spot size with the bending radius for two different mesh refinements. It can be observed from the curves that as the bending radius reduces, initially its spot size does not vary much but then, the spot size increases and the increase is sharper as the bending radius is reduced further. However, it can be noted that the spot size value is remarkably stable with the change in the mesh division used. A more detailed discussion about spot size is provided in Chapter 6.



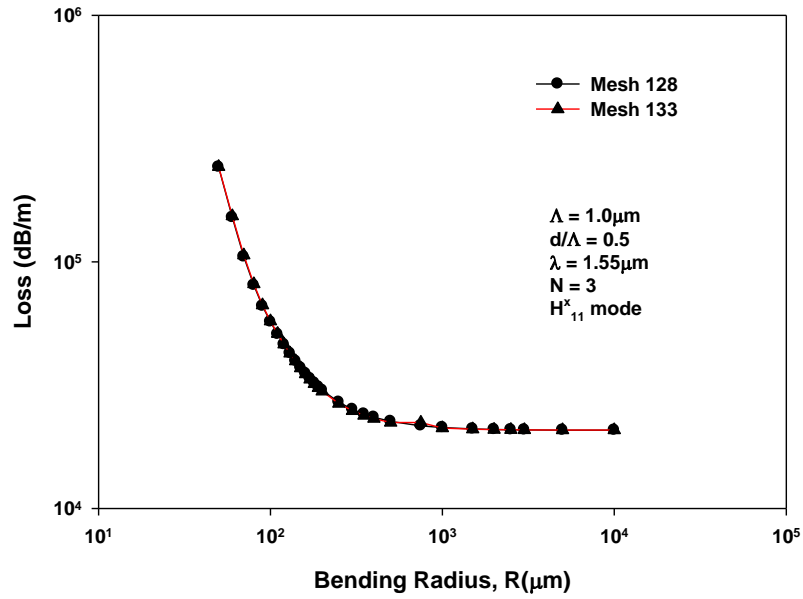


Fig. 4. 4: Variation of modal loss with the bending radius,  $R$ , for mesh divisions 128 and 133.

Figure 4.4 shows the variation of the bending loss with the bending radius for two different mesh refinements. It can be observed from the curves that as the bending radius are reduced, the loss increases and the increase is sharper as for lower values of bending radius. For higher values of bending radius,  $R$ , the loss curve represents only the leakage loss. However, when  $R$  is reduced, modal field continuously shifts away from the bending centre (on the left) and bending loss increases. It can be noted that there is virtually no difference between the two loss curves which signifies that calculated loss values are very stable with the mesh division used in this work.

The modal solution may also depend on the size of the orthodox computational domain considered or location and/or width of PML used. Variation of bending loss with the bending radius with the distance of the air-holes in the outermost ring to the nearest PML region was tested to ascertain if there would be any interaction which could affect the simulations. This was tested using various values of  $d/\Lambda$  there by varying the PML distance. It was observed that this did not affect the results of the experiments during simulation which means the distance of the air-holes to the nearest the PML doesn't affect the result. The width of the PML is taken as 40% of the length of the computational domain (x-direction) after testing which then implies that it was a very

appropriate dimension to employ for accurate results in the simulations carried out to calculate leakage and bending losses in the photonic crystal fibres.

#### 4.4 Results of Numerical Experiments

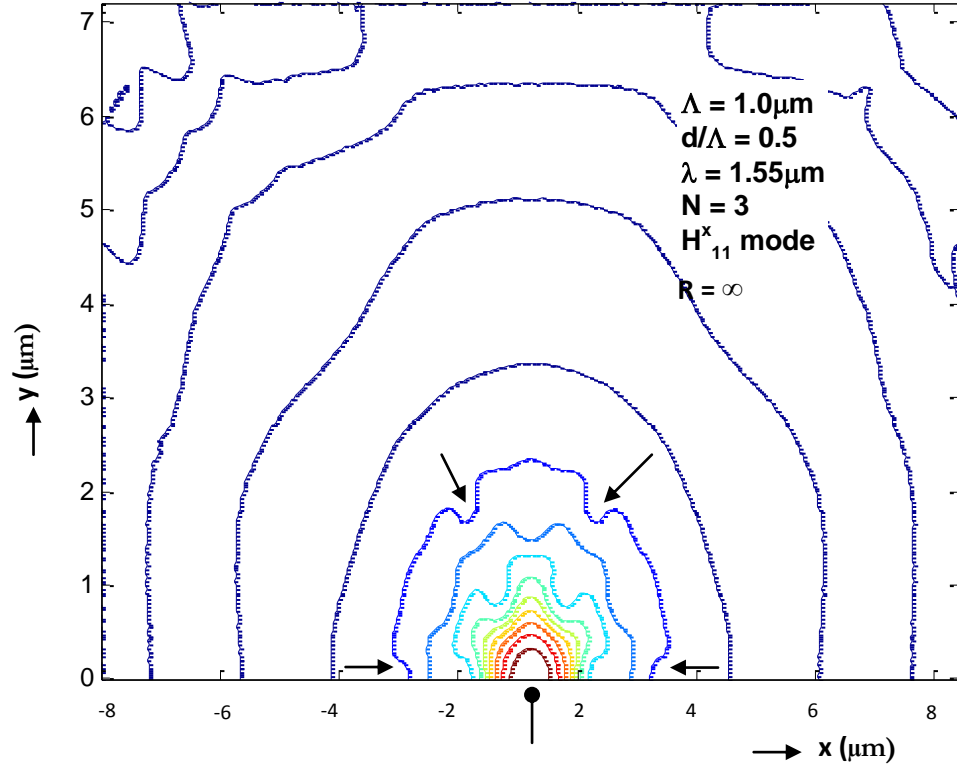


Fig. 4. 5:  $H_x$  field profile of the  $H_x^{11}$  mode  $R = \infty$ ,  $\Lambda = 1.0\mu\text{m}$ ,  $d/\Lambda = 0.5$ .

Figure 4.5 shows the  $H_x$  field contour of the fundamental  $H_x^{11}$  mode in a straight PCF for pitch  $\Lambda = 1.0\mu\text{m}$  and  $d/\Lambda = 0.5$ . It can be seen that the field is confined to the core. The four arrows in the profile shows the position of the air-holes while the circle-headed arrow at the bottom shows the centre and it can be seen that at this straight PCF the field is symmetric along the vertical axis, well confined within the core and it fits around the air-holes. There is no visible leakage of the field to the right side into the cladding region when the PCF is straight. The spot size of this mode is approximately  $4.0\mu\text{m}^2$ .

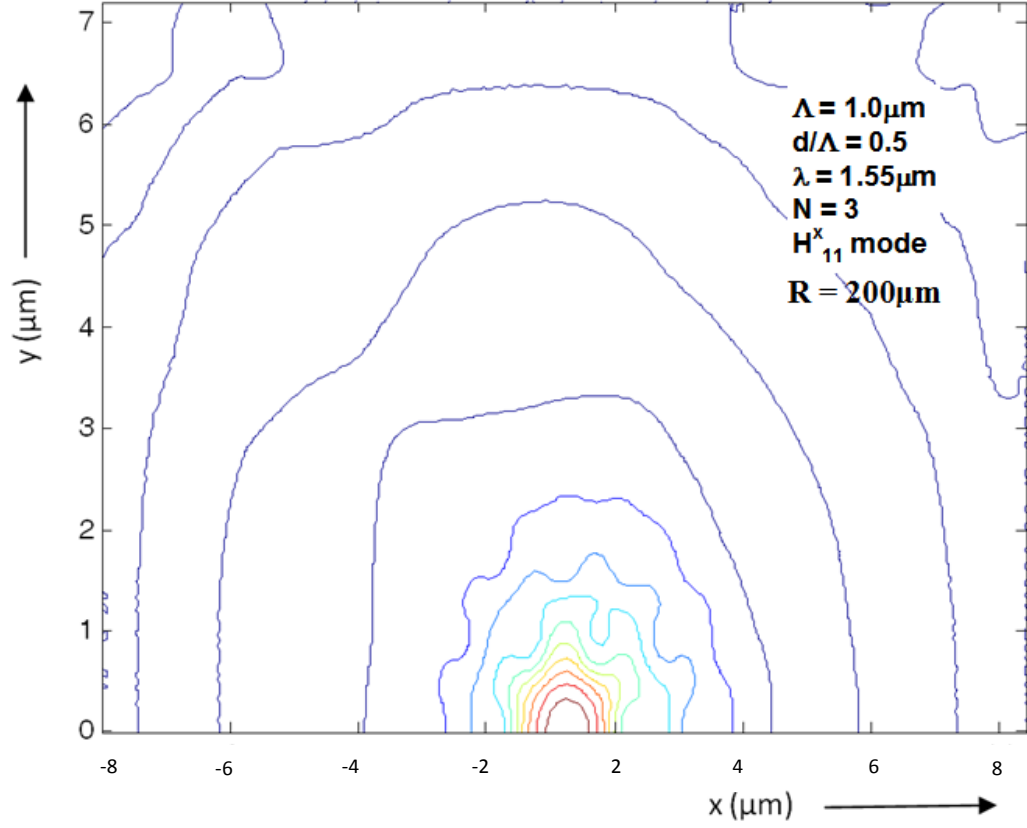


Fig. 4. 6:  $H_x$  field profile of the  $H_{11}^x$  mode at  $R = 200\mu\text{m}$ , with  $\Lambda = 1.0\mu\text{m}$  and  $d/\Lambda = 0.5$ .

However, as the bending is introduced the field profile changes and Fig. 4.6 shows the  $H_x$  field contour for pitch  $\Lambda = 1.0\mu\text{m}$ ,  $d/\Lambda = 0.5$  at  $R = 200\mu\text{m}$ . It can be seen that the PCF is quite resistant to bending as can be seen that the field has not leaked too much even at  $R = 200\mu\text{m}$ . However, it can be observed that modal field has moved more towards the right, away from the bending direction. The spot size is increased very slightly and is approximately  $4.07\mu\text{m}^2$ .

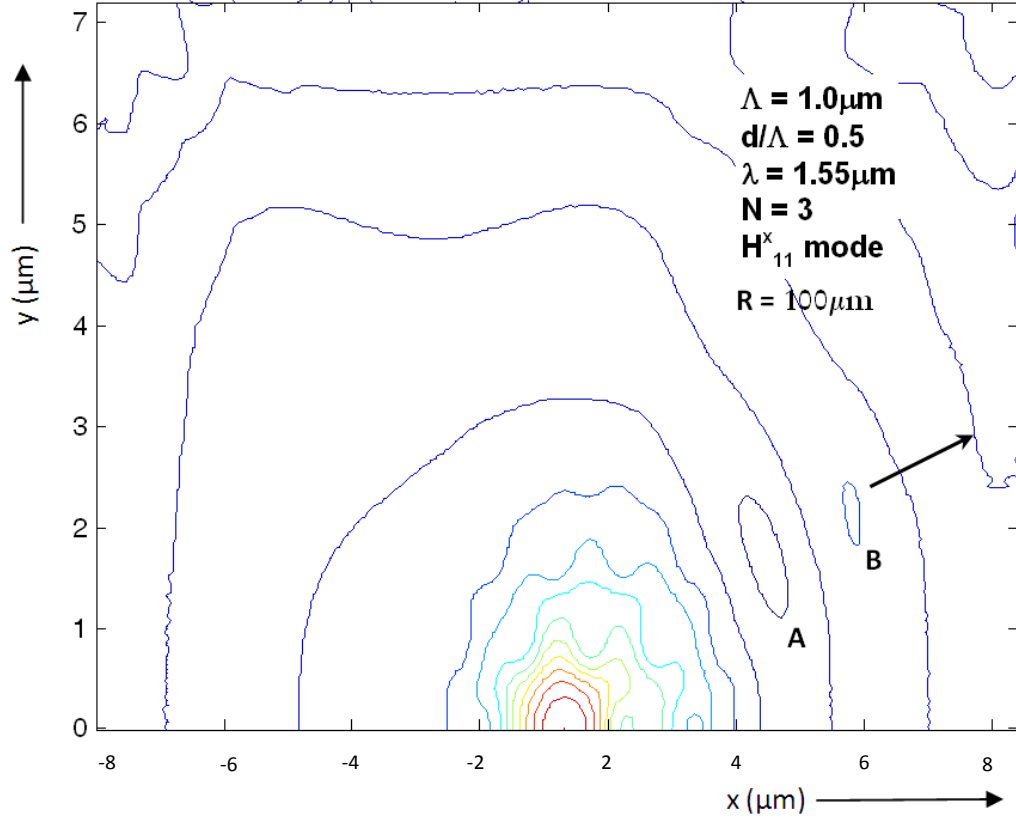


Fig. 4. 7:  $H_x$  field contours for the  $H_x^{11}$  mode at  $R = 100\mu\text{m}$ , with  $\Lambda = 1.0\mu\text{m}$ ,  $d/\Lambda = 0.5$ .

As the bending radius is reduced further, Fig. 4.7 shows the  $H_x$  field plot for pitch  $\Lambda = 1.0\mu\text{m}$ ,  $d/\Lambda = 0.5$  when  $R = 100\mu\text{m}$ . From this figure, it can be observed that the field has leaked more into the cladding. It should be noted that for the arrangement shown in this figure there is an air-hole on the x-axis for the first ring of air-holes. This reduces leaking of the energy straight in that direction. So, the leakage direction shown by 'A' and 'B' is in the direction in between two air-holes (in the first ring) through the silica bridging area. The spot size has increased considerably to  $4.8\mu\text{m}^2$  as the bending radius has been reduced.

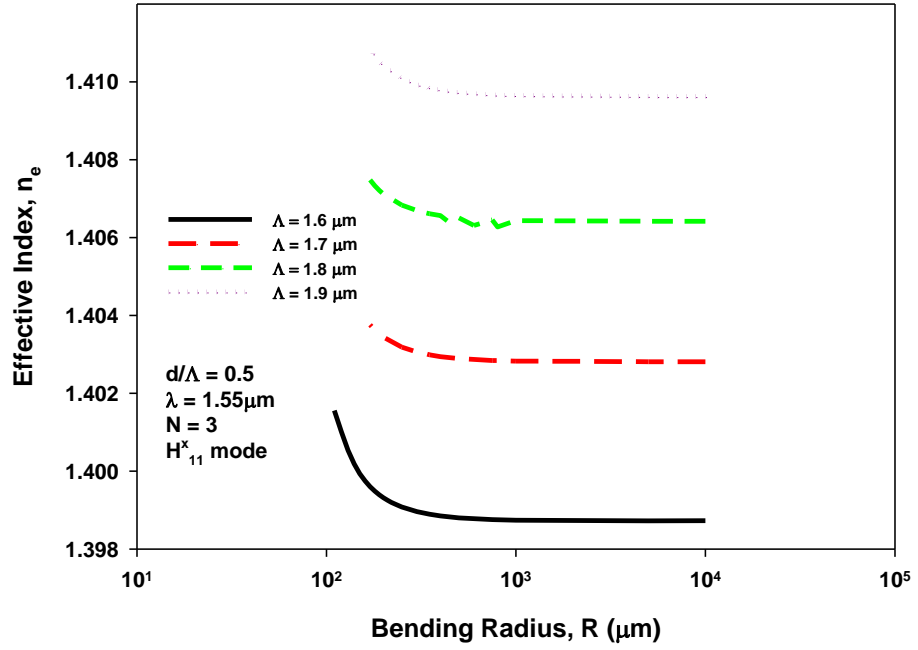


Fig. 4. 8: The variation of effective index with the bending radius for  $\Lambda = 1.6\mu\text{m}$ ,  $1.7\mu\text{m}$ ,  $1.8\mu\text{m}$  and  $1.9\mu\text{m}$ .

Next, the modal solutions of bent PCF are carried out for different pitch lengths,  $\Lambda$ . Figure 4.8 shows the variations of effective indices with the bending radii for  $\Lambda = 1.6\mu\text{m}$ ,  $1.7\mu\text{m}$ ,  $1.8\mu\text{m}$  and  $1.9\mu\text{m}$ . It can be seen that the effective index increases as the bending radius,  $R$ , decreases for all the pitch values. It can also be seen that as the pitch is increased the effective indices increase as well. This is because modes are more confined in the solid silica core area which is now larger and the effective refractive index approaches the index of the core.

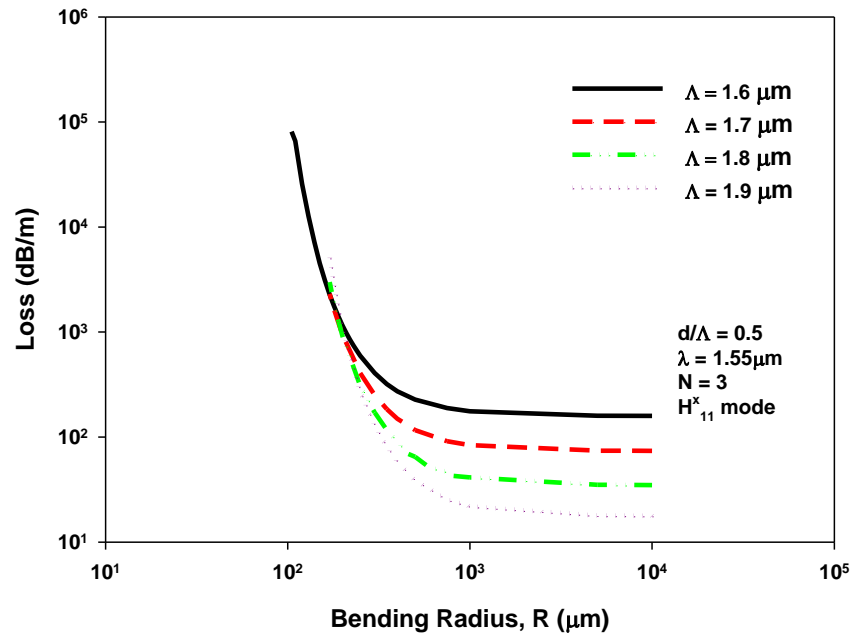


Fig. 4. 9: The variation of bending losses with the bending radius,  $R$  for  $\Lambda = 1.6\mu\text{m}$ ,  $1.7\mu\text{m}$ ,  $1.8\mu\text{m}$  and  $1.9\mu\text{m}$ .

The variations of bending losses with the bending radius,  $R$ , for different pitch lengths,  $\Lambda$ , are shown in Fig. 4.9. Higher value of  $\Lambda$  makes the mode better confined; which reduces loss as shown for higher bending radius. For all these cases, as the bending radius,  $R$  decreases, the loss increases. However, for larger  $\Lambda$ , rate of loss increase with  $R$  is faster particularly for lower  $R$  values. So, it is possible that for lower  $R$ , bending loss for a larger  $\Lambda$  could be higher than that for a PCF with a smaller  $\Lambda$  as shown here the dotted line for  $\Lambda = 1.9\mu\text{m}$ , crossing the loss value of  $\Lambda = 1.6\mu\text{m}$ , shown by a solid line.

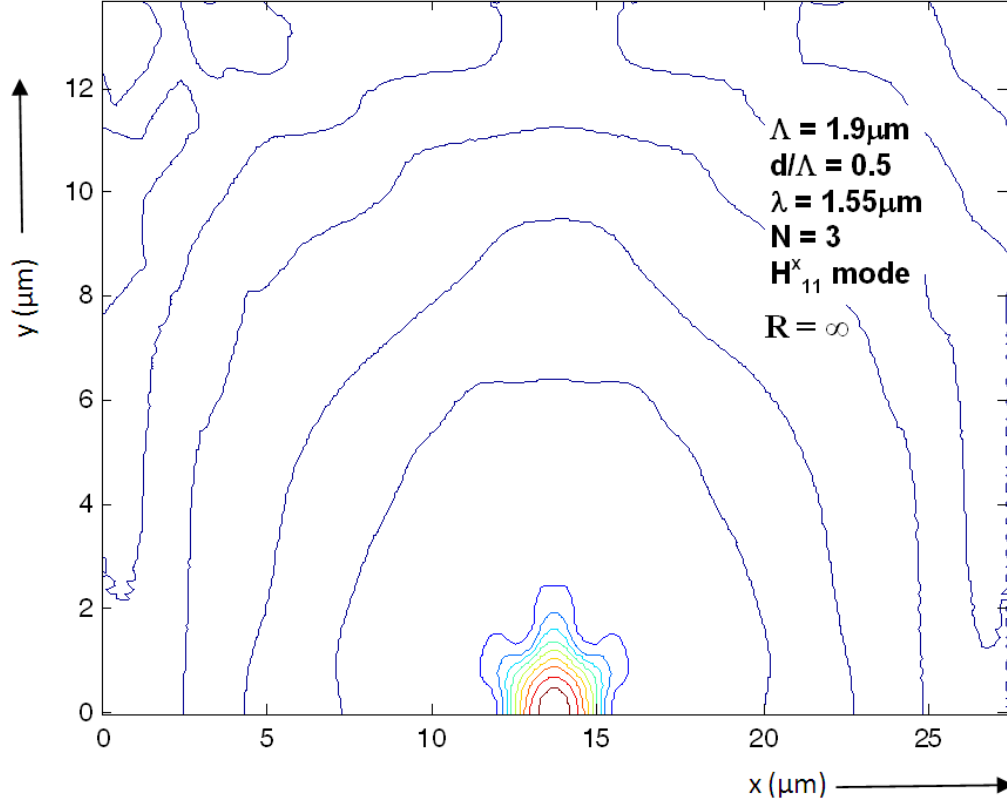


Fig. 4. 10:  $H_x$  field contours for the  $H_{11}^x$  mode  $R = \infty$ ,  $\Lambda = 1.9\mu\text{m}$ ,  $d/\Lambda = 0.5$ .

Figure 4.10 shows the 2-D field plot of the fundamental  $H_{11}^x$  mode for  $\Lambda = 1.9\mu\text{m}$  and  $d/\Lambda = 0.5$ . With  $R = \infty$ , it can be observed that the field is well confined and symmetrical within the core. Compared with the field for  $\Lambda = 1.0\mu\text{m}$  and  $R = \infty$  as shown in Fig. 4.5, the positions of the air-holes are clearly visible from the field profiles refracting from the air-holes of the first ring. The spot size is approximately  $5.9\mu\text{m}^2$ .

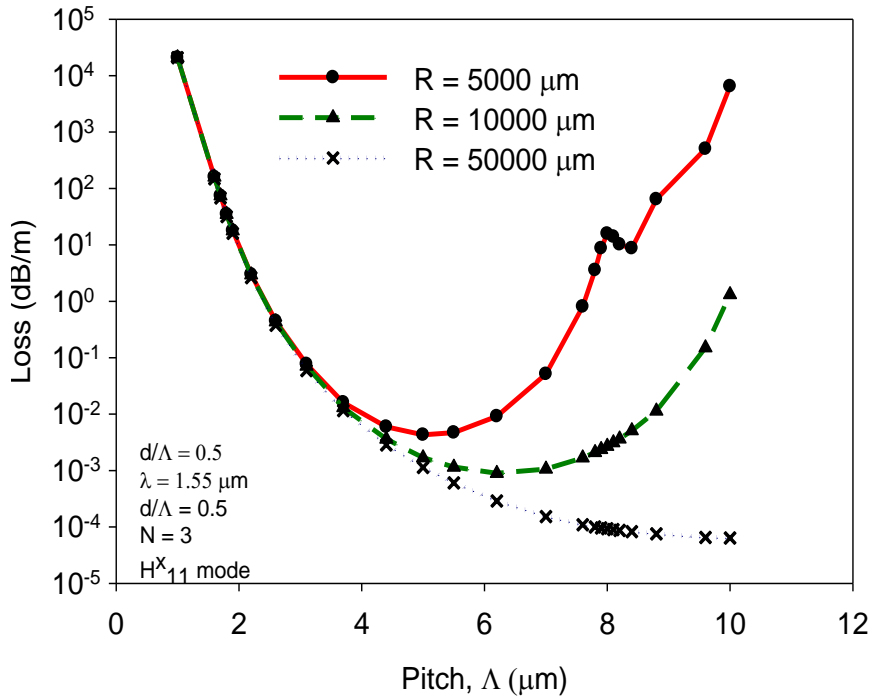


Fig. 4. 11: Variation loss with the pitch lengths for  $R = 5000\mu\text{m}$ ,  $10000\mu\text{m}$  and  $50000\mu\text{m}$

Figure 4.11 shows the variation of loss as the pitch length is varied. As pitch length increases for the various values of bending radius,  $R$  considered, the loss decreases to minimum value then it begins to increase again. It can also be observed that the higher the bending radius considered the loss is smaller.

When the bending radius is large, as the bending loss is smaller, total loss mostly represent the leakage loss. For a large bending radius,  $R = 50\text{mm}$ , as the pitch increases, initially, loss values decreases. This is due to stronger confinement of the modes for larger pitch length. However, it can be observed that for bending radius,  $R = 5\text{mm}$ , as the pitch increases, although initially bending loss reduces but further increase of the pitch causes the bending loss to increase. This is due to the availability of larger silica bridging area in between air-holes which is susceptible to leakage loss at very small bending radii. The discontinuity in the curves observed around pitch 6 to 8  $\mu\text{m}$  is due to mode degeneration, which is discussed later.



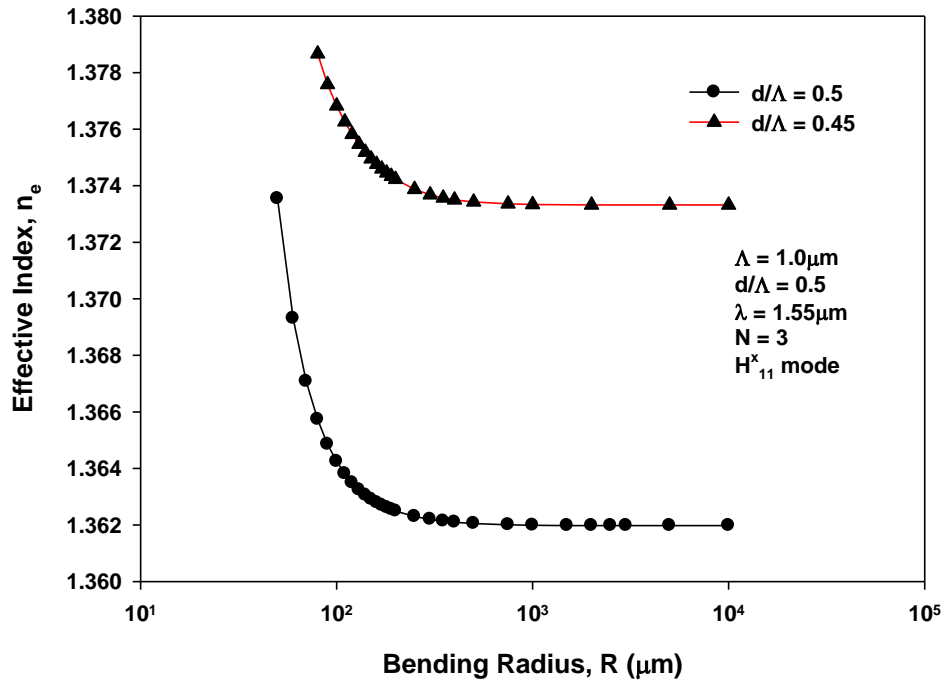


Fig. 4. 12: The variation of effective index with bending radius,  $R$  for  $d/\Lambda = 0.5$  and  $d/\Lambda = 0.45$ .

Next, the effect of air-hole radius on the modal properties, particularly on the bending loss is also studied. Figure 4.12 shows the graph of the variation of effective index with the bending radius,  $R$  for  $d/\Lambda = 0.5$  and  $d/\Lambda = 0.45$ . It can be seen from this figure that the effective index increases as  $R$  is reduced and has a sharp increase at lower values of  $R$  for both the  $d/\Lambda$  values. It can also be seen that the effective index is higher for  $d/\Lambda = 0.45$  than for  $d/\Lambda = 0.5$ . The higher  $d/\Lambda$ , as in this example,  $d/\Lambda = 0.5$  has bigger air-holes and results in more air fraction in the cladding area. This leads to lower equivalent index of the cladding and thus effective index reduces. However, for higher  $d/\Lambda$  as the index contrast between core and cladding is increased, modes will be more confined in the core.

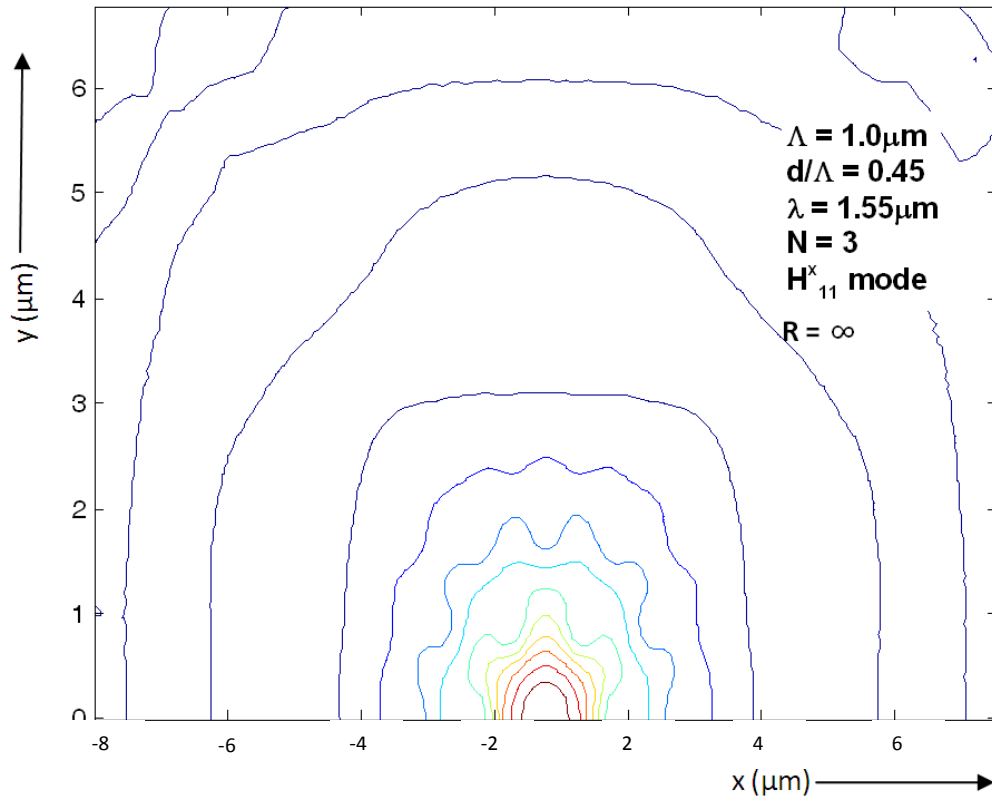


Fig. 4. 13:  $H_x$  field profile of the  $H_{11}^x$  mode  $R = \infty$ ,  $\Lambda = 1.0\mu\text{m}$ ,  $d/\Lambda = 0.45$

Figure 4.13 shows the 2-D  $H_x$  field plot of the  $H_{11}^x$  mode for pitch  $\Lambda = 1.0\mu\text{m}$  and  $d/\Lambda = 0.45$  when  $R = \infty$ . It has smaller air-holes compared to when  $d/\Lambda = 0.5$  and  $\Lambda$  is the same for both cases. It can be seen that the field has been less confined in the core, compared to  $d/\Lambda = 0.5$ , which was shown in Fig. 4.5. The spot size is approximately  $5.0\mu\text{m}^2$ .

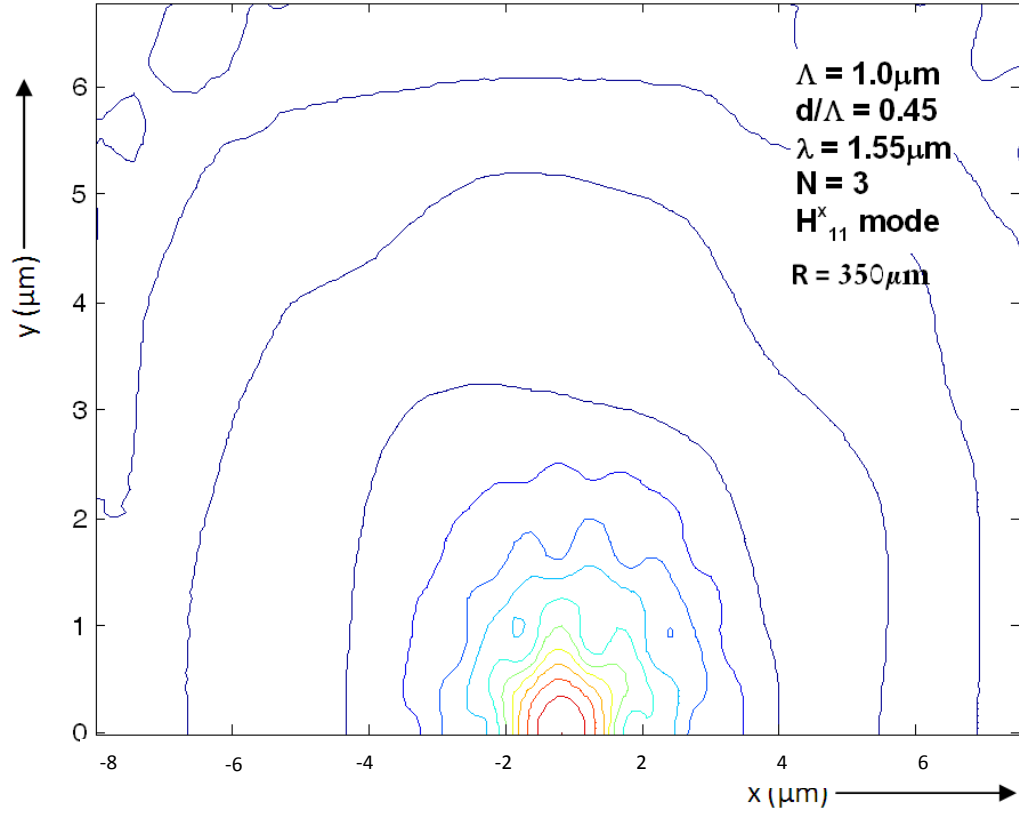


Fig. 4. 14:  $H_x$  field profile of the  $H_{x11}$  mode  $R = 350\mu\text{m}$ ,  $\Lambda = 1.0\mu\text{m}$ ,  $d/\Lambda = 0.45$

Figure 4.14 shows the  $H_x$  field plot of the  $H_{x11}$  mode for pitch  $\Lambda = 1.0\mu\text{m}$ ,  $d/\Lambda = 0.45$ , and  $R = 350\mu\text{m}$ . In this case it has smaller air-holes than  $d/\Lambda = 0.5$ , which was shown earlier. It can be observed that the field has leaked a little into the cladding. The spot size has increased to  $5.4\mu\text{m}^2$ , compared to that of a straight PCF shown in Fig. 4.13.

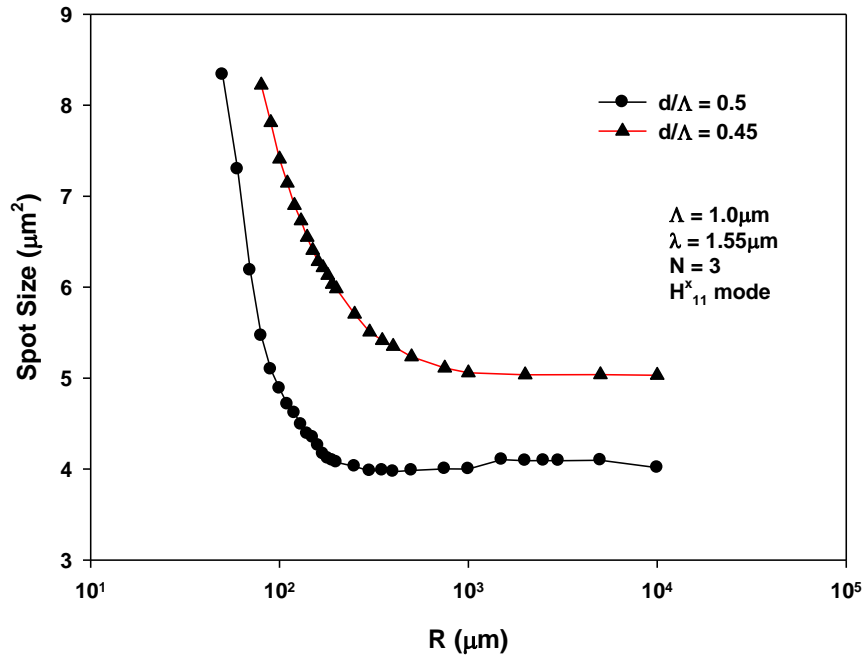


Fig. 4. 15: The variation of spot size with bending radius,  $R$  for  $\Lambda = 1.0 \mu\text{m}$   $d/\Lambda = 0.5$  and  $d/\Lambda = 0.45$ .

Figure 4.15 shows the variation of spot size with bending radius,  $R$ . The spot size increases as bending radius is reduced and has a sharp increase at lower values of the bending radius. It can also be seen the spot size is higher for  $d/\Lambda = 0.45$  than for  $d/\Lambda = 0.5$ . For higher  $d/\Lambda$ , as example when  $d/\Lambda = 0.5$  it has bigger air-holes compared to  $d/\Lambda = 0.45$  and this causes the field to be squeezed by the larger air-holes and thus resulting in smaller spot sizes.

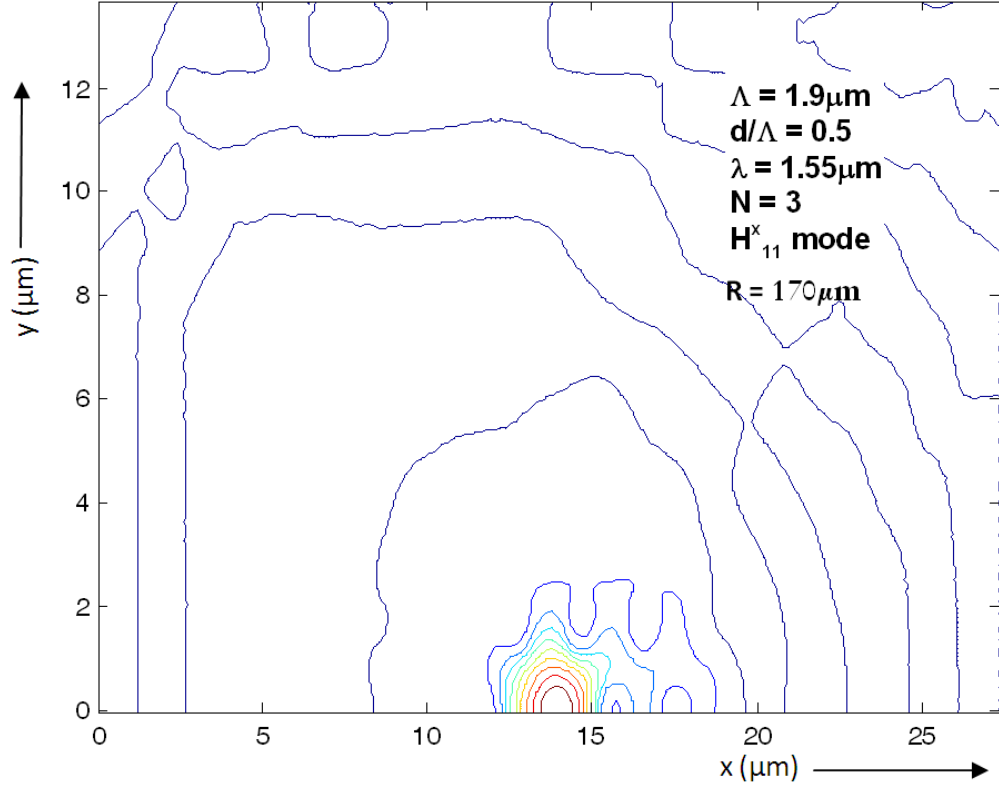


Fig. 4. 16:  $H_x$  field contours for the  $H_x^{11}$  mode  $R = 170\mu\text{m}$ ,  $\Lambda = 1.9\mu\text{m}$ ,  $d/\Lambda = 0.5$ .

Figure 4.16 shows the 2-D field plot for  $\Lambda = 1.9\mu\text{m}$ ,  $d/\Lambda = 0.5$ , and  $R = 170\mu\text{m}$ . It can be observed that the field is no longer well confined or symmetrical within the core but it has leaked considerably into the cladding region. It can be observed that the field has moved more towards the right side and its spot size is approximately  $6.0\mu\text{m}^2$ .

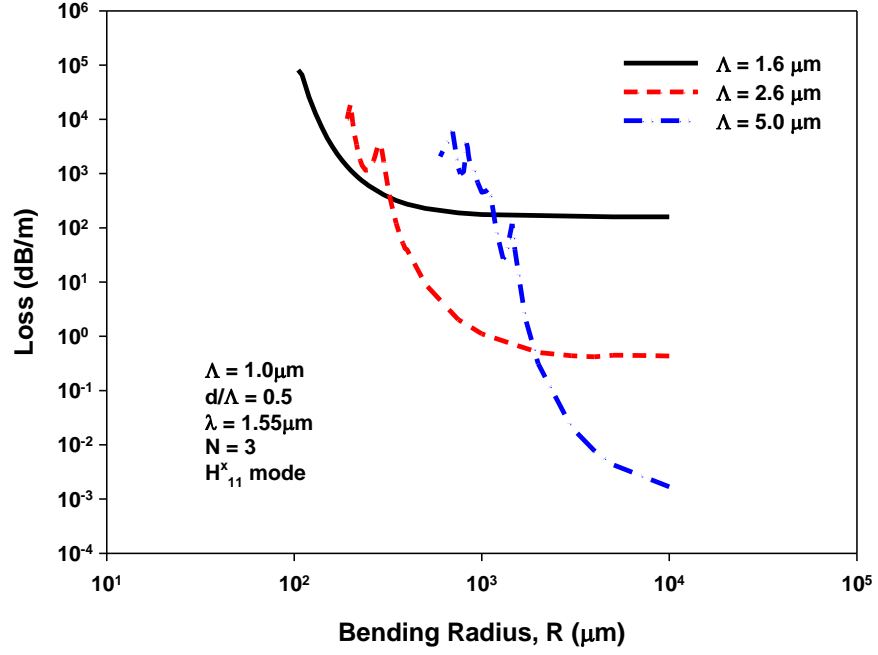


Fig. 4. 17: Variation of bending loss against bending radius,  $R$ , for  $\Lambda = 1.6\mu\text{m}$ ,  $2.6\mu\text{m}$  and  $5.0\mu\text{m}$  for  $H_x^{11}$  mode and  $d/\Lambda = 0.5$ .

Next, the bending losses for several cases of larger pitch lengths are presented and shown in Fig. 4.17. When bending radius is very high, total loss is dominated by the leakage loss and this value is low for bigger pitch length,  $\Lambda$ . For these cases, as the bending radius is reduced, the bending loss increases progressively and as a result the total loss also increases. It can be noted that when pitch length is larger, increases in the bending loss with the bending radius are more rapid as the bending radius is reduced, compared to the case with a lower pitch length,  $\Lambda = 1.6\mu\text{m}$  shown by a solid line. But it also can be observed that in such a case, at a lower bending radius, the usual nonmonotonic nature modifies with oscillations in the total loss values. In these cases, it has been observed that the modal and leakage properties of both the quasi-TE and the quasi-TM modes are almost similar along with the transition in their loss properties, also appearing at similar locations. When the pitch length is increased further, for  $\Lambda = 5.0\mu\text{m}$  the leakage loss is significantly reduced to  $10^{-3}\text{ dB/m}$  and a PCF with a larger dimension is often then preferred. However, in this case the PCF is more susceptible to bending and the total loss value increases rapidly as the bending radius is reduced: for some fixed radii, this value can even be higher than that of a PCF with a lower pitch value. However, in this case of a larger  $\Lambda$ , the oscillations in the loss values are more

frequent and appear to be random in nature. Similar features have also been observed experimentally (Yu and Chang 2004).

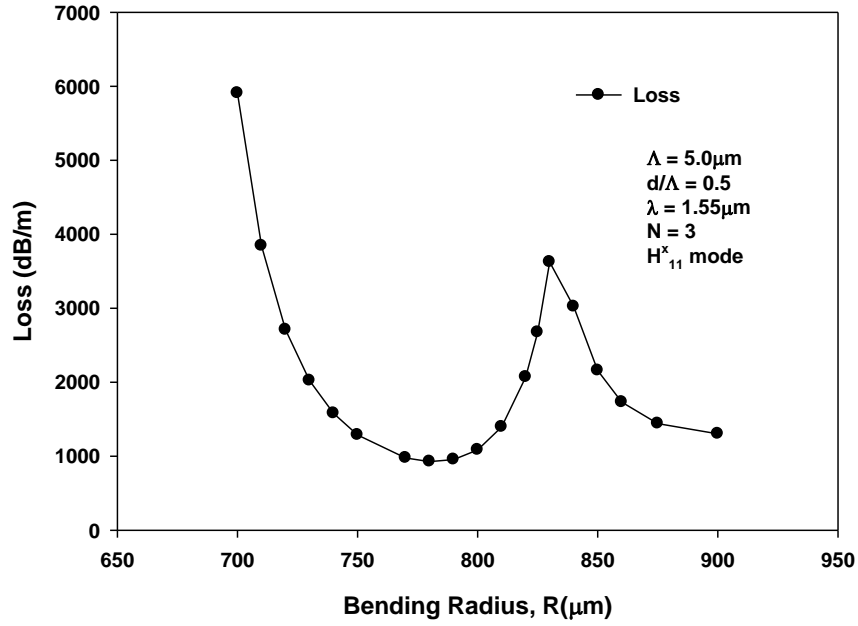


Fig. 4. 18: The variation of bending loss against bending radius, R, for values of R between 700μm to 900μm, when  $\Lambda = 5.0\mu\text{m}$ ,  $d/\Lambda = 0.5$ .

To identify the cause of such oscillations, for  $\Lambda = 5.0\mu\text{m}$  additional numerical simulations are carried out for R values scale between 700μm to 900μm. Figure 4.18 shows the graph for loss values for  $\Lambda = 5.0\mu\text{m}$ ,  $d/\Lambda = 0.5$  and R values between 700μm to 900μm. This graph clearly illustrates the transitory behaviour in its bending loss variation for this PCF.

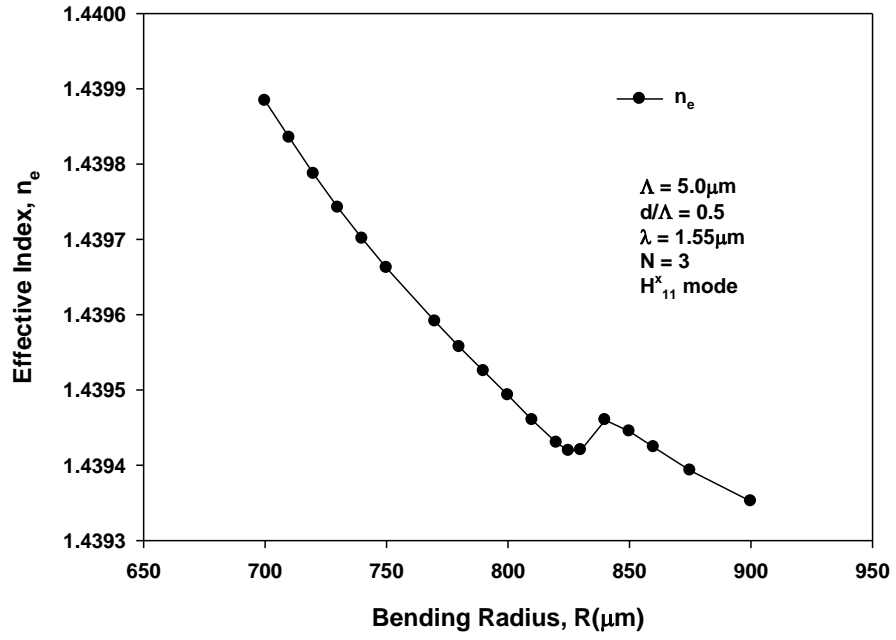


Fig. 4. 19: The variation of effective index against bending radius,  $R$ , for values of  $R$  between  $700\mu\text{m}$  to  $900\mu\text{m}$ ,  $\Lambda = 5.0\mu\text{m}$ ,  $d/\Lambda = 0.5$ .

To understand the origins of these oscillations, additionally, its effective index values are also shown. Figure 4.19 shows the variation of the effective index for  $R$  between  $700\mu\text{m}$  to  $900\mu\text{m}$ ,  $\Lambda = 5.0\mu\text{m}$  and  $d/\Lambda = 0.5$ . This graph correlates the oscillatory behaviour observed in bending loss of PCF. Here it can be seen that as if two separate effective index curves meet near  $R = 840\mu\text{m}$ , with an abrupt change. To understand it further, its spot size is also studied and shown in Fig. 4.20.



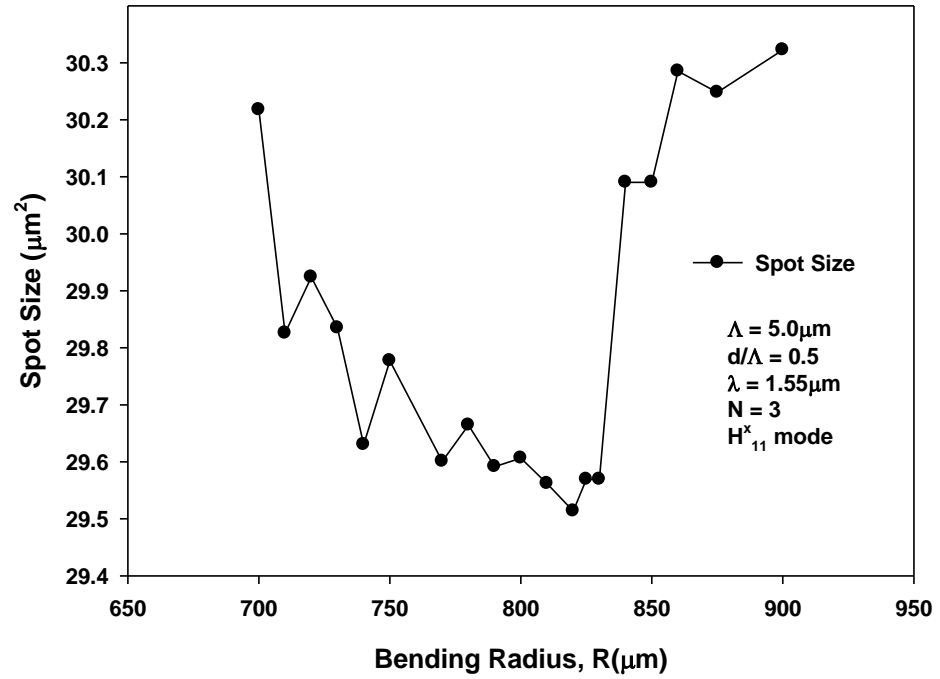


Fig. 4. 20: The variation of spot size against bending radius,  $R$ , for values of  $R$  between  $700\mu\text{m}$  to  $900\mu\text{m}$ ,  $\Lambda = 5.0\mu\text{m}$ ,  $d/\Lambda = 0.5$ .

Figure 4.20 shows the variations of the spot size for  $R$  between  $700\mu\text{m}$  to  $900\mu\text{m}$ . This graph is to illustrate the oscillatory behaviour observed in bending of PCF. Although the spot size shows smaller variations, but in region near  $R = 850$  to  $900\mu\text{m}$ , spot size is clearly shown to reduce as bending radius is reduced. However, between values of  $R = 700$  to  $800\mu\text{m}$ , it exhibits different features. There are also changes in the spot size, besides the effective index and loss values. Following these observations, the field variations, contour plots, line diagrams and 3-D field profiles have been thoroughly studied for this range.

As shown later in Fig. 4.33 variations of effective index with bending radius are identical for both the quasi-TM and quasi-TE modes and from Fig. 4.34, the variation of bending loss with bending radius are almost identical for both the quasi-TM and quasi-TE modes. Hence, in the presentations that follow, the graphs of both  $H_y$  and  $H_x$  modes are discussed.

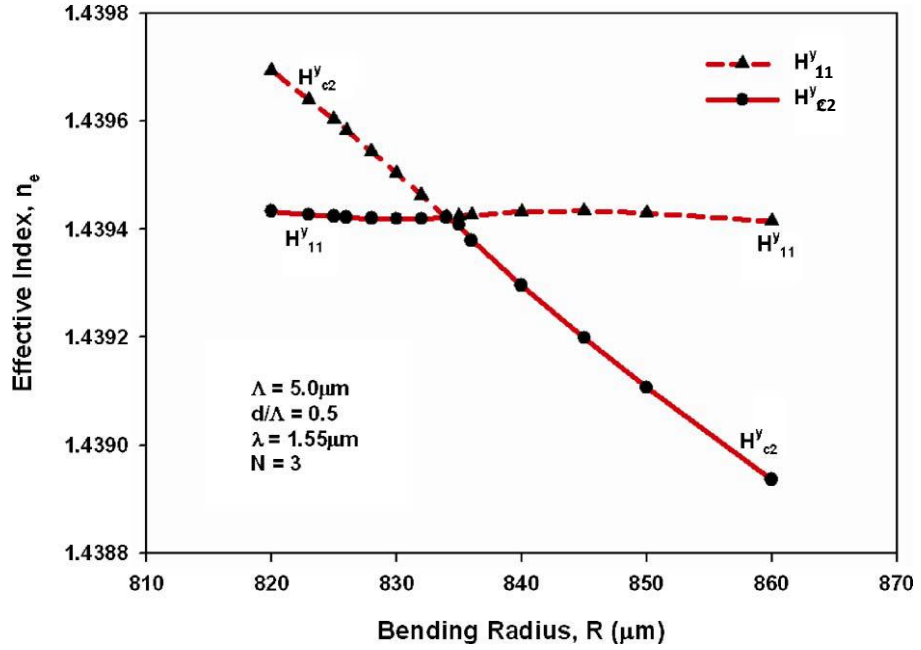


Fig. 4. 21: Variation of the effective indices with the bending radius for the quasi-TE modes.

To study mode degeneration more closely, the smaller bending radius range is considered in some further detail using an expanded range near  $R = 840\mu\text{m}$  and creating many additional simulated results. The variation of the effective index for the quasi-TE mode with the bending radius is shown in Fig. 4.21. In this region, two distinct modes can be easily identified. Their field profiles are shown later. The dashed line in Fig. 4.21 represents the first  $H_{11}^y$  eigenmode, with a higher effective index and the second eigenmode,  $H_{c2}^y$ , is shown by a solid line: it has a lower effective index for the range of bending radius shown here. In a way similar to the formation of the even and odd-like supermodes of two nonidentical coupled waveguides (Lizawa *et al.* 2008)], these two curves never cross each other, but these two modes go through a transition near  $R \sim 840\mu\text{m}$ , when they are phase matched. The horizontal sections of these two lines represent the  $H_{11}^y$  core mode confined at the centre of the PCF. The slanted line represents a highly dispersive  $H_{c1}^y$  cladding mode, which is located on the right side of the core and between the two air-holes for a bent PCF. This cladding mode has a smaller core area but with a progressively higher local equivalent refractive index value as the bending radius is reduced. For a specific bending radius, the effective index of this cladding mode becomes equal to that of the core mode and they become degenerate. It should be noted that the dispersion properties of the quasi-TE and quasi-TM polarized modes for both the core and the cladding modes are similar. The loss values for these

first  $H_{11}^y$  and second  $H_{c2}^y$  modes are shown in Fig. 4.22 by a solid and a dashed line, respectively. Parts of these two curves form the lower section, which shows the loss values of the  $H_{11}^y$  core mode, is around 2000 dB/m. On the other hand, the upper lines represent the  $H_{c2}^y$  cladding modes with significantly higher loss values, around 14000 dB/m. However, these two curves also go through a transition near  $R \sim 835 \mu\text{m}$ . The upper curve goes through a local minimum near the mode degeneration point, being mixed with a less lossy  $H_{11}^y$  core mode. Similarly the loss value of the lower curve also peaks near the resonance due to being mixed with a highly lossy cladding mode.

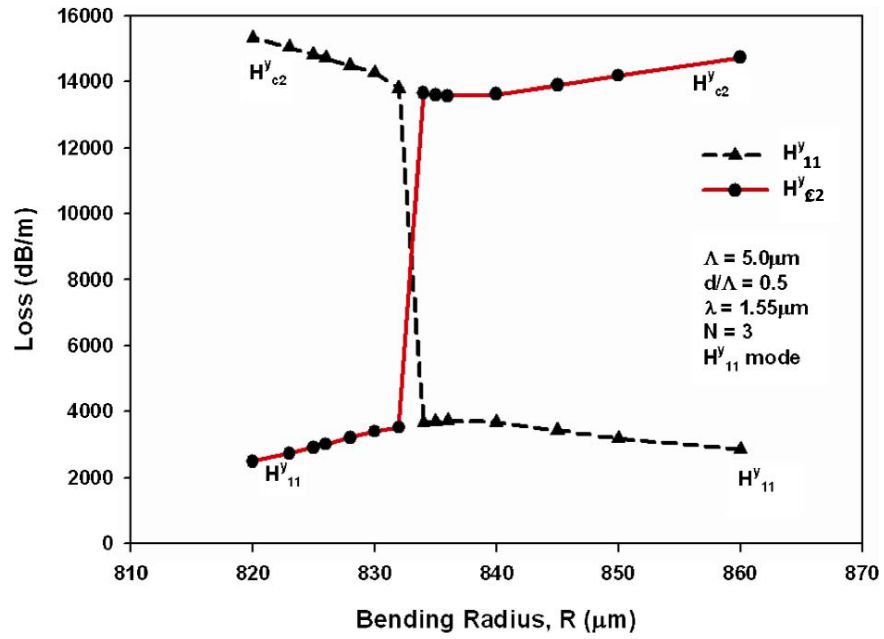


Fig. 4. 22: Variation of the total losses with the bending radius R.

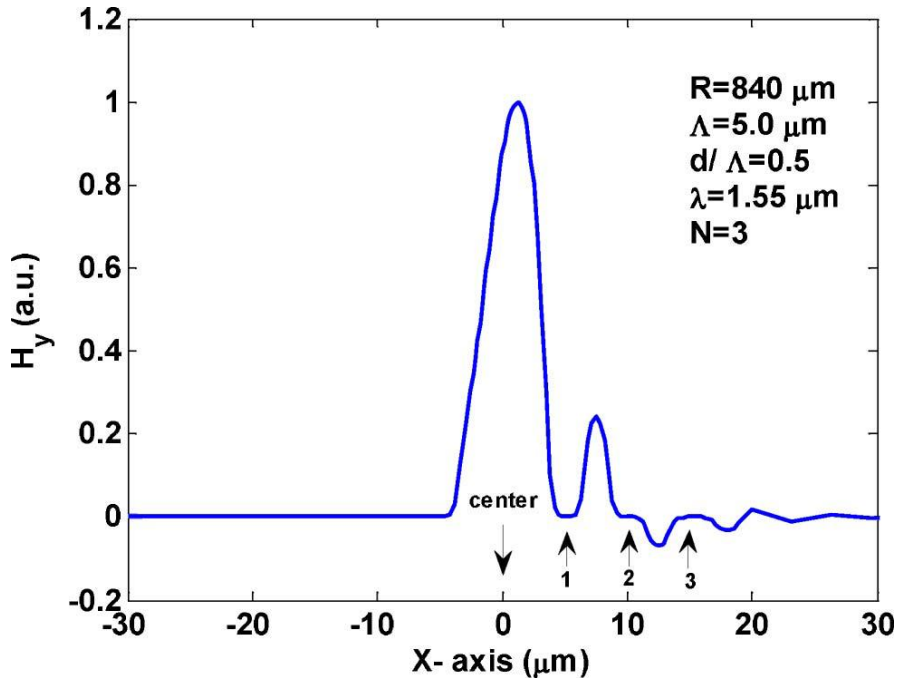


Fig. 4. 23: Variation of the  $H_y$  field along the x-axis for  $R = 840\mu\text{m}$ ,  $\Lambda = 5.0\mu\text{m}$ ,  $d/\Lambda = 0.5$ .

Next  $H_y$  field profile of the  $H_{11}^y$  mode is shown to demonstrate the transition of the mode. Figure 4.23 shows the  $H_x$  mode variation along the x-axis for  $R = 840\mu\text{m}$ , a radius slightly bigger than the degeneration point and  $\Lambda = 5.0\mu\text{m}$  and  $d/\Lambda = 0.5$ . It can be observed that the main peak is almost at the centre but slightly shifted to the right due to the bend whereas the minor peak has a magnitude approximately 0.22 a. u. The modal field profile expands more on the right as the PCF is bending to the left. It can also be seen that there are low fields near the two air-holes on the right (Locations of air-holes are shown by arrows, where field is nearly equal to zero). It can be noted that the first minor peak is also positive, same sign as that of the main lobe in the core. These minor peaks can be part of the clad mode which can form in the bent PCF.

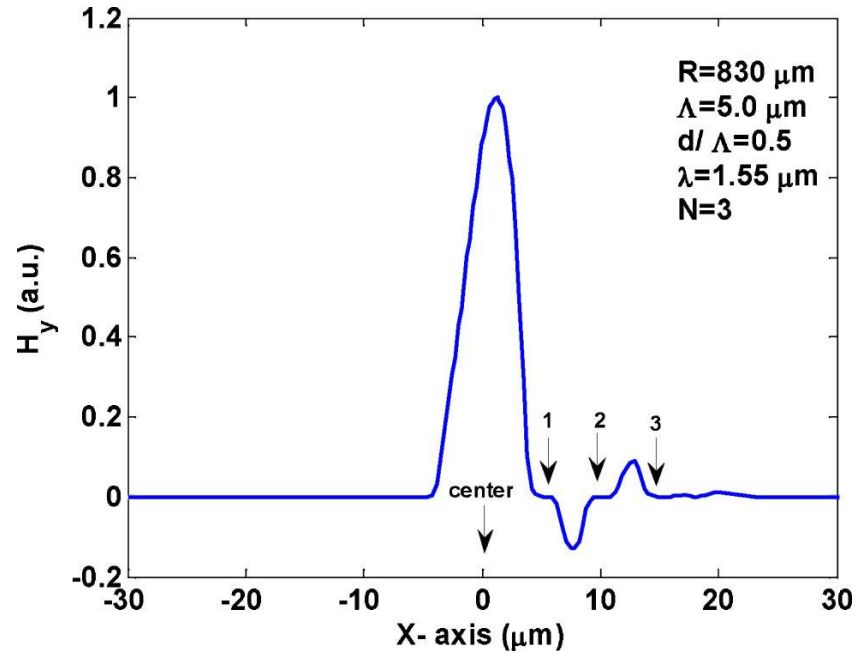


Fig. 4. 24:  $H_y$  field profile along the X axis for the  $H^y_{11}$  core when  $R = 830 \mu\text{m}$  below the degeneration point.

The field for  $R = 830 \mu\text{m}$ , for a value slightly lower than the degeneration point, is shown in Fig. 4.24. The two radii values,  $R = 830 \mu\text{m}$  and  $R = 840 \mu\text{m}$  were selected on the two sides of the crossing point shown in Fig. 4.21. As the clad mode crosses the  $H^y_{11}$  mode,  $n_e$  curve, its mode order changes, which is identified by the sudden change of the first minor peaks sign with a magnitude approximately  $-0.18 \text{ a. u.}$

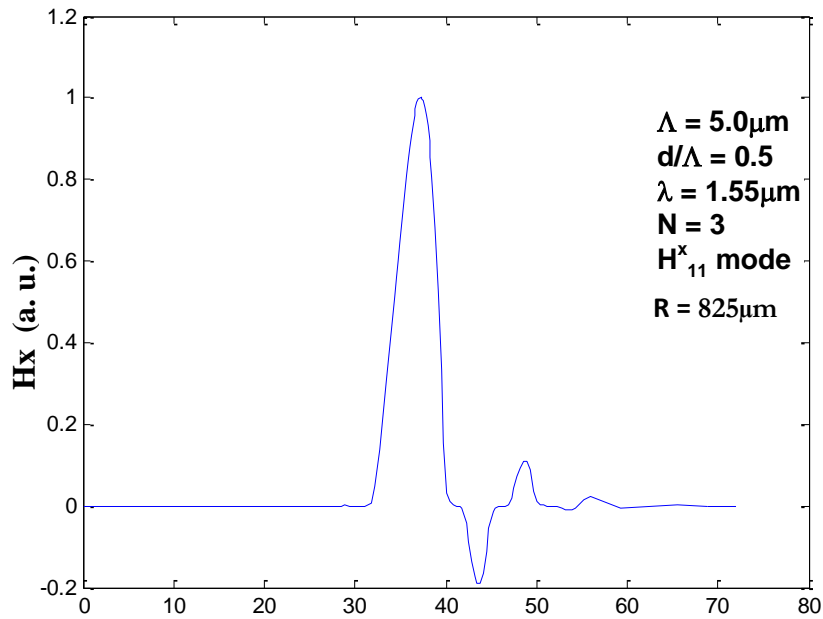


Fig. 4. 25: Variation of the  $H_x$  field along the x-axis  $R = 825 \mu\text{m}$ ,  $\Lambda = 5.0 \mu\text{m}$ ,  $d/\Lambda = 0.5$

Next, field variation is shown for slightly reduced bend. Figure 4.25 shows the graph for field along the x-axis for  $R = 825\mu\text{m}$ ,  $\Lambda = 5.0\mu\text{m}$  and  $d/\Lambda = 0.5$ . It clearly shows three secondary peaks along with the main peak near the centre. It can be observed that the first secondary peak is negative and it is totally different from that shown in Fig 4.23. Also, its value increased slightly compared to that at  $R = 830\mu\text{m}$  with magnitude approximately  $-0.2$  a. u. This shows mode transformation from one form to the other, which was observed in the change in the effective index, bending loss and spot size. The mode profiles shown in Figs. 4.24 and 4.25 can be considered as coupled supermodes. Two coupling guided-wave regions are non-identical so the amplitudes of modes in these regions are different. Similar abrupt changes in the field profiles have been identified at the various transition points.

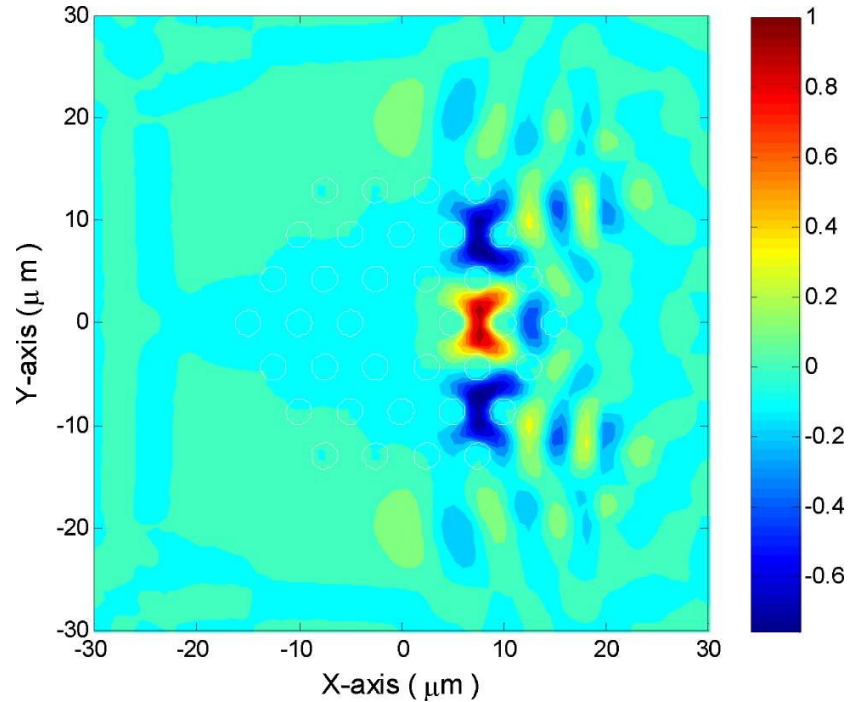


Fig. 4. 26:  $H_y$  contour of the higher order cladding mode when  $R = 833 \mu\text{m}$ .

To show these cladding modes, a contour plot of this mode is shown next. Figure 4.26 shows  $H_y$  contour plot for the  $H_{c2}^y$  mode at  $R = 833 \mu\text{m}$ . This is a higher order cladding mode and it can be observed that the intensity of the mode is seen clearly in the cladding region. The positions of the air-holes in the cladding are indicated by circles.

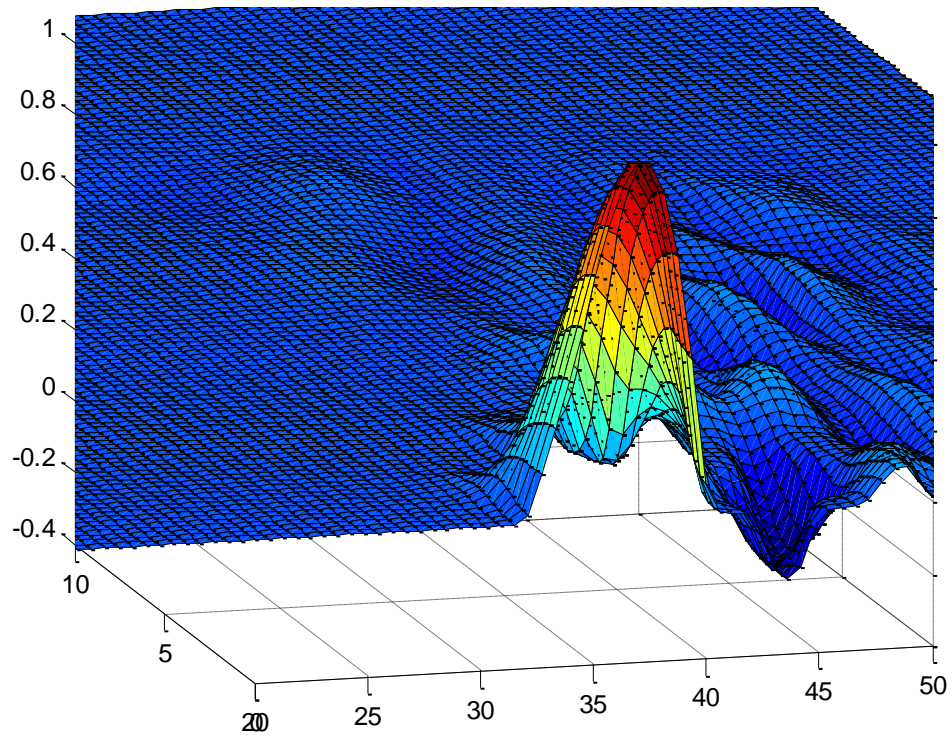


Fig. 4. 27:  $H_x$  3-D field for the  $H_x^{11}$  mode  $R = 825\mu\text{m}$ ,  $\Lambda = 5.0\mu\text{m}$ ,  $d/\Lambda = 0.5$ .

For clarity the 3-D profiles for the  $H_x^{11}$  mode  $R = 825\mu\text{m}$  is also shown. Figure 4.27 shows the graph for field along the x-axis for  $R = 825\mu\text{m}$ ,  $\Lambda = 5.0\mu\text{m}$ ,  $d/\Lambda = 0.5$ . It can be observed in Fig. 4.24 (for  $R = 825\mu\text{m}$ ) that there is a negative secondary peak as well as another positive secondary peak. The ripples at the right side of the cladding region indicate radiation loss. These field profiles shown between for  $R = 825\mu\text{m}$  and  $R = 850\mu\text{m}$ , clearly show the differences and their effects in the variation of its spot sizes was shown in Fig. 4.20. This created an abrupt discontinuity in its effective index curve and a sharp increase in its loss value.

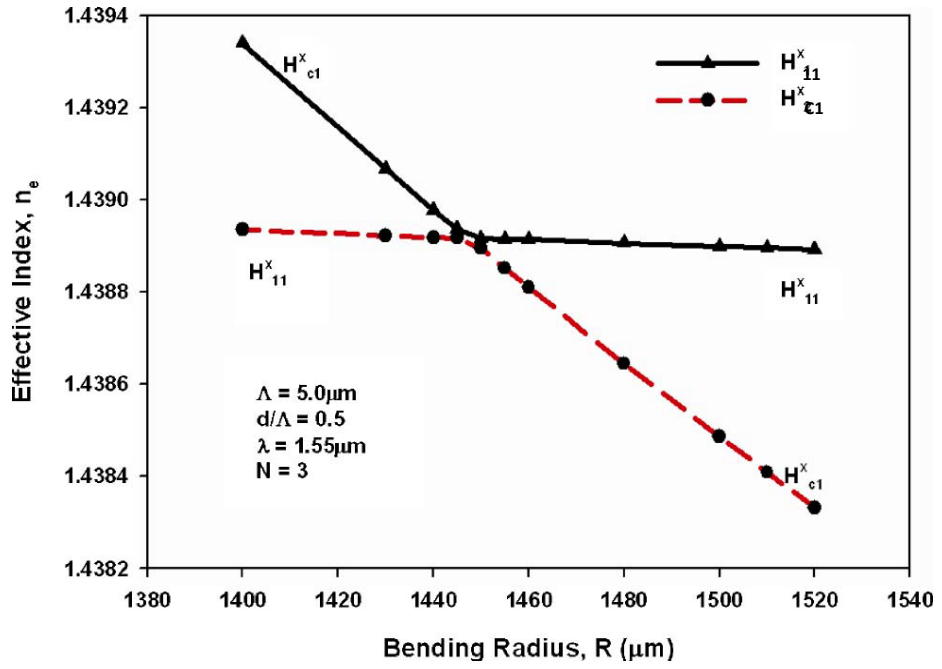


Fig. 4. 28: Variation of the effective indices with the bending radius  $R$ .

Besides the transition around  $R \sim 833\mu\text{m}$ , there were additional transitory behaviours which are shown in Fig. 4.28. The variation of effective indices with bending radius is studied next around  $R = 1460\mu\text{m}$  as another oscillatory peak was visible in Fig. 4.17 in this region.

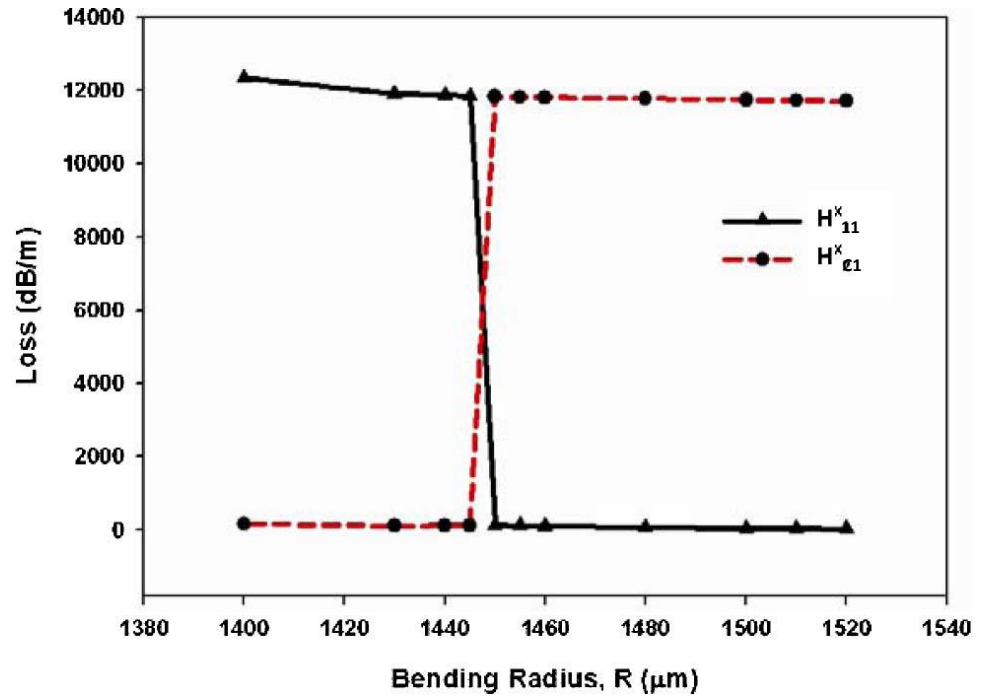


Fig. 4. 29: Variation of the total losses with the bending radius  $R$ .



The loss values for these first  $H_{11}^x$  and second  $H_{21}^x$  modes are shown in Fig. 4.29 by a solid and a dashed line, respectively. Parts of these two curves form the lower section, which shows the loss values of the  $H_{11}^x$  core mode, is around 100 dB/m. On the other hand, the upper lines represent the  $H_{cl}^x$  cladding modes with significantly higher loss values, around 12000 dB/m. However, these two curves also go through a transition near  $R \sim 1445 \mu\text{m}$ , which is similar to the effective index curves shown in Fig. 4.22. The upper curve goes through a local minimum (which is not clearly visible) near the mode degeneration point, being mixed with a less lossy  $H_{11}^x$  core mode. Similarly the loss value of the lower curve also peaks near the resonance due to being mixed with a highly lossy cladding mode. In this case it should be noted that the core mode has a lower loss (about 100 dB/m) compared to a higher loss (2000 dB/m) shown in Fig. 4.22, for a lower bending radius.

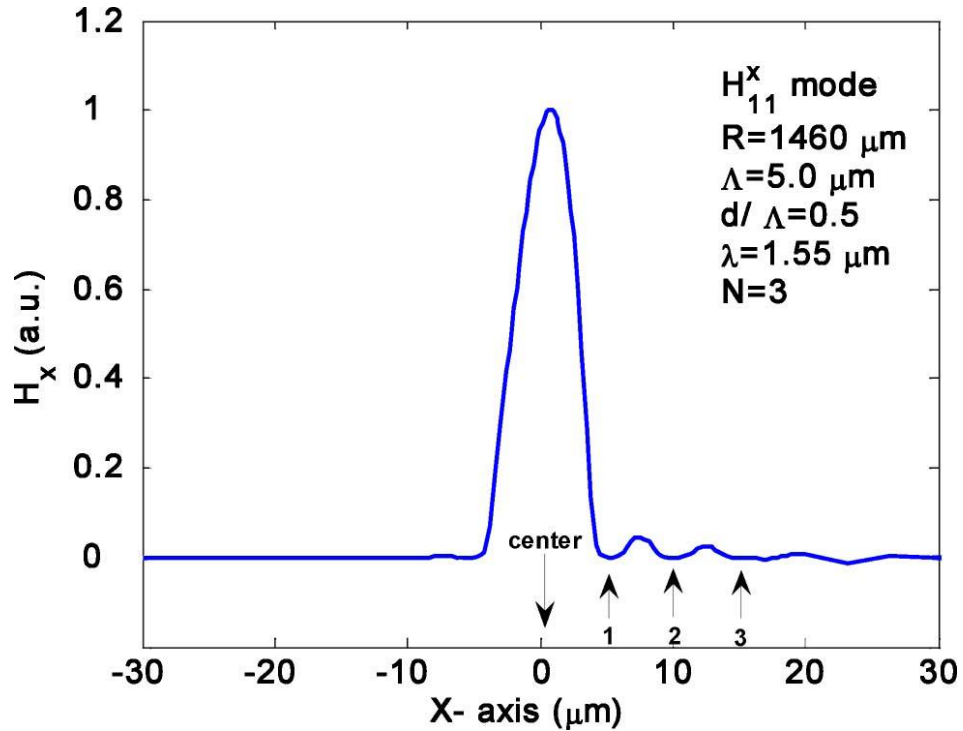


Fig. 4. 30:  $H_x$  field profile of the  $H_{11}^x$  core mode along the x axis through the centre of the core when  $R = 1460 \mu\text{m}$ .

The variation of the  $H_x$  field for the  $H_{11}^x$  core mode along the centre of the guide in the x direction is shown in Fig. 4.30 when  $R$  was around  $1460 \mu\text{m}$ . It can be observed that field is predominantly confined at the centre of the PCF core: however, its maximum value is shifted slightly to the right of the waveguide centre, shown by an arrow. Two

local peaks are also visible and are located in the silica bridge region between the first and second air-hole rings and the second and third air-hole rings (shown as 1, 2, and 3 in Fig. 4.30), respectively. These peaks are only visible on the right of the core, not on the left side, as following the conformal transformation; the higher local equivalent index value on right allows such local modes to be formed on the right side of the core. Its spot size and effective area are  $31.5$  and  $30.0 \mu\text{m}^2$ , respectively. At this particular bending radius (where  $R = 1460 \mu\text{m}$ ), a local cladding mode also exists with its effective index slightly lower than the  $H_{11}^x$  core mode. The locations of the air-holes are shown by circles. It can clearly be observed that this cladding mode is formed between the air-holes of the second and third rings. The  $H_x$  field contour for this  $H_{c1}^x$  cladding mode is shown in Fig. 4.31. The spot size area of this mode is smaller ( $\sigma = 26.1 \mu\text{m}^2$ ), being restricted to a smaller silica bridging region (but its  $A_{\text{eff}} = 37.4 \mu\text{m}^2$  is rather large as the field spreads slowly), but this mode is highly dispersive with a higher loss value. When the bending radius is reduced below the degeneration point ( $R < 1445 \mu\text{m}$ ) the effective index of the cladding mode becomes higher than that of the  $H_{11}^x$  core mode and the two eigenvalues swapped their positions.

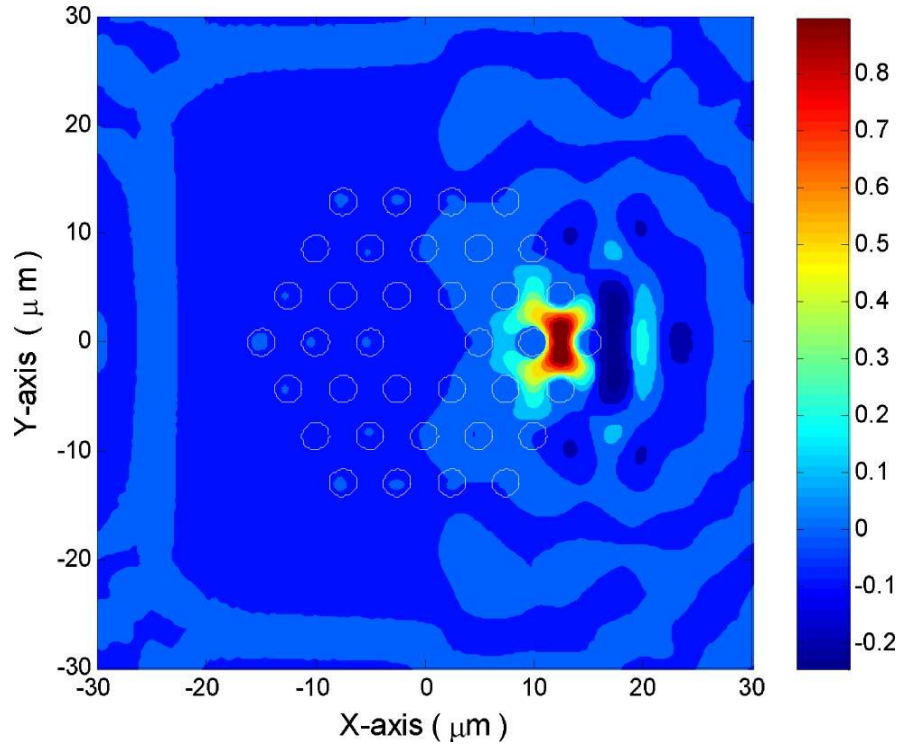


Fig. 4. 31:  $H_x$  field contour for  $H_{c1}^x$  cladding mode when  $R = 1460 \mu\text{m}$ .

Figure 4.30 shows the field profile for the bending radius  $R = 1460 \mu\text{m}$  for the  $H_{11}^x$  mode. It is observed that there is a variation along the x-axis as discussed in previous

figures. At this high bending radius the peaks of the variations are positive and not very high in relation to the core mode. Whereas, in Fig. 4.31, we have shown the contour plot of the  $H_{c1}^x$  cladding mode at  $R = 1460 \mu\text{m}$ . It can be observed that the intensity of the mode has shifted to the right side into the cladding region and it is highest between the second and the third ring of air-holes.

Next the polarization issues of such modal degeneration are studied.

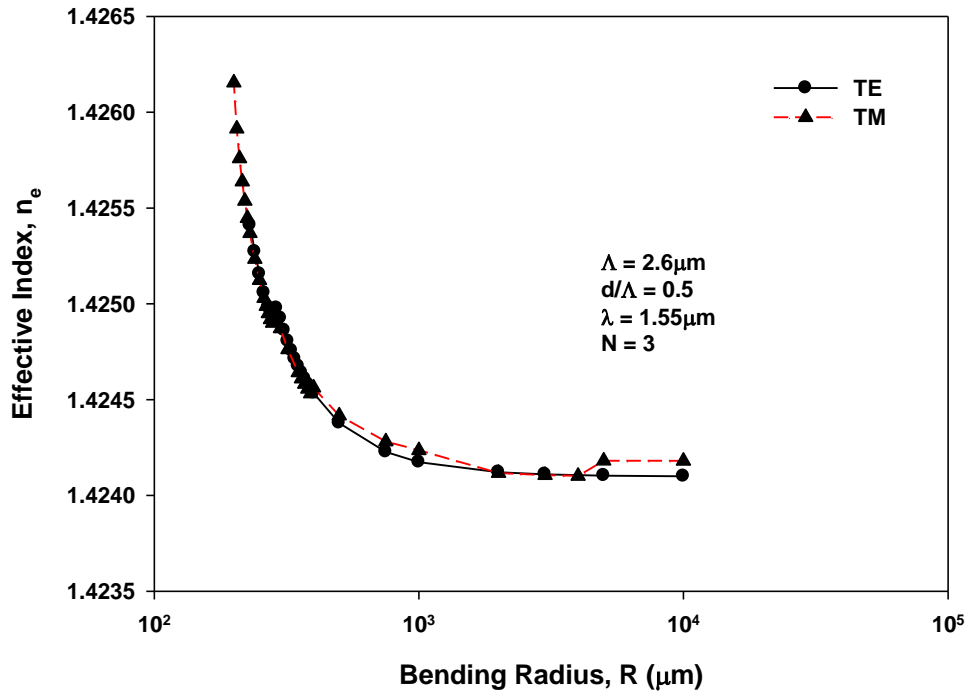


Fig. 4. 32: The variation of effective index with bending radius,  $R$  for  $\Lambda = 2.6 \mu\text{m}$ , for both the quasi-TE and quasi-TM modes.

In the work carried out in this chapter, it was observed that the effective index of the quasi-TM,  $H_x^{11}$  mode and that of the quasi-TE,  $H_y^{11}$  mode were nearly identical. Figure 4.32 shows the variation of effective index with bending radius,  $R$  for both the polarizations. It can be seen from Fig. 4.32 that the effective index increases as bending radius is reduced and has a sharp increase at lower values of bending radius. It shows small abrupt changes around  $R = 600 \mu\text{m}$ , but positions were identical for both the quasi-TE and quasi-TM polarizations.

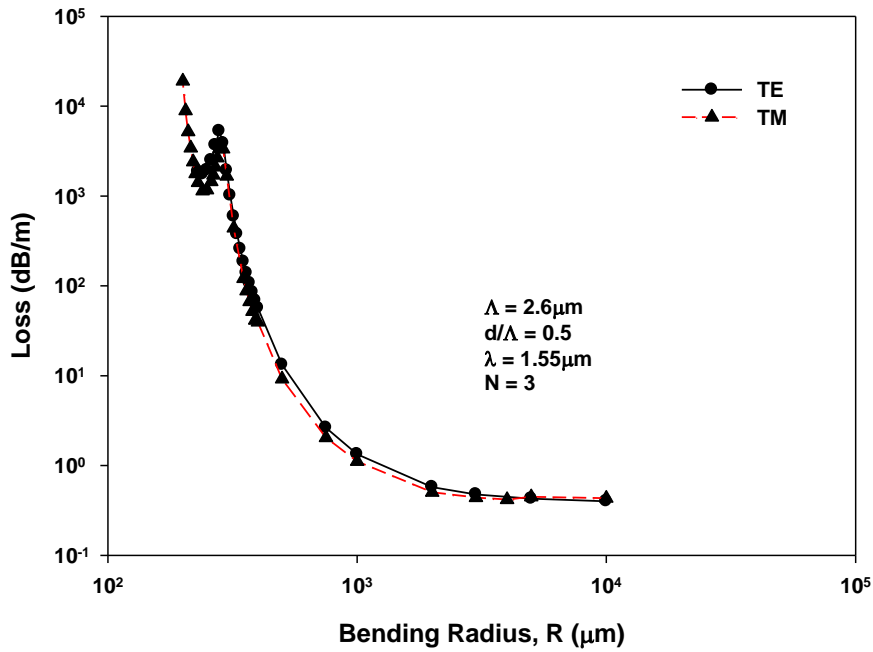


Fig. 4. 33: The variation of loss with bending radius,  $R$  for  $\Lambda = 2.6 \mu\text{m}$ , for both quasi-TE and quasi-TM modes.

It was also observed from the work carried out in this chapter that the bending loss for the quasi-TM and quasi-TE modes is identical also. Figure 4.33 shows the variation of loss with bending radius,  $R$ . It can be seen from Fig. 4.33 that the loss increases as bending radius is reduced and has a sharp increase at lower values of bending radius. It shows small abrupt changes around  $R = 600 \mu\text{m}$  for the quasi-TE and quasi-TM polarizations. This correlates with the change in effective index shown in Fig. 4.33. Similar detailed field profiles, spot size variations were studied and the abrupt changes are due to the transition of the modal profiles. This also shows the degeneration happens for both the polarizations and these are not numerical artefact.

## 4.5 Summary

In this chapter, the origin of localized cladding modes in the silica bridging regions between the air-holes is studied for the first time, with results obtained as summarized in the figures above. This shows that these silica bridging areas are smaller than the PCF core (where an air-hole is missing) and for a straight PCF particularly when  $\Lambda$  is larger, these cladding modes with the lower effective indices do not interact with the PCF core mode. However, for a bent PCF, as the local equivalent index is increased in

the cladding region and this increase is more for small bending radius and also local indices are higher for a silica region further away from the core on the right side. The dispersion slopes of these modes are higher and for smaller bending radii they can be phase matched to the core mode to form coupled supermodes. It is also shown that these cladding modes can also cover several bridging regions simultaneously and also support the higher order modes. This mode degeneration causes a mixing of these modes, the formation of the supermodes and the transformation from one mode to another. These cause rapid changes in their modal properties, their effective index, the spot size and the bending loss values. A higher pitch value or larger  $d/\Lambda$  ratio which increases the silica bridging regions and such mode degeneration can appear at a higher bending radius, which may often be encountered in practical applications. In these cases, the mode degeneration appears more frequently and shows as noisy loss values in experimental measurements. Resulting from this work, the origin of these fundamental and higher order cladding modes, the coupling between them and ultimately the coupling of these cladding supermodes with the fundamental core mode have been reported for the first time and these can affect the design of various PCF-based applications. The study of this mode degeneration gives insight to the practical application of PCFs and the optimum handling conditions during many “real world” applications. This understanding can also be useful in the study of PCF-based devices, thereby exploiting bending loss, for example by using effectively single mode waveguides with differential modal losses and single polarization waveguides with highly differential polarization dependent bending losses or additionally, in the design of optical attenuators, for example. The application to the design of single mode single polarization PCF is presented in the next Chapter.

## CHAPTER FIVE: Polarization Maintaining Fibre

### 5.0 Abstract

In this chapter, design approach of a highly birefringent PCF is considered for its use as a single mode single polarization waveguide. This was achieved by increasing diameters of four air-holes in the first ring and thus making the PCF asymmetric resulting in the core being more elliptical. By operating the PCF close to cutoff, differential loss between the two polarized modes was enhanced. It is also shown that by bending this asymmetric PCF, the differential modal loss can be further enhanced.

### 5.1 Polarization Maintaining Optical Fibres

Polarization maintaining optical fibre (PMF) is a type of optical fibre which maintains the polarization state of the light waves that are launched into it, thereby maintaining the polarization plane during the propagation. It does this with little or no cross coupling of optical power between the polarizations modes. This type of fibre is very useful today because of the increasing demand for higher bandwidth by using polarization division multiplexing and polarization mode dispersion above 10Gbps data rate and as well as the increasing complexity of optical networks in modern telecommunications systems (Goure and Verrier 2002; Poli *et al.* 2007; Agrawal 2008).

Polarization maintaining optical fibres are also used for special applications like fibre optic sensing (Chan *et al.* 2007), interferometry and quantum key distribution (Lu *et al.* 2011). They are also be commonly used in telecommunications for the connection between a source laser and a modulator since the modulator requires light of a specific polarization as input. They are rarely used for long distance transmission because polarization maintaining optical fibre is relatively expensive and has higher attenuation than the single mode fibres (Goure and Verrier 2002; Poli *et al.* 2007; Agrawal 2008).

There are several types of polarization maintaining optical fibres available; one kind of such fibres are the asymmetric geometric high birefringence (Hi-Bi) fibres, such as the elliptical core fibre or the D-shaped cladding fibre (Liu *et al.* 1994). The core or the cladding of this kind of fibre is usually deformed from a circular shape to generate an asymmetry in the fibre structure. The other kind is the stress-induced hi-bi fibre. This

kind of fibre is fabricated with stress applying zones so that a particular stress status can be maintained in the fibre such as the Panda type and the Bow-tie type by using elasto-optic effect or via rods of another material of different thermal expansion included within the cladding of the fibre (Liu *et al.* 1994).

## 5.2 Photonic Crystal Fibre as a Polarization Maintaining Optical Fibre

There are different polarization maintaining optical fibres employed so that the polarization of light is maintained as the light is propagated through the fibre. These fibres are Panda type, Bow-tie type, photonic crystal fibre and elliptical clad type. Figure 5.1(a) shows the Panda type polarization maintaining optical fibre, Fig 5.1 (b) shows the Bow-tie type polarization maintaining optical fibre and Fig 5.1(c) shows the elliptical clad type polarization maintaining optical fibre. On the other hand, a simple photonic crystal fibre (PCF) can also be designed as a polarization maintaining optical fibre as well.

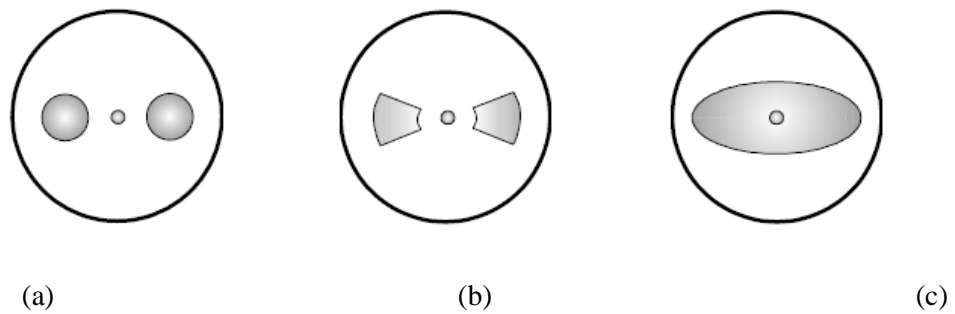


Fig. 5. 1: The panda type (b) the bow-tie and (c) the elliptical clad type polarization maintaining optical fibres (Liu *et al.* 1994)

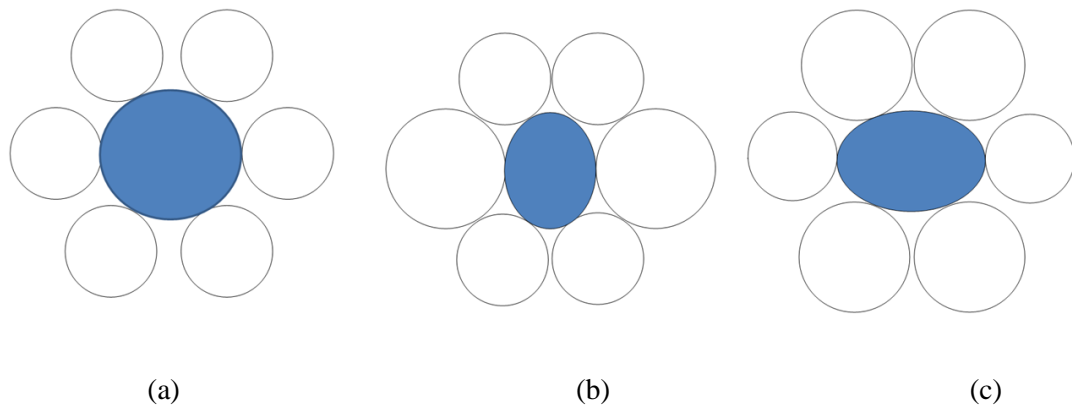


Fig. 5. 2: The core and the first ring of air-holes in a PCF (a) with all the air-holes of the same diameter thus the core is circular (b) two larger air-holes on the side of the core making the core elliptical, height > width (c) two larger air-holes above the core and two larger air-holes below the core makes the core elliptical, width > height.

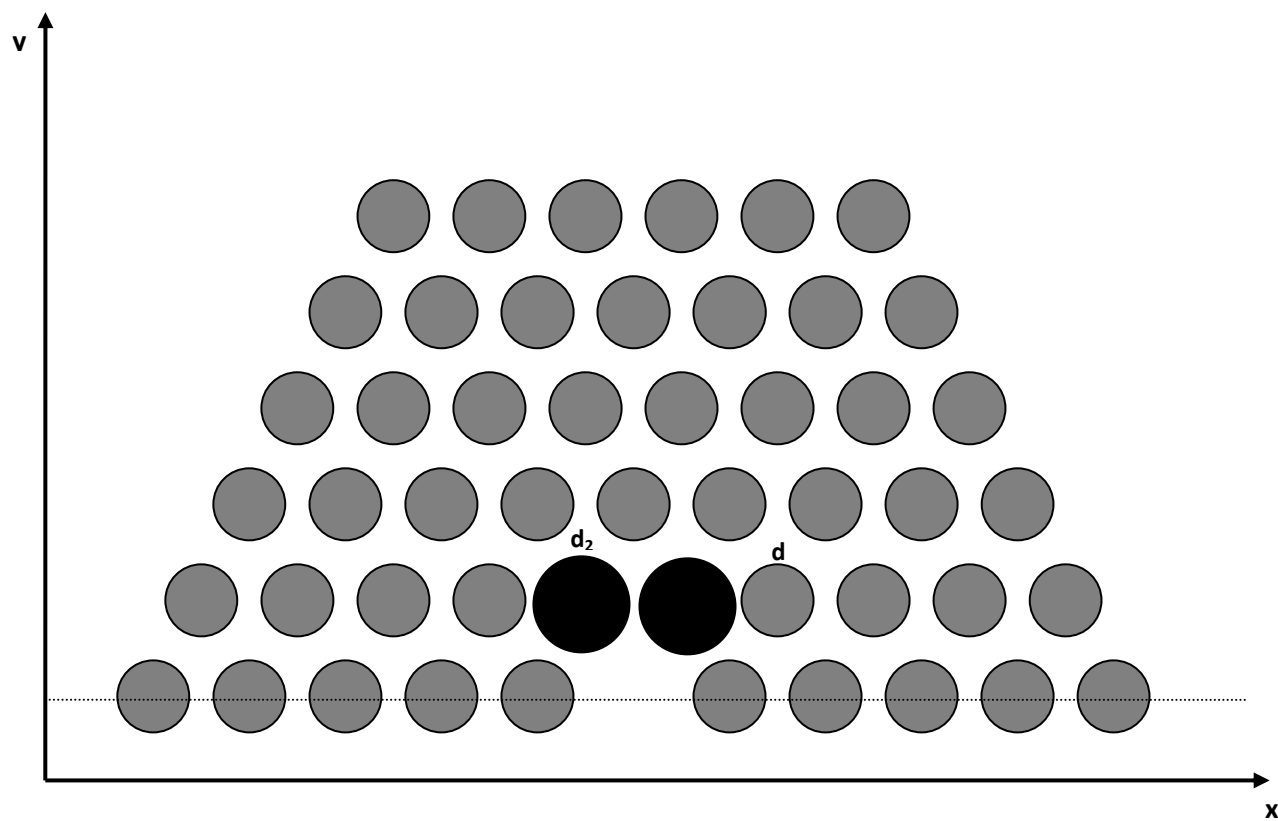


Fig. 5. 3: A graph depicting half of the cross-section of a PCF;  $d \neq d_2$



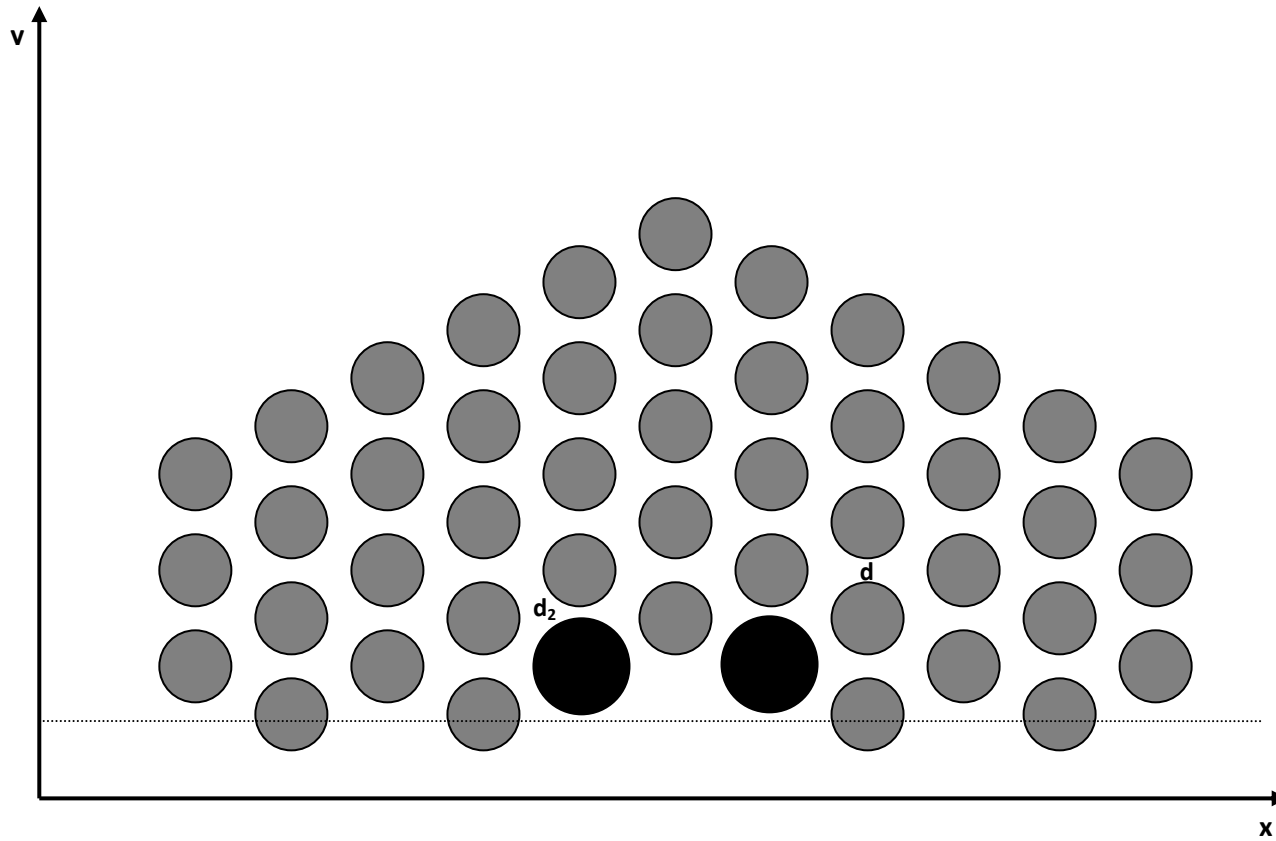


Fig. 5. 4: A graph depicting half of the cross-section of a PCF;  $d \neq d_2$ , same as shown in Fig. 5.3 but with a 90 degree rotation.

Photonics Crystal Fibre (PCF) have several advantages that by varying the size and location of the air-holes, the fibre mode shape, non-linearity, dispersion and birefringence can reach values that are not achievable in conventional fibres. Photonic crystal fibres can also be designed to carry higher power than conventional fibre and their wavelength dependent properties can be manipulated to improve their performance in certain applications. It has been mentioned earlier that an ordinary PCF with 6-fold symmetry has near zero birefringence and the air-hole arrangement of the first ring is shown in Fig. 5.2(a). It is well known that air-holes in the first ring dominate the modal properties of such PCFs. However, polarization maintaining photonic crystal fibres can be designed by destroying the 90 degree rotational symmetry. In this case, different air-hole diameters along two orthogonal axes near the core region provide an effective index difference between the two orthogonal polarization modes. As is observed in Figs. 5.2(b) where the height > width and 5.2(c) where the width > height, thus making the core more elliptical in shape ensuring increased birefringence. It has been shown that

their birefringence is of the order of  $10^{-3}$ , which is one order of magnitude larger than that of conventional polarization maintaining optical fibres and better polarization maintaining characteristics are expected (Suzuki *et al.* 2001).

### 5.3 Straight Single Mode Single Polarization Asymmetric PCF

In this study, index guiding silica PCF with the air-holes arranged in a triangular lattice is considered first. The refractive index of the silica used is taken as 1.444 at an operating wavelength of 1.55  $\mu\text{m}$ . A typical PCF with  $60^\circ$  rotational symmetry can support two fundamental  $H_{11}^y$  (quasi-TE) and  $H_{11}^x$  (quasi-TM) modes and with higher  $\Lambda$  and  $d/\Lambda$  values, but it may also support additional higher-order modes of a given polarization. This structure possesses a birefringence as it does not have the necessary  $90^\circ$  rotational symmetry, but this value being very small which has often been ignored. The modal birefringence of a PCF can be increased by breaking the rotational symmetry of having air-holes of different diameters. Initially, the asymmetric arrangement considered here is similar to that considered in previous work (Rahman *et al.* 2006; Kejalakshmy *et al.* 2008b), where the diameters ( $d_2$ ) of the four air-holes in the first ring are larger than those of the other air-hole diameters ( $d$ ) as seen in Fig. 5.3. Later on, orientation of the structural asymmetry is also studied for a bent PCF as shown in Fig. 5.4. In Fig. 5.5, the variations of the effective indices of the quasi-TE and quasi-TM modes, with respect to the ratio  $d_2/\Lambda$ , are shown for a PCF with  $d/\Lambda = 0.5$  and  $\Lambda = 1.6 \mu\text{m}$ . Effective index decreases as the  $d_2/\Lambda$  is increased both the TE and TM polarizations due the increase in the air fraction. The effective index is lower in the case of the TM mode than that of the TE mode. For this arrangement, as its equivalent height is smaller than its equivalent width, the effective index of the quasi-TM ( $H_{11}^x$ ) mode is lower than that of the quasi-TE ( $H_{11}^y$ ) mode as observed in Fig. 5.2. This also yields a significantly high modal birefringence. Here, the birefringence is defined as the difference between the effective indices of the  $H_{11}^x$  and  $H_{11}^y$  modes,  $B = |n_x - n_y|$ . The quasi-TM mode (with the dominant  $H_x$  and  $E_y$  fields) has a smaller effective index value, is slightly weakly confined compared to the TE mode and expands more into the cladding region, which also makes it highly exposed to the bigger air-holes. It can be observed that, as the value of  $d_2/\Lambda$  increases, the effect of structural asymmetry increases further, as does the modal birefringence. It should be noted that the modal

birefringence shown here is higher than that of a “Panda” or “Bow-tie” fibre and this can be achieved by using simple air-hole diameter adjustment.

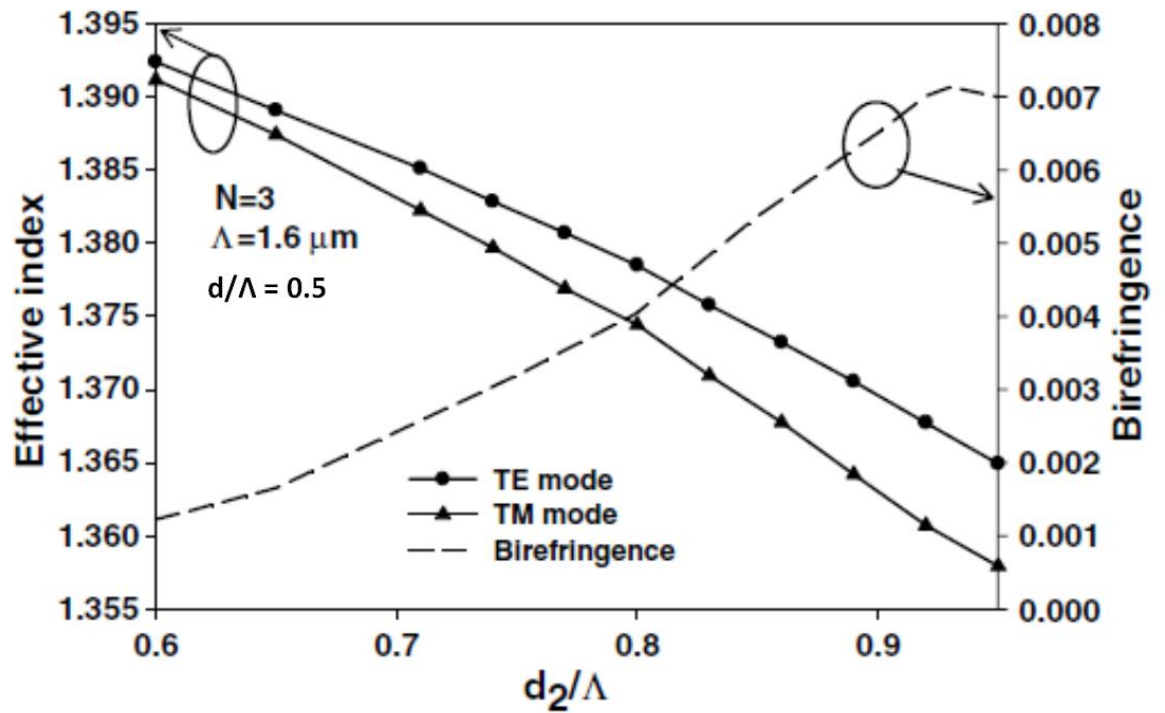


Fig. 5. 5: Variation of effective index and birefringence with  $d_2/\Lambda$ .

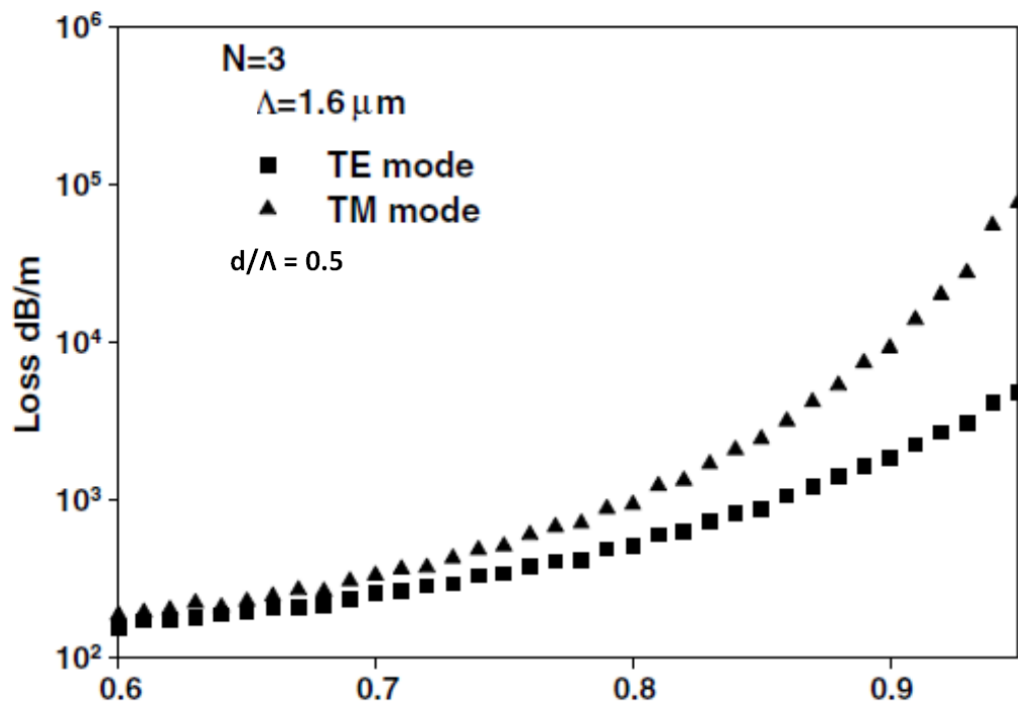


Fig. 5. 6: Variation of the TE and TM modal losses with  $d_2/\Lambda$ .

All the modes in a PCF suffer from leakage loss. For a PCF with structural asymmetry, leakage losses for quasi-TE and TM modes are different. In Fig. 5.6, it is observed that as  $d_2/\Lambda$  is increased, the loss increases as well for both the TM and TE modes. As the air-hole diameter is increased, its core size is reduced, which pushes modes more towards their cut off. It can also be observed that the loss for the TM mode is always higher than that of the TE mode.

In the design of a single polarization single mode PCF, a dimensionless differential loss ratio, LR, is studied. To identify their relation, LR can be defined as the ratio of leakage loss of TM mode ( $\alpha_{TM}$ ) to the leakage loss of TE mode ( $\alpha_{TE}$ ) and it is given as follows:

$$LR = \alpha_{TM} / \alpha_{TE} \quad (5.1)$$

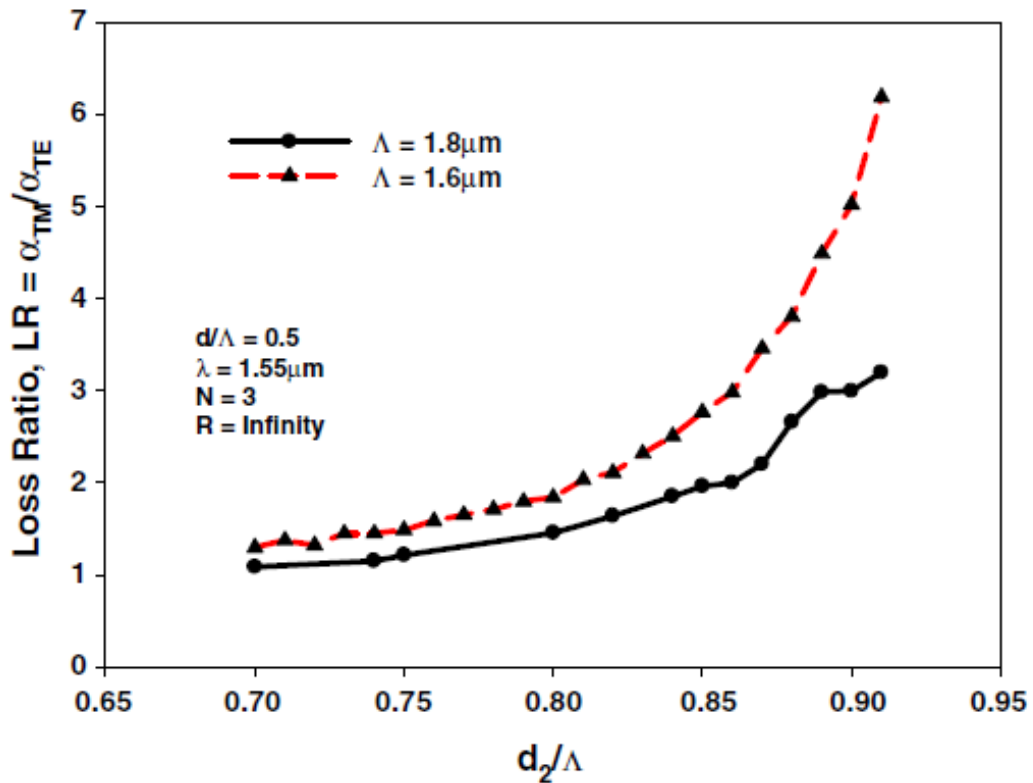


Fig. 5. 7: Variation of the differential LR with  $d_2/\Lambda$  for pitches 1.6 and 1.8  $\mu\text{m}$ .

It is observed from Fig. 5.7 that as the  $d_2/\Lambda$  is increased, the loss ratio increases too for  $\Lambda = 1.6 \mu\text{m}$  and  $N = 3$ . The rate of increase is slower starting from  $d_2/\Lambda = 0.6$  but the rate of increase is steeper towards  $d_2/\Lambda = 0.9$  which could be attributed to approaching the cut-off limit. As  $d_2/\Lambda$  is increased so does the loss ratio, LR whereby the curves of  $\Lambda =$

1.6 and 1.8 $\mu\text{m}$  are compared. It can be observed that  $\Lambda = 1.6\mu\text{m}$  has a higher loss than that of  $\Lambda = 1.8\mu\text{m}$ . As was observed in previous calculations, the loss values for both TM and TE modes are higher for  $\Lambda = 1.6\mu\text{m}$  than that of  $\Lambda = 1.8\mu\text{m}$ , as for smaller pitch, PCF are operating closer to their cut off condition.

#### 5.4 Results for Bent Asymmetric PCF, $d \neq d_2$ (Non-Identical Air-holes)

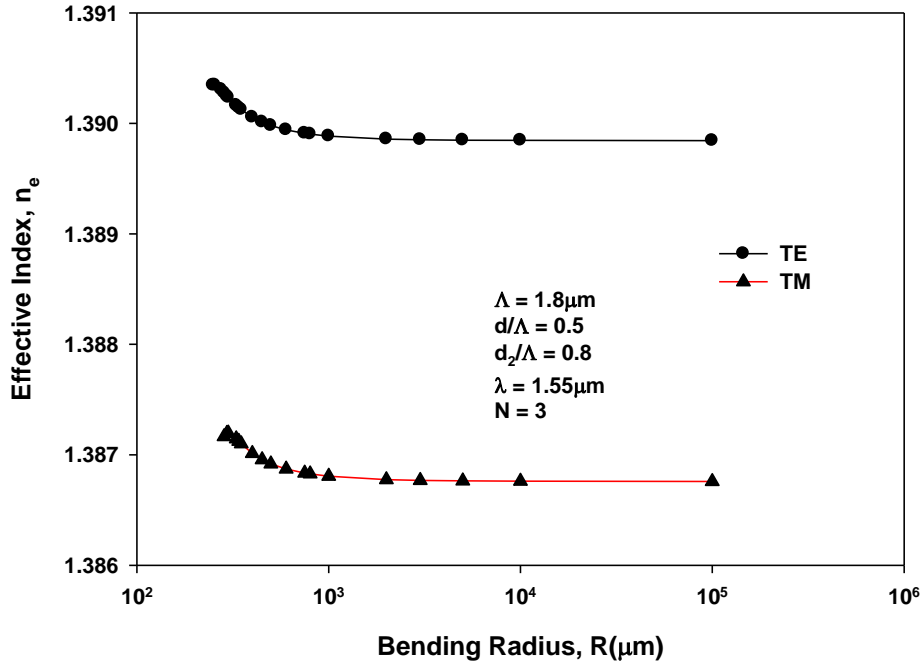


Fig. 5. 8: Variation of effective index with bending radius,  $R$  for  $\Lambda = 1.8\mu\text{m}$ ,  $d/\Lambda = 0.5$ ,  $d_2/\Lambda = 0.8$  for both quasi-TE and quasi-TM modes.

Next, the effect of bending in such highly birefringent PCF is studied. Figure 5.8 shows the variation of effective index with bending radius,  $R$  for both the fundamental quasi-TE and quasi-TM modes. In both cases, the effective index increases as bending radius is reduced. The use of conformal transformation modifies the local refractive index to its equivalent index value. For a bent guide mode shape is modified by the higher index seen at right side of the y-axis, which increases the effective indices as discussed in Chapter 4. It can also be seen the effective index is higher for the quasi-TE mode compared to the quasi-TM mode.

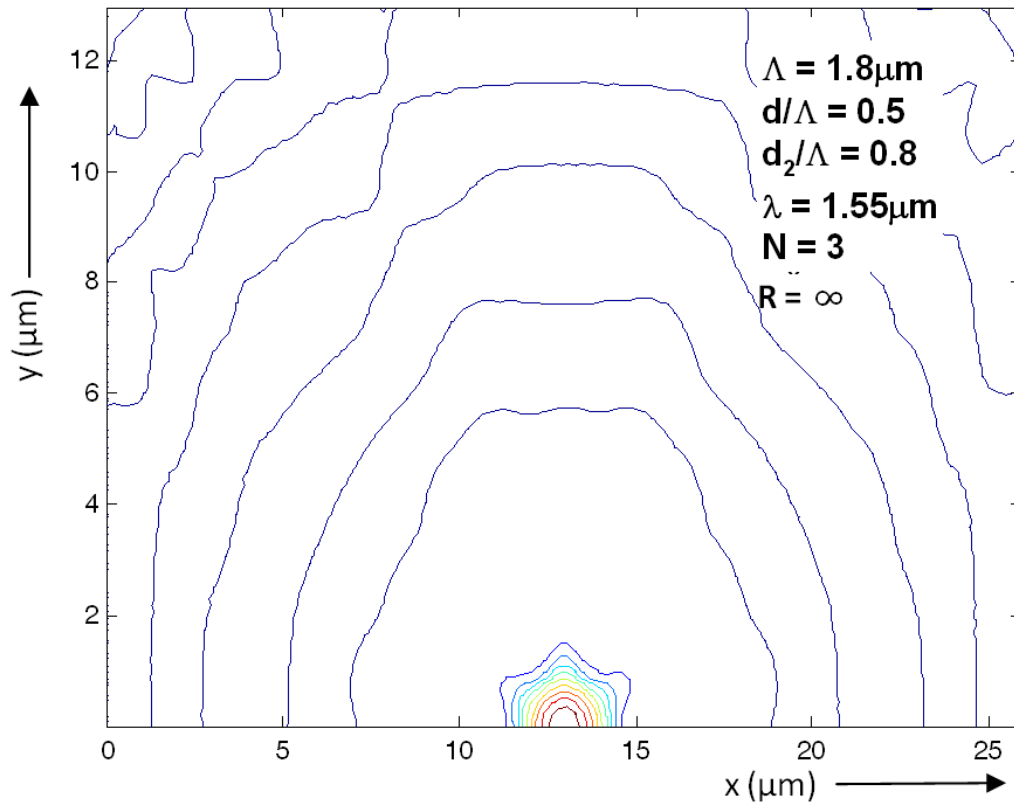


Fig. 5. 9:  $H_x$  field profile of the  $H_x^{11}$  mode at  $R = \infty$ ,  $\Lambda = 1.8$ ,  $d_2/\Lambda = 0.8$ .

Figure 5.9 shows the  $H_x$  field plot of the  $H_x^{11}$  mode for pitch  $\Lambda = 1.8\mu\text{m}$ ,  $d/\Lambda = 0.5$  and  $d_2/\Lambda = 0.8$  and at  $R = \infty$ . It can be noted that  $H_x$  field is the dominant component of the quasi-TM,  $H_x^{11}$  mode. The field is well confined within the core. The six-fold rotational symmetry of the field is broken because of the air-hole diameters in the first ring are different as  $d \neq d_2$ . It can be noted at that for  $d_2 > d$ , width of the core is larger than its height.

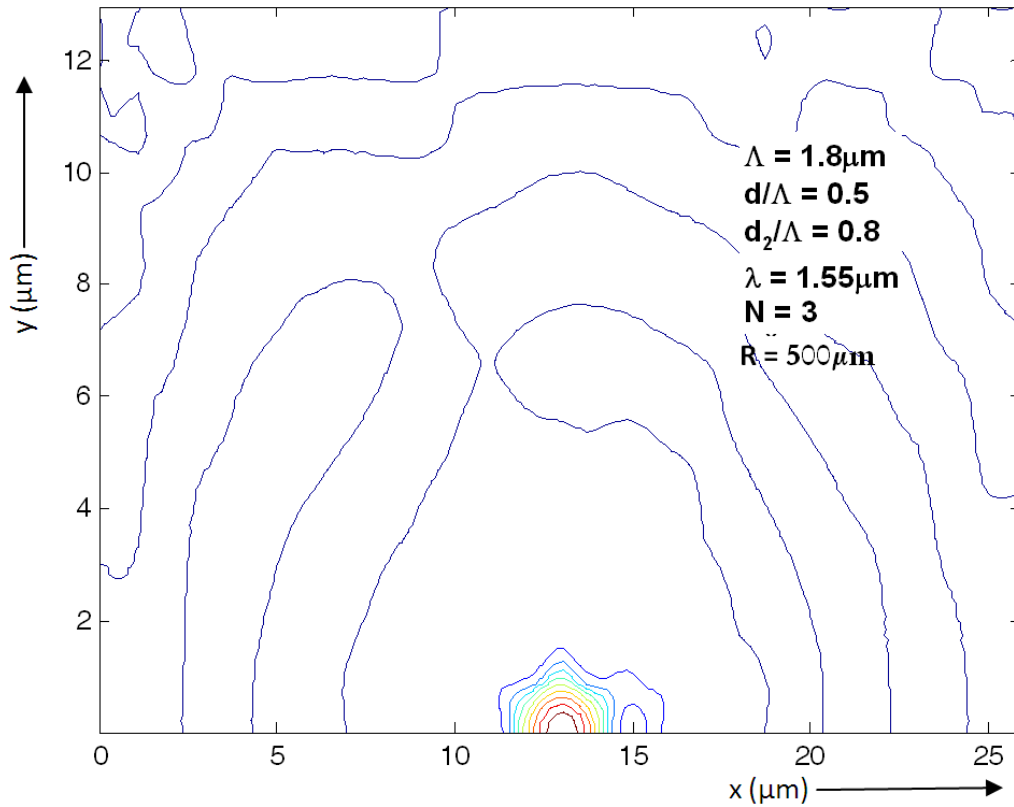


Fig. 5. 10:  $H_x$  field profile of the  $H_x^{11}$  mode at  $R = 500\mu\text{m}$ ,  $\Lambda = 1.8$ ,  $d_2/\Lambda = 0.8$ .

Figure 5.10 shows the  $H_x$  field plot of the  $H_x^{11}$  mode for pitch  $\Lambda = 1.8\mu\text{m}$ ,  $d/\Lambda = 0.5$  and  $d_2/\Lambda = 0.8$  and at  $R = 500\mu\text{m}$ . It can be observed that the field shifts to the right side, more into the cladding. It can be clearly observed that a smaller magnitude field encircles one air-hole on the x-axis in the first ring. The symmetry of the field is broken because of the variation of the air-hole diameter  $d_2$  and because  $d \neq d_2$ .

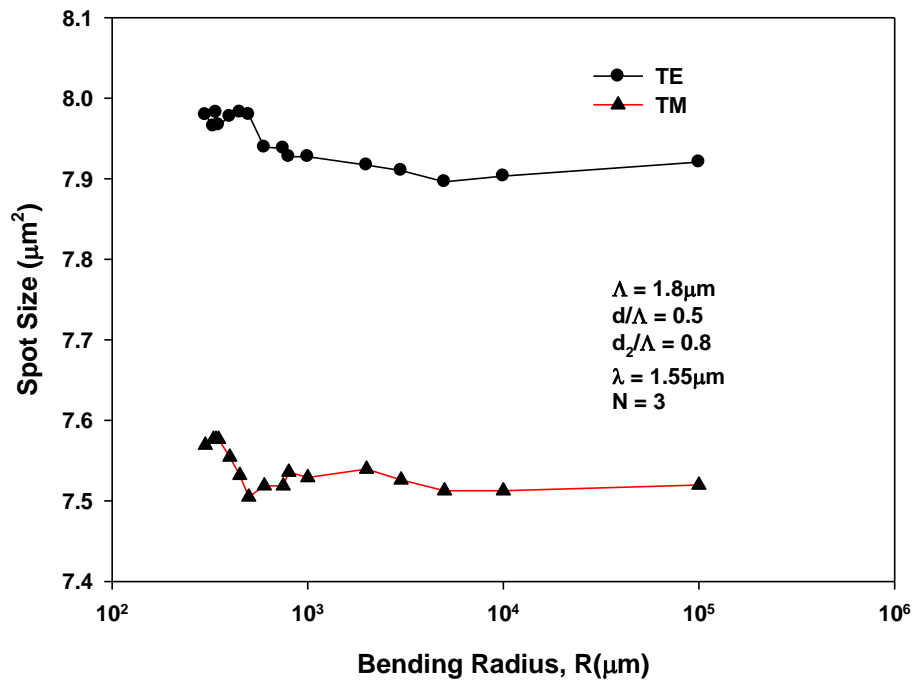


Fig. 5. 11: Variation of spot size with the bending radius, R for  $\Lambda = 1.8\mu\text{m}$ ,  $d/\Lambda = 0.5$ ,  $d_2/\Lambda = 0.8$  for both quasi-TE and quasi-TM modes.

Figure 5.11 shows the variation of the spot size with the bending radius, R. The spot size increases as bending radius is reduced but it is noted that the variation is small. This particular example, with  $\Lambda = 1.0\mu\text{m}$ , the PCF is operating close to its cut off condition. In this case as the waveguide bends, due to the change in the refractive index profile, the spot size increases when a bend is introduced. It can also be seen that the spot size is higher for the quasi-TE polarization than that of the quasi-TM polarization. Further explanations on spot size are given in Chapter 6.



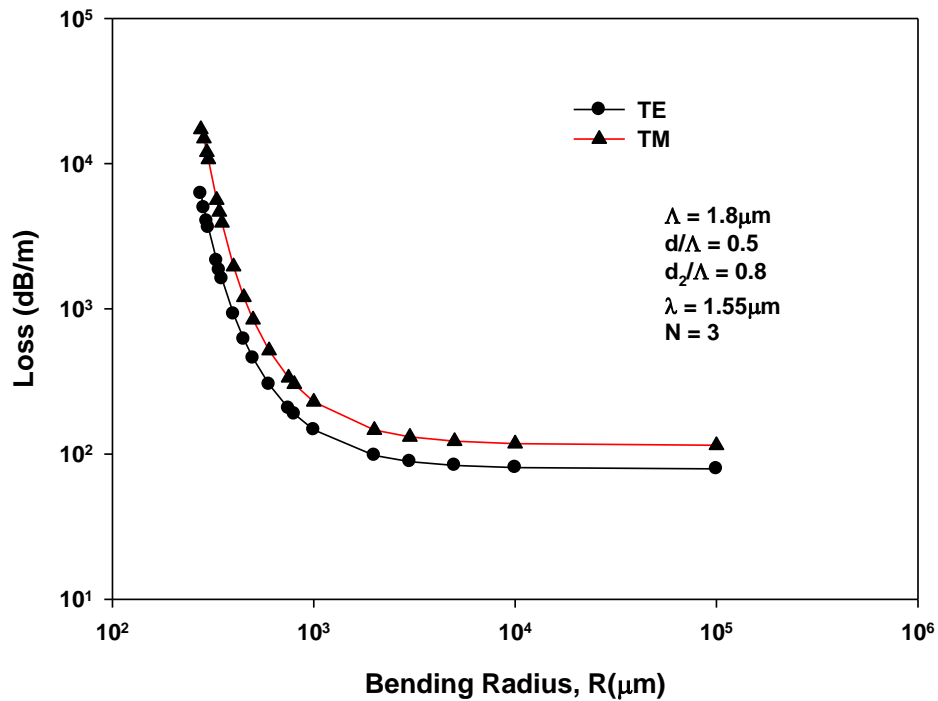


Fig. 5. 12: Variation of loss with the bending radius,  $R$  for  $\Lambda = 1.8\mu\text{m}$ ,  $d/\Lambda = 0.5$ ,  $d_2/\Lambda = 0.8$  for both quasi-TE and quasi-TM modes.

Figure 5.12 shows the variation of loss with bending radius,  $R$ . The loss increases as bending radius is reduced and there is a much sharper increase at lower values of the bending radius. Similar feature has been widely observed for bent optical fibres and bent integrated optical waveguides (Rajajaran *et al.* 2000). It can also be observed that the loss is higher for the quasi-TM polarization than that for the quasi-TE polarization. This also agrees with earlier work (Kejalakshmy *et al.* 2008a) that when  $d_2 > d$ , the quasi-TM mode approaches its cut off condition earlier than the quasi-TE mode and expected to suffer from higher losses. It was shown earlier in Chapter 4 that when  $d = d_2$  the curves for both the quasi-TE and quasi-TM modes were identical.

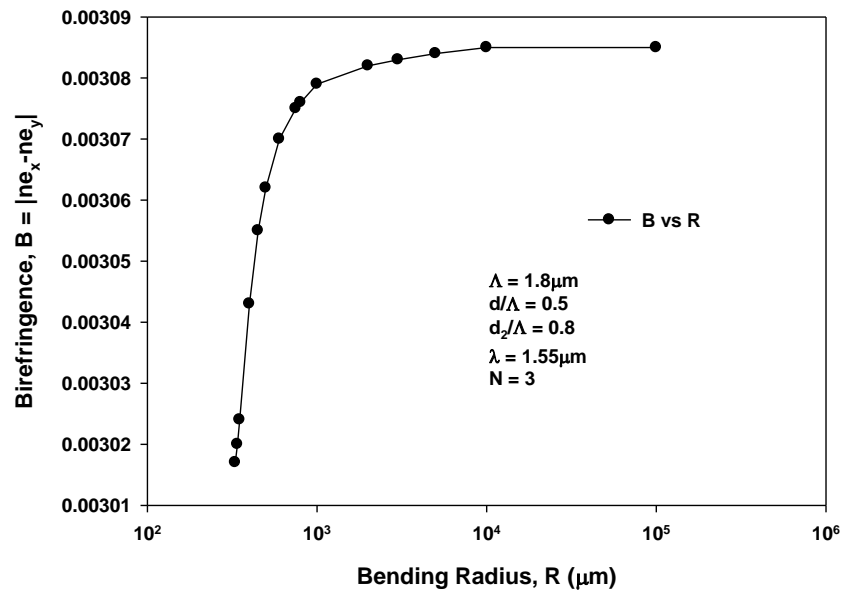


Fig. 5. 13: Variation of birefringence with bending radius,  $R$  for  $\Lambda = 1.8\mu\text{m}$ ,  $d/\Lambda = 0.5$ ,  $d_2/\Lambda = 0.8$ .

Figure 5.13 shows the birefringence with bending radius,  $R$ . It can be observed that birefringence reduces only slightly with the reduction in the bending radius,  $R$  and it tends to level out at higher values of bending radius. The birefringence value for straight PCF ( $R = \infty$ ) agrees well with earlier results (Kejalakshmy *et al.* 2008b).

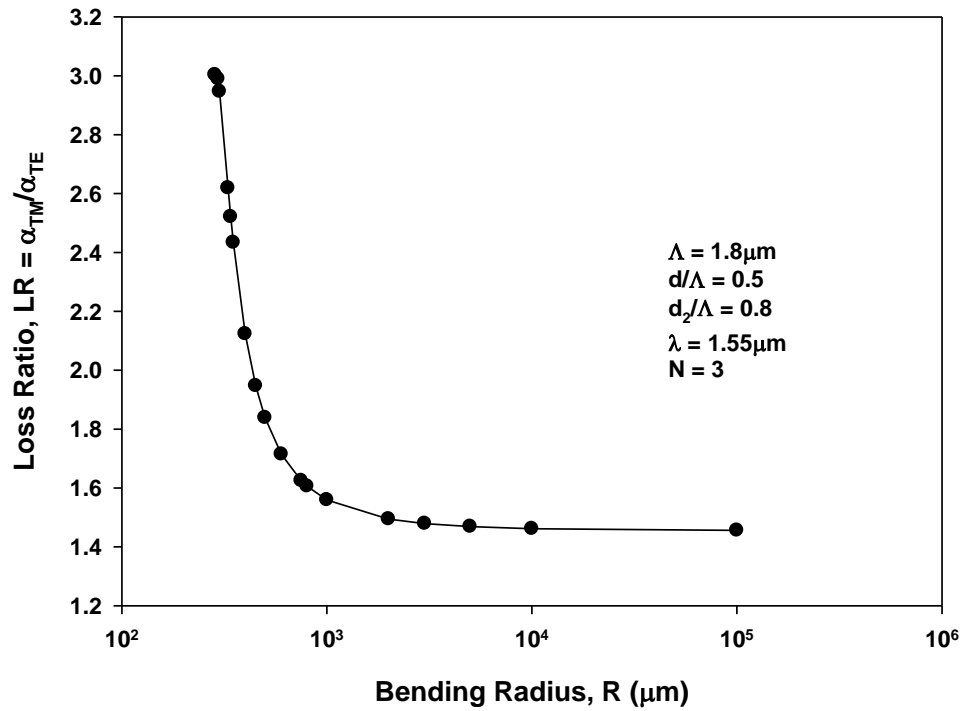


Fig. 5. 14: Variation of loss ratio with bending radius, R for  $\Lambda = 1.8\mu\text{m}$ ,  $d/\Lambda = 0.5$ ,  $d_2/\Lambda = 0.8$ .

Figure 5.14 shows the variation of loss ratio with the bending radius, R. In this case the loss ratio is defined as the ratio of loss in quasi-TM mode to that of loss in quasi-TE mode,  $LR = \alpha_{TM}/\alpha_{TE}$ . The loss ratio increases as bending radius is reduced and there is a much sharper increase at lower values of bending radius. It should be noted the bending of a PCF can be exploited to enhance the loss ratio, particularly in the design of a single polarization PCF. It can be observed that the loss ratio increased from about 1.4 to 3.0 at lower values of bending radius. This shows that loss ratio can be increased substantially by bending an asymmetric PCF.

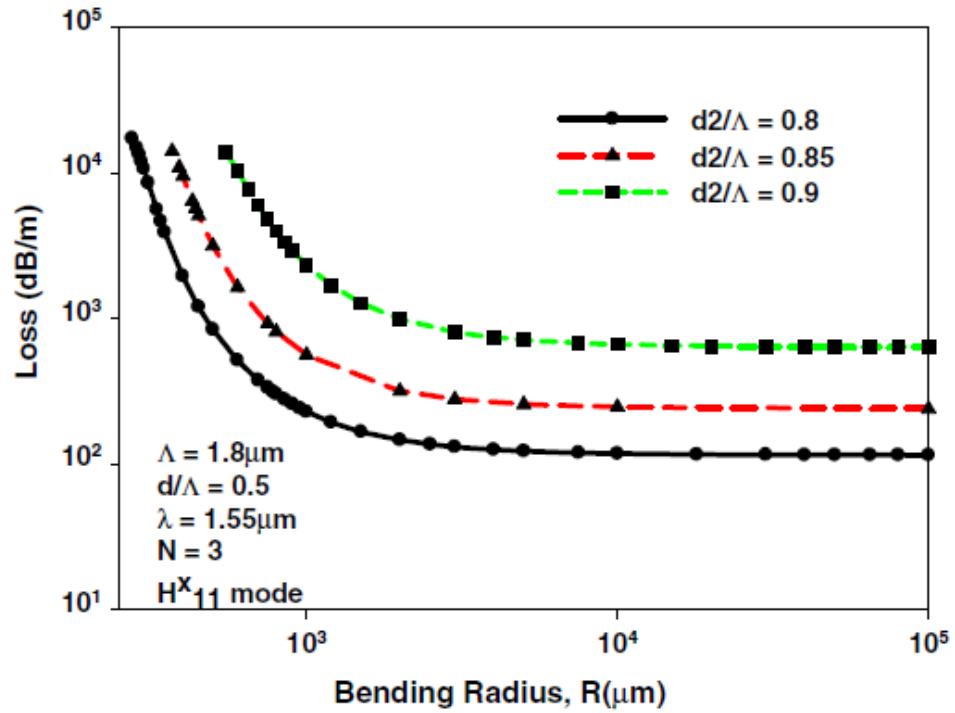


Fig. 5. 15: Variation of the bending losses with the bending radius,  $R$ , of the TM modes for different  $d_2/\Lambda$  ratios.

Figure 5.15 shows the graph of the bending loss against the bending radius for the  $H_{11}^x$  mode as  $d_2/\Lambda$  is varied. It is observed that as the bending radius is increased the loss increases and also, as the  $d_2/\Lambda$  increases, this results in increase in loss as well. As it has been mentioned, an increase in  $d_2/\Lambda$  not only increases the asymmetry, but also brings the modes close to their cut off conditions.

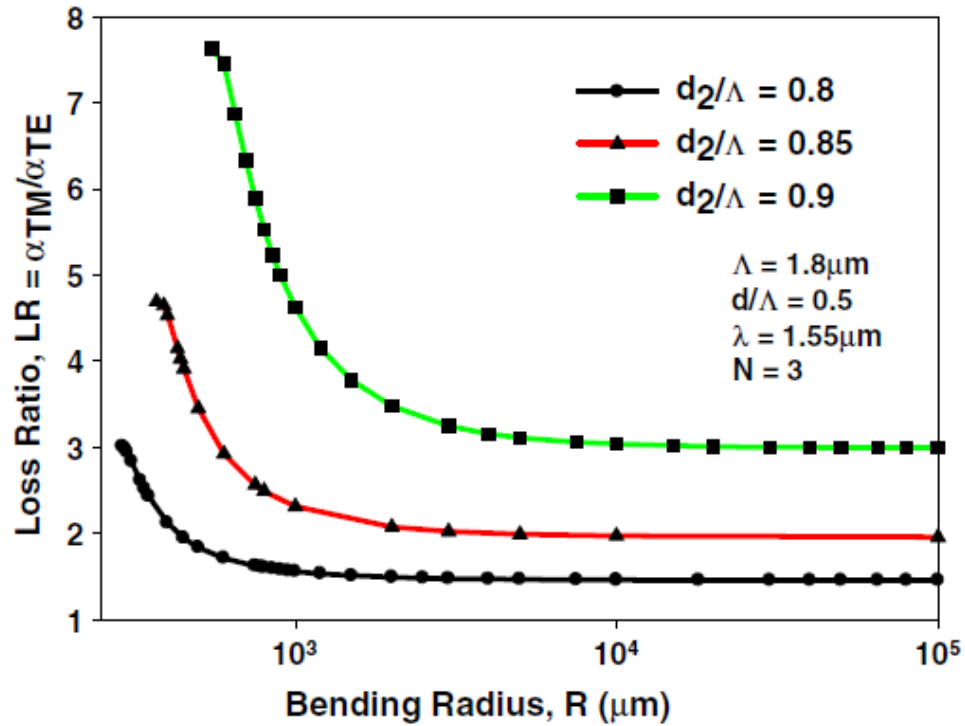


Fig. 5. 16: Variation of loss ratio with bending radius,  $R$  for  $\Lambda = 1.8\mu m$ ,  $d/\Lambda = 0.5$ ,  $d_2/\Lambda = 0.8$ , 0.85 and 0.9.

Figure 5.16 shows the variation of loss ratio,  $LR$ , with the bending radius,  $R$ , for values of  $d_2/\Lambda = 0.8$ , 0.85 and 0.9. The loss ratio increases as bending radius is reduced and there is a much sharper increase at lower values of bending radius for all values of  $d_2/\Lambda$  considered, here it can be clearly observed that loss ratio is higher for  $d_2/\Lambda = 0.9$  than for  $d_2/\Lambda = 0.85$  which is as well higher than in the case of  $d_2/\Lambda = 0.8$  as the asymmetry was increased. It can also be seen that the loss ratio increases significantly in all three cases for high bending radius than at low bending radius. It can be noted that the higher the value of  $d_2/\Lambda$ , the peak for loss ratio is attained at a slightly higher bending radius value. The peak loss value is higher for the higher values of  $d_2/\Lambda$ .

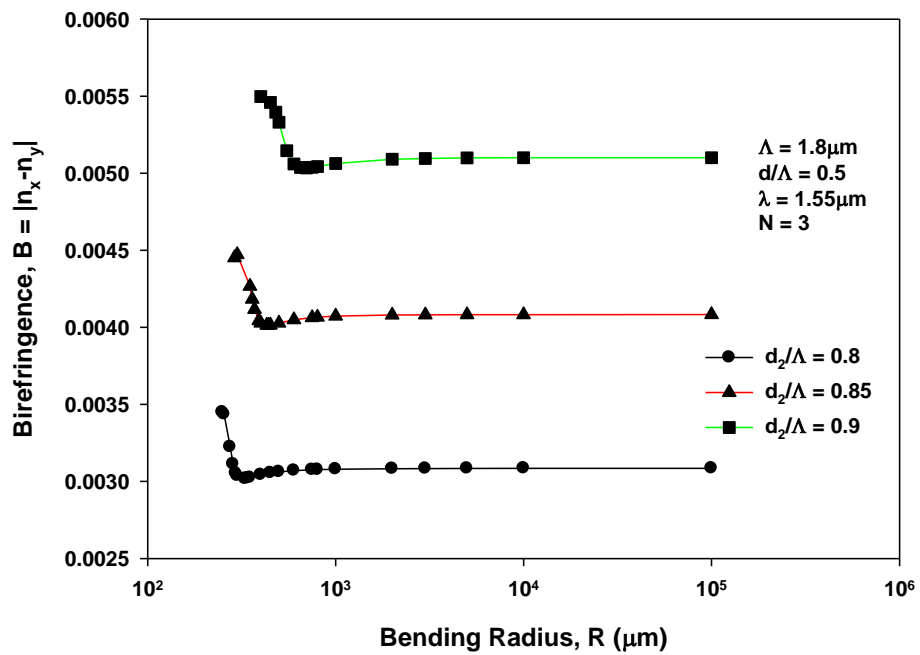


Fig. 5. 17: Variation of birefringence with bending radius,  $R$  for  $\Lambda = 1.8\mu\text{m}$ ,  $d/\Lambda = 0.5$ ,  $d_2/\Lambda = 0.8, 0.85$  and  $0.9$ .

Figure 5.17 shows the variation of birefringence with bending radius,  $R$ , for values of  $d_2/\Lambda = 0.8, 0.85$  and  $0.9$ . The curves for birefringence are fairly straight at higher values of bending radius for all values of  $d_2/\Lambda$  considered. As the bending radius is reduced, initially  $B$  reduced slightly and very close to cutoff, it increases slightly. However, as expected birefringence values are higher for higher structural asymmetry with larger  $d_2/\Lambda$  values.

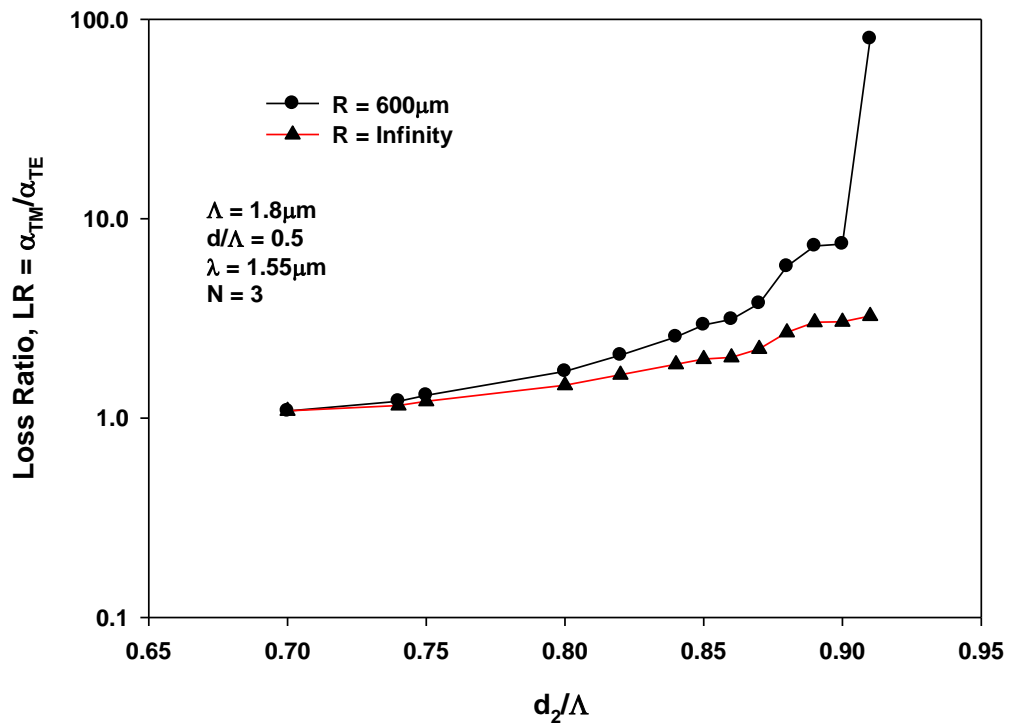


Fig. 5. 18: Variation of loss ratio with  $d_2/\Lambda$ ,  $\Lambda = 1.8\mu m$  for  $R = \infty$  and  $600\mu m$ .

Modal birefringence and loss ratio increases as asymmetry of the PCF is increased and this is studied next. Figure 5.18 shows the variation of loss ratio with  $d_2/\Lambda$  and  $\Lambda = 1.8\mu m$  for a straight PCF and a case with  $R = 600\mu m$ . The loss ratio increases as the value of  $d_2/\Lambda$  is increased for a straight PCF. However, it is very interesting to observe that the loss ratio increases further when PCF is bent for the same  $d_2/\Lambda$ . This suggests that bending can be introduced to enhance the loss ratio of an asymmetric highly birefringent PCF. This can be used in the design of a better single polarization PCF.

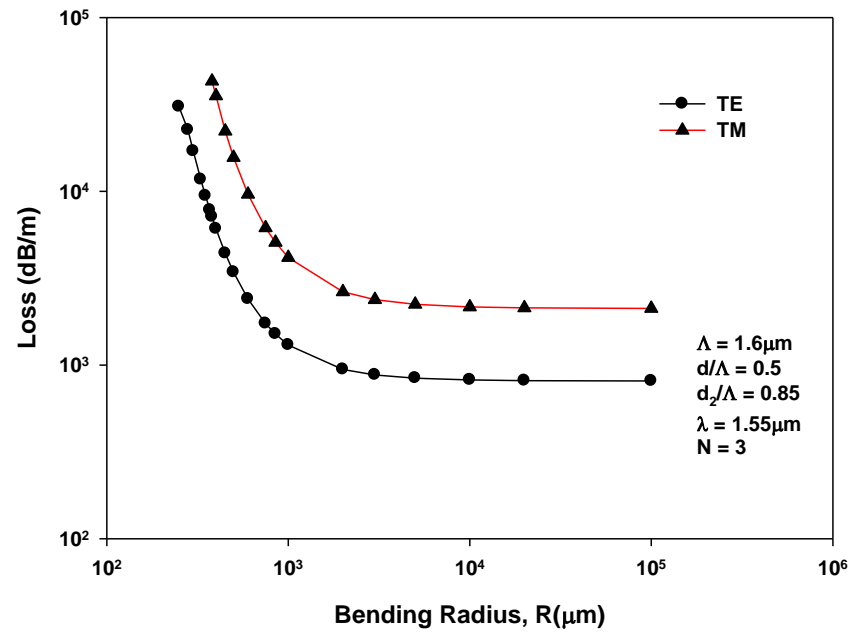


Fig. 5. 19: Variation of loss with bending radius,  $R$  for  $\Lambda = 1.6\mu\text{m}$ ,  $d/\Lambda = 0.5$ ,  $d_2/\Lambda = 0.85$  for both quasi-TE and quasi-TM modes.

In Fig. 5.7, it was shown that for asymmetric but straight PCF, loss ratio increases as pitch was reduced. Next, loss ratio of a bent PCF with a lower pitch is studied. Figure 5.19 shows the variation of loss with bending radius,  $R$  for a smaller pitch length,  $\Lambda = 1.6\mu\text{m}$ . The loss increases as bending radius is reduced and there is a much sharper increase at lower values of bending radius. It can also be seen the loss is higher for quasi-TM than for quasi-TE polarization.



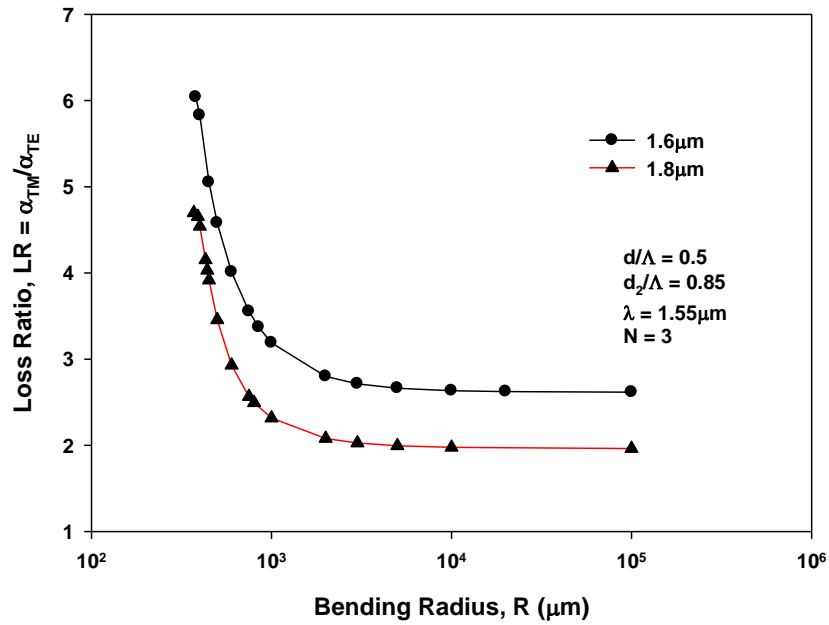


Fig. 5. 20: Variation of loss ratio with bending radius, R for  $\Lambda = 1.6\mu\text{m}$  and  $\Lambda = 1.8\mu\text{m}$ ,  $d/\Lambda = 0.5$ ,  $d_2/\Lambda = 0.85$ .

Figure 5.20 shows the variation of loss ratio, LR, with the bending radius, R. The loss ratio increases as bending radius is reduced and there is a much sharper increase at lower values of bending radius for both  $\Lambda = 1.6\mu\text{m}$  and  $\Lambda = 1.8\mu\text{m}$ . The loss ratio for a small pitch,  $\Lambda = 1.6\mu\text{m}$  reached its peak earlier and it is greater than that for  $\Lambda = 1.8\mu\text{m}$ . As was observed earlier, the loss for quasi-TM mode and that of quasi-TE mode are higher for  $\Lambda = 1.6\mu\text{m}$  than that of  $\Lambda = 1.8\mu\text{m}$  thus, resulting in higher LR for  $\Lambda = 1.6\mu\text{m}$  than that of  $\Lambda = 1.8\mu\text{m}$ .

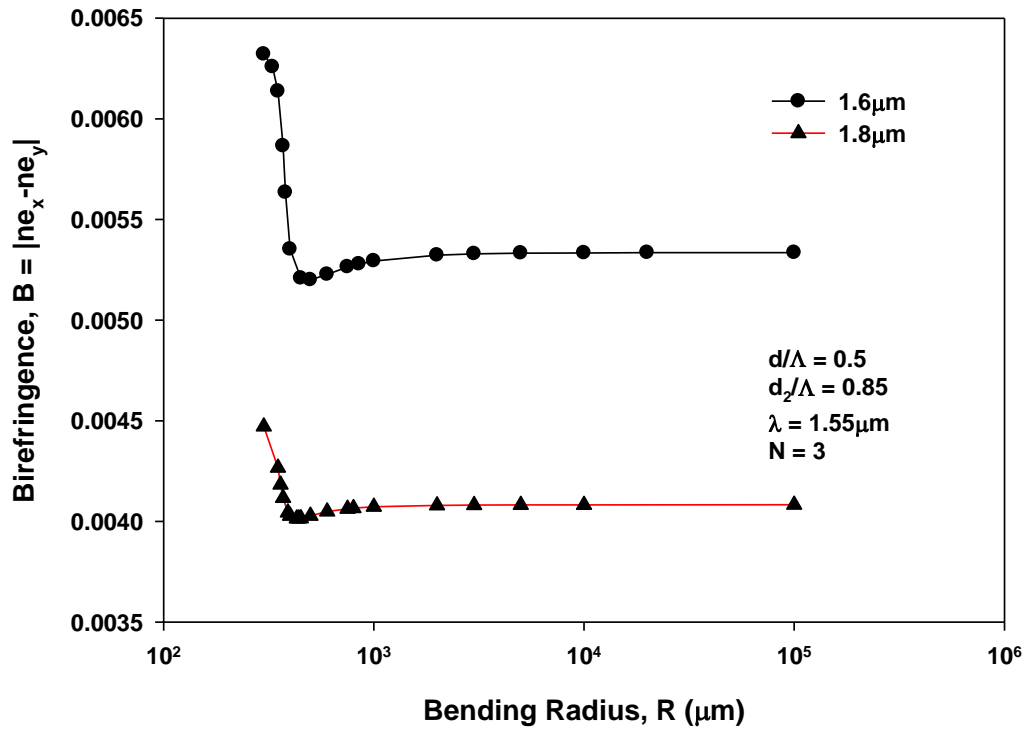


Fig. 5. 21: Variation of birefringence with bending radius, R for  $\Lambda = 1.6\mu\text{m}$  and  $\Lambda = 1.8\mu\text{m}$  with  $d/\Lambda = 0.5$ ,  $d_2/\Lambda = 0.85$ .

Figure 5.21 shows the variation of birefringence with bending radius, R. The curves for birefringence are fairly straight at higher values of bending radius for both  $\Lambda = 1.6\mu\text{m}$  and  $\Lambda = 1.8\mu\text{m}$ . It can be seen that the birefringence for  $\Lambda = 1.6\mu\text{m}$  is higher than that for  $\Lambda = 1.8\mu\text{m}$  when  $d/\Lambda$  and  $d_2/\Lambda$  were kept constant at 0.5 and 0.85 respectively. It was observed previously that effective index was higher for  $\Lambda = 1.8\mu\text{m}$  in both the quasi-TM and quasi-TE polarizations because of the lower air fraction than in the case of  $\Lambda = 1.6\mu\text{m}$ . This results in higher B for  $\Lambda = 1.6\mu\text{m}$  than for  $\Lambda = 1.8\mu\text{m}$ .

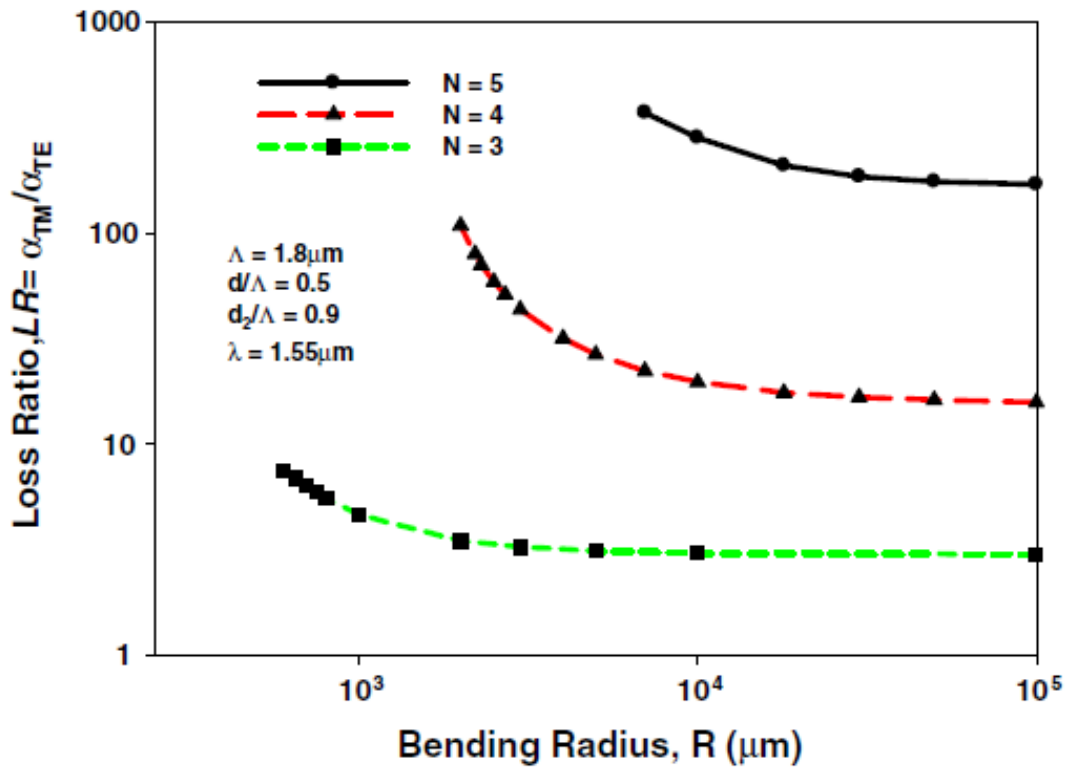


Fig. 5. 22: Variation of the LR with the bending radius for different N values.

In Fig. 5.22 the variations of the loss ratio, LR, with bending radius are presented as the number of rings, N, is varied. So, this suggests that LR can be enhanced by operating a bent PCF near their cutoff but with higher number of air-hole rings.

It is necessary to evaluate the range of  $d_2/\Lambda$  for which a given PCF will have SMSP operation, with a lower TE modal loss. This analysis can be carried out by evaluating the length of PCF that is necessary to offer a larger loss to the quasi-TM mode than that of the quasi-TE mode (say, by an amount of 20 dB—or any other ratio can be defined). This length (in cm) of PCF,  $L_{20}$  dB, to achieve 20 dB differential loss can be defined as:

$$L_{20}dB = \frac{20dB}{\alpha_{TM} - \alpha_{TE}} \quad (5.2)$$

where  $\alpha_{TE}$  and  $\alpha_{TM}$  are loss values for the fundamental quasi-TE and quasi-TM modes given in decibels per centimetre. Figure 5.23 shows the variation of a PCF with a length of  $L_{20}$  dB (in centimetres) with respect to R for different  $d_2/\Lambda$  values. It can be seen that the length of the PCF section that is necessary can be of the order of a fraction of a

metre and with higher pitch ratio when the quasi-TM modes can be suppressed effectively. However, a PCF for a specific application should be determined based on the combined factor of the  $L_{20\text{dB}}$  and the total TE modal loss. From Fig. 5.23, it can be seen that the value of the length,  $L_{20\text{dB}}$ , can be varied over a wide range by varying the number of rings and bending radius. As an example, when  $N = 5$  and  $R$  is 0.5 cm, the required PCF length to achieve the 20 dB differential loss is only 0.2cm.

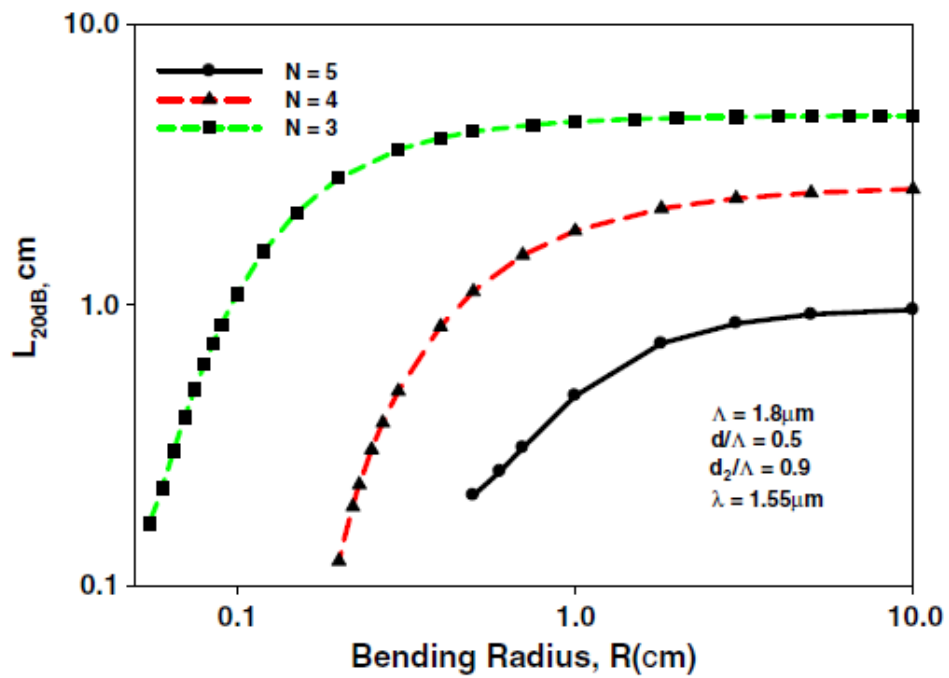


Fig. 5. 23: Variation of  $L_{20\text{dB}}$  length with the bending radius for different  $N$  values.

However, when the bending radius is increased to 1.0 cm, which would be easier, depending on the stiffness of the PCF, the length required would be increased to 0.4 cm, which would also be easier to handle. For these designs, the length and corresponding total TE loss values are shown in Fig. 5.24 to achieve a 20 dB differential loss. It can be observed that total TE loss values could be less than 1 dB and the length of the PCF section could be below 5 cm. For the examples given earlier, with  $N = 5$  and  $R = 1$  cm, the required length was 0.4 cm and its corresponding total TE loss is only 0.07 dB. The length may be too short to handle it conveniently, but it should be noted that, if the length is increased by 10 times to 4 cm, which would allow it to be more easily handled, in this case the total TE loss would increase to 0.7 dB. This is still a low value and the differential loss would be 200 dB, a significantly improved value. Similarly, for  $N = 5$

and  $R = 0.5$  cm, if the length is increased to 2 cm, the differential loss would be 200 dB with the total TE loss only 0.5 dB. These TE loss values for a 200 dB differential loss are shown separately by a chained line with stars. Similarly other fabrication parameters, such as the pitch length, the air-hole-to-pitch ratio,  $d/\Lambda$  and the asymmetry (via the  $d_2$  value) can be adjusted to obtain a suitable design for a specific application.

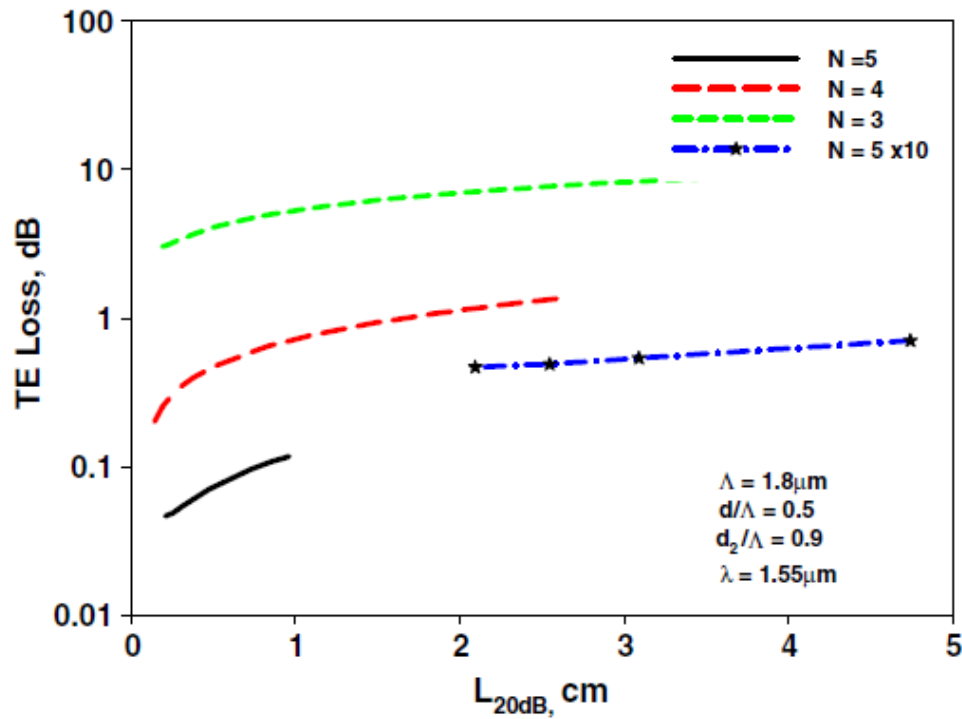


Fig. 5. 24: Variation of  $L_{20dB}$  length with respect to the TE loss for different  $N$  values.

The bending loss depends not only on the polarization states, as shown above, but also on the air-hole orientation and the bending plane. When the hole orientation is rotated by  $90^\circ$  (and the bending plane remains the same) as shown in Fig. 5.4, modal properties and the bending loss value change. Variation of the bending loss with the bending radius for both polarization states and for both hole orientations are shown in Fig. 5.25. It should be noted that, in the original hole orientation (Rahman *et al.* 2006; Kejalakshmy *et al.* 2008b), the effective height of the waveguide is smaller than its effective width. The resulting waveguide asymmetry gives the modal birefringence and the differential LR. For this particular orientation, the effective index of the  $H_{11}^x$  mode is lower and its bending loss is higher compared to the  $H_{11}^y$  mode as shown for the holes orientation in Fig. 5.3. On the other hand, when the orientation of the larger four air-

holes is rotated by  $90^\circ$  as shown in Fig. 5.4, its effective height becomes smaller than its effective width. It can be observed that the bending loss of the  $H_{11}^y$  mode in the original orientation (Fig. 5.3) is similar to the bending loss of the  $H_{11}^x$  mode in the rotated structure (Fig. 5.4) and vice versa. However, this nearly reverses the modal properties, as the  $H_{11}^x$  mode of the original orientation behaves similar to the  $H_{11}^y$  mode in the rotated structure. However, as in the bent PCF, due to the lack of symmetry along the vertical axis, the bending losses for the  $H_{11}^x$  and  $H_{11}^y$  modes are slightly different, which is clearly shown in Fig. 5.25.

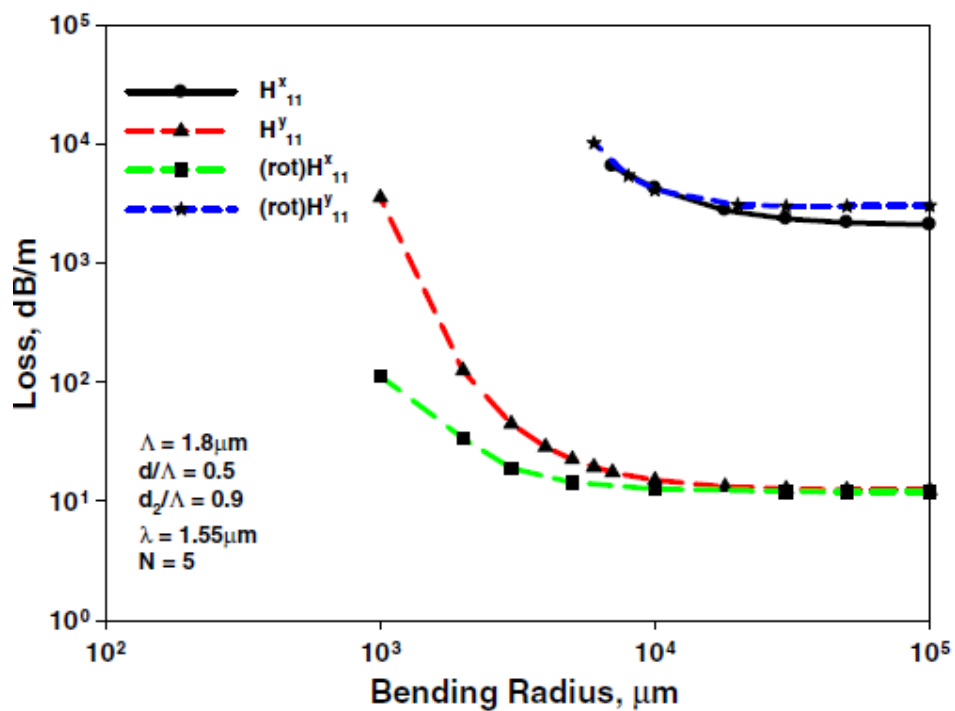


Fig. 5. 25: Variation of the loss with the bending radius for two different asymmetric orientations.

Modal confinement and bending loss also depend on the operating wavelength. Variation of the bending loss for the quasi-TE ( $H_{11}^y$ ) and quasi-TM ( $H_{11}^x$ ) modes with the wavelength for both the original orientation and  $90^\circ$  rotated structures are shown in Fig. 5.26. In this case, the structural parameters are taken as  $\Lambda = 1.8 \mu\text{m}$ ,  $d/\Lambda = 0.5$ ,  $d_2/\Lambda = 0.9$ ,  $N = 5$  and  $R = 1 \text{ cm}$ . It can be observed that, as the operating wavelength is increased, the bending loss is increased as its modal confinement also reduces and the modal field spreads more into the cladding area. It has already been mentioned that,

when the structural asymmetry is rotated by  $90^\circ$ , quasi-TE modes would be comparable to quasi-TM modes of the rotated structure and vice versa.

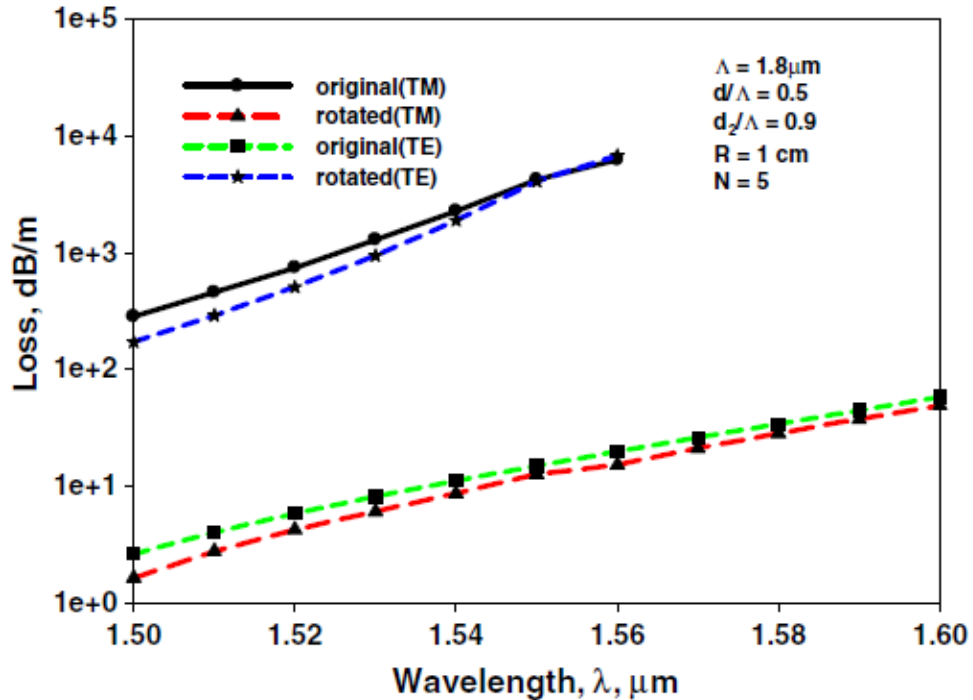


Fig. 5. 26: Variation of loss with the operating wavelength for two different asymmetry orientations.

## 5.6 Summary

In this chapter, the design of a SMSP PCF has been reported in which for the first time (Rahman *et al.* 2011), it has been shown that, by bending an asymmetric PCF, it can be observed that the differential loss polarization dependent loss can be significantly increased. The design approach was developed by exploiting the differential bending loss and then analyzed through the use of a rigorous full-vectorial FEM. Initially, the bending of the PCF has been assumed to be in the X–Y plane. It has been shown that, for this asymmetry arrangement chosen here, the TM modal loss is higher than that of the TE mode. However, the differential LR increases with any excessive bending beyond a critical value of the bending radius. Such a critical bending radius can be tuned with a suitable adjustment of the value of  $d_2/\Lambda$ . The LR increases with the number of air-hole rings,  $N$ , in the PCF cladding. These results can be used to assist in designing the single polarization condition in a bent PCF. The PCFs designs analysed are all

single-mode guides when operated closer to their cutoff conditions. Furthermore, the effects of structural asymmetry have also been carried out to evaluate the effect on the SMSP of a PCF due to bending for different air-hole orientations. Variations of the bending loss for the quasi-TE and quasi-TM modes with the different operating wavelengths are also presented. Such a PCF, which only guides one polarization state, can be used for various linear, nonlinear, and sensing applications. It is also shown here that the bending losses of  $H_{11}^x$  and  $H_{11}^y$  depend on the pitch,  $\Lambda$ , the asymmetry via the value of  $d_2/\Lambda$ , the number of rings,  $N$ , the operating wavelength and the bending radius and so, the differential loss will depend on the fabrication tolerances relating to the parameters  $\Lambda$ ,  $d$ , and  $d_2$ . However, since the differential loss also depends on the bending radius, it is expected that, by adjusting the bending radius, the effect of the fabrication tolerances may also be compensated for a wide range of applications, such as attenuators or polarization maintaining applications. In the next Chapter, the butt coupling of a PCF to a single mode fibre is analysed.



## CHAPTER SIX: Mode Coupling

### 6.0 Abstract

The butt coupling between a tapered PCF and a conventional optical fibre is presented. When a PCF is tapered, the mode field area expands into the cladding region which helps with the reduction of mismatch between the mode field area of the PCF and that of the conventional optical fibre. The Least Squares Boundary Residual (LSBR) method in conjunction with the Finite Element Method (FEM) was employed for these analyses.

### 6.1 Introduction

Photonic Crystal Fibres (PCF) (Russell 2003; Russell 2006) can be used as potential waveguides and devices which may exploit their characteristics of being single moded, having higher modal birefringence and offering adjustable spot size and dispersion properties which may be tailored for various linear and nonlinear applications. Initially PCF was considered to be an endlessly single mode fibre, but later numerical studies such as using the multipole method and the finite element method, have revealed that the cutoff conditions are critically controlled by the diameter to pitch ratio (Kuhlmey *et al.* 2002; Mortensen 2002; Kejalakshmy *et al.* 2008b). However, a wider single mode operating range can still be useful for many applications. Their Mode Field Areas (MFA) are also controllable and thus able to achieve both large and small spot sizes. PCF with large spot size or even hollow core PCF are suitable for high power delivery. On the other hand, as an example, PCFs with smaller MFAs can be envisaged by enhancing their power density and tailoring their dispersion properties for various nonlinear applications, such as supercontinuum generation. Such a PCF with small core can also allow easy access to the evanescent fields for the design of optical sensors. However, practical difficulties related to achieving efficient coupling of a PCF with a smaller MFA to the input/output sections have often been considered as creating a serious drawback in the exploitation of the PCF technology. Unlike fusion splicing in conventional Single Mode Fibre (SMF), joining a PCF is difficult as the integrity of the air-holes is difficult to preserve, even though several recent efforts in fusion splicing of a PCF to a SMF have been reported (Bennett *et al.* 1999; Chong and Rao 2003; Wang *et*

*al.* 2008). However, to obtain a low-loss coupling is particularly challenging due to the large mismatch between the MFA of a PCF and that of a SMF. A short gradient index fibre lens has also been considered (Yablon and Bise 2005) by incorporating this component between the two coupling sections with different MFAs. Use of a fused biconical taper, often used for a passive fibre coupler, has also been envisaged by placing a PCF and a pre-tapered SMF side by side and twisting and tapering them for efficient evanescent coupling (Liu *et al.* 2009). A PCF can also be tapered adiabatically to adjust its MFA (Nguyen *et al.* 2005a; Nguyen *et al.* 2005b). As example, if the up-tapered part has a larger width near the end, its MFA increases and the coupling loss to a SMF can be relatively low, as reported in the literature (Chandalia *et al.* 2001; Town and Lizier 2001). However, these terminal sections with a large core dimension are likely to be multimoded which could also restrict the flexibility of the PCF applications. On the other hand, if the dimensions of a tapered PCF are adiabatically reduced, when the core mode approaches cutoff, the MFA would also increase. Such reduction in size is possible, as PCFs have been routinely tapered to control their dispersion properties with their pitch reduced from 3.0  $\mu\text{m}$  to 500 nm (Leon-Saval *et al.* 2004) and even below 300 nm (Magi *et al.* 2004).

When a PCF is operating near the cutoff condition, as the pitch is reduced, this leads to the expansion of the mode field into the cladding region with air-holes (Rahman *et al.* 2006). This could expand the MFA to a size similar to that of a SMF which would make coupling between them easier. For this purpose, a PCF section can be tapered to bring it close to the cutoff condition. However, as it expands very rapidly when approaching cutoff, it may be difficult to control as any small fabrication errors can make the MFA unstable when it expands exponentially. A similar problem exists in coupling a laser beam with a small asymmetric shape to a SMF with a larger circular beam profile. In that context, monolithically integrated spot size converters (SSC) have been reported (Rajarajan *et al.* 1998; Wongcharoen *et al.* 2001), designed to transform the spot size of the output laser beam to allow for efficient coupling. To control the MFA with its fabrication tolerances, for the first time it has been suggested in this work, that a secondary guide can be considered. This approach is evaluated by using a rigorous full-vectorial finite element method and the Least Squares Boundary Residual (LSBR) method. It is also shown here that the MFA can be stabilized; this is to take account for

the possible changes that may occur during the manufacturing processes of a tapered PCF. Coupling between waveguide sections with different spot sizes have been a consistent problem, such as for photonic crystals (Barclay *et al.* 2004), plasmonic waveguides (Lu *et al.* 2011; Zhao *et al.* 2011) and also for efficient light extraction (Weirer *et al.* 2009; Li *et al.* 2011), where the approach presented here, the use of tapered guided wave section, can be considered.

## 6.2 Mode Field Study of a Single Mode Fibre

In this section, the MFA is studied in some detail; however it is important to note that there have been various alternative definitions to represent this particular parameter. The MFA can be represented by the spot size,  $\sigma$ , the effective area,  $A_{\text{eff}}$  and the Area second moment of intensity,  $A_{\text{SMI}}$ . The spot size is usually defined as the area where the field intensity falls to  $1/e$  of its maximum value (or where power intensity is  $1/e^2$ ) (Rajarajan *et al.* 1998; Wongcharoen *et al.* 2001).

On the other hand, the effective area, is defined as:

$$A_{\text{eff}} = \left( \int |E|^2 dA \right)^2 / \int |E|^4 dA \quad (6.1)$$

where,  $E$  is electric field profile (Technology 2008).

Similarly, another similar alternative is the area second moment of the optical intensity, given as:

$$A_{\text{SMI}} = 2 \sqrt{\int x^2 I(x, y) dx dy / \int I(x, y) dx dy} \quad (6.2)$$

where  $I(x, y)$  is second moment of intensity distribution profile (Technology 2008).

Mode field profile of a PCF is complex due to the presence of many air-holes. So, to test these alternative definitions of MFA, a simple waveguide is considered. Initially, a simple circular fibre is considered to study its different MFAs. The refractive indices of the silica cladding and the Ge-doped core are taken as 1.445 and 1.4502 respectively at the operating wavelength of 1.55  $\mu\text{m}$ . Since, the TE and TM modes are degenerate; only the quasi-TM mode (with the dominant  $H^x$  and  $E^y$  fields) is considered in this test.

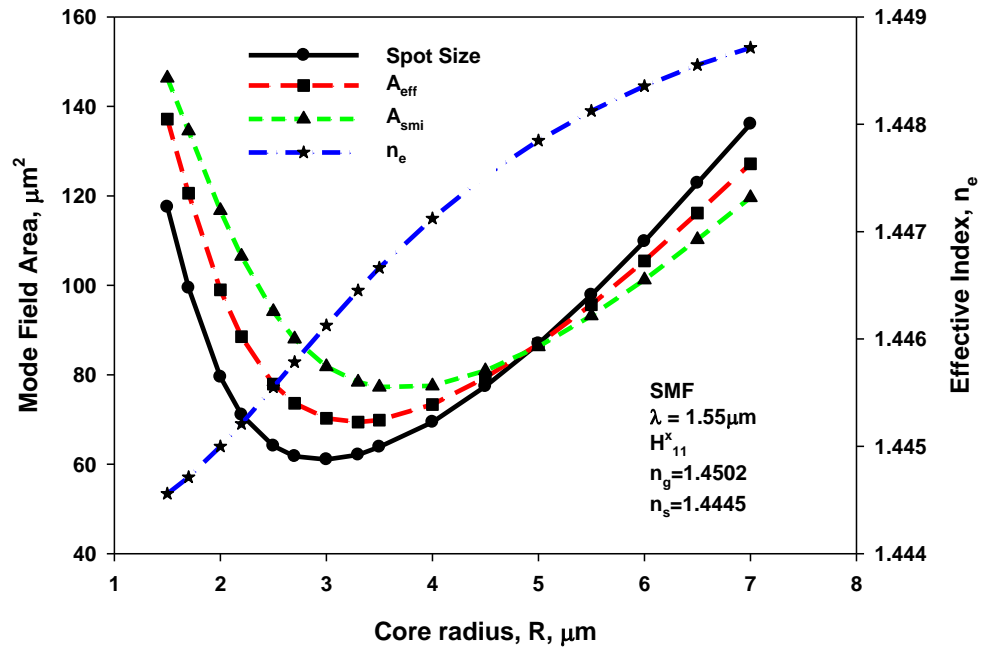


Fig. 6. 1: Variation of mode field area and effective index of a SMF against core radius,  $R$ .

Several MFA definitions were studied carefully for different core radii. Variations of the effective index and the different MFAs with the core radius for this optical fibre are shown in Fig. 6.1. It is shown that as the core radius is reduced, the effective index is monotonically reduced. As the core radius is reduced, initially the MFAs reduce as the core area is also reduced, but as cutoff region approaches, the MFAs begin to increase again. When the waveguide dimension is too small, it is unable to confine the mode inside the core and field starts expanding more into the cladding. However, the values and expansion regimes of these MFA parameters are slightly different. These mode field areas were slightly different for most of the radii values but they were identical at  $R = 5.0 \mu\text{m}$ .

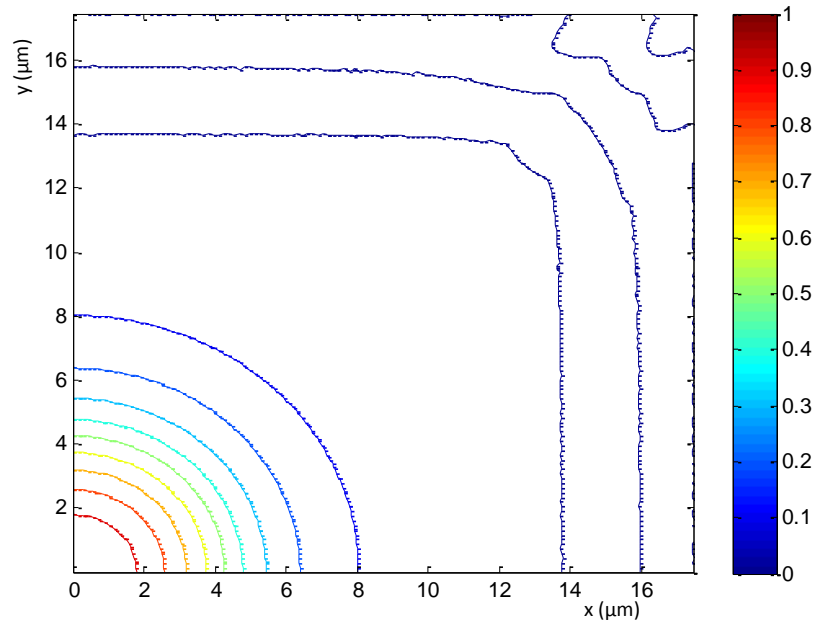


Fig. 6. 2: 2-D  $H_x$  field profile for a Single Mode Fibre exploiting 2-fold symmetry with only quarter of the structure simulated.

A SMF often has a radius of between 4.5 and 5.0  $\mu\text{m}$ . Figure 6.2 shows the 2-D field profile for a Single Mode Fibre with core radius,  $R = 4.5\mu\text{m}$ . In this case, the resulting spot size  $= 77.70\mu\text{m}^2$ ,  $A_{\text{eff}} = 80.85\mu\text{m}^2$  and  $A_{\text{SMI}} = 84.61\mu\text{m}^2$  are of similar values. The contour lines clearly show concentric field lines. To show their variation along the radial direction, its variation profile along the x-axis is shown next.

To study their differences, the modal field profiles for different radii are shown in Figs. 6.3, 6.4 and 6.5. Actual field profiles, as obtained from the mode solver are shown by solid lines. From the original field profile, first its  $1/e$  distance is calculated and then this distance is used to obtain its approximate Gaussian profile as shown by a dashed line. A closer investigation has revealed that the actual field profile (shown by a solid line) for  $R = 5.0 \mu\text{m}$  closely follows a Gaussian profile and this suggests that for a Gaussian shaped field profile, all the different MFA definitions may lead to a similar value. However, when the radius was larger than 5.0  $\mu\text{m}$ , as is seen from Fig. 6.4, it was observed that in the field decay rate in the cladding was faster than its equivalent Gaussian profile suggests. Similarly, for a radius smaller than 5.0  $\mu\text{m}$ , as is seen from Fig. 6.5, the field decays slowly in the cladding region compared to its equivalent Gaussian fitting profile. Thus an MFA defined by different approaches will likely have

different values when the mode field is not Gaussian in shape. These three figures illustrate that when radius is  $\sim 5.0 \mu\text{m}$  then its modal field profile is Gaussian in nature but the profile deviates when radii are different.

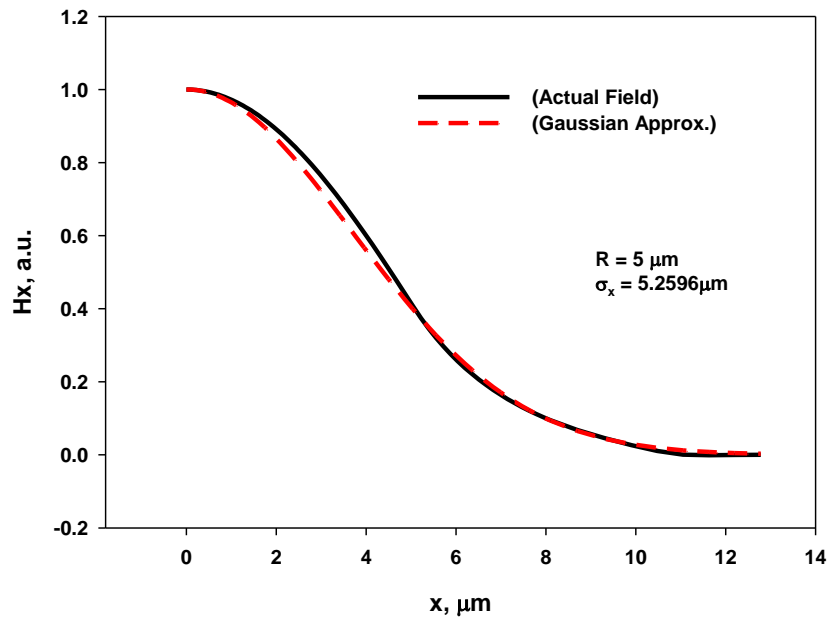


Fig. 6. 3: Comparing Gaussian field profile and the obtained profile for  $R = 5.0 \mu\text{m}$

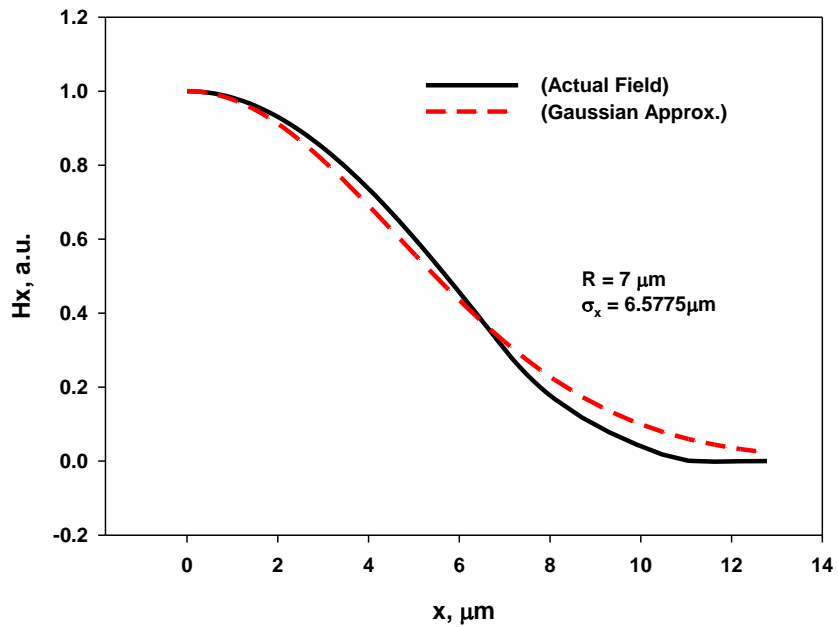


Fig. 6. 4: Comparing Gaussian field profile and the obtained profile for  $R = 7.0 \mu\text{m}$ .

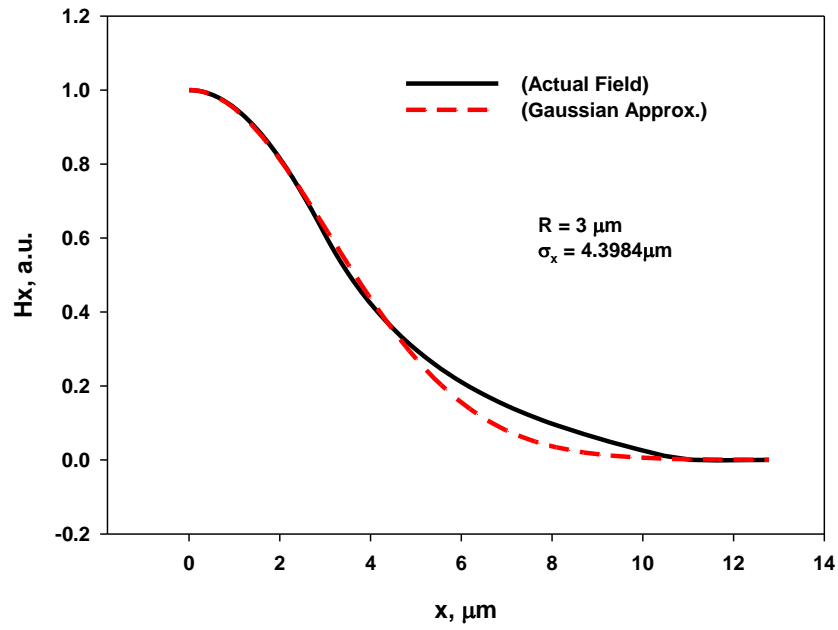


Fig. 6. 5: Comparing Gaussian field profile and the obtained profile for  $R = 3.0\mu\text{m}$

It has been shown in Fig. 6.1 that if fibre diameter is reduced, near modal cutoff spot size increases rapidly. This feature in a PCF can be used, by incorporating a taper, when reducing the pitch can increase the spot size, as operating close to cutoff.

### 6.3 Analysis of a Tapered PCF

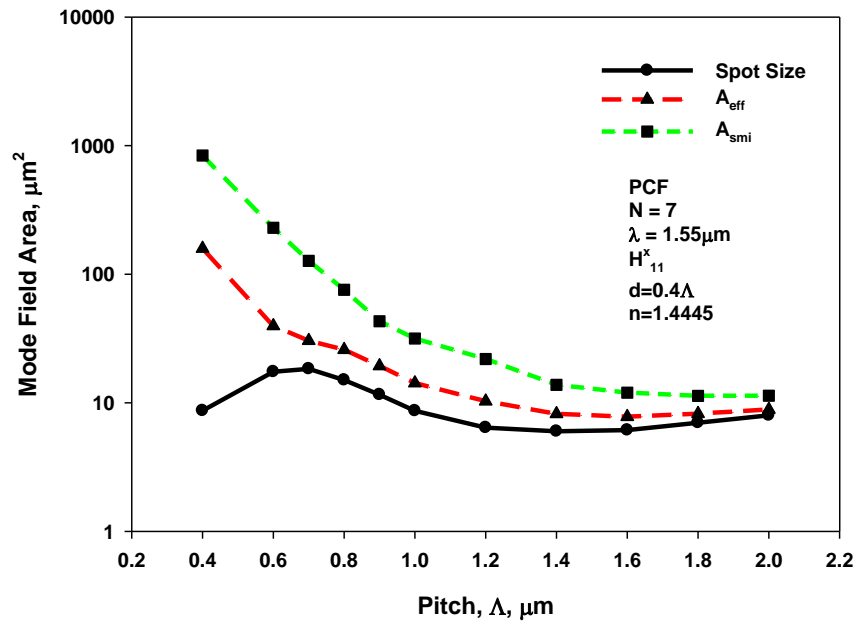


Fig. 6. 6: Variation of mode field areas of a PCF against the pitch,  $\Delta$ .

In this section, the MFA of a PCF, the main subject of this research, is thoroughly investigated. The PCF considered here has number of rings,  $N$  (in this case, initially  $N = 7$ ) and its silica refractive index is taken as 1.445 at the operating wavelength of  $1.55 \mu\text{m}$ . The pitch,  $\Lambda$ , is varied from  $2.0$  to  $0.4 \mu\text{m}$  with an air-hole diameter,  $d = 0.4\Lambda$ . Variations of the different MFA parameters with the pitch length,  $\Lambda$ , are shown in Fig. 6.6. The log scale is used for the MFA to illustrate the lower range more clearly. As the radius is reduced, the MFA initially reduces but then begins to increase again. It can be seen that all these parameters increase as the modal cutoff is approached; however, its spot size,  $\sigma$ , also shows a saturation. It should be noted that for a low-index contrast SMF, the modal field reduces monotonically in the cladding. However, due to the presence of air-holes in a PCF, the field profile does not decay monotonically outside the core region. In the definition of the spot size, only the localized field values are considered, whereas the  $A_{\text{eff}}$  and  $A_{\text{SMI}}$  use the integration of field profile and these yields more stable values. Although, these values give some indication of their MFAs and are useful to identify the size for optimum coupling, however, to calculate the coupling efficiency the rigorous LSBR approach will be used.

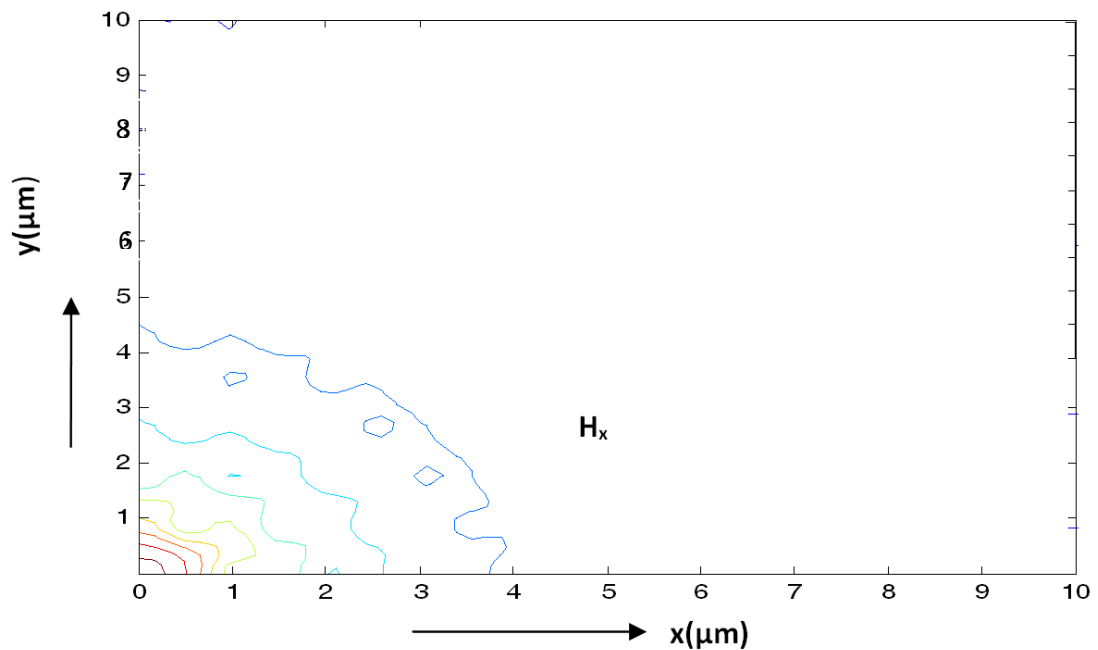


Fig. 6. 7:  $H_x$  field profile of the  $H_{11}^x$  mode for  $N = 7$ ,  $\Lambda = 1.0$ ,  $d/\Lambda = 0.4$ , and  $d_7/\Lambda = 0.8$ .



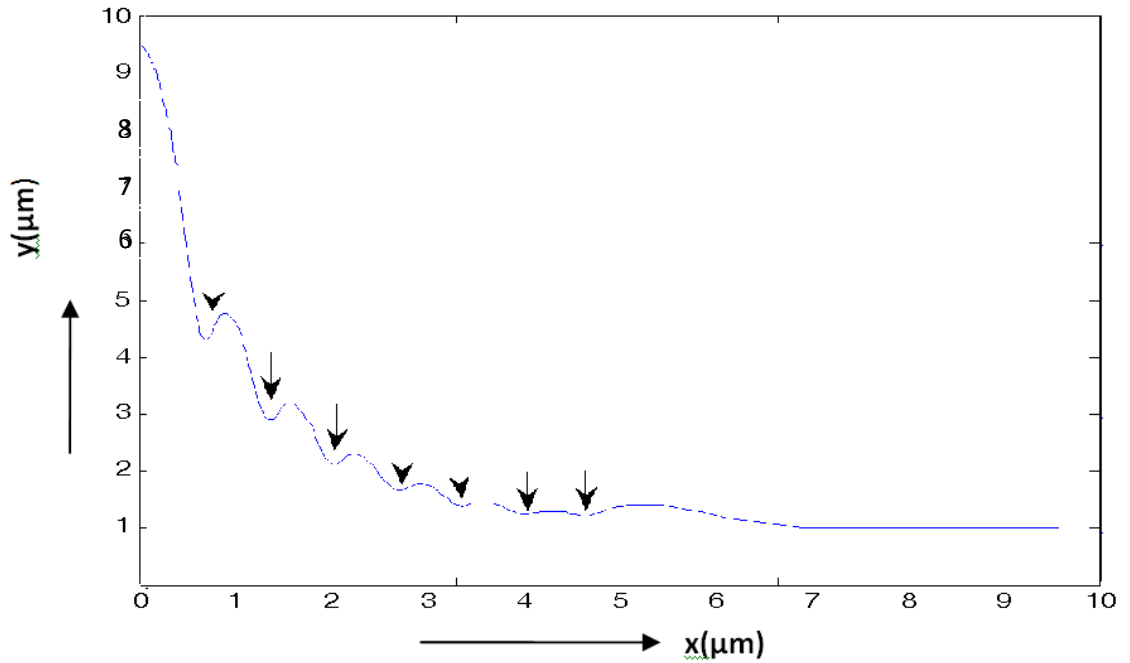


Fig. 6. 8: Variation of  $H_x$  field profile along  $x$   $N = 7$ ,  $\Lambda = 1.0$ ,  $d/\Lambda = 0.4$ , and  $d_7/\Lambda = 0.8$ .

The  $H_x$  field profile for the  $H_{11}^x$  mode is shown in Fig. 6.7 for a PCF with 7 air-hole rings, when  $\Lambda = 1.0 \mu\text{m}$  and for all the rings  $d/\Lambda = 0.4$  except for the last ring where  $d_7/\Lambda = 0.8$ . It can be observed that the field contours are not concentric circles, but show ‘cheese-like’ holes due to the presence of the air-holes. Variation of the  $H_x$  field along the  $x$ -axis is also shown in Fig. 6.8, which clearly demonstrating the field variations are not monotonic and the location field minima around the air-holes are shown by arrows. Hence, the simple spot size, which depends on the local field values, can be more unreliable when used to describe the MFA of a PCF. Subsequently to gauge the field expansion, the more stable term  $A_{\text{eff}}$  is used in this work.

In Fig. 6.9, the variations of effective areas,  $A_{\text{eff}}$ , with pitch for PCFs having  $d = 0.4\Lambda$  is compared with that of  $d = 0.5\Lambda$  with all air-holes are equal. The effective area of  $d = 0.4\Lambda$  is higher than that of  $d = 0.5\Lambda$  and as the pitch decreases, there is a sharp increase at lower values of pitch. In Fig. 6.10, PCFs having  $d = 0.5\Lambda$  for all air-holes is compared with that of  $d = 0.5\Lambda$  but with the outermost air-holes increased to  $d_5 = 0.8\Lambda$ . Variations of the effective areas with the pitch for a PCF with 5 air-hole rings are shown in Fig. 6.11. Here the effect of the field expansion for two different air-hole ratios,  $d/\Lambda$ , is shown, besides the effect of having a larger air-hole in the last ring. When all the air-holes are of identical diameter and equal to either  $0.4\Lambda$  or  $0.5\Lambda$ , the value of  $A_{\text{eff}}$

increases exponentially as  $\Lambda$  is reduced. It can be observed that for a smaller  $d/\Lambda = 0.4$ , the effective area,  $A_{\text{eff}}$  becomes higher due to the smaller size of the air-holes compared to that when  $d/\Lambda = 0.5$ . It can also be observed that as larger air-holes were introduced in the outermost ring (5<sup>th</sup> ring) as shown in Fig. 6.11, the value of the MFA is forced to remain flatter than it would have been otherwise at lower values of pitch as is seen in Fig. 6.10. In the case of  $d/\Lambda = 0.4$ , all the air-holes in the first 4 rings have their dimension,  $d = 0.4\Lambda$ , except the 5<sup>th</sup> ring which has a larger dimension, denoted by  $d_5 = 0.8\Lambda$ . This ensures that the MFA is stable at the lower pitch values without it expanding exponentially and the mode expansion slows down by the last ring, which has larger air-holes. This would allow stable coupling to occur without much error or uncertainty even if there were structural variations occurring during the fabrication or tapering. This figure also demonstrates that a PCF with smaller air-holes in most of the inner rings and larger air-holes in the last ring is expected to produce a larger  $A_{\text{eff}}$ , which is also reasonably stable with the pitch variation. There are also some random variations which occur due to mode degeneration with the cladding modes as shown in Chapter 4. There are similarities between these variations observed in Fig. 6.11 to those already shown in Figs. 6.9 and 6.10.

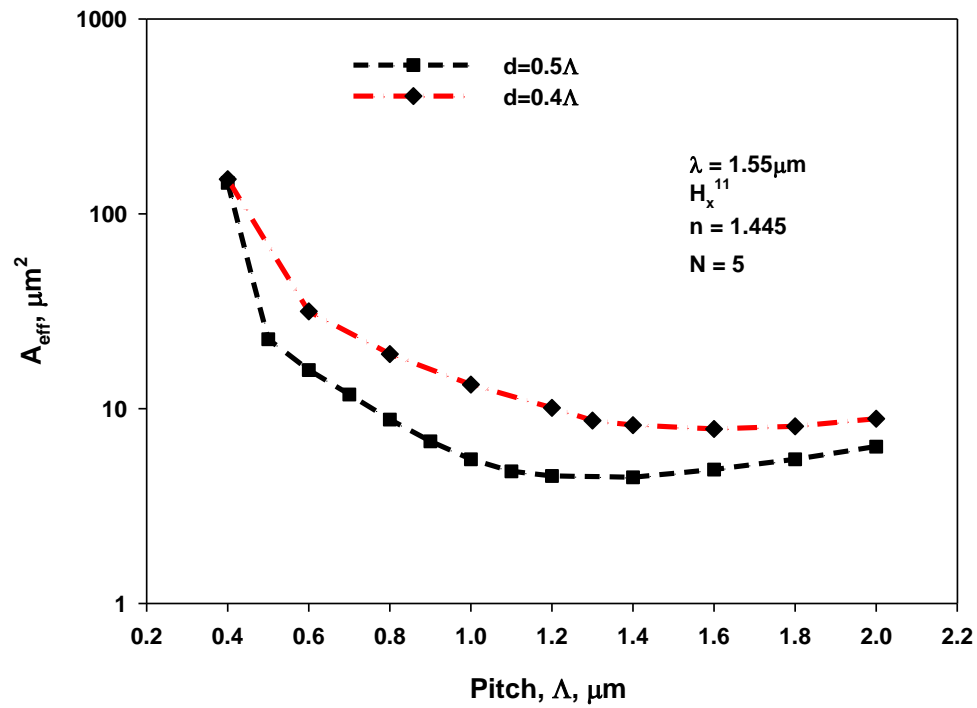


Fig. 6. 9: Variations of the  $A_{\text{eff}}$  with the pitch length for PCF having  $d/\Lambda = 0.4$  and  $0.5$  for  $N = 5$  with all air-holes equal.

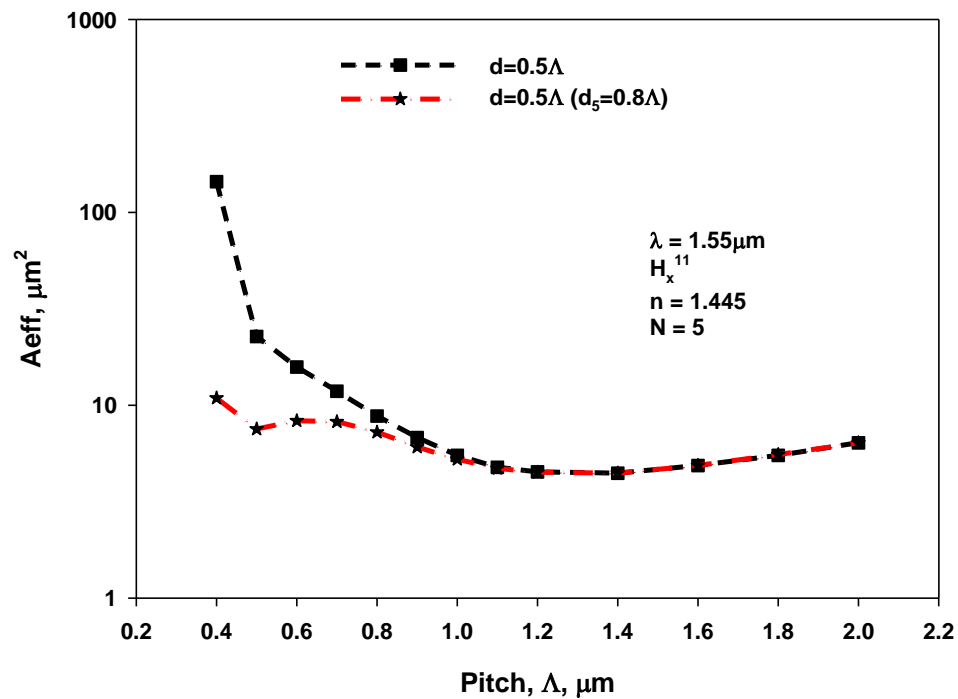


Fig. 6. 10: Variations of the  $A_{\text{eff}}$  with the pitch length for PCF having  $d/\Lambda = 0.5$  for  $N = 5$  with the outermost ring having larger air-holes.

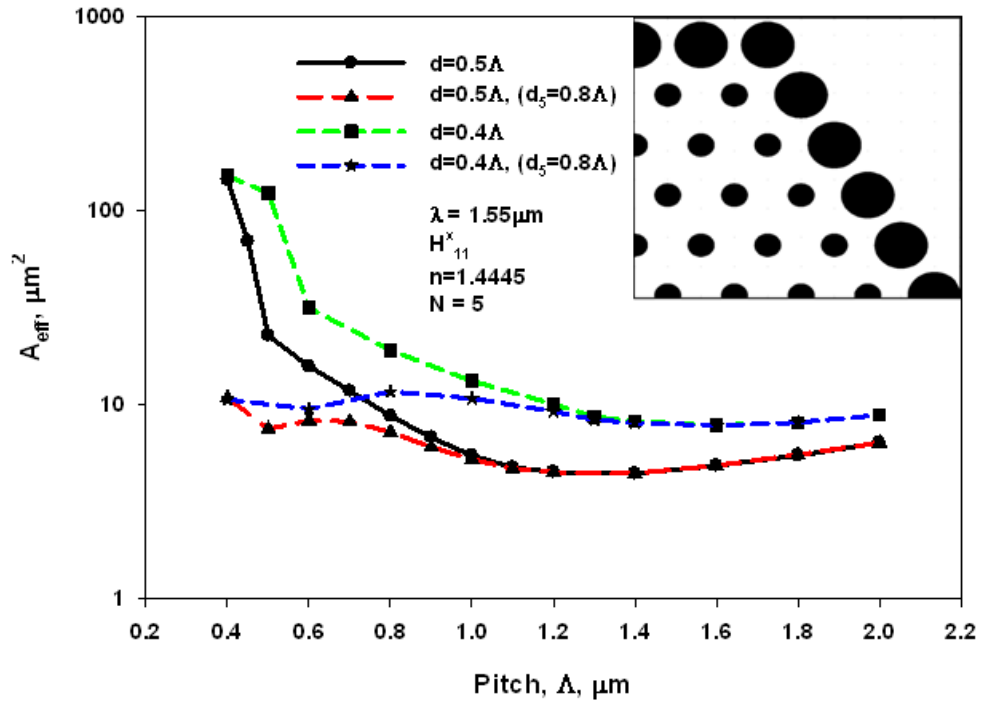


Fig. 6. 11: Variations of the  $A_{\text{eff}}$  with the pitch length for PCF having  $d/\Lambda = 0.4$  and  $0.5$  for  $N = 5$ .

However, in order to achieve MFA comparable to that of a SMF, it is necessary to increase the number of air-hole rings. Next, the variations of the effective areas,  $A_{\text{eff}}$ , with the pitch are shown in Fig. 6.12 for two different numbers of air-hole rings, given by  $N = 5$  and  $7$ . In both cases,  $d/\Lambda$  is taken as  $0.4$  and additional curves are also shown when the air-hole diameter in the last ring is increased to  $0.8\Lambda$ . It can be noted that when all the air-hole diameters are of the same size for all the rings, the value of  $A_{\text{eff}}$  increases progressively as the pitch,  $\Lambda$ , is reduced. When the number of rings is large, the value of  $A_{\text{eff}}$  is slightly larger as there is a larger cladding region available into which the mode can expand. It is also shown in Fig. 6.12 that by using  $7$  rings ( $N = 7$ ) and having the same diameter air-holes in the last ring ( $7^{\text{th}}$ ), a higher  $A_{\text{eff}}$  value can be obtained, but this would be very sensitive to the pitch value. However, as the air-hole diameter of the last ring is increased, in both cases, the value of  $A_{\text{eff}}$  stabilizes. It can be also noted here that this  $A_{\text{eff}}$  value is stable when the air-hole diameter in the last ring is large, where  $d = 0.8\Lambda$  and with a smaller value of the pitch,  $A_{\text{eff}}$  shows a lower variation with the pitch. This suggests that if the terminal dimension of a tapered PCF is taken as  $\Lambda = 0.7\mu\text{m}$ , a smaller variation of pitch due to the fabrication tolerances would not change  $A_{\text{eff}}$  significantly. For  $N = 7$ , when all the air-holes in the first  $6$  rings have the

dimension,  $d = 0.4\Lambda$  (except the air-holes in the 7<sup>th</sup> ring with the dimension of  $d_7 = 0.8\Lambda$ ), the stabilized value of MFA is around  $20 \mu\text{m}^2$ .

As can be observed, when the number of rings in the cladding,  $N$ , is increased, this results in an increase in the MFA as well. This shows that with a higher number of rings it is possible to achieve a very high MFA that is comparable to that of a SMF or if needed to be comparable to that of an Erbium Doped Fibre Amplifier (EDFA); this would then result in a lowering of the insertion loss when butt-coupled to these fibres.

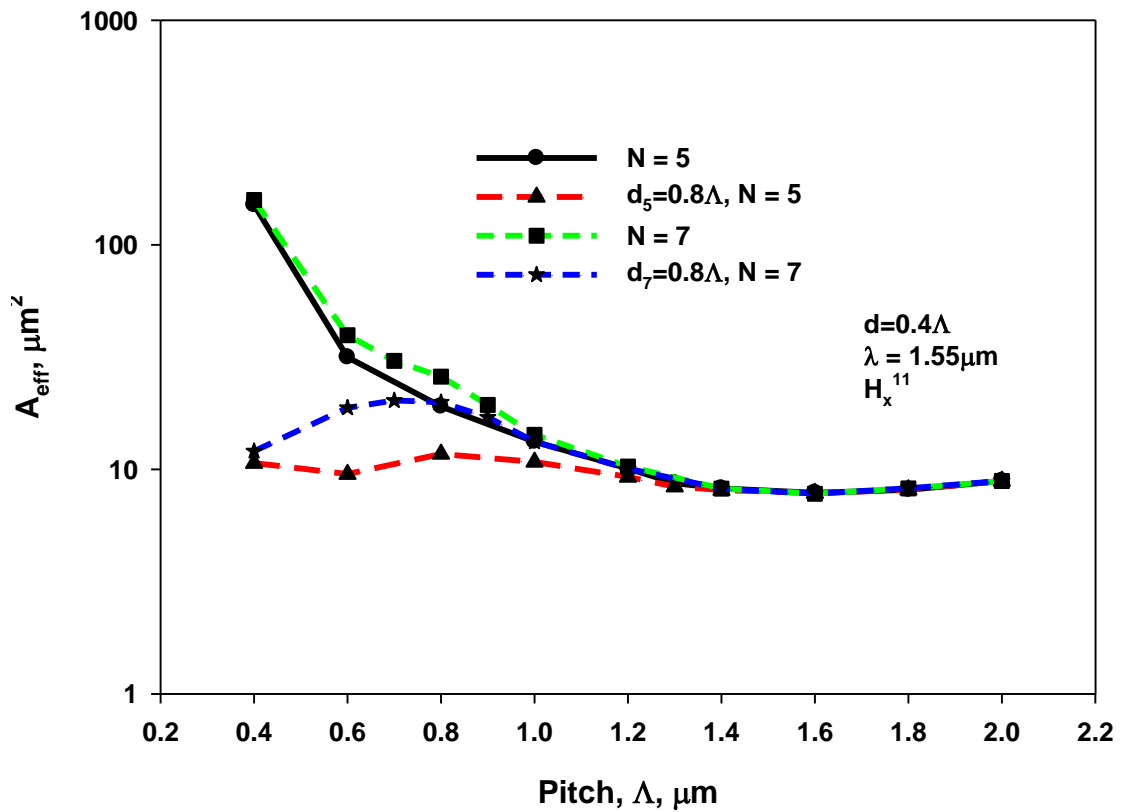


Fig. 6. 12: Variations of the  $A_{\text{eff}}$  with the pitch length for PCF having  $d/\Lambda = 0.4$  for  $N = 5$  and  $N = 7$ .

#### 6.4 Coupling between Photonic Crystal Fibre and Optical Fibre

Finally, the Coupling Efficiency is rigorously calculated by using the Least Squares Boundary Residual (LSBR) method (Rahman and Davies 1988). In Fig. 6.12, it was shown that a stable value of  $A_{\text{eff}} = 20 \mu\text{m}^2$  can be obtained for  $N = 7$  with all the air-hole diameters,  $d = 0.4\Lambda$  except that of the last ring, where  $d_7 = 0.8\Lambda$ . A typical Erbium Doped Fibre Amplifier (EDFA) may have an  $A_{\text{eff}}$  value around  $25 \mu\text{m}^2$  and a SMF have

its  $A_{\text{eff}}$  around  $80 \mu\text{m}^2$ . Thus a tapered PCF with  $N = 7$ ,  $d/\Lambda = 0.4$  and a final (7<sup>th</sup>) hole ratio  $d_7/\Lambda = 0.8$ , as shown above, could be efficiently coupled to an EDFA or a lensed fibre with a similar MFA.

The variations of the Coupling Efficiency with the pitch length for a PCF with 7 rings are shown in Fig. 6.13 when it is butt-coupled to an EDFA. In this case the core and cladding indices of the EDFA are taken to be 1.46178 and 1.445, respectively and its radius is taken as  $2.5 \mu\text{m}$ . When all the air-holes are equal to  $0.4\Lambda$ , the Coupling Efficiency to this EDFA is shown by a dashed line and when the diameters of the air-holes in the last ring are increased to  $0.8\Lambda$ , this is shown by a solid line. A log-scale is used for the coupling efficiency to show the lower value more clearly.

It can be observed that with the outer rings having larger air-holes, as the pitch length is reduced from  $2.0$  to  $0.5 \mu\text{m}$ , the coupled power is seen to be stable over the range of lower values of pitch (for  $\Lambda = 0.7 - 1.0 \mu\text{m}$ ) as shown by the solid line. In this case the value of the MFA of the PCF has an expanded, but also a stable value as shown earlier in Fig. 6.11, yielding a very stable power Coupling Efficiency with its maximum value of  $\sim 0.95$  can be achieved at  $\Lambda = 0.85 \mu\text{m}$  as can be seen in Fig. 6.13.

However, the power coupling to an EDFA, for a PCF with all the air-holes identical (dashed line), not only shows a lower Coupling Efficiency but also shows a random variation in the coupling coefficient. This is due to the degeneration of the core mode with the cladding mode as discussed in Chapter 4, which is particularly frequent near cutoff. Previously it had been reported that a PCF near cutoff or when bent shows that the loss value is erratic due to mode degeneration (Bourliaguet *et al.* 2003; Rahman *et al.* 2009) of the core mode with the surface modes in the extensive solid outer cladding. Similarly, it has been observed here that the presence of a larger air-hole reduces the silica area near the boundary and consequently reduces the possibility of mode degeneration, resulting in a more stable coupling efficiency. Hence it is shown that by increasing the diameter of the last air-hole ring, the expanded modes are more isolated from the high index outer cladding region and mode degeneration is also avoided. Thus a stable coupling can be achieved over a range of the pitch lengths which is stable during the possible change of the pitch when the PCF is tapered. Such an approach would also be more tolerant against waveguides misalignment, as the spot sizes are being expanded in this case.

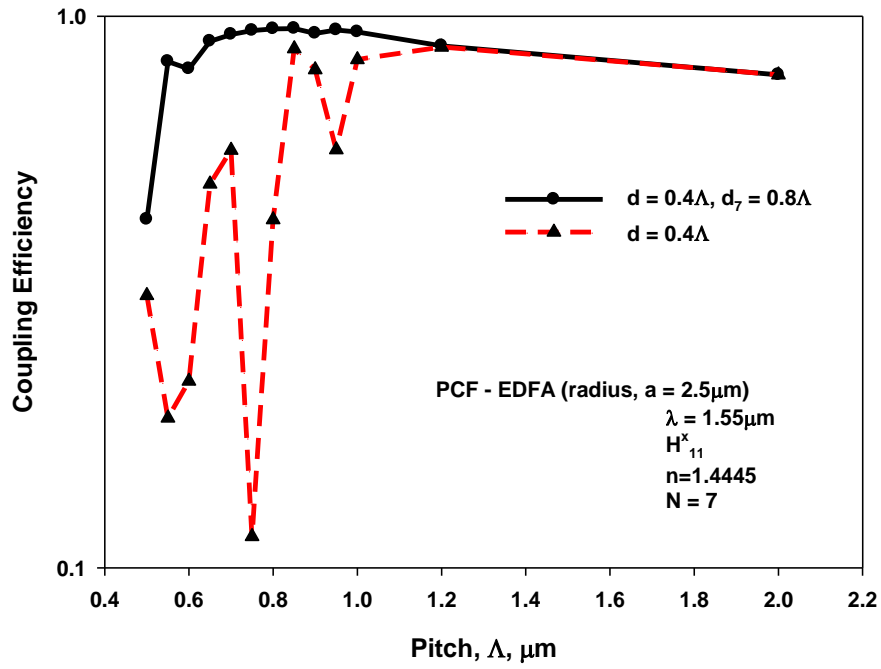


Fig. 6. 13: Variations of the coupled power to a EDFA with the tapered pitch,  $\Delta$ , of a PCF.

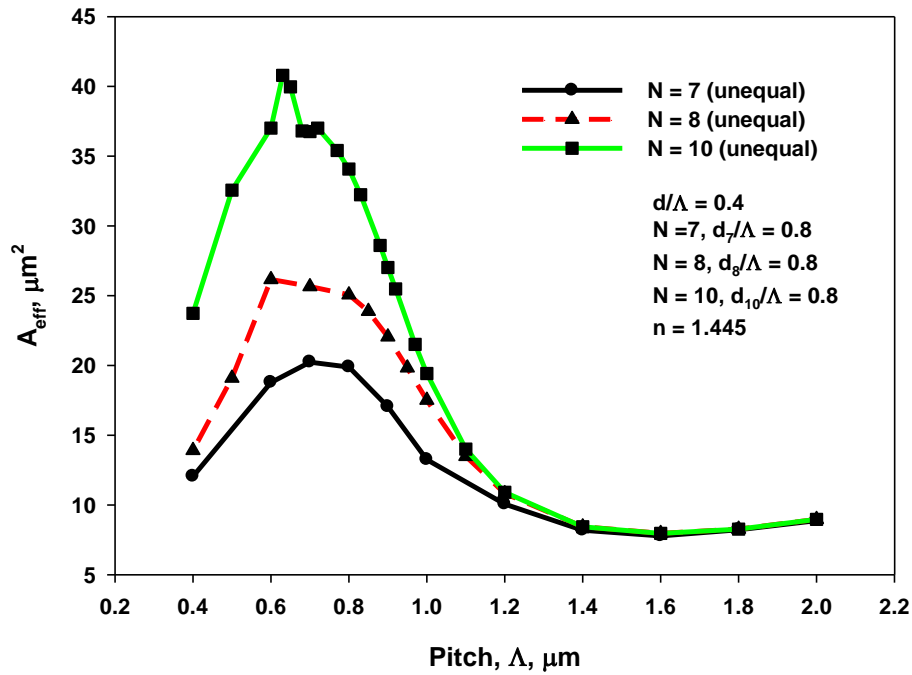


Fig. 6. 14: Variations of the  $A_{\text{eff}}$  with the pitch length for PCFs having  $d/\Delta = 0.4$  and outermost  $d/\Delta = 0.8$  for  $N = 7, 8$  and  $10$ .

Next, an attempt was made to couple a PCF to SMF and various approaches were considered. Generally, the spot size of a PCF is small compared to that of SMF and

when coupling them, a large fraction of the power is lost. A new concept is studied here to obtain an efficient coupling between PCF and SMF by introducing a tapered PCF end section. The PCF can be tapered and to have a larger diameter of air-holes in the outer ring.

Next, the number of rings is increased further to study the degree to which expansion of spot size which can be achieved. The variation of the effective area,  $A_{\text{eff}}$  with the reduction of the pitch,  $\Lambda$ , is shown in Fig. 6.14 for  $N = 7, 8$  and  $10$ . In all the cases, the air-hole diameter of the last ring has been increased to  $0.8\Lambda$  to stabilize the mode field area near their cutoff conditions.

In each case as the pitch is reduced, the MFA increases as the PCF designs approaches their cutoff, but due to the presence of larger air-holes in all the cases the MFA reaches a maximum value. However, it can be observed that for higher ring numbers, the maximum  $A_{\text{eff}}$  value was higher, which would allow efficient coupling to an optical fibre with a large MFA.

From the work done it is clear that different numbers of rings are best suited for coupling of a PCF to a SMF, EDFA or lensed fibre. Next, the mode shape area required from the different optical fibres, all of which guide a single moded waveguide, is studied by adjusting the radius and index contrast to maintain to have the identical  $V$  parameters. The  $V$  parameter was used to calculate the radius,  $a$ , of the single mode fibre for it to be single moded and it is given below:

$$V = \frac{2\pi a}{\lambda} \sqrt{n_g^2 - n_s^2} \quad (6.3)$$

The  $V$  parameter was used to calculate the radius,  $a$ , of the single mode fibre for it to be single moded,  $V = 2.2382$ . In this case, the cladding refractive index is taken as  $1.445$  and the core index is adjusted for each fibre diameter to have the same normalized dimension,  $V$ .



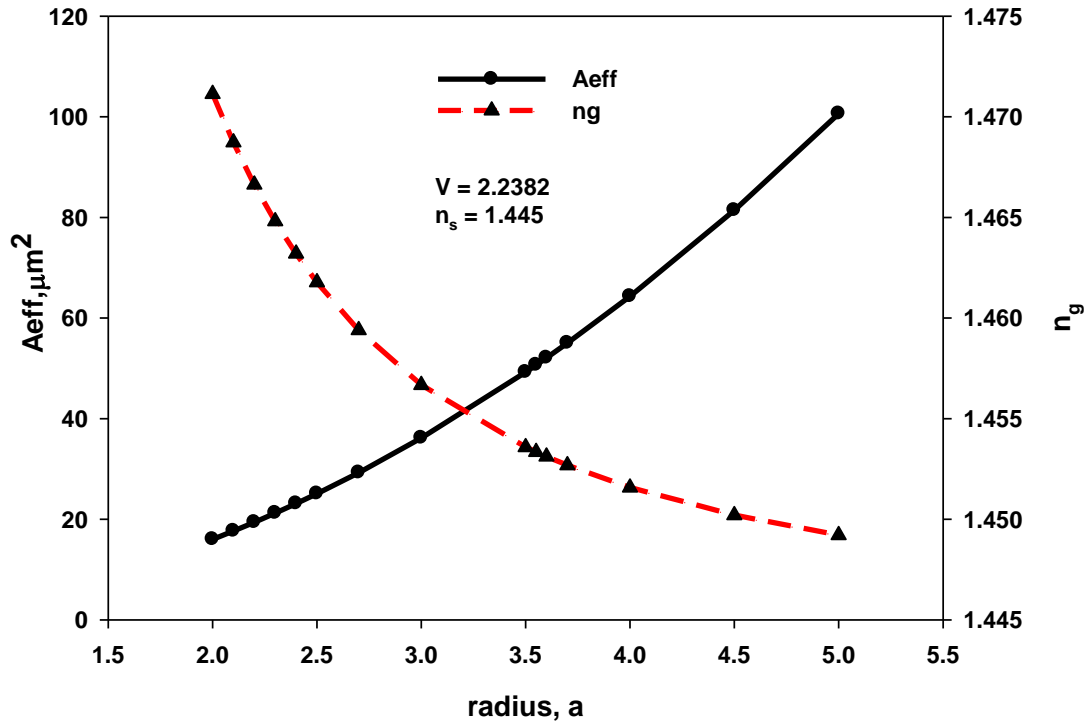


Fig. 6. 15: Variation of  $A_{eff}$  and core refractive index difference,  $n_g$  of a SMF against fibre radius,  $a$ .

The variation of the required refractive index of the core with its radius,  $a$ , is shown in Fig. 6.15, designed to maintain the single modedness by keeping the V parameter fixed at  $V = 2.2382$ , which is that of a typical SMF. The variation of the MFA,  $A_{eff}$  with the radius for this fibre with a constant value of V (where  $V = 2.2382$ ), is also shown here. It can be observed that as  $a$  is reduced, the value of  $A_{eff}$  also reduces but  $n_g$  increases. This study is aimed at to get the suitable radius and optimal doping,  $\Delta n$  (the refractive index difference) for the core to achieve single modedness of an optical fibre.

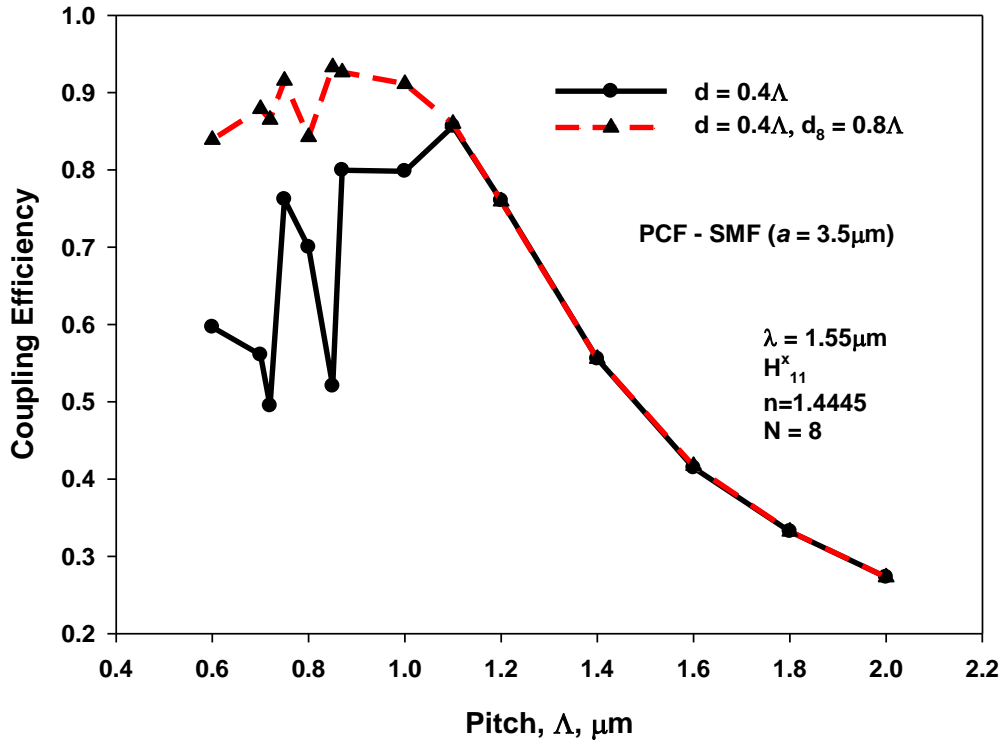


Fig. 6. 16: Variation of Coupling Efficiency to PCF with tapered pitch,  $\Lambda$  and SMF,  $a = 3.5\mu\text{m}$ .

Next, the butt-coupling between a tapered PCF with  $N = 8$  to an optical fibre with  $a = 3.5\mu\text{m}$  ( $V = 2.2382$ ) is studied. The variation of the coupling efficiency of a PCF with  $N = 8$  to an optical fibre with  $a = 3.5\mu\text{m}$  with the final pitch length,  $\Lambda$ , is shown in Fig. 6.16 for both equal air-holes and also larger air-holes in the last ring (8<sup>th</sup>) by a dashed and a solid line, respectively.

It is shown here that the maximum coupling efficiency (of 95%) can be achieved when the pitch length was  $0.85\mu\text{m}$  and butt-coupled to this fibre with  $a = 3.5\mu\text{m}$ . During the tapering process, if the pitch value varies between  $0.7\mu\text{m}$  to  $1.0\mu\text{m}$ , the coupling efficiency will still be above 90%. This shows the design is very stable, with the possible adjustment of the terminating pitch length for a tapered PCF. However, using the design principle discussed, for coupling to a SMF,  $A_{\text{eff}}$  needs to be further increased to a value close to that of a SMF. As the number of rings is further increased, the expansion of the mode field profile closer to cutoff increases as well, hence, allowing for more effective coupling to a SMF.

Therefore, it can be seen that when a PCF is down-tapered for coupling, the variations in the dimensions of the pitch or the diameter of the air-holes that may arise as a result

of the fabrication or tapering process would not affect appreciably the power coupled between a PCF and an SMF or an EDFA.

## 6.5 Summary

In this chapter, a novel design approach for a PCF which could be considered as a candidate for efficient coupling to an optical fibre has been presented (Uthman *et al.* 2012). Initially various MFA parameters and field profiles for a SMF and a PCF were studied. It has been shown here that a smaller air-hole diameter and a larger number of rings would allow the  $A_{\text{eff}}$  value to reach a higher value, which can be achieved by operating a PCF near cutoff. However, its expansion near cutoff can be very rapid and unstable, but by increasing the air-hole diameter in the last ring, this parameter can be stabilized with the variation of the fabrication tolerances. Using this approach presented above, it is possible to avoid uncertainty resulting from the variations in the dimensions of the pitch or the diameters of the air-holes in the PCF as a result of fabrication or tapering, thereby ensuring that the PCF can be successfully coupled to an optical fibre without any significant loss in coupled power. Additionally, it is also shown here that the largest air-holes in the last ring reduce the mode degeneration with the cladding modes. As the PCF is tapered to reduce its dimension, close to its modal cutoff its MFA expands and by introducing larger air-holes in the outer ring, it is shown here that expansion of MFA can be stabilized against fabrication tolerances. In this work, a beam propagation approach is not used, rather, modal solutions are carried out for each reduced dimension and junction analysis is carried out to obtain possible coupling efficiency. During the tapering process it has been assumed that the pitch,  $\Lambda$ , reduces gradually while keeping the  $d/\Lambda$  ratio constant. However, the air-holes can also collapse and the air-hole/pitch ratio can also change although this may give an additional flexibility but also an additional parameter to optimise the situation. Once the nature of the deviations is known *a priori* then a rigorous numerical approach, such as that presented above, can be used to optimize the designs before their fabrication for experimental validation. In this approach, as the PCF operates near cutoff, it is normally expected that the leakage and bending losses will be increased. However, in this approach since larger hole diameters are used in the last air-hole ring, in fact rather, lower leakage and bending losses are expected. Furthermore, if required, additional air-hole rings with larger air-hole diameters can be included and the design can be

optimized to reduce leakage and bending losses further. The application of PCF in the terahertz (THz) region designed with polymer and using the conventional and equiangular spiral PCF is analysed and presented in the next Chapter.

## CHAPTER SEVEN: Photonic Crystal Fibre for Terahertz

### 7.0 Abstract

This chapter presents the work done on wave guidance in the THz regime. Two types of materials namely, Teflon and TOPAS for THz guidance were used in the simulations. The conventional Hexagonal PCF that was discussed from the beginning of this thesis was compared to Equiangular Spiral PCFs. Lastly, a new porous core PCF design for low loss THz guidance is presented together with its bending loss calculations.

### 7.1 Introduction

Terahertz radiation (or THz waves), generally identified as covering the 0.1 to 10 THz frequency band, lies between the lower microwave frequencies and higher optical frequencies and has attracted widespread attention in recent years. Numerous applications of such radiation have been reported including medical diagnostics (Crawley *et al.* 2003; Woodward *et al.* 2003), testing of pharmaceutical drugs (Strachan *et al.* 2005) and defect detection in electronic circuits (Kiwa *et al.* 2003), amongst others. Devices operating in the THz regime can be used in hazardous or security sensitive areas for monitoring drugs (Kawase *et al.* 2003; Jepsen *et al.* 2011), gas (Jacobsen *et al.* 1996), explosives (Shen *et al.* 2005; Liu *et al.* 2006) or weapons and also in the study and better understanding of the dynamics of complex natural biological systems. This has led to a concerted effort in the development of better THz sources and detectors and as a result, the last decade has seen significant technical advances in THz wave generation (Kohler *et al.* 2002) and detection (Wu *et al.* 1996; Karpowicz *et al.* 2008). However, most of the THz systems that are available today and for which market introduction are sought are based on free-space transmission, due to lack of suitable low-loss flexible waveguides.

The development of low-loss THz waveguides has been challenging as almost all presently available materials are highly absorbent in this frequency band. Previously, circular metallic guides, like stainless steel solid wires (Wang and Mittleman 2004) or hypodermic needles (Gallot *et al.* 2000) have been considered but these waveguides are highly lossy, these being in the order of 500 dB/m. Plasmonic modes are always very lossy and in case of a metal rod, the mode field also extends well into the outer open

space, which is less controllable. Although a THz wave cannot be guided inside a hollow dielectric tube (unless the Bragg principle is used), if this tube is coated with a metal layer, a plasmonic mode can form inside the hollow core, where the guiding environment can be better controlled or manipulated. It has been shown that by incorporating an additional thin dielectric layer (Bowden *et al.* 2007), the mode field can be drawn away from the lossy plasmonic interface and as a consequence the overall loss value can be reduced (Themistos *et al.* 2007). However, often these waveguides have rather large diameter and not very flexible and for a small diameter, the loss value also increases.

On the other hand, most of the optical waveguides are dielectric waveguides, which arises due to the availability of very low-loss materials at these important wavelengths. However, at the THz frequency range most of the dielectric materials are lossy. Previously, it had been demonstrated that a simple polyethylene (PE) fishing line can guide THz waves (Chen *et al.* 2006). Currently, polymers are the materials of choice for making flexible terahertz dielectric waveguides, i.e., polymethyl methacrylate (PMMA) (Ponseca *et al.* 2008), Teflon (Goto *et al.* 2004), high-density polyethylene (HDPE) (Han *et al.* 2002; Chen *et al.* 2006), and TOPAS (Nielsen *et al.* 2009) are widely used as they have lower reported losses in the THz frequency range and they are relatively easy to process. Jin *et al.* (Jin *et al.* 2006) have carried out an extensive study on the loss values of various polymer materials in the THz frequency range.

However, because the absorption losses in these dielectric materials are still very high a variety of guiding mechanism have been reported to reduce the overall modal losses. Dry air has one of lowest material losses in the THz frequency range and as such when a dielectric rod is surrounded by air operating very close to its cut-off condition leads the mode field to extend into the low index air cladding region and such sub-wavelength waveguides have been reported (Chen *et al.* 2006). The main disadvantage of this design is that mode extends considerably into the surrounding air cladding and the power is propagated mostly outside the waveguide: this strongly interacts with the surrounding environment and the bending loss would also be expected to be excessively high.

PCF is a class of optical fibre where many air-holes run along the length of the waveguide (Russell 2003) and where light is guided by the modified TIR when the equivalent refractive index of the porous cladding is less than that of the solid core, as was discussed in Chapter 2. PCFs are being used as waveguides which exploit their unique characteristics of being endlessly single-moded and which offer adjustable spot size and dispersion properties for various linear and nonlinear applications. As a fraction of the power can be confined and guided in the air-holes, this can reduce modal loss and, Han *et al.* (Han *et al.* 2002) and Goto *et al.* (Goto *et al.* 2004) have fabricated HDPE and Teflon PCF, respectively for THz wave guidance.

## 7.2 Equiangular Spiral Photonic Crystal Fibre

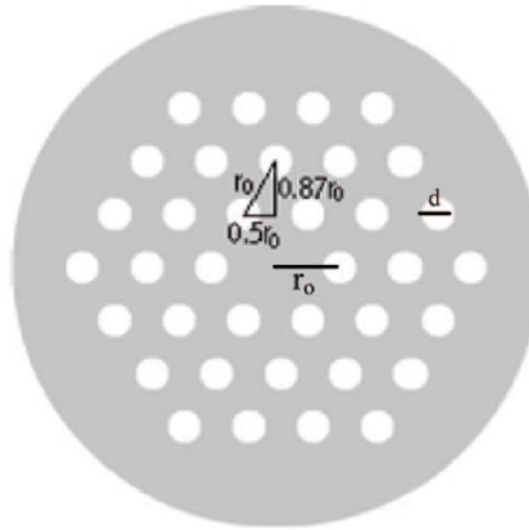


Fig. 7. 1: Schematic of the Hexagonal Photonic Crystal Fibre structure

In this section the new class of photonic crystal fibre called the Equiangular Spiral Photonic Crystal Fibre (ES-PCF) design in TOPAS for use in the Terahertz regime is presented together with a comparison with the hexagonal PCF. For comparison, first, a schematic of the Hexagonal Photonic Crystal Fibre is shown in Fig. 7.1. The Hexagonal PCF has a hexagonal air-hole arrangement in which the separation between air-holes is constant and is also equal to the distance from the centre of the structure to the centre of the air-holes in the first ring (it is normally termed  $\Lambda$ ). The diameter of the air-holes is also fixed and equal to  $d$ . The optical properties of the Hexagonal PCF are determined chiefly by the pitch,  $\Lambda$  and the  $d/\Lambda$  ratio.

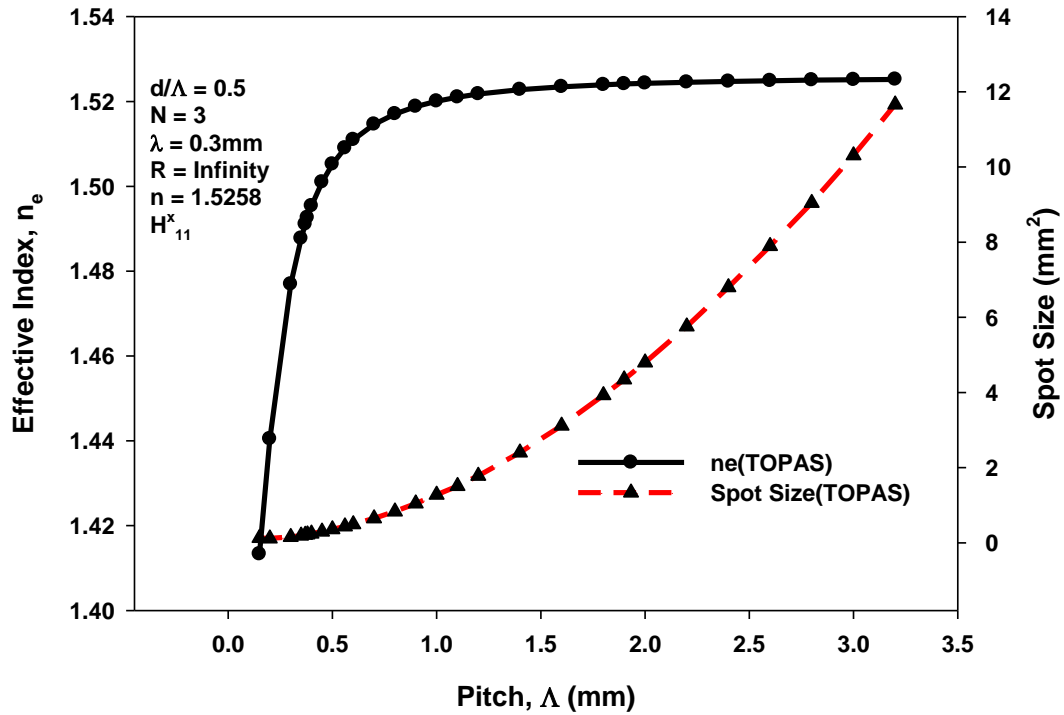


Fig. 7. 2: Graph of effective index against pitch and spot size against pitch in hexagonal TOPAS.

Some comparisons of PCF operating in this THz frequency range have also been carried out in this project. Initially, modal solutions of simple PCFs made of TOPAS and Teflon are obtained. Figure 7.2 shows the variations of the effective index and spot size with the pitch for a hexagonal PCF made of TOPAS. In this case,  $\lambda = 0.3\text{mm}$  corresponds to a frequency of 1 THz. This PCF has 3 air-hole rings and  $d/\Delta$  was taken as 0.5. The refractive index of TOPAS is taken as 1.5258. It can be observed as  $\Delta$  is reduced, effective index reduces as well. It can also be observed that as  $\Delta$  is reduced, the spot size reduces and the mode approaches its cutoff.



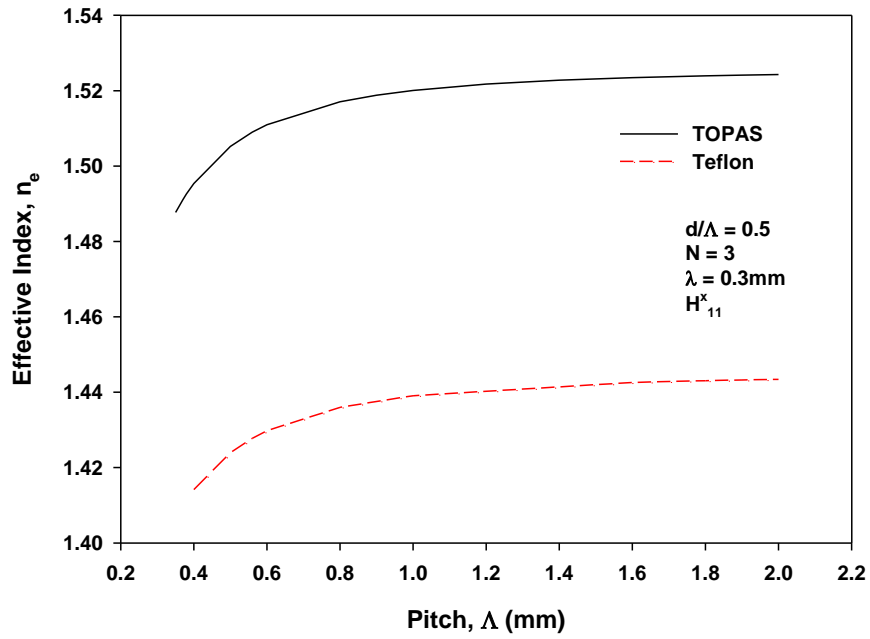


Fig. 7. 3: Graph comparing effective index for Teflon and TOPAS PCFs with respect to pitch.

Figure 7.3 shows the variation of effective index against the pitch comparing PCF made of both TOPAS and Teflon. The refractive index of TOPAS is taken as 1.5258 whereas that of Teflon is 1.445 at the wavelength of 0.3mm. It can be observed that as the pitch is reduced, the effective index reduces too and when cutoff is approached, the decrease is sharper for both the cases of TOPAS and Teflon PCF. The differences in their effective indices are comparable to the difference in their refractive indices.

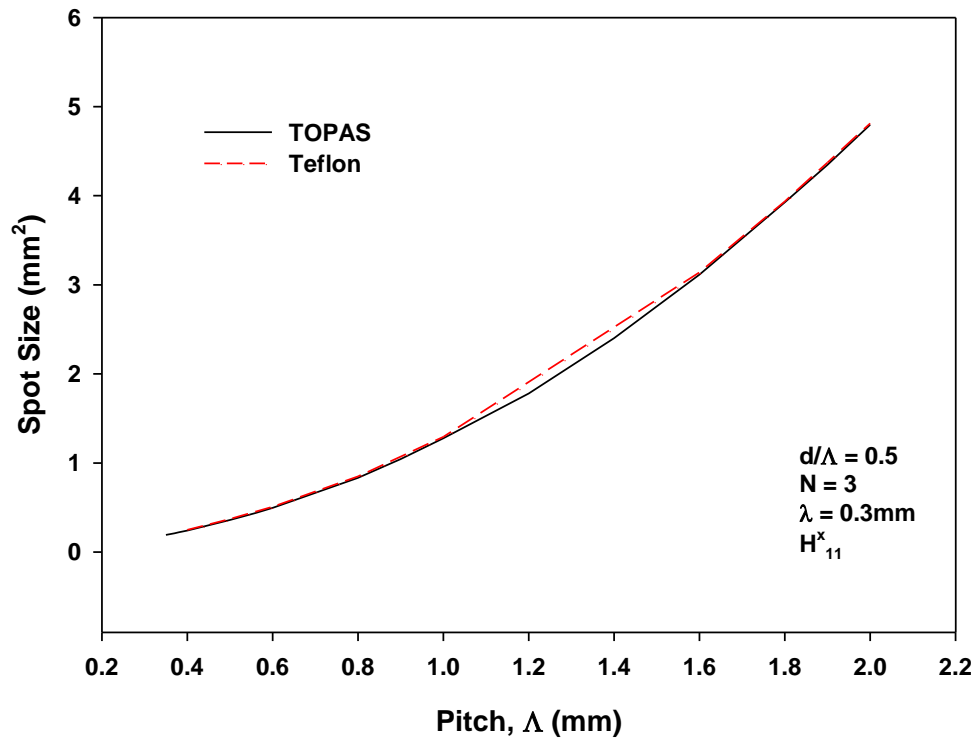


Fig. 7. 4: Variations of spot sizes for Teflon and TOPAS PCFs with the pitch

Figure 7.4 shows the comparison of spot size against the pitch in hexagonal PCF made of TOPAS and Teflon. As the pitch is reduced, it is observed that the spot size decreases as well. It can be noted that their spot sizes are nearly similar.

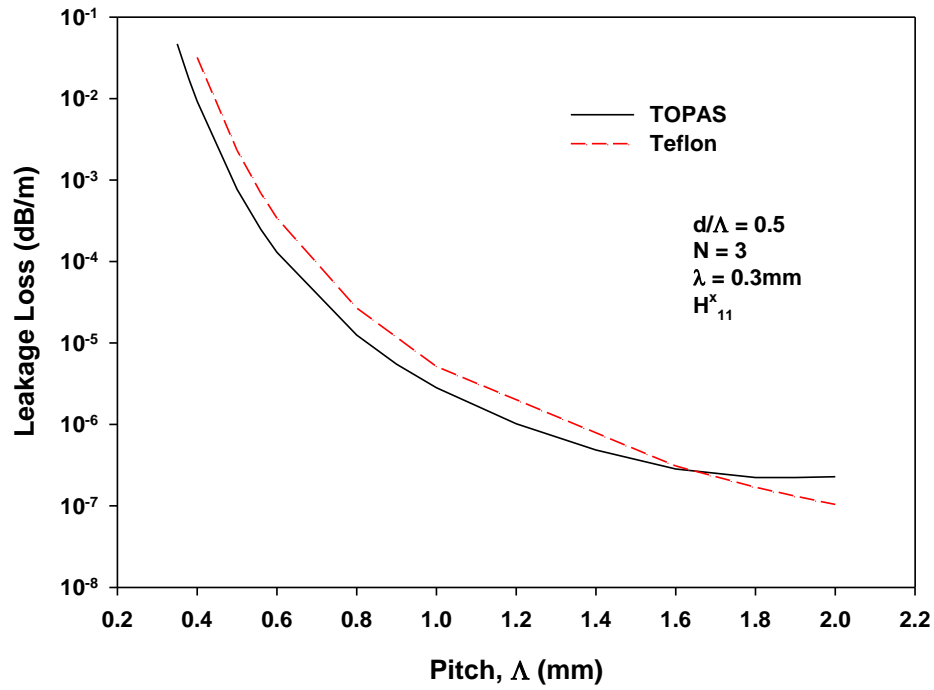


Fig. 7. 5: Variations of the leakage loss in Teflon and TOPAS PCFs with the pitch.

Figure 7.5 shows the variation of leakage loss against the pitch comparing both types of PCF, made from TOPAS and Teflon. It is observed that the loss decreases with increase in the value of pitch. In this case it can be easily observed that the leakage loss is negligible, unless the  $\Lambda$  is too small and the PCFs are operating very close to their cutoff. There is a need to have flexible waveguides in engineering applications because waveguides are generally subjected to bending in their practical applications.

Next, the results of the bending loss calculations for both Teflon and TOPAS based PCFs are presented. This work was carried out by applying the PML and additionally conformal transformation as described in Chapter 3.

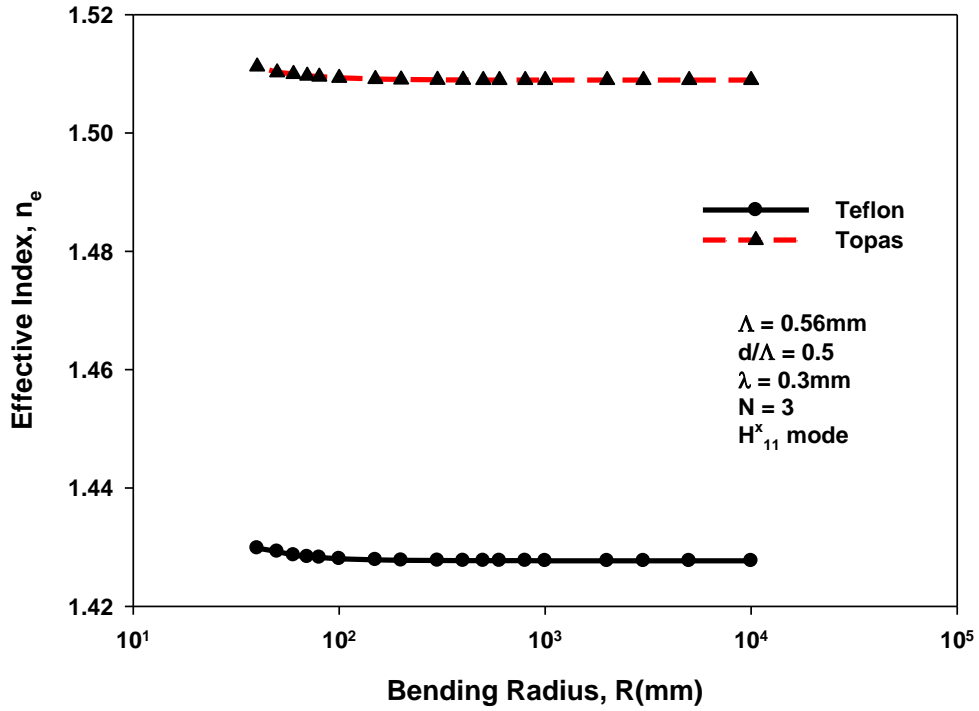


Fig. 7. 6: Graph comparing effective index in Teflon and TOPAS with respect to bending radius.

Figure 7.6 shows the variations of the effective indices with the bending radius. The materials considered here are TOPAS and Teflon and the refractive indices for Teflon and TOPAS were taken as 1.445 and 1.5258 at operating wavelength of 0.3 mm (frequency of 1 THz). It can be observed that as the bending radius is reduced the effective index increases.

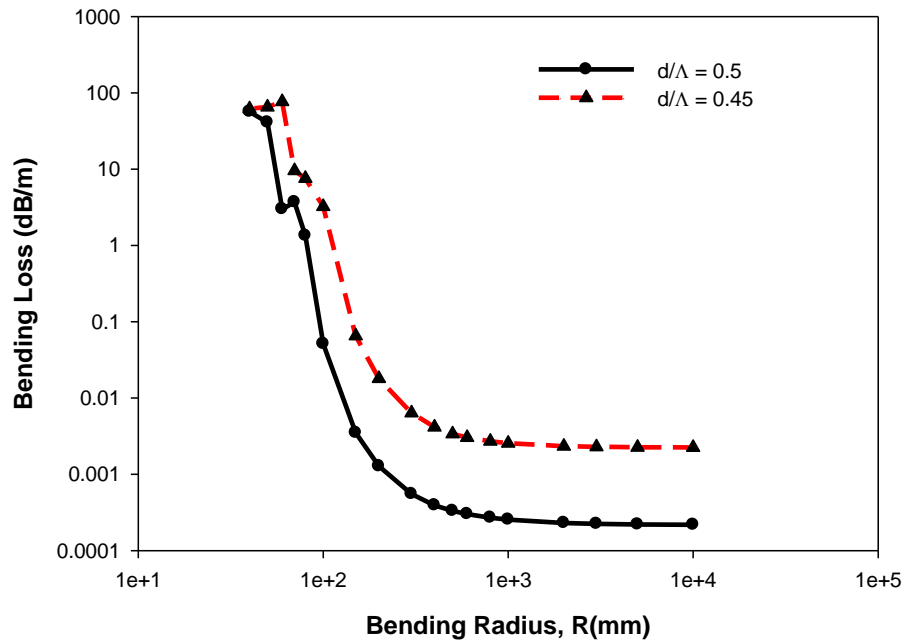


Fig. 7. 7: Graph of loss against bending radius in TOPAS for hexagonal arrangement with  $d/\Lambda = 0.45$  and  $0.5$ .

Figure 7.7 shows variations of bending loss against the bending radius in hexagonal PCFs for two different  $d/\Lambda$  values,  $0.45$  and  $0.5$  for a TOPAS PCF. It can be observed that the bending loss decreases as the bending radius is increased. It can also be observed that as the  $d/\Lambda$  is increased, the loss decreases as well. As the size of the air-holes is increased, the gap between the air-holes reduces and thus leading to reduction in loss as well.

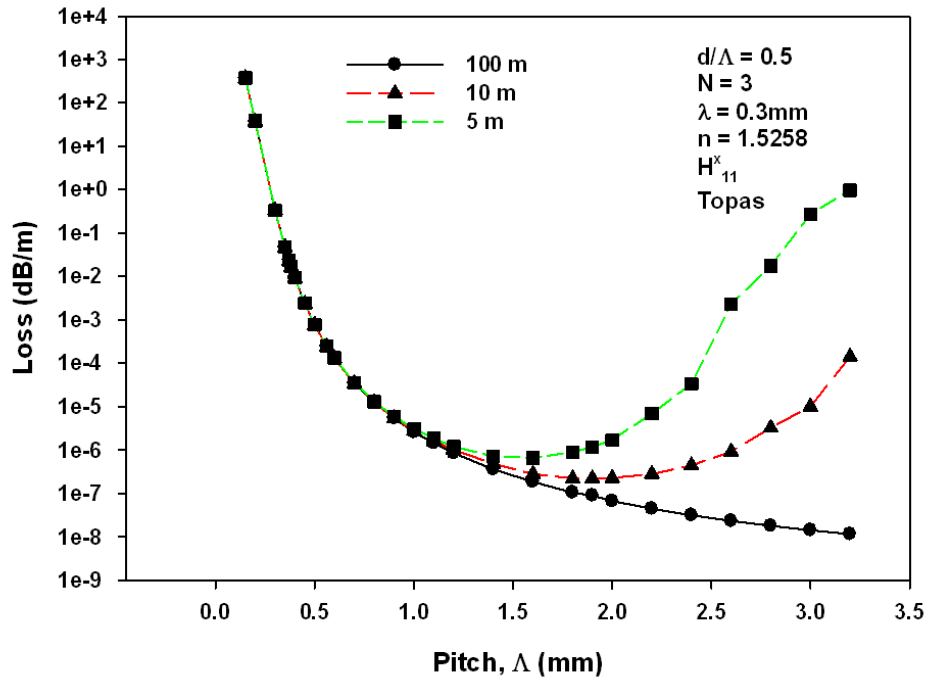


Fig. 7. 8: Graph comparing loss Hexagonal TOPAS with respect to pitch for bending radius of 5m, 10m and 100m.

Figure 7.8 shows the variation of loss against the pitch for several fixed bending radii. The material used here is TOPAS with bending radius of 5 metre, 10 metre and infinity (100 metres). It can be observed here that as the pitch is increased, the loss decreases as well. It is observed that as the pitch is increased above 1.5mm, the loss begins to increase in the case of a waveguide with 5 metre bending radius and that with a 10 metre bending radius. This similar phenomenon was observed with silica PCF operating at 1.55  $\mu\text{m}$  wavelength as well and that was reported in Chapter 4; and this increase is due to the availability of larger bridging area between the air-holes which is susceptible to leakage loss at very small bending radii.

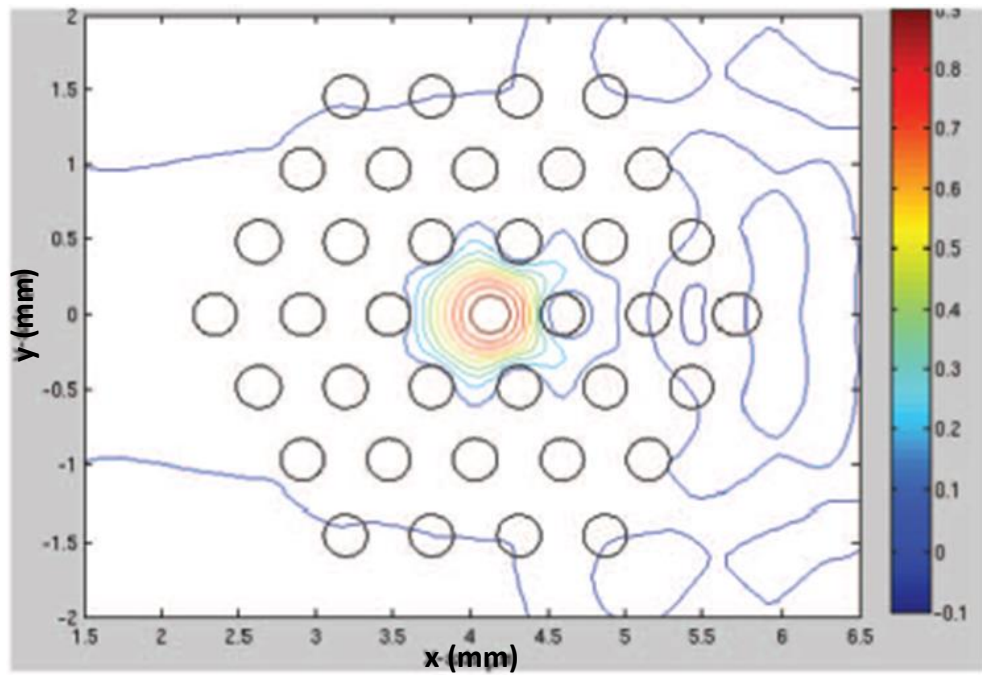


Fig. 7. 9: Field profile in the bent Hexagonal PCF in Teflon, where bend radius = 60mm.

It is observed in Fig. 7.9, which shows the fundamental mode in the bent hexagonal PCF (to show the effect of the air-holes, the air-holes are also drawn in the figure), in Teflon. When the fibre is bent in this hexagonal PCF arrangement, the field tends to spread out of the core as was reported in the results from previous chapters. In the Hexagonal PCF the distance between the first and second ring of air-holes is large enough to allow the field to escape from the core through this bridge especially when bent, as can be seen clearly in Fig. 7.9. When the addition of Material Loss is considered there is a marked increase in the Modal Loss values due to the modal field residing mostly in the solid polymer core and the Material Loss dominating. In this section so far, modal characteristics of TOPAS and Teflon based PCFs with hexagonal air-hole arrangement are presented at 1 THz operating frequency.

Next, a very special design of PCF is considered known as the Equiangular Spiral PCF (ES-PCF). The equiangular spiral PCF designs, in which air-holes are arranged in a spiral pattern governed by the golden ratio, where the design has been inspired by the optimal arrangement of sunflower seeds as found in nature. The air-hole arrangement in the Equiangular Spiral PCF design mimics the ‘spiramirabilis’ and appears in nature in nautilus shells and sunflower heads. It leads to efficient feature growth/packing of seeds and the growth of this type of curve does not alter the shape of the curve. In the Equiangular Spiral Photonic Crystal Fibre, as shown in Fig. 7.10, each arm of air-holes

forms a single Equiangular Spiral of radius  $r_0$ , angular increment  $\theta$  and the radius of each air-hole is fixed ( $r$ ). In the Equiangular Spiral, the radii drawn at any equal intervals of  $\theta$  are in a geometric progression; therefore, the pitch (distance between air-holes) in a ring increases with the ring number.

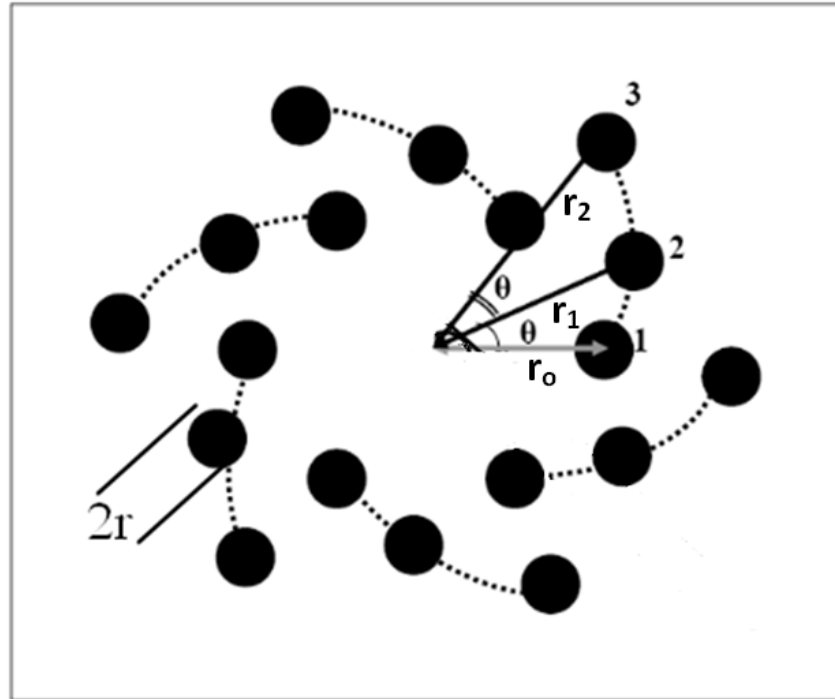


Fig. 7. 10: Schematic of the Equiangular Spiral Photonic Crystal Fibre.

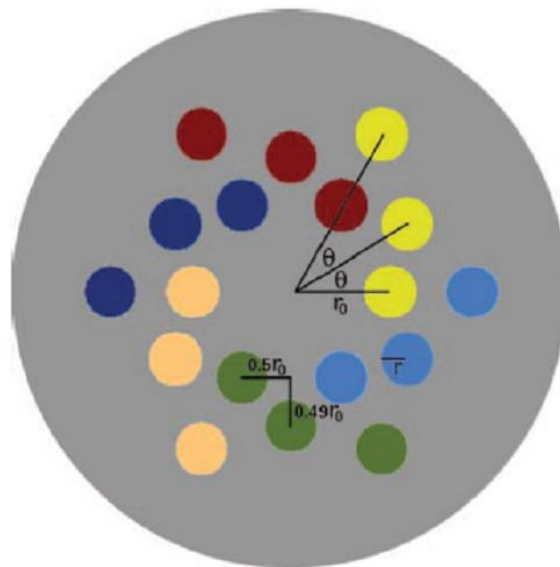


Fig. 7. 11: Schematic of the ES-PCF structure



A schematic of the ES-PCF is shown in Fig. 7.11 and it has 6 arms and 3 rings with  $\theta = 30^\circ$ . Each arm of air-holes, (depicted by air-holes of same colour); air-hole radius, ( $r$ ) forms a single equiangular spiral of radius  $r_o$ , angular increment  $\theta$  and  $n$  in this case is number of arms (narm), given by the polar equation:

$$r_{n+1} = r_n \cdot e^{\theta \cot \alpha} \quad (7.1)$$

$$\alpha = \frac{(n-2)\pi}{2n} \quad (7.2)$$

Where  $\alpha$  is the constant angle between a radius of the equiangular spiral and the tangent at the end point of the radius and  $r_{n+1}$  is the distance of the  $n+1^{\text{th}}$  air-hole along the spiral arm from the centre of the structure. Each air-hole is separated by an angular increment of  $\theta$  with respect to the previous and/or successive air-hole in the same arm as shown in Fig. 7.10. Distance for each ring progressively increases, following the definition of  $r_{n+1}$  for each ring. To compare with the hexagonal PCF,  $r_o$  is taken as  $\Lambda$ . The total number of air-holes in each arm represents the number of rings in the equiangular spiral PCF and the total number of air-holes is thus simply the product of the number of arms with the number of rings.

The x and y coordinates of the centre of each air-hole can be found from Equation (7.1) and the angle they make with the first air-hole. In the equiangular spiral PCF it has been found that it is possible to tune the modal characteristics of the field by choosing a suitable combination of values for the fibre parameters: the number of arms ( $n$ ),  $\theta$  (spiral angle),  $r_o$ , (spiral radius),  $r$ , (air-hole radius), and the number of rings.

In order to ease comparison between the ES-PCF structure with that of the conventional Hexagonal PCF (shown in Fig. 7.1), the following parameters were optimised for the ES-PCF: number of arms = 7, number of rings = 5, thus number of air-holes = 35 and  $\theta = 27^\circ$ . These are the parameters associated with the results presented subsequently in this chapter unless where stated otherwise.

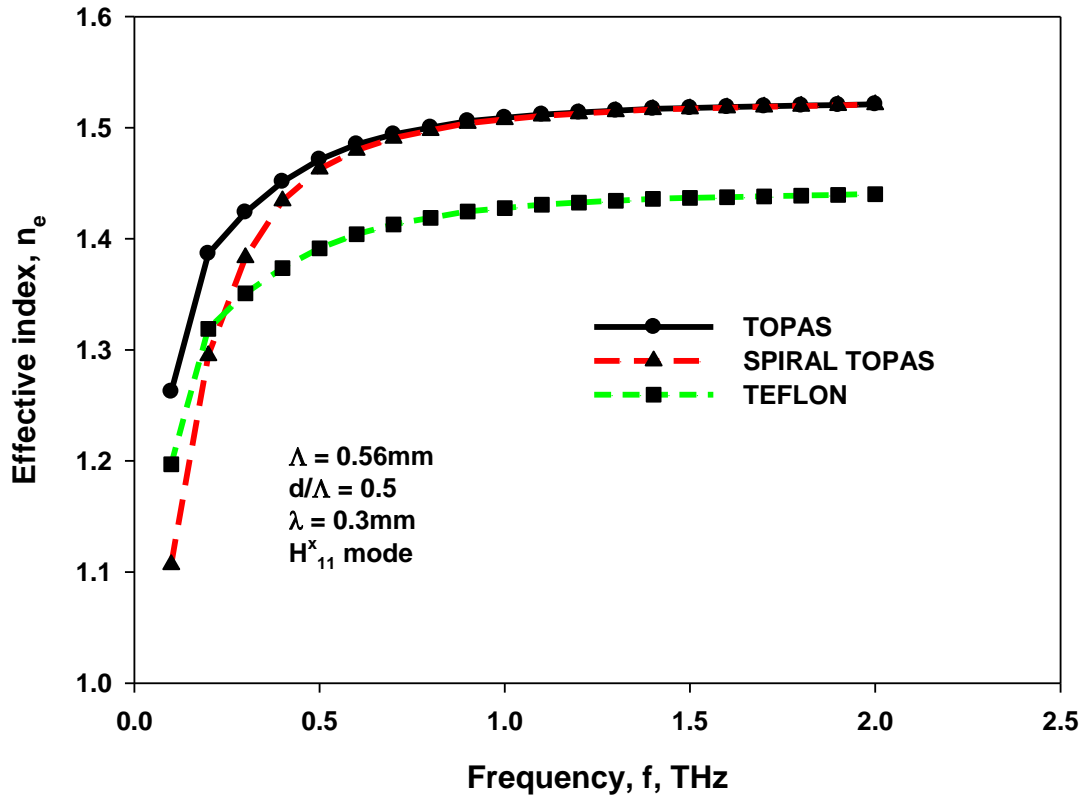


Fig. 7. 12: Graph comparing the effective index verses frequency for Hexagonal TOPAS, equiangular spiral TOPAS and Hexagonal Teflon.

Figure 7.12 shows the variations of the effective indices against THz frequency for 3 different PCFs, namely Hexagonal PCF in TOPAS and Teflon and spiral PCF in TOPAS. As the frequency is decreased, the effective index decreases as well in all cases. When frequency is increased, modes are well confined for all the cases and effective indices of TOPAS PCFs, Equiangular Spiral and Hexagonal PCFs were almost identical.

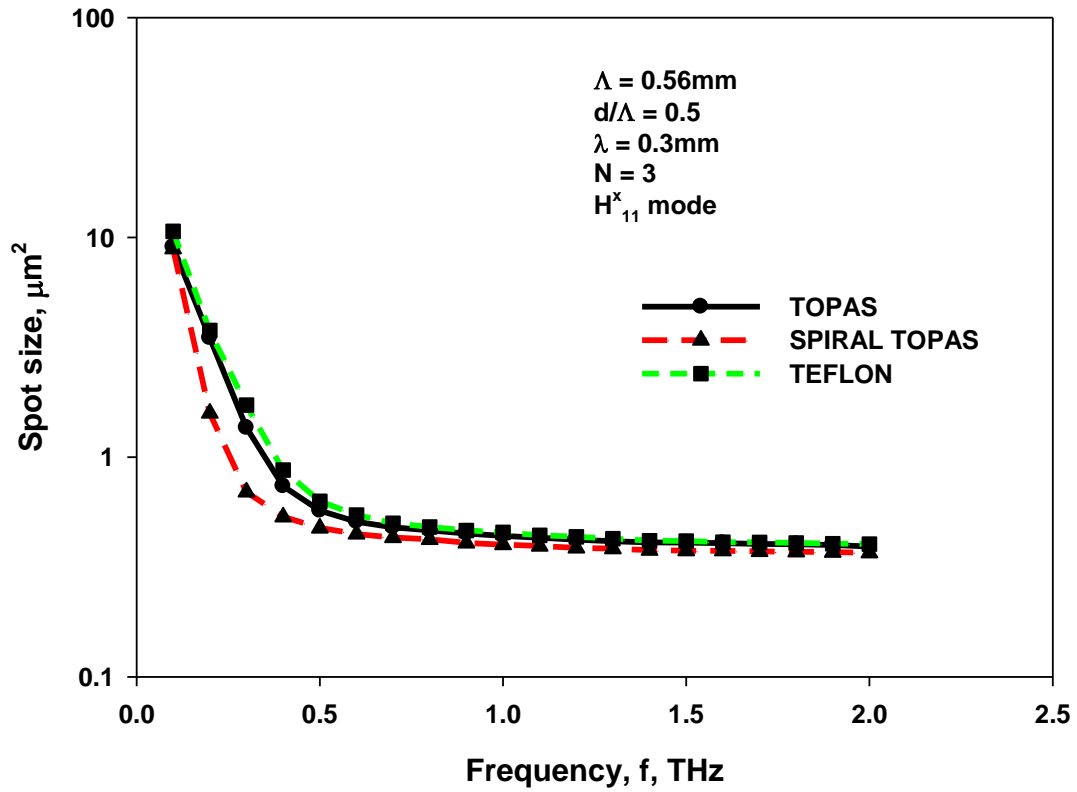


Fig. 7. 13: Graph of spot size against frequency for hexagonal TOPAS, equiangular spiral TOPAS and Hexagonal Teflon.

Figure 7.13 shows the variations of spot size against THz frequency for Hexagonal PCF in TOPAS, spiral PCF in TOPAS and Hexagonal PCF in Teflon. As the frequency is decreased, the spot size increases as well in all cases, because modes approach their cutoff. The spot sizes of the guided modes are similar in all the PCFs over this entire range as is seen in Fig. 7.13. We explain here the mechanism for the lower bending loss in the equiangular spiral PCF.

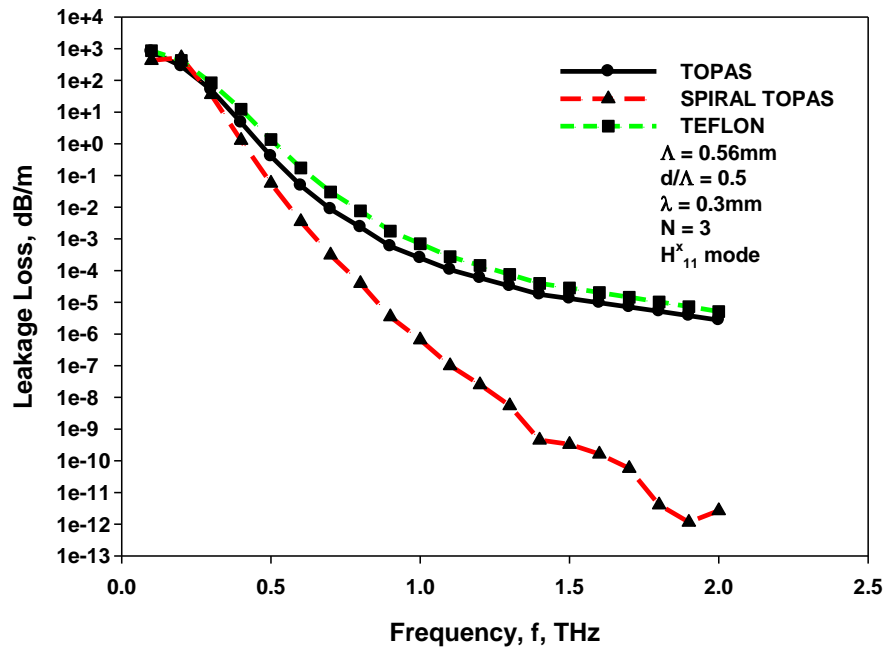


Fig. 7. 14: Graph of loss against frequency in hexagonal PCF, equiangular spiral PCF in TOPAS and hexagonal PCF in Teflon.

Figure 7.14 shows the variations of the leakage loss against THz frequency for the 3 PCFs, as discussed earlier. As the frequency is increased, the loss decreases in all cases, as the mode is more confined in the core. It can be noted here, that in the typical operating region, say between 1 – 2 THz, leakage losses for all 3 cases are very low. However, it can be observed that leakage loss for the Equiangular Spiral PCF is significantly lower at higher operating frequency.

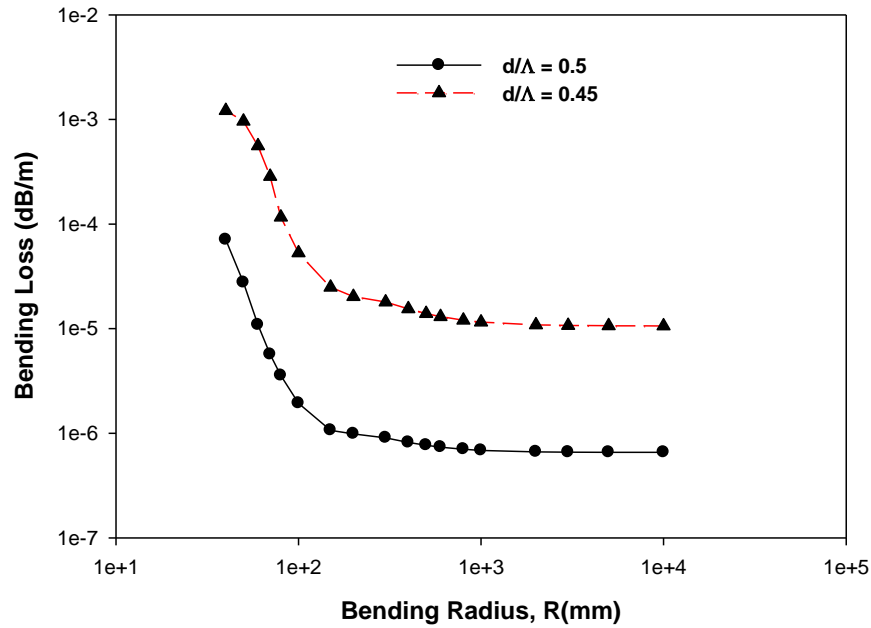


Fig. 7. 15: Graph of bending loss against bending radius in equiangular spiral PCF with  $d/\Lambda = 0.45$  and  $0.5$ .

Figure 7.15 shows the graph of bending loss against bending radius for two Equiangular Spiral PCF with  $n_{arm} = 7$ ,  $n_{ring} = 5$ , that is 35 air-holes in total and angle of 27 degrees but with two different  $d/\Lambda = 0.45$  and  $0.5$ , respectively. The loss is higher for  $d/\Lambda = 0.45$  because there is lesser fraction of air in the cladding because when the  $d/\Lambda$  is lower, there is a larger gap between air-holes through which more power can escape.

The bending of a PCF leads to the distortion of the optical mode which loses its shape and tends to move towards regions of higher equivalent refractive index (Heiblum and Harris 1975; Rahman *et al.* 2009; Rahman *et al.* 2011). In the equiangular spiral PCF the bridge regions of high refractive index between air-holes are much smaller and narrower than in the Hexagonal PCF (distance of the air-holes in the second ring from the first ring is  $0.49 r_0$  in the equiangular spiral PCF while it is  $0.87 r_0$  in the Hexagonal PCF). By choosing an appropriate value of  $\theta$ , the placements of air-holes in the second ring may block the spread of the field into the polymer regions between the holes.

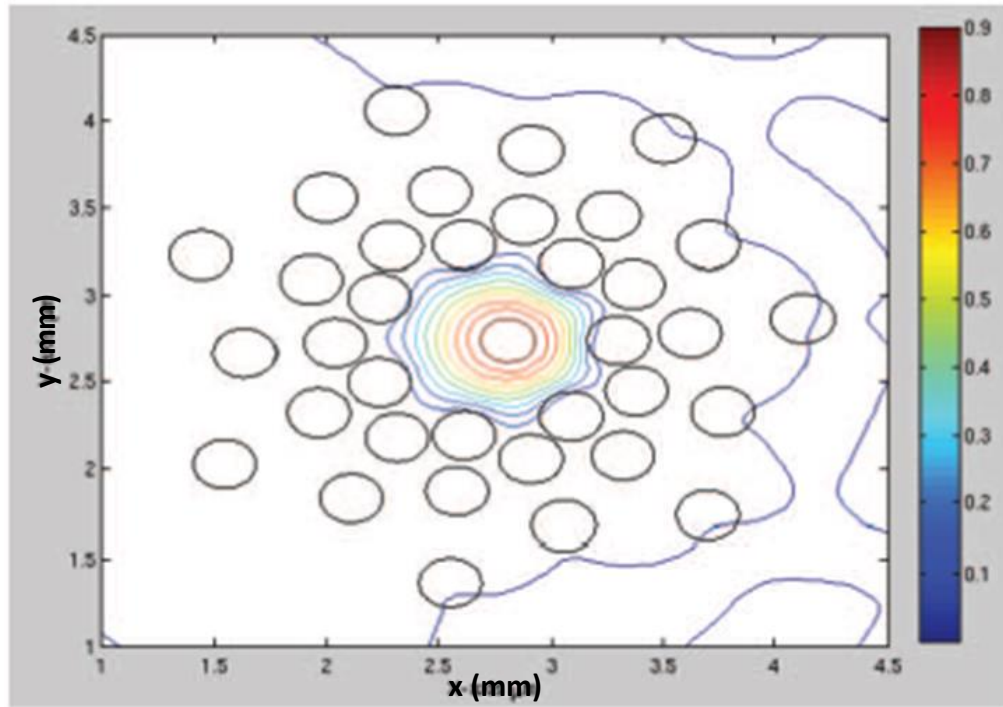


Fig. 7. 16: Field profile in the bent Equiangular Spiral Photonic Crystal Fibre, where bend radius = 60mm.

Figure 7.16 shows the fundamental mode profile in the bent equiangular spiral PCF and to show the effect of the air-holes, the air-holes are also drawn in the figure. A similar behaviour is observed in hexagonal Teflon PCF. This is the main cause that even when the fibre is bent, in the equiangular spiral PCF the field is blocked from spreading out of the core by the second ring of air-holes. The location of air-holes in the second ring can be controlled by the parameter  $\theta$  as shown in Fig. 7.10 and leakage loss of an Equiangular Spiral (PCF) can be significantly reduced. When the addition of material loss is considered there is a marked increase in the modal loss values due to the modal field residing mostly in the solid polymer core and the material loss dominating.

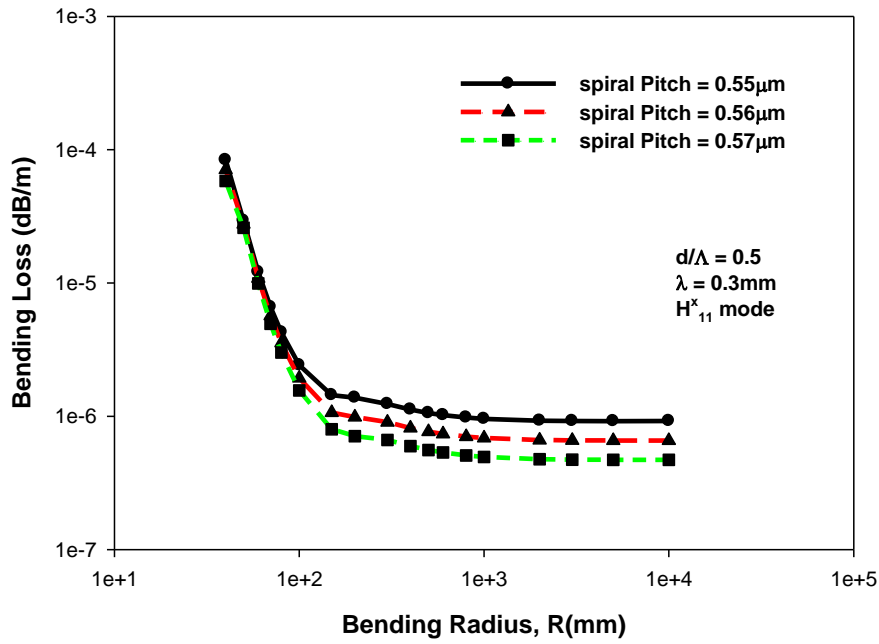


Fig. 7. 17: Graph of loss against bending radius in Teflon for equiangular spiral arrangement with  $\Lambda = 0.55, 0.56$  and  $0.57$  with  $n_{arm} = 7$ ,  $n_{ring} = 5$  and  $\theta = 27^\circ$ .

Figure 7.17 shows the variations of bending loss against bending radius in equiangular spiral PCFs considering spiral pitch of 0.55mm, 0.56mm and 0.57 mm, respectively. It can be observed that the bending loss decreases as the spiral pitch is increased and when the bending radius is 10cm, the bending loss is 0.1dB/m, which confirms that these waveguides can be used in many practical applications when the PCF is subjected to random bends. This is a similar trend observed earlier with the hexagonal PCF. It can also be observed that as the pitch is increased the mode is better confined in the core and bending loss is smaller.

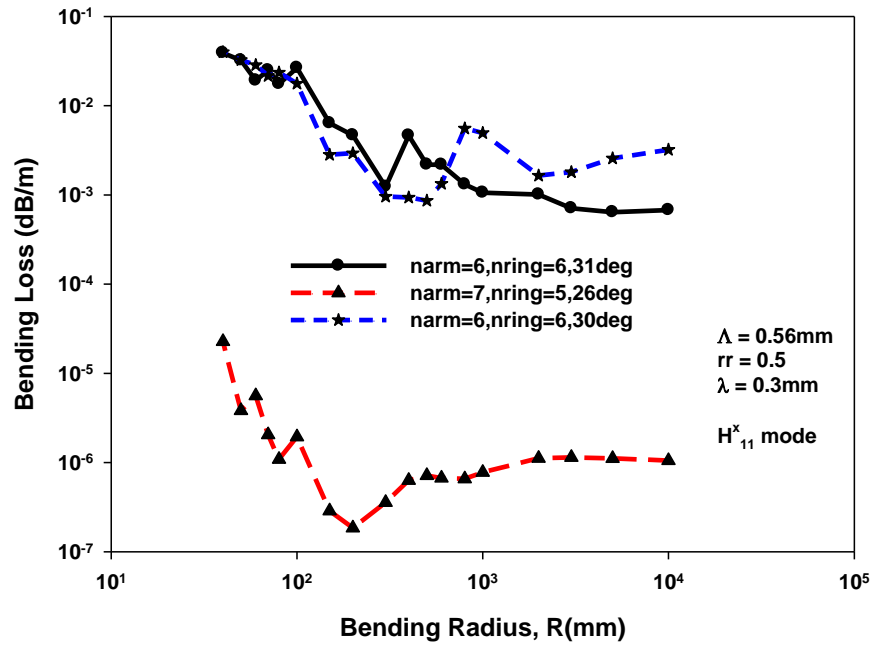


Fig. 7. 18: Graph of bending loss against bending radius using various configurations of spiral TOPAS PCF arrangement.

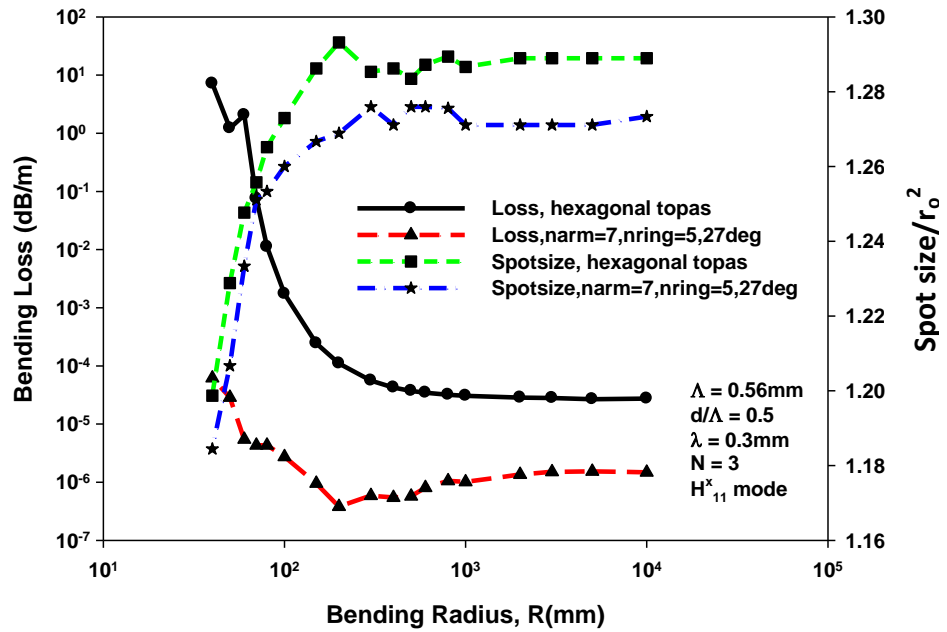


Fig. 7. 19: Variation of bending loss against bending radius and normalised spotsize against bending radius for hexagonal PCF and equiangular spiral PCF in TOPAS.

The modal loss shows a sharp increase as the bend radius decreases below 10cm for the Hexagonal PCF (LMA) design, while for the equiangular spiral PCF it remains almost



constant. Bend loss is the dominant loss mechanism for such small bend radii; the equiangular spiral PCF does not allow the modal field to escape into the cladding in a way similar to the Hexagonal PCF or oscillation in the Bending Loss due to mode degeneration (Rahman *et al.* 2009). Figures 7.18 and 7.19 shows the graphs of some of the results obtained in the process of optimizing the parameters of ES-PCF to aid in the comparison with conventional hexagonal PCF. Figure 7.18 shows the graph of bending loss against bending radius in TOPAS using various configurations of spiral PCF arrangement compared to hexagonal arrangement. The most important parameter varied here is the angle to see its effect. The graphs were then plotted for some possible designs.

Often, loss for a well confined mode is lower. So in this case, spot size of two different designs, one hexagonal PCF and another ES-PCF are adjusted to have similar spot size. Figure 7.19 show the graph of Loss against bending radius and normalised spot size against bending radius for Hexagonal PCF and that of Equiangular PCF with parameters  $\Lambda = 560\mu\text{m}$ ,  $r = 125\mu\text{m}$ ,  $d/\Lambda = 0.45$  and for the ES-PCF: 7 arms, 5 rings,  $r_o = 560\mu\text{m}$ ,  $r = 250\mu\text{m}$ ,  $\theta = 27^\circ$ . A slightly different radius of air-holes is used here. It is observed that the loss is significantly lower in Equiangular PCF than in Hexagonal PCF the curves of the spot size are slightly lower for Equiangular PCF as well.

A key characteristic for THz waveguides is the Modal Loss (ML), which is the sum of the Confinement Loss (CL), the Bending Loss (BL) and the Material Loss (MaL) associated with the mode. A comparison of the Modal Loss in the Hexagonal PCF (the Large Mode Area (LMA) design) (Nielsen *et al.* 2009), and an equiangular spiral PCF which has been optimized with 36 air-holes as in the case of the LMA where the key fibre parameters used are as follows for the LMA:  $\Lambda = 560\mu\text{m}$ ,  $r = 125\mu\text{m}$ ,  $d/\Lambda = 0.45$  and for the ES-PCF: 7 arms, 5 rings,  $r_o = 560\mu\text{m}$ ,  $r = 250\mu\text{m}$ ,  $\theta = 27^\circ$ . Figure 7.19 shows the Modal Loss and the normalized spot size variation with the bend radius. To separate out the effect of the air-hole arrangement, this initial result assumes a loss less material, although Material Loss is included in later results. From Fig. 7.19 it can be seen that for large bend radii (100-10000mm), the loss is primarily Confinement Loss and the equiangular spiral PCF loss is about three orders of magnitude lower than for the Hexagonal PCF. For a fair comparison we have used equal number of air-holes, same air-holes diameter and also comparable spot size. For bending radii lower than 100mm

(where Confinement Loss and Bending Loss are present), the Hexagonal PCF suffers severe mode leakage while the mode is extremely well confined in the equiangular spiral PCF with loss lower by 5-6 orders of magnitude. Thus, for applications where fibres may need to be wound on tight spools, the equiangular spiral PCF can show the better loss performance (Bending Loss  $\sim 10\text{dB/cm}$  even for very tight bends  $\sim 2\text{ cm}$ ). At large bend radii (where the loss is primarily due to Material Loss and Confinement Loss) the loss values are almost similar for both PCF designs. Even when examining the Confinement Loss variation with frequency for straight fibres, both PCFs exhibit almost similar performance. At high bending radii the Confinement Loss is much lower than the Material Loss with the Confinement Loss is low but as Material Loss is the effect of equiangular spiral PCF and Hexagonal PCF is almost similar even when the Confinement Loss of the equiangular spiral PCF was less.

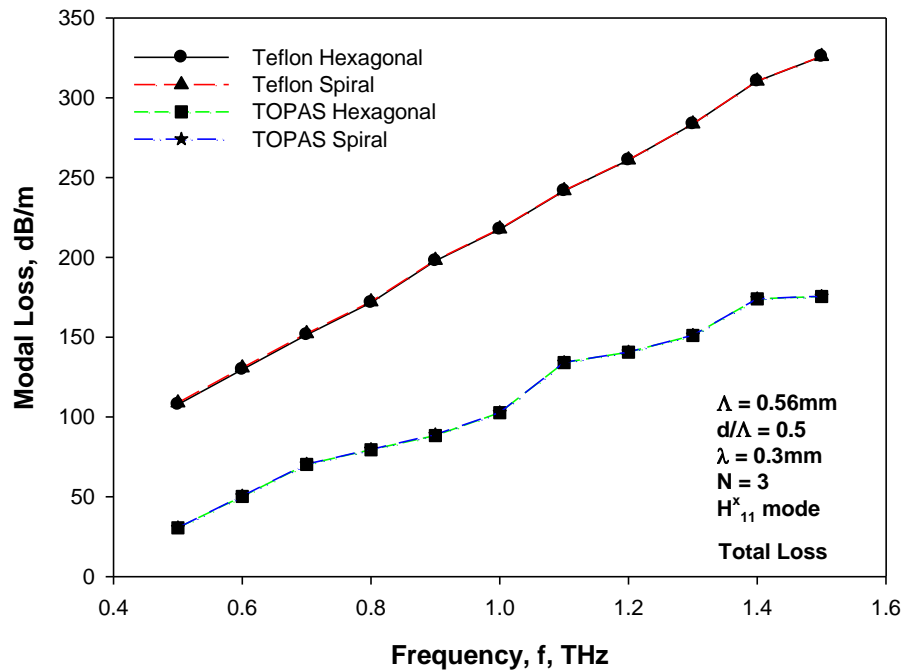


Fig. 7. 20: Graph of loss against frequency in hexagonal PCF and equiangular spiral PCF in Teflon with inclusion of material loss.

Figure 7.20 above shows the variations of loss against the THz operating frequency in hexagonal and equiangular spiral PCFs without bending. It is observed that the inclusion of material loss (the data for material loss were obtained from published experimental results (Jin *et al.* 2006)) does not alter the loss curves for both hexagonal PCF and equiangular PCF in TOPAS and Teflon. The imaginary refractive index for

Teflon was taken as 0.00119 whereas that for TOPAS was 0.000561. In these cases, material loss is much higher than other loss values.

Earlier, Nielsen *et al.* (Nielsen et al. 2009) reported two types of low loss bendable fibres in TOPAS showing two types of fabricated low loss bendable fibre in TOPAS operating in the terahertz regime. Some of the detailed simulations carried out in this chapter are based on the fabricated Hexagonal TOPAS PCF from that research group.

### 7.3 Bending Loss Calculation in Teflon

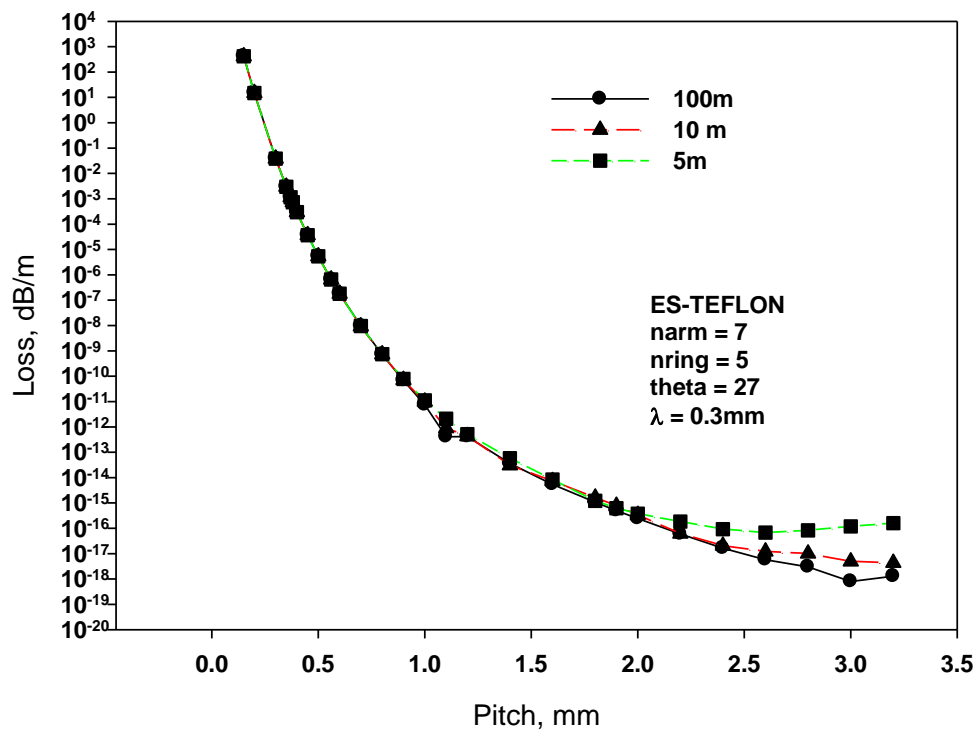


Fig. 7. 21: Graph comparing loss (without material loss) of Equiangular spiral Teflon with respect to pitch for bending radius of 5,000mm, 10,000mm and infinity.

Figure 7.21 shows the graph of loss against pitch for ES-PCF. The material used here is Teflon in THz and comparing with bending radius of 5 metre, 10 metre and infinity (100 metres). It is observed that as the pitch is increased, the loss decreases as well. However, at a cutoff point the loss begins to increase in the case of waveguide with a 5 metre and that of 10 metre bending radius. This increase happens earlier, implying

cutoff is reached a bit earlier as the bending radius is increased. This is similar to what was observed with the hexagonal PCF in Fig. 7.8, however, the loss is generally lower in equiangular spiral PCF and the cutoff condition is reached much later than in the case of Hexagonal PCF.

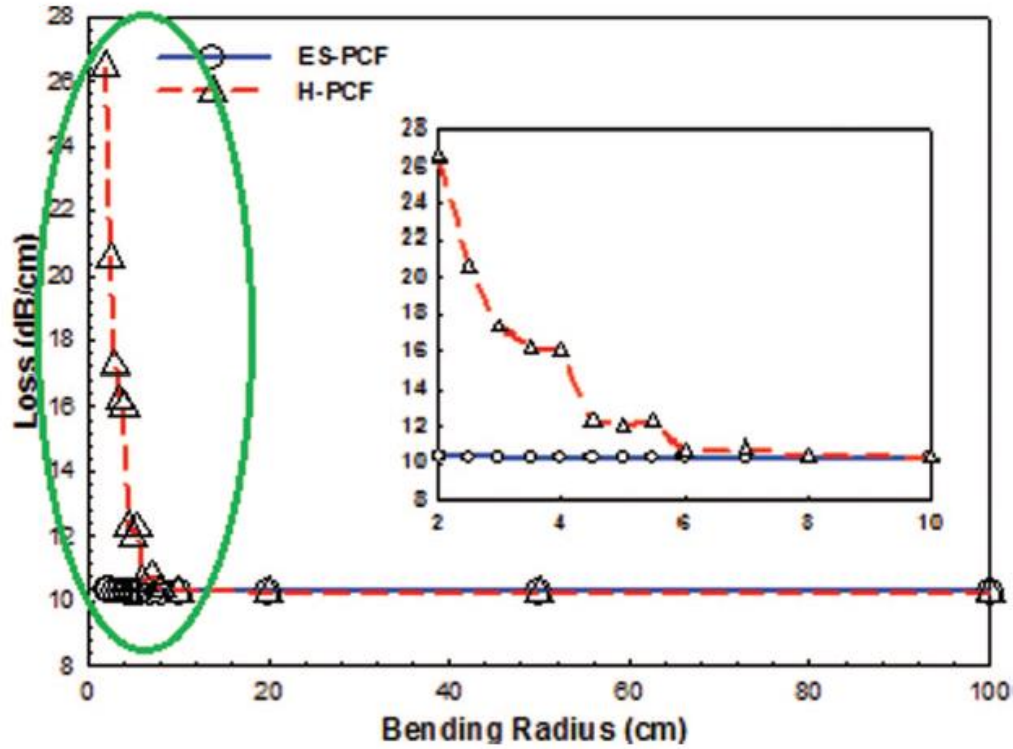


Fig. 7. 22: Modal loss (including material loss) variation with bend radius at 1THz for the Hexagonal PCF and equiangular spiral PCF.

Often, a PCF in practical applications goes through random bends. It is useful to study their bending loss. Figure 7.22 shows the bending loss graph of equiangular spiral PCF and Hexagonal PCF in Teflon from 1000cm to below 10cm. It is seen that the loss increases much more for the hexagonal PCF below 10cm and even oscillations due to mode degeneration are observed in the loss curve (as discussed in Chapter 4). However, the curve for the equiangular spiral PCF remains relatively flat. It can be observed in Fig. 7.23, which shows the field profiles for Hexagonal and ES-PCFs, that at bending radius,  $R = 40\text{mm}$ , the mode is still confined in the core for the ES-PCF but the mode has leaked more into the cladding in the case of the Hexagonal PCF.

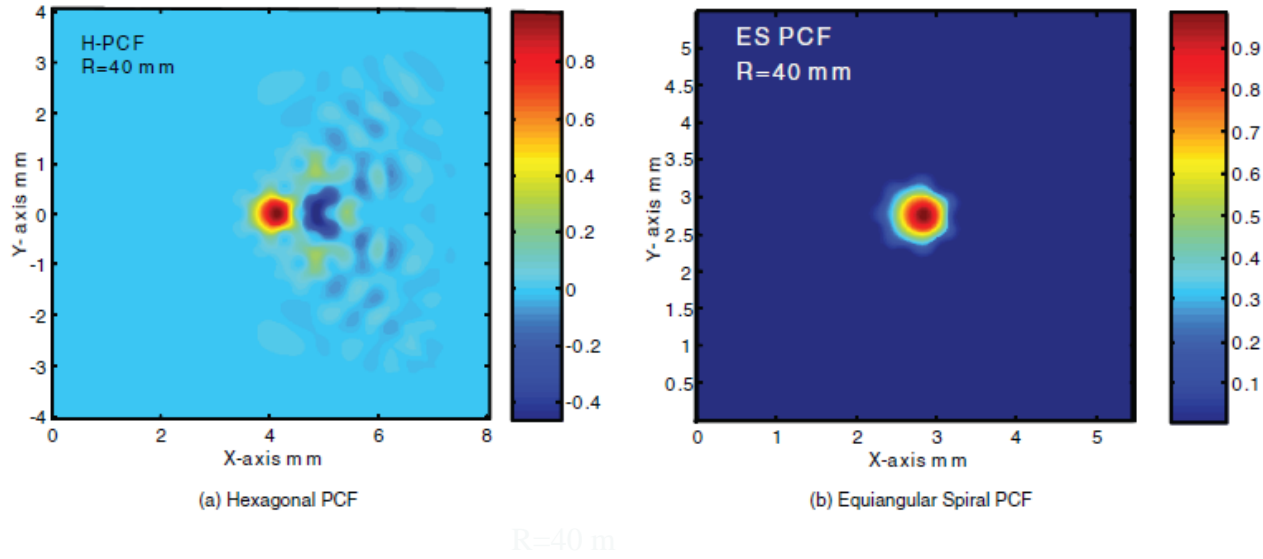


Fig. 7. 23: Field profile of the fundamental mode in the bent Hexagonal PCF (mode leaking into cladding region) and the equiangular spiral PCF with bend radius 40mm.

It has been observed through our work that the equiangular spiral PCF has ultra low bending loss and very low confinement loss compared to conventional Hexagonal PCF (H-PCF). The equiangular spiral PCF has excellent modal confinement properties, together with several parameters to allow the optimization of the performance over a range of important characteristics. The full vector Finite Element simulation has been used to characterize the design which can be fabricated by a range of techniques including extrusion and drilling. Recently, very low loss operation in a PCF made from TOPAS polymer has been demonstrated (Nielsen *et al.* 2009) and a new class of porous fibres have also been reported (Atakarmians *et al.* 2008; Hassani *et al.* 2008a; Dupuis *et al.* 2009), though achieving high porosity is not trivial (Dupuis *et al.* 2009). Here, an Equiangular Spiral (ES) PCF design as inspired by nature (Agrawal *et al.* 2009; Agrawal *et al.* 2011) in TOPAS has been presented for THz frequencies. This equiangular spiral PCF shows significantly better performance over loss compared to the conventional Hexagonal PCF (H-PCF). Spiral curves appear in plant and animal life forms as well as huge structures such as galaxies. The equiangular design presented here is adapted from the original design reported previously by our group (Agrawal *et al.* 2009; Agrawal *et al.* 2011).

#### 7.4 Low-Loss Porous Core Photonic Crystal Fibre

Although, in a PCF, a large part of the power is in the air-holes, however, results shown above for PCF with both the Hexagonal and equiangular arrangements in Teflon and

TOPAS indicate significant modal and bending loss as material loss is significant in this frequency range. So, next a novel porous core PCF is considered. It has also been reported that polystyrene foam (Zhao *et al.* 2002), with its large air fraction ratio, can have lower overall material loss, but with its refractive index close to 1.02, it needs not only air cladding for total internal reflection (TIR) based guidance, but also a larger dimension to confine most of the THz waves in its core: this is difficult for many practical applications.

Following the principle of Bragg guidance in optical fibre, hollow core designs have also been considered for guiding THz waves (Skorobogatiy and A. Dupuis 2007; Lu *et al.* 2008). Neilsen *et al.* (Nielsen *et al.* 2011) have also reported a microstructured core and honeycomb bandgap THz fibre. However, it is well known that these are narrow-band waveguides and strict periodicity needs to be maintained to satisfy the Bragg conditions (Okamoto 2006).

Recently, it has been shown that in silicon slot waveguides (Almeida *et al.* 2004; Leung *et al.* 2012), light can be guided in the low index air region. Using this concept, Nagel *et al.* (Nagel *et al.* 2006) have reported the use of sub-wavelength air-hole within a solid silica core to increase the power fraction within the air-hole to reduce the loss. Similarly, Kejalakshmy *et al.* (Kejalakshmy *et al.* 2009) have reported on a Teflon photonic crystal fibre (PCF) with metal-clad hollow defect-core supporting plasmon modes for possible THz sensing applications.

Recently, Hassani *et al.* (Hassani *et al.* 2008b) and Ung *et al.* (Ung *et al.* 2011) have also reported a porous core design to take advantage of the guiding offered through the low-loss air-holes. In this case, they have used a relatively larger  $d/\Lambda$  ratio to have a larger power fraction in the air-holes (where  $d$  is the air-hole diameter and the pitch,  $\Lambda$ , is the centre-to-centre distance between two adjacent air-holes). However, as a large  $d/\Lambda$  is used in this case, the equivalent index of the core was very low and the authors had to consider air cladding for the TIR. As a consequence they also had to consider a large core diameter, which was 70 times the operating wavelength; equal to 21 mm for mode confinement as the index contrast between the porous core and air-cladding was very small. In their work (Hassani *et al.* 2008b) they report the maximum confinement in the air-holes of the core was around 58% and in that design, the total power in the air

was around 80%, which indicates that remaining 20% power was confined in the solid PE. They have also mentioned that total confinement in the PE could be as low as 8%, and in that case the expected loss value would be only 10dB/m.

In this section, a novel concept, using porous core and also porous cladding, is discussed. In this case the  $d/\Lambda$  ratio of the cladding air-holes must be larger than that in the core to create a differential refractive index contrast to confine the THz waves within the waveguide. In this case, all the power will be fully confined inside the waveguide and the system performance will not be affected by the surrounding medium. Here, optimization of the power fraction in the air-holes is shown, with the fabrication parameters, including their bending loss calculations.

#### 7.4.1 Numerical Solution for Porous-Core PCF

In this study a Teflon PCF is considered with the number of air-hole rings,  $N_{\text{clad}} = 4$  in the cladding and also  $N_{\text{core}} = 4$  in the core. To achieve the maximum porosity, at the centre of the core a similar air-hole is considered rather than a solid rod. In this case, if the outer pitch,  $\Lambda_o$ , is equal to diameter of the porous core ( $D$ ), which is 9 times ( $2 * N_{\text{core}} + 1$ ) the inner pitch,  $\Lambda_i$ , then it would be easier to use the conventional stack-and-draw technique to fabricate such a porous-core PCF. The refractive index of Teflon is taken to be 1.445. In this case, the bulk material loss for Teflon has been considered to be  $0.3 \text{ cm}^{-1}$  or 130 dB/m (Hassani *et al.* 2008b), at 1 THz. This gives the imaginary part of the refractive index as 0.000715 at the operating frequency of 1 THz ( $\lambda = 0.3\text{mm}$ ), which is used in this work. The overall structure has a two-fold symmetry, so only a quarter of the PCF is simulated as shown in Fig. 7.24. In total, 80,000 first order triangular elements of different sizes are used to represent a quarter of the structure. The porous core is also shown as an inset at the top right corner of this figure.

It has been mentioned that the inner air-hole diameter/pitch ratio ( $d_i/\Lambda_i$ ) in the core needs to be smaller than that of the cladding ( $d_o/\Lambda_o$ ) to have a higher equivalent index necessary to support the TIR guidance. In this case, initially ( $d_i/\Lambda_i$ ) is taken as 0.5 and ( $d_o/\Lambda_o$ ) = 0.8. Variations of the effective index and the mode-size areas with the outer-pitch,  $\Lambda_o$ , are shown in Fig. 7.25. It can be observed that as the pitch value is reduced, the effective index of the fundamental  $H_{11}^x$  mode is also reduced shown by a solid line.

The cutoff condition is reached when the effective index approaches the equivalent index, often designated as the  $n_{\text{fsm}}$  (Kejalakshmy *et al.* 2009), of the cladding. For this structure, the 90 degrees rotational symmetry is nearly satisfied, so the modal properties of the quasi-TE ( $H_{11}^y$ ) and quasi-TM ( $H_{11}^x$ ) modes would be almost identical.

Variations of the mode-size areas with the pitch are also shown in Fig. 7.25. There have been different definitions used to quantify this mode-size area and for a Gaussian shaped field profile they give identical results as shown in Chapter 6. It can be observed that as the outer pitch,  $d_o/\Lambda_o$ , is reduced, initially the mode-size areas reduce since the core size is also being reduced. All three mode area definitions give similar values when  $\Lambda_o = 0.45\text{mm}$ , as in this case the field profile is close to a Gaussian shape. However, when the pitch is reduced further, the mode-size areas start to increase as the mode approaches its cutoff condition. In this case, a greater amount of the modal field will extend into the cladding areas. It should be noted that when  $\Lambda_o$  is reduced, the inner pitch,  $\Lambda_i$ , is also reduced to maintain their constant ratio to be 9, necessary for this design with  $N_{\text{core}} = 4$ .

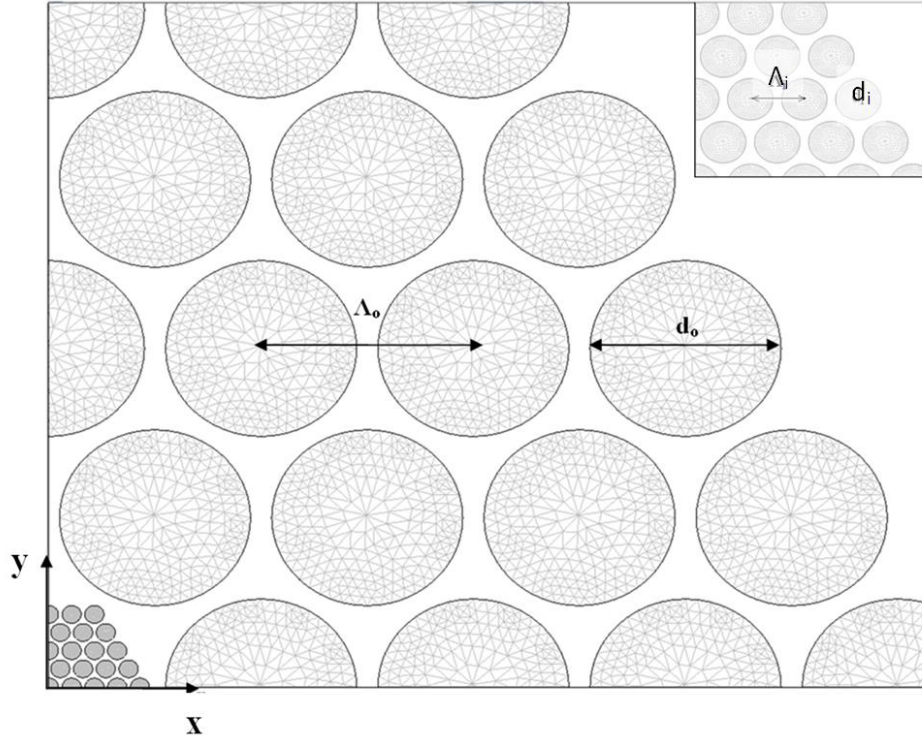


Fig. 7. 24: Representation of the porous core PCF cross-section with  $N_{\text{core}} = 4$ ,  $N_{\text{clad}} = 4$ .  $\Lambda_o$  = outer pitch and  $d_o$  = outer radius. Inset shows  $\Lambda_i$  = inner pitch and  $d_i$  = inner radius.



The variations of the power confinement in various regions with the outer pitch,  $\Lambda_o$ , are shown in Fig. 7.26. The power confinement factor,  $\Gamma$ , was determined for different regions of the porous core PCF, normalized to the total power. The confinement factor can be calculated by integrating the Poynting vector over a given region,  $\Omega_i$  as:

$$\Gamma_i = \int_{\Omega_i} \{\mathbf{E}^* \times \mathbf{H}\} d\Omega \quad (7.3)$$

Therefore, the confinement ratio is  $\Gamma = \Gamma_i / \Gamma_{total} = \int_{\Omega_i} \{\mathbf{E}^* \times \mathbf{H}\} d\Omega_i / \int_{\Omega} \{\mathbf{E}^* \times \mathbf{H}\} d\Omega$ ,

Where  $\mathbf{E}$  is the electric field and  $\mathbf{H}$  is the magnetic field of the mode. In this full-vectorial approach, all the six components of the  $\mathbf{E}$  and  $\mathbf{H}$  fields are used for the calculation of the confinement factors. Four regions have been clearly identified, air-holes in core, Teflon in core, air-holes in cladding and Teflon in cladding as  $\Gamma_{aircore}^a$ ,  $\Gamma_{solidcore}^t$ ,  $\Gamma_{airclad}^a$ , and  $\Gamma_{solidclad}^t$ , respectively.

It can be observed that as the pitch,  $\Lambda_o$ , is reduced, the power in the Teflon-core region,  $\Gamma_{solidcore}^t$ , shown by stars, initially increased and then subsequently reduced as the mode approaches its cutoff, when most of the power extends into the cladding. Similar features were shown for the power in the air-holes of the core region,  $\Gamma_{aircore}^a$ , represented by squares. On the other hand, the power in the solid Teflon area of the clad,  $\Gamma_{solidclad}^t$ , shown by triangles, initially reduces with the pitch,  $\Lambda$  and then increases when the mode approaches its cutoff condition and the power extends further into the cladding. However, the power in the cladding air-holes,  $\Gamma_{airclad}^a$ , shown by circles, monotonically increases as the pitch,  $\Lambda_o$ , is reduced and increases more rapidly when the cutoff condition approaches. It can be observed that the maximum confinement in the Teflon core,  $\Gamma_{solidcore}^t$ , is about 52% whereas the confinement in the air-holes in core,  $\Gamma_{aircore}^a$ , is only 17%, when the outer-pitch,  $\Lambda_o = 0.35$  mm. To understand the complex interaction between these parameters, the field profiles for two pitch values are shown in Fig. 7.28 and Fig. 7.29.

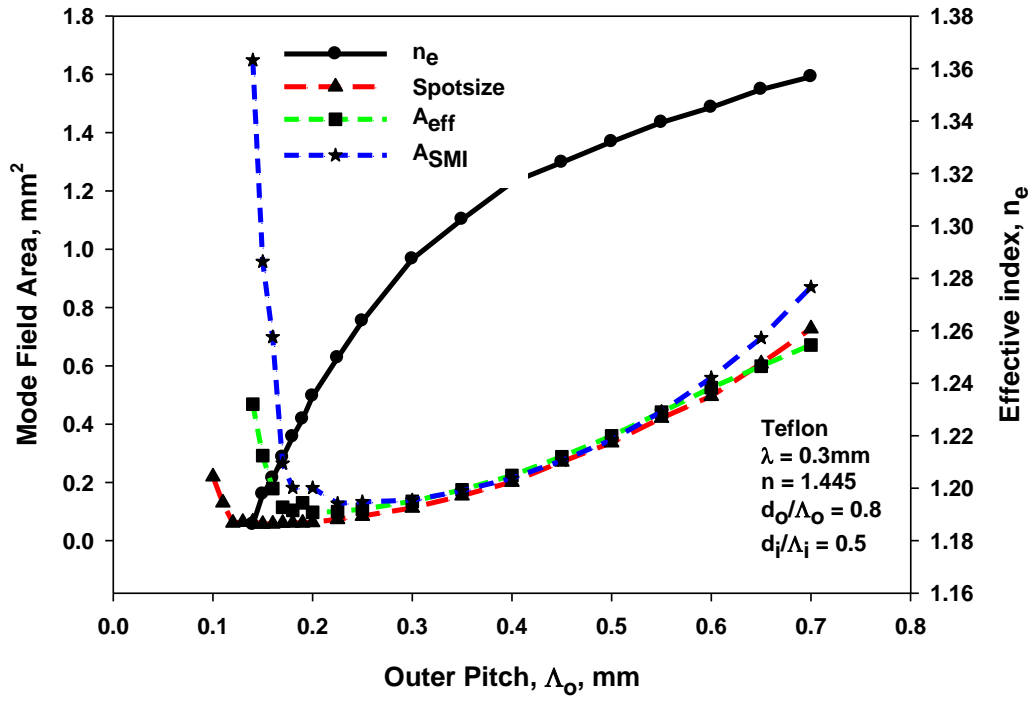


Fig. 7. 25: Variations of the mode field areas and effective index with the pitch,  $\Lambda_o$  for  $d_o/\Lambda_o = 0.8$  and  $d_i/\Lambda_i = 0.5$  for  $H_{11}^x$  Mode.

In Fig. 7.25 the mode field area and the effective index against the outer pitch radius are presented. In this case  $d_o/\Lambda_o = 0.8$  and  $d_i/\Lambda_i = 0.5$ . The mode field areas decreases as the outer pitch is decreased but start to increase again at the cutoff region. This is similar to previous results obtained.

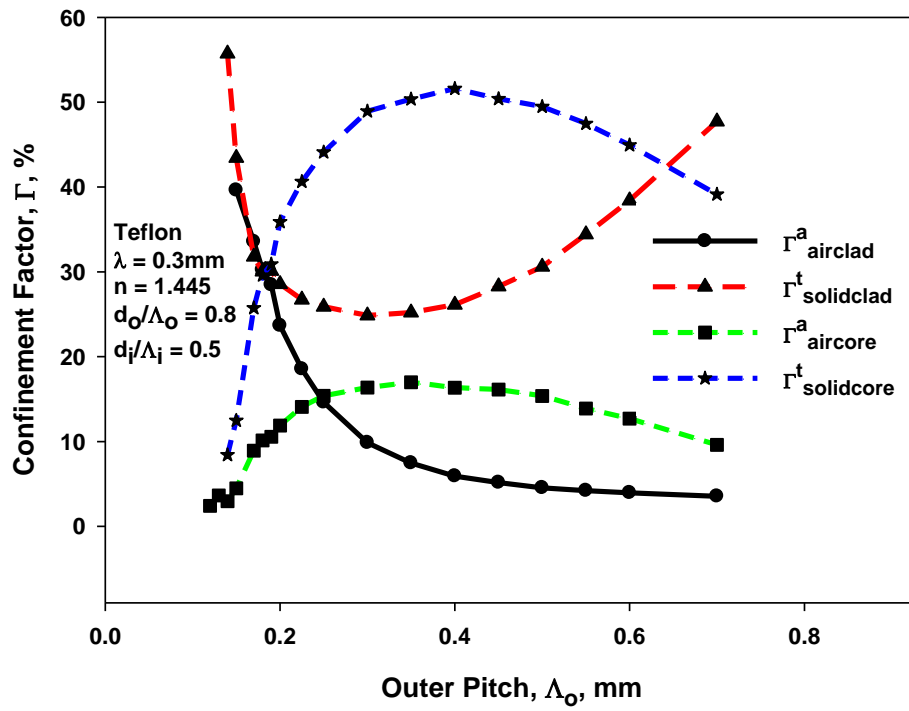


Fig. 7. 26: Variation of the confinement factors with the outer pitch,  $\Lambda_o$ , for  $d_o/\Lambda_o = 0.8$  and  $d_i/\Lambda_i = 0.5$ .

Figure 7.27 shows the variation of the confinement factors with outer pitch for  $d_o/\Lambda_o = 0.8$  and  $d_i/\Lambda_i = 0.5$ . The maximum confinement in the solid core is 52% whereas that in the air core is 15%.

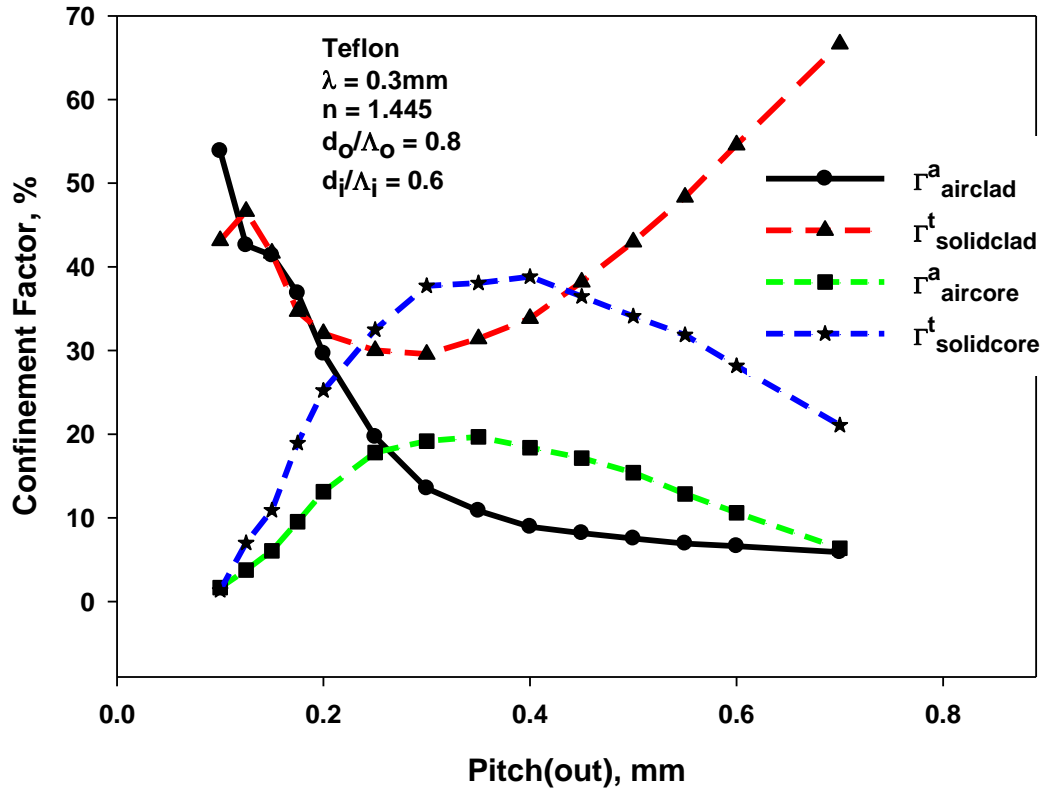


Fig. 7. 27: Variation of the confinement factors with the outer pitch,  $\Lambda_o$ , for  $d_o/\Lambda_o = 0.8$  and  $d_i/\Lambda_i = 0.6$ .

Figure 7.27 shows the variation of the confinement factors with outer pitch for  $d_o/\Lambda_o = 0.8$  and  $d_i/\Lambda_i = 0.6$ . The maximum confinement in the solid core is 39% whereas that in the air core is 18%.

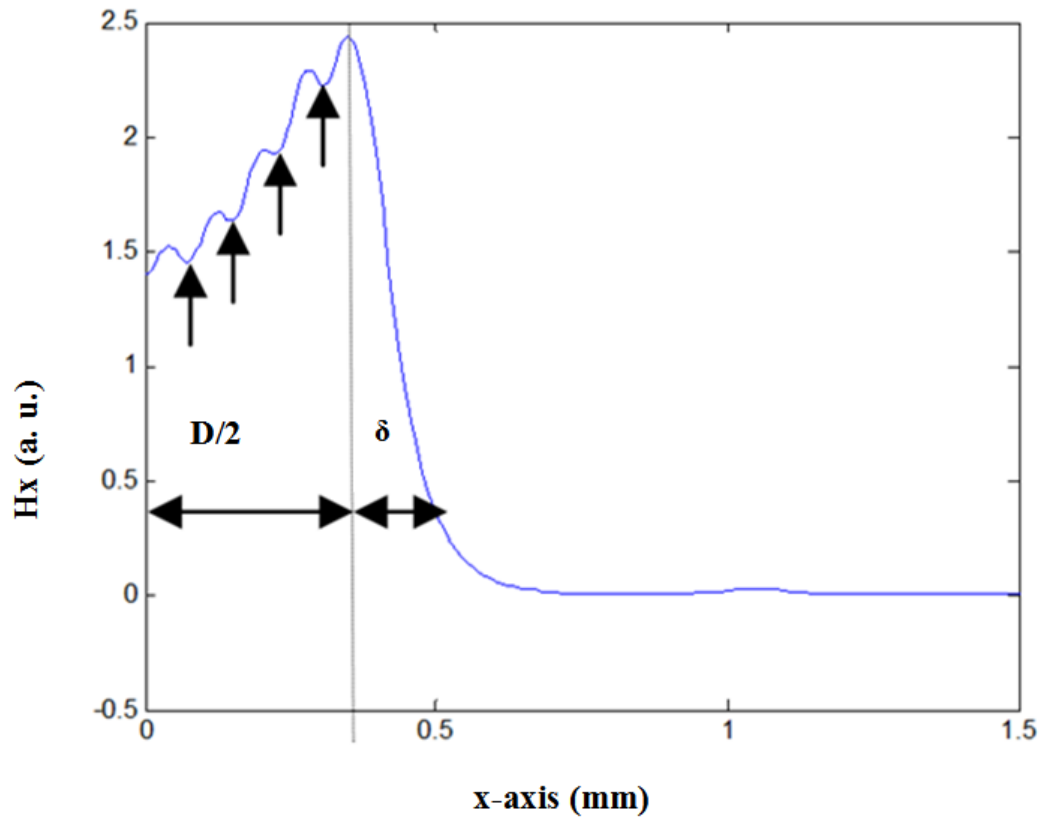


Fig. 7. 28: Variations of the  $H_x$  field of the  $H_{11}^x$  mode along the x-axis for  $\Lambda_o = 0.7$ mm.

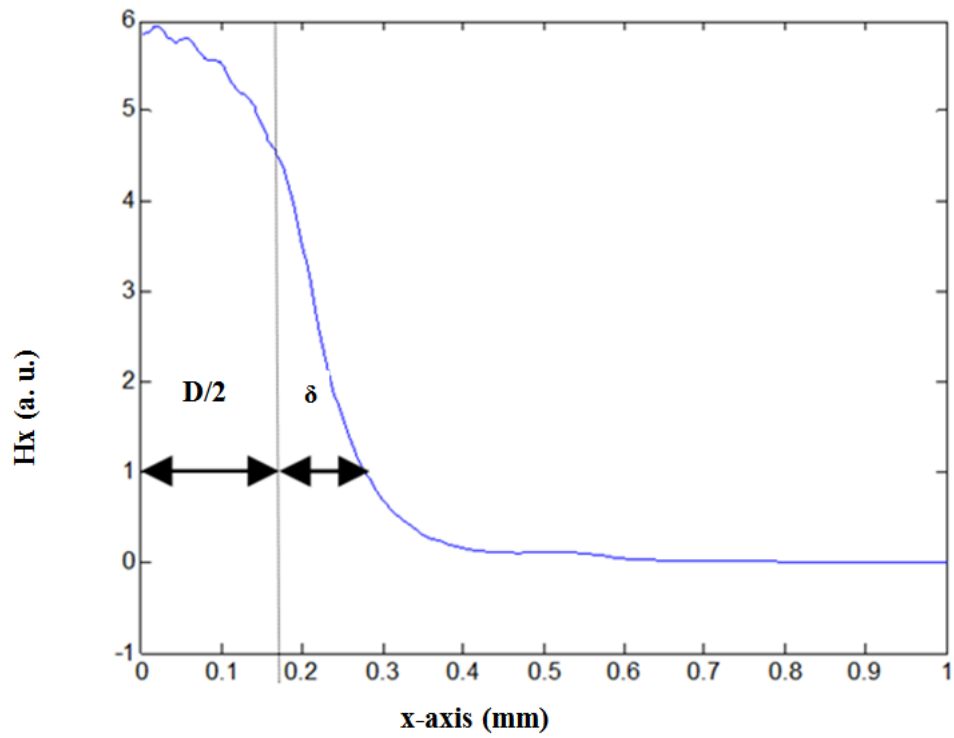


Fig. 7. 29: Variations of the  $H_x$  field of the  $H_{11}^x$  mode along the x-axis for  $\Lambda_o = 0.35\text{mm}$ , when  $d_o/\Lambda_o = 0.8$ , and  $d_i/\Lambda_i = 0.50$ .

The variations of the  $H_x$  fields of the fundamental  $H_{11}^x$  mode along the horizontal axis are shown in Fig. 7.28 and Fig. 7.29 for two different pitch values. For a higher pitch value,  $\Lambda_o = 0.7\text{mm}$ , the field profile shown in Fig. 7.28 demonstrate a reasonably well-confined mode inside the core with its decay length ( $1/e$  of the maximum field) as  $\delta = 0.12\text{ mm}$ . The field variation inside the core clearly shows the presence of the 5 air-holes (shown by arrows), along the x-axis with their local field minima. In this case, near the outer air-hole ring (of the inner core), the modal field shows its maximum value due to the presence of a large solid Teflon areas just before the first air-hole ring in the cladding. In this case, total confinement in the core was around 50%. On the other hand, for a smaller outer-pitch value,  $\Lambda_o = 0.35\text{mm}$  as shown in Fig. 7.29 field is more confined in the core ( $\Gamma_{\text{core}} = 52\%$ ), but associated with a slower decay (decay length  $\delta = 0.18\text{ mm}$ ) in the cladding.

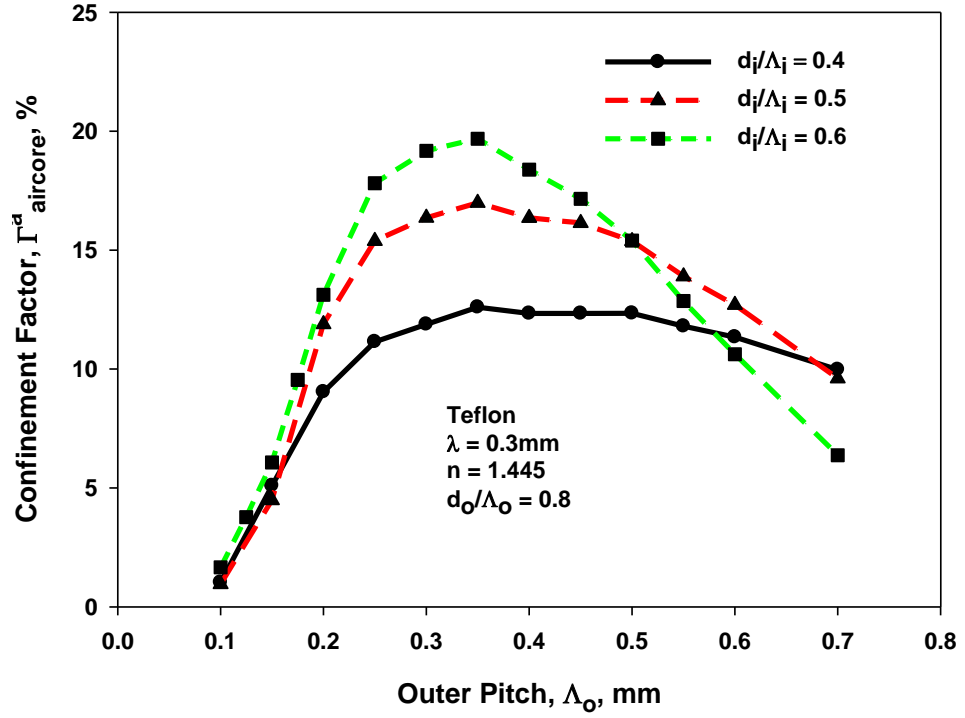


Fig. 7. 30: Variation of the confinement factor in the core air-holes,  $\Gamma^a_{\text{aircore}}$ , with the outer pitch  $\Lambda_o$  for  $d_o/\Lambda_o = 0.8$  but with different  $d_i/\Lambda_i$  values.

The variations of the power confinements in the core air-holes with the outer pitch,  $\Lambda_o$ , are shown in Fig. 7.30 for a given  $d_o/\Lambda_o$  value, but with three different  $d_i/\Lambda_i$  values. It can be observed that as the outer pitch,  $\Lambda_o$  is reduced, the power confinement in the core

air-holes,  $\Gamma_{\text{aircore}}^a$ , increases and reaches a maximum value. A further reduction of the pitch value brings this mode closer to cutoff and the mode field extends in the outer cladding so  $\Gamma_{\text{aircore}}^a$  reduces. It is also shown that as the  $d_i/\Lambda_i$  increases from 0.4 to 0.6, the maximum confinement in the core air-holes,  $\Gamma_{\text{aircore}}^a$ , also increases. This maximum value is identified as  $\Gamma_{\text{air-core}}^{\text{max}}$ . It can be observed here that in all the 3 cases, the maximum power in the core was obtained when the outer pitch,  $\Lambda_o$  was around 0.35 mm. However, there is a limit to the increment of the value of  $d_i/\Lambda_i$ , as this needs to be lower than the outer  $d_o/\Lambda_o$  value to have sufficient index contrast for the TIR guidance. To increase the air-filling area and also to avoid the field localization at the core-cladding interface, it was considered to increase both the  $d_i/\Lambda_i$  and  $d_o/\Lambda_o$  values to reduce the solid Teflon area near the core-cladding boundary.

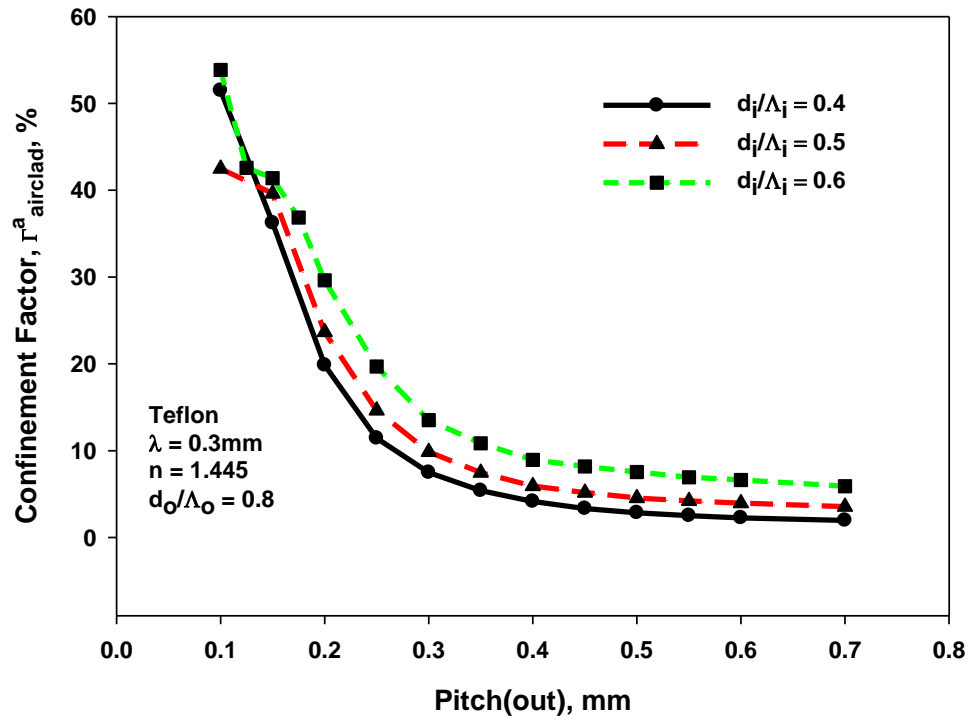


Fig. 7. 31: Variation of the confinement factor in the core air-holes,  $\Gamma_{\text{airclad}}^a$ , with the outer pitch  $\Lambda_o$  for  $d_o/\Lambda_o = 0.8$  but with different  $d_i/\Lambda_i$  values.

The variations of the power confinements in the air cladding region with the outer pitch,  $\Lambda_o$ , are shown in Fig. 7.31. As the outer pitch is reduced the air cladding confinement increases as the modes approach cutoff and field expands into the cladding.



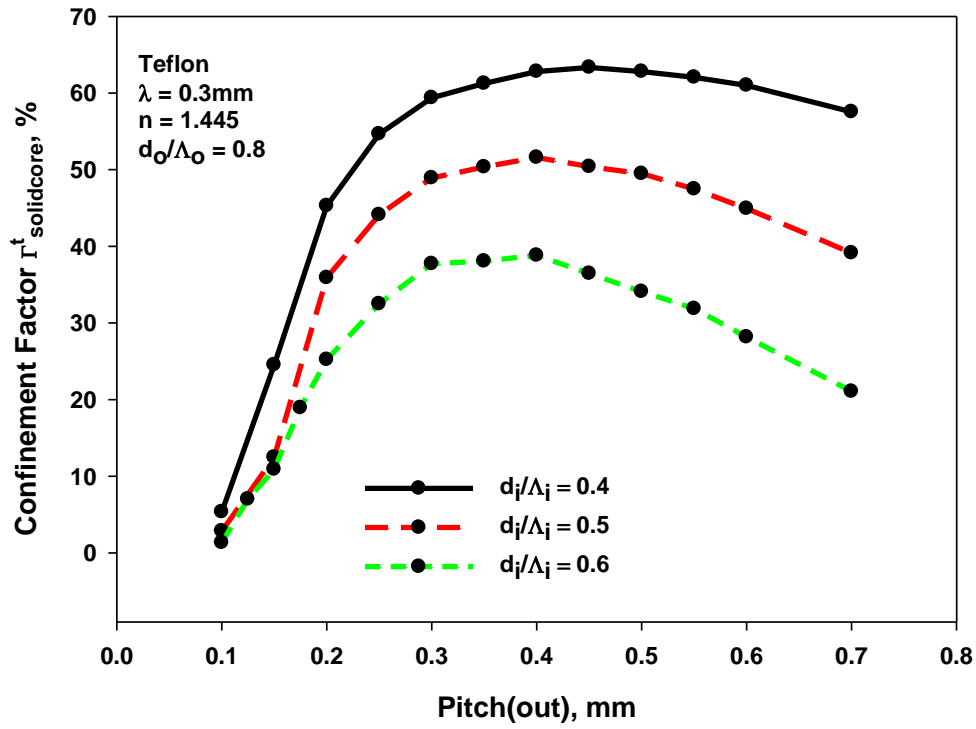


Fig. 7. 32: Variation of the confinement factor in the core air-holes,  $\Gamma^a_{\text{solidclad}}$ , with the outer pitch  $\Lambda_o$  for  $d_o/\Lambda_o = 0.8$  but with different  $d_i/\Lambda_i$  values.

The variations of the power confinements in the solid core with the outer pitch,  $\Lambda_o$ , are shown in Fig. 7.32. The curves of  $d_i/\Lambda_i = 0.4$ , 0.5 and 0.6 are presented. As can be observed, the confinement factor increases as the outer pitch is increased, it reaches the maximum at outer pitch = 0.35mm.

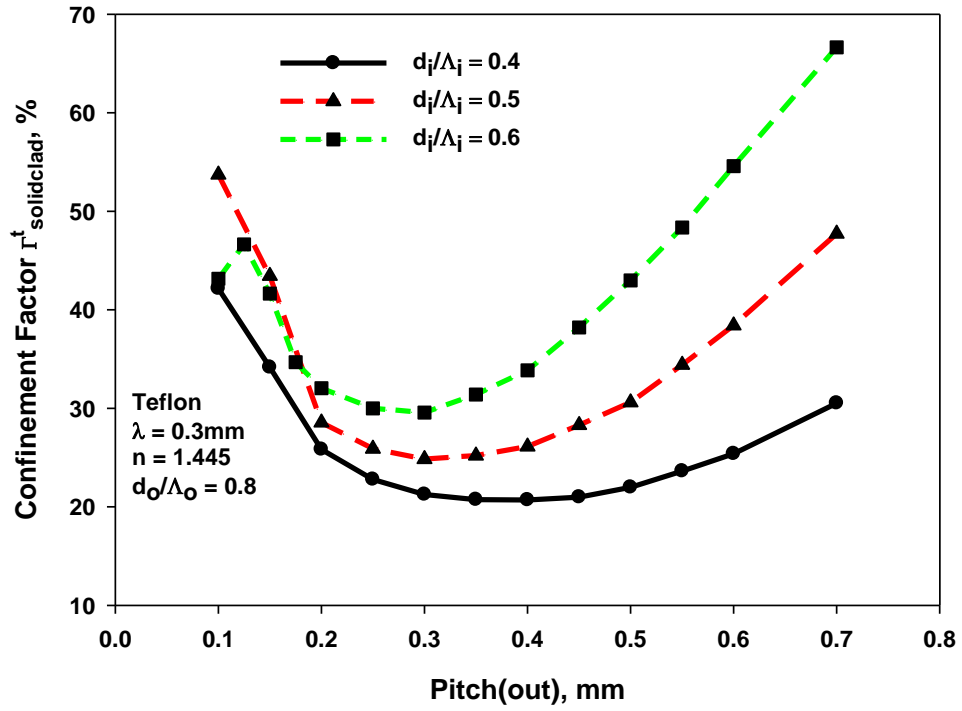


Fig. 7. 33: Variation of the confinement factor in the core air-holes,  $\Gamma_{\text{solidclad}}^{\text{clad}}$ , with the outer pitch  $\Lambda_o$  for  $d_o/\Lambda_o = 0.8$  but with different  $d_i/\Lambda_i$  values.

The variations of the power confinements in the solid cladding with the outer pitch,  $\Lambda_o$ , are shown in Fig. 7.33. The curves of  $d_i/\Lambda_i = 0.4, 0.5$  and  $0.6$  are presented. As can be observed, the confinement factor decreases as the outer pitch is increased, it reaches the minimum at outer pitch = 0.35mm.

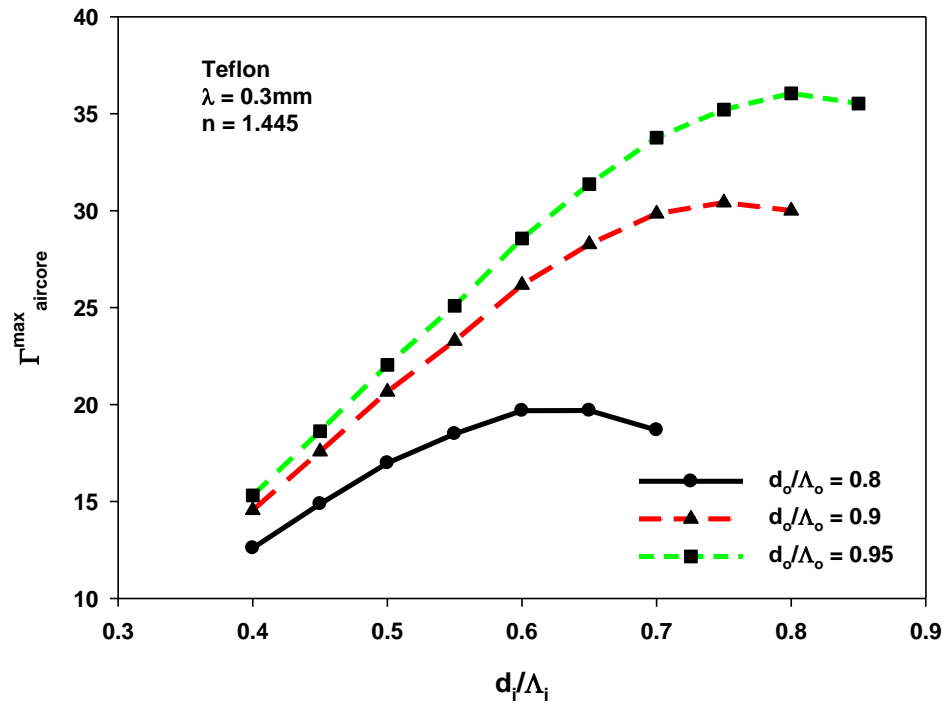


Fig. 7. 34: Variation of the maximum confinement factor in the air core with the  $d_i/\Lambda_i$  for some fixed  $d_o/\Lambda_o$  values.

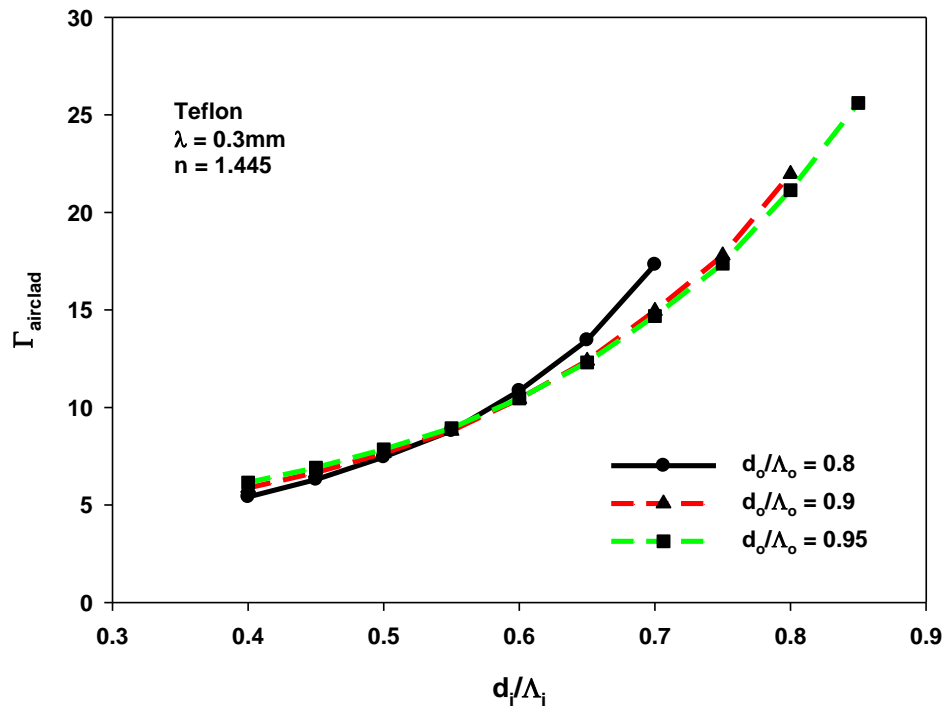


Fig. 7. 35: Variation of the maximum confinement factor in the air cladding with the  $d_i/\Lambda_i$  for some fixed  $d_o/\Lambda_o$  values.

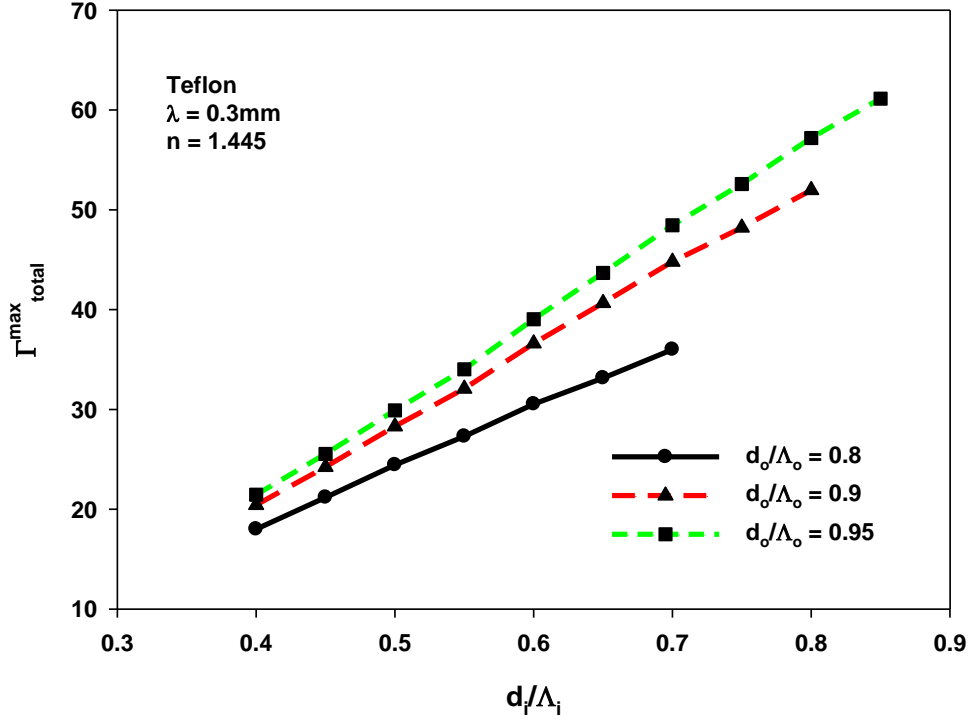


Fig. 7. 36: Variation of the total maximum confinement factor in the air core and air cladding with the  $d_i/\Lambda_i$  for some fixed  $d_o/\Lambda_o$  values.

Further, besides varying the  $\Lambda_o$  and the inner  $d_i/\Lambda_i$  values, the outer  $d_o/\Lambda_o$  values are also adjusted to get the maximum confinement in the core air-holes,  $\Gamma_{air-core}^{max}$ . The variations of the maximum power confinement in the air core, with the inner  $d_i/\Lambda_i$  are shown in Figs. 7.34. For given values of  $d_o/\Lambda_o$  and  $d_i/\Lambda_i$ , the pitch  $\Lambda_o$  is adjusted to achieve the maximum power confinement in the core air-holes,  $\Gamma_{air-core}^{max}$ . The variation of this value with  $d_i/\Lambda_i$  is shown for a fixed  $d_o/\Lambda_o$ . It was noted that for most of the cases, the outer pitch,  $\Lambda_o$  was around 0.35mm to achieve the maximum confinement in the core air-holes. It can be observed that as the value of  $d_i/\Lambda_i$  is increased, the maximum power confinement in the core air-holes also increases. However, a further increase in  $d_i/\Lambda_i$  reduces the index contrast between the core and cladding and  $\Gamma_{air-core}^{max}$  reduces as more power is extended in the cladding. It can also be noted that  $\Gamma_{air-core}^{max}$  increases as the  $d_o/\Lambda_o$  is increased. It can be observed that total power in the air-holes (both in core and cladding) reaches 58%, when  $d_o/\Lambda_o = 0.95$  and  $d_i/\Lambda_i = 0.85$ . By increasing the ratio,  $d_o/\Lambda_o$ , the maximum confinement in the air-holes,  $\Gamma_{max}$  also

increases but this also needs a higher value of  $d_i/\Lambda_i$ . It is noted here that reducing the difference between the outer/inner  $d/\Lambda$  ratios increases the maximum power confinement in the core air-holes. If it is possible to increase  $d_i/\Lambda_i$  to more than 0.85 (and  $d_o/\Lambda_o$  more than 0.95), the power fraction in the air-holes can be increased further. In the design reported (Hassani *et al.* 2008b)  $d_i/\Lambda_i$  has been considered as 0.95 and as a consequence, it had been necessary to consider an air-cladding (porous cladding with air-holes is not possible) to achieve the index contrast necessary for the TIR guidance and thus exposing the mode to external environmental influences.

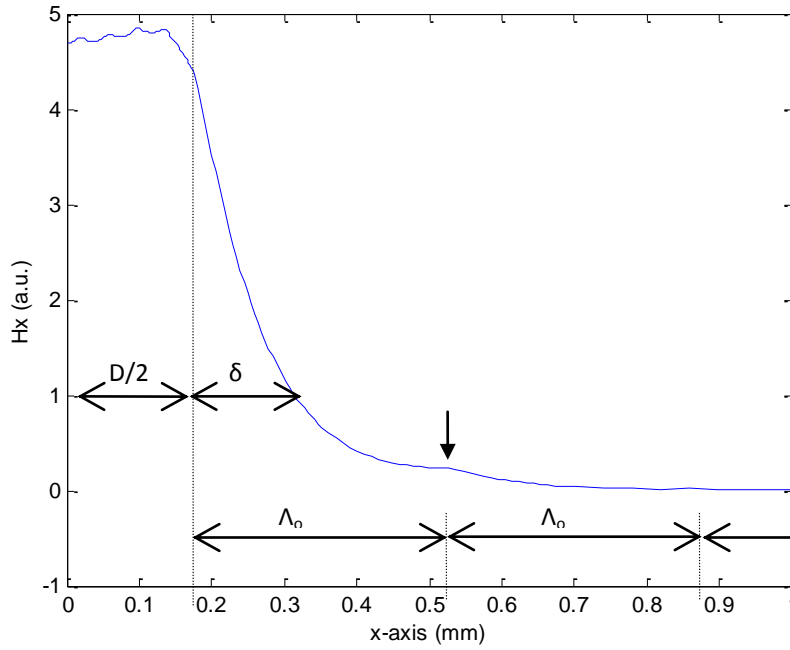


Fig. 7. 37: Variation of the  $H_x$  field along the  $x$ -axis for the  $H_{11}^x$  mode when  $\Lambda_o = 0.35\text{mm}$ ,  $d_o/\Lambda_o = 0.95$  and  $d_i/\Lambda_i = 0.85$ .

Figure 7.37 shows the  $H_x$  field variation along the  $x$ -axis for the fundamental mode  $H_{11}^x$  mode when  $\Lambda_o = 0.35\text{mm}$ ,  $d_o/\Lambda_o = 0.95$  and  $d_i/\Lambda_i = 0.85$ , a combination which achieved the maximum power confinement in the air-holes. Here the field profile is almost constant within the core with small ripples due to the presence of the air-holes inside the core. In this case, the index contrast between core and cladding is smaller and the field extends in the cladding region with the  $1/e$  decay length given by 0.23 mm but most of the power is well confined inside the waveguide. One local field maximum is shown by an arrow identifying the location between the 1<sup>st</sup> and 2<sup>nd</sup> air-hole rings where the field

value is about 0.004% of the maximum field. This also signifies that the THz energy is well confined inside the cladding and does not extend outside the waveguide, unlike the waveguides with air-cladding (Hassani *et al.* 2008b), when the field extends in the air cladding and the mode would be influenced by both environmental factors and bending.

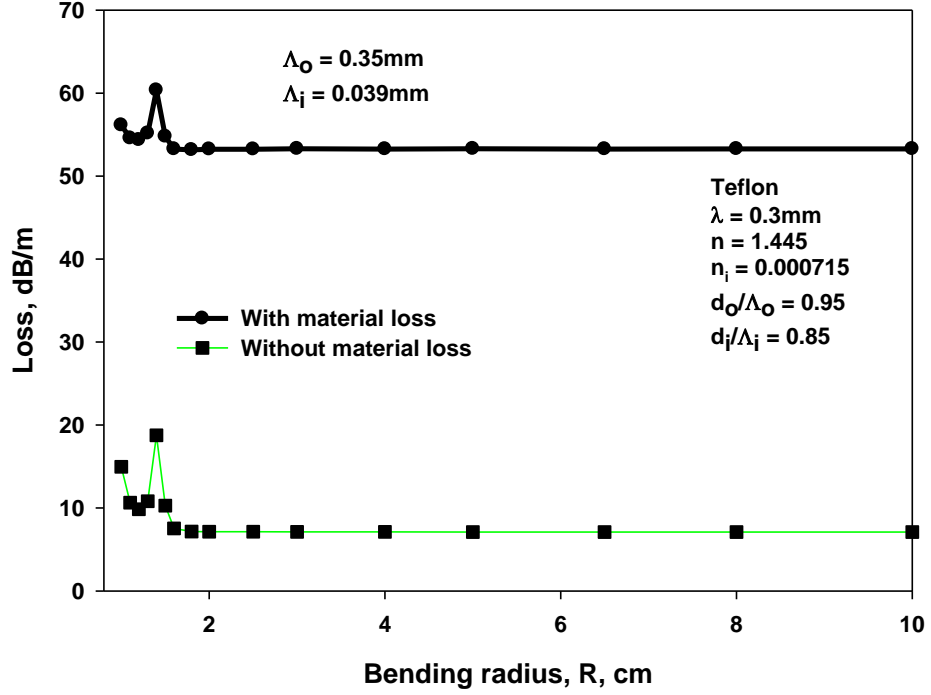


Fig. 7. 38: Variation of bending loss with bending radius, R at  $\Lambda_o = 0.35\text{mm}$  and  $\Lambda_i = 0.039\text{mm}$ .

Modal loss and the bending loss of this porous core PCF have also been studied from Chapter 4. In this analysis, a Conformal Transformation (Heiblum and Harris 1975; Rahman *et al.* 2011) was carried out to obtain the equivalent index of a bent PCF and PML regions (Berenger 1996; Rahman *et al.* 2009) are introduced to absorb the leaking power. For a bent PCF, only one-fold symmetry is available and symmetry along the vertical axis is destroyed. Figure 7.38 shows the variation of the loss values for a bent PCF with the bending radius, R. In this case, for the porous core PCF, the parameters are taken to be  $\Lambda_o = 0.35\text{mm}$ ,  $d_o/\Lambda_o = 0.95$ , and  $d_i/\Lambda_i = 0.85$ . Initially the material loss is ignored and the bending and leakage loss is shown by a dashed curve with solid squares. When bending radius is large, the loss value is around 8 dB/m, which identifies the leakage loss only. If necessary, this leakage loss can be further reduced by increasing the number of rings in the cladding region (in the present simulation  $N_{\text{clad}} = 4$

is considered) or by increasing the  $d/\Lambda$  value of the outer rings. When the bending radius,  $R$  is reduced the total loss value increases, which now includes the bending loss. It can be noted that for this particular design, the bending loss is negligible when the bending radius,  $R$ , is above 2 cm. However, as the material loss is the dominant loss-contributing factor, when this is added by considering the imaginary part of the complex refractive index of Teflon, the total loss is shown by a solid line with solid circles. It can be identified that the material loss dominates with its value around 53 dB/m. However, this value is considerably less than that of a solid core Teflon PCF, which could be as high as the bulk material loss, this being 130dB/m. It can be noted that the loss value peaks when  $R = 1.4$  cm, and this is due to the mode coupling between the PCF mode and a cladding mode and appearance of such more degeneration was reported earlier (Rahman *et al.* 2009).

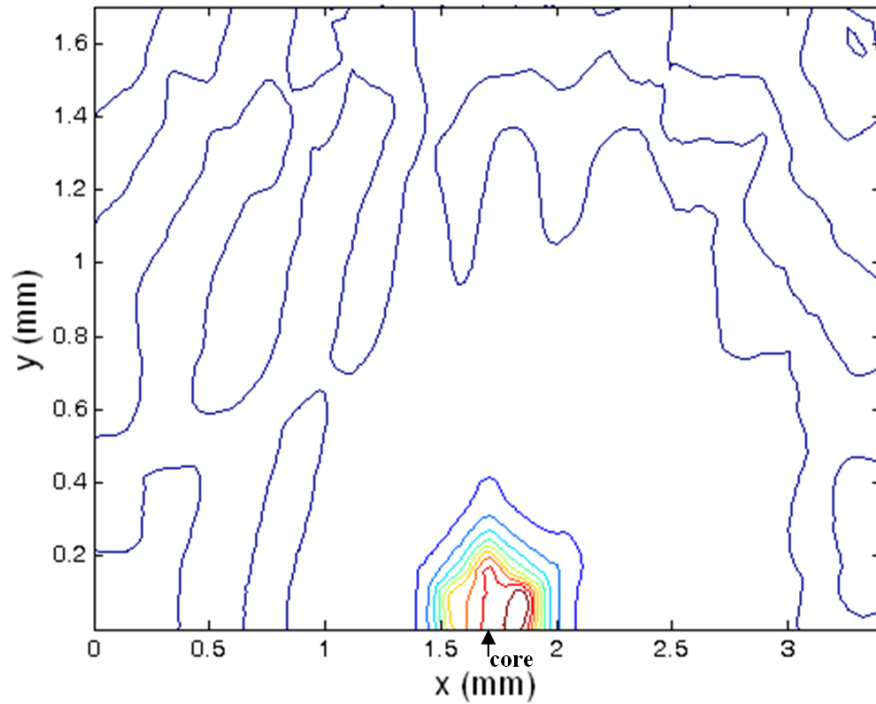


Fig. 7. 39:  $H_x$  field profile of the bent PCF for the fundamental  $H_{11}^x$  mode for bending radius, 1.5 cm.

The  $H_x$  field profile of the bent PCF for the fundamental  $H_{11}^x$  mode is shown in Fig. 7.39, when the bending radius is 1.5 cm. Only half of the PCF structure is shown, as symmetry along the horizontal axis was exploited during the simulation. It can be observed that the centre of the mode field has shifted towards the right (away from the



bending centre) and the influence of the air-holes in the first cladding ring is clearly visible.

## 7.5 Summary

The focus of this Chapter has been on PCF design for the THz band. Initially, an equiangular spiral PCF design has been presented which has shown the ability for very effective control of the modal field – in some cases better than the hexagonal design and thus allowing significantly lower bend loss. The fabrication of the equiangular spiral PCF should be possible using the extrusion and/or drilling and is not beyond present capabilities or more challenging than for other designs. Using porous core PCF the aim has been to reduce the effects of Material Loss. This is a novel design incorporating both a porous core and also a porous clad, this being a better design than a traditional PCF with porous cladding (Han *et al.* 2002; Goto *et al.* 2004) or a porous core (Hassani *et al.* 2008b; Ung *et al.* 2011) fibre with air-cladding. A rigorous full-vectorial modal solution approach is used to optimize the index contrast and the dimensions to maximize the power confinement in the air-holes.

It is shown here that by using a porous core along with the porous cladding of a conventional PCF, the power confinement in the air-holes can be significantly increased, which will reduce the effect of material loss by 60% for the solid Teflon. The overall loss value can be further reduced if the material loss can be reduced or the fabrication technology improved to allow a higher  $d/\Lambda$  value than 0.95 (for the outer  $d/\Lambda$ ), which is considered in this study. It has been shown the leakage loss and the bending losses for such a PCF are very small for practical applications. The manufacturing technology for PCF operating at optical frequencies has matured and PCFs with a sub-micron pitch are routinely being fabricated. Compared to that, PCF for THz frequencies with a pitch 100 times larger would be relatively easy to fabricate and such a PCF has also been fabricated (Han *et al.* 2002; Goto *et al.* 2004). In the design reported here, when a THz PCF with additionally porous core (Ung *et al.* 2011) is considered, the 20-40  $\mu\text{m}$  inner pitch dimensions are easily feasible and the fabrication process does not introduce any additional challenge. The design shown here, with a fixed  $\Lambda_o/\Lambda_i$  ratio depending on number of air-hole rings,  $N_{\text{core}}$ , in the core, would be compatible for more widely used draw-and-stack approaches. The availability of a low-

loss flexible waveguide will allow both distributing THz waves and also a waveguide to act as part of a functional device for processing the signals. The reliability and the performance of a THz system can be improved by having a compact, flexible, robust and low-loss waveguide for the remote delivery of high power.

## CHAPTER EIGHT: Conclusion and Further Work

### 8.0 Review of the Aims and Objectives of the Work

The broad aim of the work undertaken in this thesis was, as set out in Chapter 1, to Design, Characterize and Optimize Photonic Crystal Fibre (PCF) for practical applications with current optical systems. This was achieved in the work reported and in the examples chosen by implementing the rigorous full vectorial Finite Element Method (FEM) **H**-field formulation together with the conformal transformation and the Perfectly Matched Layer (PML) boundary. Several materials used in the simulations included silica for a wavelength of  $1.55\mu\text{m}$ , Teflon and TOPAS at frequencies around the 1 THz regions. Designs of PCF considered included Hexagonal PCF arrangements with cladding containing from 3 rings up to 10 rings with a solid core, Hexagonal PCF arrangement containing cladding with a porous core and PCF with Equiangular Spiral PCF air-hole arrangements.

The research carried out and presented in this thesis meets the specific objectives set out in Chapter 1 as discussed in summary below. The theoretical background of the finite element method based on the variational principle to perform modal analysis of various waveguide structures was presented in Chapter 3 with discussions beginning by introducing Maxwell's equations. The properties of various numerical methods often used in analysing waveguide problems were also briefly examined. An elaborate mathematical description given for the vector **H**-field based FEM formulation with some aspects of the method such as the boundary conditions, shape functions and methods aimed at eliminating spurious solutions analysed. Also, a rigorously convergent least squares boundary residual method is described for analysing the discontinuities in optical waveguides. The method is also capable of calculating the power transfer between two waveguides by obtaining the scattering matrix; and the role of the finite element program in utilising the LSBR technique.

Further, by applying the methods in Chapter 3, the aim has been to calculate the leakage and bending losses associated with the PCF for several designs by varying the pitch ( $\Lambda$ ) and diameter of air-holes ( $d$ ) thereby optimising the designs that would provide the

lowest loss and that would be less susceptible to bending for telecommunications applications at wavelength of  $1.55\mu\text{m}$ . The results obtained by applying the above discussed methods were presented in detail in Chapter 4 and also published in *Applied Optics*, as shown in the List of Publications. First, the origin of localized cladding modes in the silica bridging regions between the air-holes was studied and results presented. These silica bridging areas are smaller than the PCF core (where an air-hole is missing) and for a straight PCF; these modes with the lower effective indices do not interact with the PCF core mode. However, for a bent PCF, as the local equivalent index is increased in the cladding region, the dispersion slopes of these modes are higher and for smaller bending radii they can be phase matched to the core mode to form coupled supermodes. It was also shown that these cladding modes can also cover several bridging regions simultaneously and also support the higher order modes. This mode degeneration causes a mixing of these modes, the formation of the supermodes and the transformation from one mode to another. These cause rapid changes in their modal properties, their effective index, the spot size and the bending loss values. A higher pitch value which increases the silica bridging regions and such mode degeneration can even appear at a higher bending radius, which may often be encountered in practical applications.

Secondly, having established the optimal PCF designs and bending radii for low loss transmission, the first ring of air-holes was altered to increase the birefringence of the PCF for single mode single polarization guidance. This was also enhanced by controlling or reducing the bending radius of the PCF. The design of a Single Mode Single Polarization (SMSP) PCF was reported in Chapter 5 and also published in *Applied Optics* as shown in the List of Publications. The design approach was developed by exploiting the differential bending loss and then analyzed through the use of a rigorous full-vectorial FEM. It has been shown that, for asymmetry arrangement used in our work, the TM modal loss is higher than that of the TE mode. However, the differential LR increases with any excessive bending beyond a critical value of the bending radius. Such a critical bending radius can be tuned with a suitable adjustment of the value of  $d_2/\Lambda$ . The LR increases with the number of air-hole rings,  $N$ , in the PCF cladding. These results can be used to assist in designing the single polarization condition in a bent PCF. The PCF designs analysed are all single-mode guides when

operated closer to their cutoff conditions. Furthermore, the effects of structural asymmetry have also been carried out to evaluate the effect on the SMSP of a PCF due to bending for different air-hole orientations. Variations of the bending loss for the TE and TM modes with the operating wavelengths are also presented. Such a PCF, which only guides one polarization state, can be used for various linear, nonlinear and sensing applications. It is also shown here that the bending losses of  $H_{11}^x$  and  $H_{11}^y$  modes depend on the pitch,  $\Lambda$ , the asymmetry via the value of  $d_2/\Lambda$ , the number of rings,  $N$ , the operating wavelength and the bending radius and, so, the differential loss will depend on the fabrication tolerances relating to the parameters  $\Lambda$ ,  $d$ , and  $d_2$ . However, since the differential loss also depends on the bending radius, it is expected that, by adjusting the bending radius, the effect of the fabrication tolerances may also be compensated for a wide range of applications, such as attenuators or polarization maintaining applications.

Following that, an important issue that needed to be addressed was how to couple the PCF to a conventional single mode fibre or to other waveguides like the erbium doped fibre amplifier. This was investigated using the Least Squares Boundary Residual (LSBR) method in conjunction with the FEM and the power transmission at the boundary of discontinuity when butt coupling between the PCF and conventional fibre were obtained. A novel design approach for a PCF which could be considered as a candidate for efficient coupling to an optical fibre has been presented in Chapter 6 and also published in *IEEE Photonics Journal* as shown in the List of Publications. Initially various MFA parameters and field profiles for a SMF and a PCF were studied. It has been shown here that a smaller air-hole diameter and a larger number of rings would allow the  $A_{\text{eff}}$  value to reach a higher value, which can be achieved by operating a PCF near cutoff. However, its expansion near cutoff can be very rapid and unstable, but by increasing the air-hole diameter in the last ring, this parameter can be stabilized with the variation of the fabrication tolerances. Using this approach presented above, it is possible to avoid uncertainty resulting from the variations in the dimensions of the pitch or the diameters of the air-holes in the PCF as a result of fabrication or tapering, thereby ensuring that the PCF can be successfully coupled to an optical fibre without any significant loss in coupled power. Additionally, it is also shown here that the larger air-holes in the last ring can reduce the degeneration of the core mode with the cladding modes. During the tapering process it has been assumed that the pitch,  $\Lambda$ , reduces

gradually while keeping the  $d/\Lambda$  ratio constant. However, the air-holes can also collapse and the air-hole/pitch ratio can also change although this may give an additional flexibility or uncertainty but also an additional parameter to optimise the situation.

In closing, the application of the PCF to the Terahertz (THz) region as a low loss waveguide was also investigated. Several polymer materials were analyzed for this purpose and the conventional PCF was compared to an equiangular spiral PCF arrangement. This was presented in Chapter 7 and published in *AIP Advances* as shown in the List of Publications. An equiangular spiral PCF design has been presented which has shown the ability for very effective control of the modal field – in some cases better than the hexagonal design and thus allowing significantly lower bend loss. Further, the operating bandwidth of the equiangular spiral PCF can be larger than in porous fibres. The fabrication of the equiangular spiral PCF should be possible using extrusion and/or drilling.

Finally, a novel design of porous core PCF aimed at further reducing the leakage and bending losses in the THz regime was also investigated which provided some unique guiding properties. This is shown in Chapter 7 as well and published in *IEEE Photonics Journal* as shown in the List of Publications. Using a porous core PCF, it is shown here that it was possible to reduce the effects of Material Loss and thus, this novel design incorporating both a porous core and also a porous clad was studied, this being a better design than a PCF with porous cladding or that of a porous core fibre with air-cladding. It is shown that by using a porous core along with the porous cladding of a conventional PCF, the power confinement in the air-holes can be significantly increased, which reduced the effect of material loss by 60% for the solid Teflon. The overall loss value can be further reduced if the material loss can be reduced or the fabrication technology improved to allow a higher  $d/\Lambda$  value than 0.95 (for the outer  $d/\Lambda$ ), which is considered in this study. It has been shown that the leakage loss and the bending losses for such a PCF are very small for practical applications. The manufacturing technology for PCF operating at optical frequencies has matured and PCFs with a sub-micron pitch are routinely being fabricated. Compared to that, PCF for THz frequencies with a pitch 100 times larger would be relatively easier to fabricate. The reliability and the performance of a THz system can be improved by having a compact, flexible, robust and integrable waveguide for the remote delivery of high power.

## 8.1 General Conclusions and Directions for Further Work

Optical fibres have made a very significant impact on the world in general and the way we communicate with each other. This point is further emphasized by the fact that following the pioneering paper by one of the founding researchers in this field, Professor Charles K. Kao (Kao and Hockman 1966), he was awarded the Nobel Prize in 2009. This project has aimed to add to the body of knowledge in the field on optical fibre research, building on the brief history of the development of optical technology and basic modal properties of optical fibres presented at the beginning of the thesis. Next, the main focus of the thesis, which is work on the special type of optical fibre known as the photonic crystal fibre (PCF) was introduced to provide the foundation for the discussions that were to follow subsequently. The history and development of the PCF, which came about in 1996, including the fabrication technique was discussed and the guidance principle and the structure of the PCF were shown. The Design and Characterisation of the Photonic Crystal Fibre was carried out by simulation using rigorous full vectorial **H**-field formulation Finite Element Method (FEM) to perform the numerical experiments required to calculate leakage and bending losses, insertion losses with a view to minimising those losses as well as applying them to novel applications in engineering photonics.

The work presented in this thesis has been published in major international journals and presented at major international conferences (as discussed above) with a view to making a useful contribution to the study of photonics through research in optical fibre design and further meeting one of the objectives set out in Chapter 1.

The research reported in the thesis has opened up scope for further work which could be carried out in this field by prospective students. All areas studied here provide scope for further study to enhance the designs needed for better optical fibre-based devices. In the work reported in Chapter 6 for instance, PCFs with up to 10 rings in the cladding are considered; with larger outer rings, these have been considered for coupling to SMFs. It may be possible to use more rings of air-holes and as such larger air-holes in the outer rings to stabilize the mode field areas. New approaches and new materials could be considered for future research work and some materials like chalcogenide glasses may offer significant promise especially with regards to applications in technologies

requiring nonlinear applications. A new way of designing and analysing a triangular core fibre can be obtained using three large hollow tubes stacked together similar to PCF fabrication. Also, work in THz regime could be enhanced to a possibility of including a hollow core which would bring about some really interesting properties especially with regarding improvement to attenuation, for high power delivery and in sensing applications. Some work could be carried out on more ways to harness the bending of PCF to an advantage especially in tailoring dispersion. Thus overall there is considerable opportunity for on-going research in this field which could positively impact the community.



## LIST OF PUBLICATIONS BY THE AUTHOR

### JOURNAL PUBLICATIONS

**M. Uthman**, B. M. A. Rahman, N. Kejalakshmy, A. Agrawal and K. T. V. Grattan, "Design and characterization of low-loss porous-core photonic crystal fibre", *IEEE Photonics Journal*, Vol. 4, No. 6, pp. 2315-2325, (2012).

**M. Uthman**, B. M. A. Rahman, N. Kejalakshmy, A. Agrawal, H. Abana and K. T. V. Grattan, "Stabilized large mode area in tapered photonic crystal fibre for stable coupling", *IEEE Photonics Journal*, Vol. 4, No. 2, pp. 340-349, (2012).

A. Agrawal, N. Kejalakshmy, **M. Uthman**, B. M. A. Rahman, A. Kumar, and K. T. V. Grattan, "Ultra low bending loss equiangular spiral photonic crystal fibres in the terahertz regime", *AIP Advances*, Vol. 2, No. 2, 022140, (2012).

B. M. A. Rahman, **M. Uthman**, N. Kejalakshmy, A. Agrawal, K. T. V. Grattan, "Design of bent photonic crystal fibre supporting a single polarization", *Applied Optics*, Vol. 50 Issue 35, pp. 6505-6511 (2011).

B. M. A. Rahman, N. Kejalakshmy, **M. Uthman**, A. Agrawal, T. Wongcharoen, K. T. V. Grattan, "Mode degeneration in bent photonic crystal fibre study by using the finite element method", *Applied Optics*, Vol. 48 Issue 31, pp. G131-G138 (2009).

### CONFERENCE PAPERS

B. M. A. Rahman, **M. Uthman**, A. Quadir, N. Kejalakshmy, C. Markides, C. Themistos, "Low-loss waveguides and devices for compact THz systems (*Invited Paper*) " Terahertz Physics, Devices, and Systems VII: Advanced Applications in Industry and Defense, Baltimore, Maryland United States, SPIE, Conference 8716, 29 April - 3 May 2013.

B. M. A. Rahman, C. Themistos, H. Tanvir, **M. Uthman**, A. Quadir, C. Markides, "Low-loss waveguides for THz guidance and devices" Proc. SPIE 8624, Terahertz, RF, Millimetre, Submillimetre-wave technology and Applications VI, 862414, San Francisco, California, March 2013.

C. Themistos, H. Tanvir, **M. Uthman**, A. Quadir, C. Markides, and B. M. A. rahman, "Design optimization of low-loss THz waveguides and Devices by using the finite element method", (*Invited Paper*), Global Photonics, Singapore, Dec. 2012.

- B. M. A. Rahman, **M. Uthman**, N. Kejalakshmy and K. T. V. Grattan, “Rigorous characterization of photonic crystal fiber, devices and its coupling”, OSA and Japan Appl. Physics conference, Matsutama, Japan, Sept, 2012.
- B. M. A. Rahman, N. Kejalakshmy, A. Agrawal, **M. Uthman**, I. N. M. Wijeratne, K.T.V.Grattan, “Finite Element Characterisation of Photonic Crystal Fibres” #88455, SBMO/IEEE MTT-S, IMOC, Brazil, 2011.
- A. Agrawal, N. Kejalakshmy, **M. Uthman**, B. M. A. Rahman, K. T. V. Grattan, “Ultra Low Bending Loss Spiral Photonic Crystal Fibres in Terahertz Regime”, CLEO: Science and Innovations (CLEO: S and I) paper: CThN1, Baltimore, 2011.
- B. M. A. Rahman, N. Kejalakshmy, A. Agrawal, **M. Uthman**, and K. T. V. Grattan, “Single mode and single polarization operation in photonic crystal fibres”, Proc. of SPIE Vol. 7714, 77140J, Brussels, 2010.
- B. M. A. Rahman, A. Agrawal, N.Kejalakshmy, **M. Uthman**, Y. Azabi, K. T. V. Grattan, “P16 Progress in Finite Element Analysis of Photonic Crystal Fibres”OWTNM 2010, The XVIII<sup>th</sup> International Workshop on Optical Waveguide Theory and Numerical Modelling held in Cambridge, UK April 9-10, 2010.
- B. M. A. Rahman, N. Kejalakshmy, A. Agrawal, **M. Uthman**, and K. T. V. Grattan, “Characterization of photonic crystal fibers by using a full-vectorial finite element method” Proceedings of ICOP 2009-International Conference on Optics and Photonics 6369, 636904, CSIO, Chandigarh, India, 30 Oct.-1 Nov. 2009.

## APPENDIX

### Evaluation of Element Matrices

The elements of matrices  $[A]_e$  and  $[B]_e$  in equation (3.57) can be evaluated by expressing the derivatives of the shape function vectors in terms of the shape function coefficients, as determined in (3.56) and (3.57) and by performing the integration of the shape functions with the aid of (3.46).

$$[A]\{H\} - \omega^2 [B]\{H\} = 0 \quad (1)$$

The global matrices  $[A]$  and  $[B]$  are expressed as:

$$[A] = \sum_{e=1}^n [A]_e = \sum_{e=1}^n \int_{\Delta} \frac{1}{\hat{\epsilon}} [Q]^* [Q] d\Omega \quad (2)$$

And

$$[B] = \sum_{e=1}^n [B]_e = \sum_{e=1}^n \hat{\mu} \int_{\Delta} [N]^T [N] d\Omega \quad (3)$$

In equation (2) the matrix  $[A]$  has matrices  $Q$  and  $Q^*$  which can be written as follows:

$$[Q] = \begin{bmatrix} [0] & -\frac{\partial[N]}{\partial z} & \frac{\partial[N]}{\partial y} \\ \frac{\partial[N]}{\partial z} & [0] & -\frac{\partial[N]}{\partial x} \\ -\frac{\partial[N]}{\partial y} & \frac{\partial[N]}{\partial y} & [0] \end{bmatrix} \quad (4)$$

Replacing  $\frac{\partial}{\partial z}$  with  $-j\beta$  the following  $[Q]$  matrix is obtained:

$$[Q] = \begin{bmatrix} [0] & j\beta[N] & \frac{\partial[N]}{\partial y} \\ -j\beta[N] & [0] & -\frac{\partial[N]}{\partial x} \\ -\frac{\partial[N]}{\partial y} & \frac{\partial[N]}{\partial y} & [0] \end{bmatrix} \quad (5)$$

Consequently, the  $Q^*$  matrix is defined as:

$$[Q]^* = \begin{bmatrix} [0] & j\beta[N]^T & \frac{\partial[N]^T}{\partial y} \\ -j\beta[N]^T & [0] & -\frac{\partial[N]^T}{\partial x} \\ -\frac{\partial[N]^T}{\partial y} & \frac{\partial[N]^T}{\partial x} & [0] \end{bmatrix} \quad (6)$$

Where  $[N]$  is defined as:

$$[N] = [N_1 \ N_2 \ N_3] \quad (7)$$

$$\therefore j\beta[N] = [j\beta N_1 \ j\beta N_2 \ j\beta N_3] \quad (8)$$

This results in the formation of the  $[A]_e$  matrix as:

$$[A]_e = \frac{1}{\varepsilon} \int_{\Delta} [Q]^* [Q] d\Omega \quad (9)$$

$$\Rightarrow \frac{1}{\varepsilon} \int_{\Delta} \begin{bmatrix} [0] & j\beta[N]^T & \frac{\partial[N]^T}{\partial y} \\ -j\beta[N]^T & [0] & -\frac{\partial[N]^T}{\partial x} \\ -\frac{\partial[N]^T}{\partial y} & \frac{\partial[N]^T}{\partial x} & [0] \end{bmatrix} \times \begin{bmatrix} [0] & j\beta[N] & \frac{\partial[N]}{\partial y} \\ -j\beta[N] & [0] & -\frac{\partial[N]}{\partial x} \\ -\frac{\partial[N]}{\partial y} & \frac{\partial[N]}{\partial x} & [0] \end{bmatrix} d\Omega \quad (10)$$

$$\Rightarrow \frac{1}{\varepsilon} \int_{\Delta} \begin{bmatrix} \beta^2[N]^T[N] - \frac{\partial[N]^T}{\partial y} \frac{\partial[N]}{\partial y} & -\frac{\partial[N]^T}{\partial y} \frac{\partial[N]}{\partial x} & -j\beta[N]^T \frac{\partial[N]}{\partial x} \\ \frac{\partial[N]^T}{\partial x} \frac{\partial[N]}{\partial y} & \beta^2[N]^T[N] + \frac{\partial[N]^T}{\partial x} \frac{\partial[N]}{\partial x} & -j\beta[N]^T \frac{\partial[N]}{\partial y} \\ -j\beta \frac{\partial[N]}{\partial x} [N] & -j\beta \frac{\partial[N]^T}{\partial y} [N] & \frac{\partial[N]^T}{\partial y} \frac{\partial[N]}{\partial y} - \frac{\partial[N]^T}{\partial x} \frac{\partial[N]}{\partial x} \end{bmatrix} d\Omega \quad (11)$$

The  $[B]_e$  element matrix of equation (3) can be defined as:

$$[B]_e = \mu \int_{\Delta} [N]^T [N] d\Omega \quad (12)$$

Where the matrix [N] is defined as:

$$[N] = \begin{bmatrix} N_1 & N_2 & N_3 & 0 & 0 & 0 & 0 & 0 & 0 \\ 0 & 0 & 0 & N_1 & N_2 & N_3 & 0 & 0 & 0 \\ 0 & 0 & 0 & 0 & 0 & 0 & N_1 & N_2 & N_3 \end{bmatrix} \quad (13)$$

Which can also be written as:

$$N = \begin{bmatrix} [N] & [0] & [0] \\ [0] & [N] & [0] \\ [0] & [0] & [N] \end{bmatrix} \quad (14)$$

Where [N] is a row vector defined as  $[N] = [N_1 \ N_2 \ N_3]$ . The transpose of [N]

Can be defined as  $[N]^T$  which can be represented as:

$$[N]^T = \begin{bmatrix} [N_1] & [0] & [0] \\ [N_2] & [0] & [0] \\ [N_3] & [0] & [0] \\ [0] & [N_1] & [0] \\ [0] & [N_2] & [0] \\ [0] & [N_3] & [0] \\ [0] & [0] & [N_1] \\ [0] & [0] & [N_2] \\ [0] & [0] & [N_3] \end{bmatrix} = \begin{bmatrix} [N_1]^T & [0] & [0] \\ [0] & [N_2]^T & [0] \\ [0] & [0] & [N_3]^T \end{bmatrix} \quad (15)$$

Hence the  $[B]_e$  matrix in equation (12) can be written as:

$$\begin{aligned} [B]_e &= \mu \int_{\Delta} \begin{bmatrix} [N]^T & [0]^T & [0]^T \\ [0]^T & [N]^T & [0]^T \\ [0]^T & [0]^T & [N]^T \end{bmatrix} \times \begin{bmatrix} [N] & [0] & [0] \\ [0] & [N] & [0] \\ [0] & [0] & [N] \end{bmatrix} d\Omega \\ &= \mu \int_{\Delta} \begin{bmatrix} [N]^T [N] & [0]^T [0] & [0]^T [0] \\ [0]^T [0] & [N]^T [N] & [0]^T [0] \\ [0]^T [0] & [0]^T [0] & [N]^T [N] \end{bmatrix} d\Omega \end{aligned} \quad (16)$$

Now the integrating the individual shape functions inside the matrix will result:

$$\begin{aligned}
\int_{\Delta} [N]^T [N] d\Omega &= \int_{\Delta} \begin{bmatrix} [N_1] \\ [N_2] \\ [N_3] \end{bmatrix} \times \begin{bmatrix} [N_1] & [N_2] & [N_3] \end{bmatrix} d\Omega \\
&= \int_{\Delta} \begin{bmatrix} (N_1)^2 & N_1 N_2 & N_1 N_3 \\ N_2 N_1 & (N_2)^2 & N_2 N_3 \\ N_3 N_1 & N_3 N_2 & (N_3)^2 \end{bmatrix} d\Omega \quad (17) \\
&= \begin{bmatrix} \int_{\Delta} (N_1)^2 d\Omega & \int_{\Delta} N_1 N_2 d\Omega & \int_{\Delta} N_1 N_3 d\Omega \\ \int_{\Delta} N_2 N_1 d\Omega & \int_{\Delta} (N_2)^2 d\Omega & \int_{\Delta} N_2 N_3 d\Omega \\ \int_{\Delta} N_3 N_1 d\Omega & \int_{\Delta} N_3 N_2 d\Omega & \int_{\Delta} (N_3)^2 d\Omega \end{bmatrix}
\end{aligned}$$

For a triangular element, the shape functions can be integrated using the relation:

$$\int_{\Delta} N_m^l N_2^m N_3^n d\Omega = \frac{l!m!n!}{(l+m+n+2)} 2A_e \quad (18)$$

Hence the integral elements in the matrix relation shown in equation (17) can be expressed as:

$$\begin{aligned}
\int_{\Delta} N_1^2 d\Omega &= \frac{2!0!0!}{4!} \cdot 2A_e = \frac{A_e}{6} = \int_{\Delta} N_3^2 d\Omega \\
\int_{\Delta} N_1 N_2 d\Omega &= \frac{1!1!0!}{4!} \cdot 2A_e = \frac{A_e}{12} = \int_{\Delta} N_2 N_1 d\Omega \\
\int_{\Delta} N_1 N_3 d\Omega &= \frac{1!0!1!}{4!} \cdot 2A_e = \frac{A_e}{12} = \int_{\Delta} N_3 N_1 d\Omega \\
\int_{\Delta} N_2 N_3 d\Omega &= \frac{0!1!1!}{4!} \cdot 2A_e = \frac{A_e}{12} = \int_{\Delta} N_3 N_2 d\Omega
\end{aligned} \quad (19)$$

Now, if we consider a matrix  $[K]$  where  $[K]$  can be defined in terms of the shape function integrals as:

$$[K] = \mu \int [N]^T [N] d\Omega \quad (20)$$

Thus using the shape function definition in equation (19) the above relation for  $[K]$  can be expressed as:

$$[K] = \begin{bmatrix} \mu \frac{A_e}{6} & \mu \frac{A_e}{12} & \mu \frac{A_e}{12} \\ \mu \frac{A_e}{12} & \mu \frac{A_e}{6} & \mu \frac{A_e}{12} \\ \mu \frac{A_e}{12} & \mu \frac{A_e}{12} & \mu \frac{A_e}{6} \end{bmatrix} \quad (21)$$

Therefore the  $[B]_e$  matrix in equation (16) can be represented in terms of the  $[K]$  matrix as:

$$[B]_e = \begin{bmatrix} [K] & [0]^T [0] & [0]^T [0] \\ [0]^T [0] & [K] & [0]^T [0] \\ [0]^T [0] & [0]^T [0] & [K] \end{bmatrix} \quad (22)$$

The integral elements of the  $[A]_e$  matrix in equation (11) can be further expressed as:

$$\int_{\Delta} \beta^2 [N]^T [N] d\Omega = \begin{bmatrix} \beta^2 \frac{A_e}{6} & \beta^2 \frac{A_e}{12} & \beta^2 \frac{A_e}{12} \\ \beta^2 \frac{A_e}{12} & \beta^2 \frac{A_e}{6} & \beta^2 \frac{A_e}{12} \\ \beta^2 \frac{A_e}{12} & \beta^2 \frac{A_e}{12} & \beta^2 \frac{A_e}{6} \end{bmatrix} \quad (23)$$

$$\int_{\Delta} \frac{\partial [N]^T}{\partial y} \frac{\partial [N]}{\partial y} d\Omega = \int_{\Delta} \begin{bmatrix} \frac{\partial N_1}{\partial y} \\ \frac{\partial N_2}{\partial y} \\ \frac{\partial N_3}{\partial y} \end{bmatrix} \times \begin{bmatrix} \frac{\partial N_1}{\partial y} & \frac{\partial N_2}{\partial y} & \frac{\partial N_3}{\partial y} \end{bmatrix} d\Omega$$

Which can be expanded into the following 3 x 3 matrix as:

$$\int_{\Delta} \frac{\partial[N]^T}{\partial y} \frac{\partial[N]}{\partial y} d\Omega = \int_{\Delta} \begin{bmatrix} \left(\frac{\partial N_1}{\partial y}\right)^2 & \frac{\partial N_1}{\partial y} \frac{\partial N_2}{\partial y} & \frac{\partial N_1}{\partial y} \frac{\partial N_3}{\partial y} \\ \frac{\partial N_2}{\partial y} \frac{\partial N_1}{\partial y} & \left(\frac{\partial N_2}{\partial y}\right)^2 & \frac{\partial N_2}{\partial y} \frac{\partial N_3}{\partial y} \\ \frac{\partial N_3}{\partial y} \frac{\partial N_1}{\partial y} & \frac{\partial N_3}{\partial y} \frac{\partial N_2}{\partial y} & \left(\frac{\partial N_3}{\partial y}\right)^2 \end{bmatrix} d\Omega \quad (24)$$

The elements of the matrix in equation (24) can be expressed after integration as:

$$\int_{\Delta} \left(\frac{\partial N_1}{\partial y}\right)^2 d\Omega = \int_{\Delta} c_1^2 d\Omega = c_1^2 A_e$$

$$\int_{\Delta} \frac{\partial N_1}{\partial y} \frac{\partial N_2}{\partial y} d\Omega = \int_{\Delta} c_1 c_2 d\Omega = c_1 c_2 A_e$$

$$\int_{\Delta} \frac{\partial N_1}{\partial y} \frac{\partial N_3}{\partial y} d\Omega = \int_{\Delta} c_1 c_3 d\Omega = c_1 c_3 A_e \quad (25)$$

$$\int_{\Delta} \frac{\partial N_3}{\partial y} \frac{\partial N_1}{\partial y} d\Omega = \int_{\Delta} c_3 c_1 d\Omega = c_3 c_1 A_e$$

$$\int_{\Delta} \frac{\partial N_3}{\partial y} \frac{\partial N_2}{\partial y} d\Omega = \int_{\Delta} c_3 c_2 d\Omega = c_3 c_2 A_e$$

$$\int_{\Delta} \left(\frac{\partial N_3}{\partial y}\right)^2 d\Omega = \int_{\Delta} c_3^2 d\Omega = c_3^2 A_e$$



Hence the matrix in equation (24) can be re-written as:

$$\int_{\Delta} \frac{\partial[N]^T}{\partial y} \frac{\partial[N]}{\partial y} d\Omega = \begin{bmatrix} c_1^2 A_e & c_1 c_2 A_e & c_1 c_3 A_e \\ c_2 c_1 A_e & c_2^2 A_e & c_2 c_3 A_e \\ c_3 c_1 A_e & c_3 c_2 A_e & c_3^2 A_e \end{bmatrix} \quad (26)$$

Similarly, the  $\int_{\Delta} -\frac{\partial[N]^T}{\partial y} \frac{\partial[N]}{\partial x} d\Omega$  term in equation (20) can be expressed as:

$$\int_{\Delta} -\frac{\partial[N]^T}{\partial y} \frac{\partial[N]}{\partial x} d\Omega = \int_{\Delta} \begin{bmatrix} -\frac{\partial N_1}{\partial y} \\ -\frac{\partial N_2}{\partial y} \\ -\frac{\partial N_3}{\partial y} \end{bmatrix} \times \begin{bmatrix} -\frac{\partial N_1}{\partial x} & -\frac{\partial N_2}{\partial x} & -\frac{\partial N_3}{\partial x} \end{bmatrix} d\Omega \quad (27)$$

This results in the formation of the following matrix:

$$\int_{\Delta} -\frac{\partial[N]^T}{\partial y} \frac{\partial[N]}{\partial x} d\Omega = \int_{\Delta} \begin{bmatrix} -\frac{\partial N_1}{\partial y} \frac{\partial N_1}{\partial x} & -\frac{\partial N_1}{\partial y} \frac{\partial N_2}{\partial x} & -\frac{\partial N_1}{\partial y} \frac{\partial N_3}{\partial x} \\ -\frac{\partial N_2}{\partial y} \frac{\partial N_1}{\partial x} & -\frac{\partial N_2}{\partial y} \frac{\partial N_2}{\partial x} & -\frac{\partial N_2}{\partial y} \frac{\partial N_3}{\partial x} \\ -\frac{\partial N_3}{\partial y} \frac{\partial N_1}{\partial x} & -\frac{\partial N_3}{\partial y} \frac{\partial N_2}{\partial x} & -\frac{\partial N_3}{\partial y} \frac{\partial N_3}{\partial x} \end{bmatrix} d\Omega \quad (28)$$

The components in the above matrix shown in equation (28) can be re-arranged by substituting the relation of equation (3.50):

$$\int_{\Delta} -\frac{\partial[N]^T}{\partial y} \frac{\partial[N]}{\partial x} d\Omega = \begin{bmatrix} -b_1 c_1 A_e & -b_2 c_1 A_e & b_3 c_1 A_e \\ -b_1 c_2 A_e & -b_2 c_2 A_e & b_3 c_2 A_e \\ -b_1 c_3 A_e & -b_2 c_3 A_e & b_3 c_3 A_e \end{bmatrix} \quad (29)$$

Similarly other terms of equation (11) such as  $-j\beta \int_{\Delta} [N]^T \frac{\partial[N]}{\partial x} d\Omega$  can also be expressed as:

$$\begin{aligned} -j\beta \int_{\Delta} [N]^T \frac{\partial[N]}{\partial x} d\Omega &= -j\beta \int_{\Delta} \begin{bmatrix} N_1 \\ N_2 \\ N_3 \end{bmatrix} \times \begin{bmatrix} \frac{\partial N_1}{\partial x} & \frac{\partial N_2}{\partial x} & \frac{\partial N_3}{\partial x} \end{bmatrix} d\Omega \\ &= -j\beta \int_{\Delta} \begin{bmatrix} N_1 \frac{\partial N_1}{\partial x} & N_1 \frac{\partial N_2}{\partial x} & N_1 \frac{\partial N_3}{\partial x} \\ N_2 \frac{\partial N_1}{\partial x} & N_2 \frac{\partial N_2}{\partial x} & N_2 \frac{\partial N_3}{\partial x} \\ N_3 \frac{\partial N_1}{\partial x} & N_3 \frac{\partial N_2}{\partial x} & N_3 \frac{\partial N_3}{\partial x} \end{bmatrix} d\Omega \quad (30) \\ &= -j\beta \begin{bmatrix} b_1 \frac{A_e}{3} & b_2 \frac{A_e}{3} & b_3 \frac{A_e}{3} \\ b_1 \frac{A_e}{3} & b_2 \frac{A_e}{3} & b_3 \frac{A_e}{3} \\ b_1 \frac{A_e}{3} & b_2 \frac{A_e}{3} & b_3 \frac{A_e}{3} \end{bmatrix} \end{aligned}$$

Similarly,

$$-j\beta \int_{\Delta} [N]^T \frac{\partial[N]}{\partial y} d\Omega = -j\beta \begin{bmatrix} c_1 \frac{A_e}{3} & c_2 \frac{A_e}{3} & c_3 \frac{A_e}{3} \\ c_1 \frac{A_e}{3} & c_2 \frac{A_e}{3} & c_3 \frac{A_e}{3} \\ c_1 \frac{A_e}{3} & c_2 \frac{A_e}{3} & c_3 \frac{A_e}{3} \end{bmatrix} \quad (31)$$

Other terms such as  $-\int_{\Delta} \frac{\partial[N]^T}{\partial x} \frac{\partial[N]}{\partial y} d\Omega$  and  $\int_{\Delta} \frac{\partial[N]^T}{\partial x} \frac{\partial[N]}{\partial y} d\Omega$  of equation (11) can also be expressed as follows:

$$\begin{aligned}
 -\int_{\Delta} \frac{\partial[N]^T}{\partial x} \frac{\partial[N]}{\partial y} d\Omega &= \int_{\Delta} \begin{bmatrix} -\frac{\partial N_1}{\partial x} \\ \frac{\partial N_2}{\partial x} \\ -\frac{\partial N_3}{\partial x} \end{bmatrix} \times \begin{bmatrix} \frac{\partial N_1}{\partial x} & \frac{\partial N_2}{\partial x} & \frac{\partial N_3}{\partial x} \end{bmatrix} d\Omega \\
 &= \int_{\Delta} \begin{bmatrix} -\frac{\partial N_1}{\partial x} \frac{\partial N_1}{\partial y} & -\frac{\partial N_1}{\partial x} \frac{\partial N_2}{\partial y} & -\frac{\partial N_1}{\partial x} \frac{\partial N_3}{\partial y} \\ -\frac{\partial N_2}{\partial x} \frac{\partial N_1}{\partial y} & -\frac{\partial N_2}{\partial x} \frac{\partial N_2}{\partial y} & -\frac{\partial N_2}{\partial x} \frac{\partial N_3}{\partial y} \\ -\frac{\partial N_3}{\partial x} \frac{\partial N_1}{\partial y} & -\frac{\partial N_3}{\partial x} \frac{\partial N_2}{\partial y} & -\frac{\partial N_3}{\partial x} \frac{\partial N_3}{\partial y} \end{bmatrix} d\Omega \quad (32) \\
 &= \begin{bmatrix} -b_1 c_1 A_e & -b_1 c_2 A_e & -b_1 c_3 A_e \\ -b_2 c_1 A_e & -b_2 c_2 A_e & -b_2 c_3 A_e \\ -b_3 c_1 A_e & -b_3 c_2 A_e & -b_3 c_3 A_e \end{bmatrix} \\
 \int_{\Delta} \frac{\partial[N]^T}{\partial x} \frac{\partial[N]}{\partial x} d\Omega &= \int_{\Delta} \begin{bmatrix} \frac{\partial N_1}{\partial x} \\ \frac{\partial N_2}{\partial x} \\ \frac{\partial N_3}{\partial x} \end{bmatrix} \times \begin{bmatrix} \frac{\partial N_1}{\partial x} & \frac{\partial N_2}{\partial x} & \frac{\partial N_3}{\partial x} \end{bmatrix} d\Omega
 \end{aligned}$$

$$= \int_{\Delta} \begin{bmatrix} \left( \frac{\partial N_1}{\partial x} \right)^2 & \frac{\partial N_1}{\partial x} \frac{\partial N_2}{\partial x} & \frac{\partial N_1}{\partial x} \frac{\partial N_3}{\partial x} \\ \frac{\partial N_2}{\partial x} \frac{\partial N_1}{\partial x} & \frac{\partial N_2}{\partial x} \frac{\partial N_2}{\partial x} & \frac{\partial N_2}{\partial x} \frac{\partial N_3}{\partial x} \\ \frac{\partial N_3}{\partial x} \frac{\partial N_1}{\partial x} & \frac{\partial N_3}{\partial x} \frac{\partial N_2}{\partial x} & \left( \frac{\partial N_3}{\partial x} \right)^2 \end{bmatrix} d\Omega \quad (33)$$

$$= \begin{bmatrix} b_1^2 A_e & b_1 b_2 A_e & b_1 b_3 A_e \\ b_1 b_2 A_e & b_2^2 A_e & b_2 b_3 A_e \\ b_1 b_3 A_e & b_2 b_3 A_e & b_3^2 A_e \end{bmatrix}$$

$$\int_{\Delta} \left( \frac{\partial [N]^T}{\partial y} \frac{\partial [N]}{\partial y} + \frac{\partial [N]^T}{\partial x} \frac{\partial [N]}{\partial x} \right) d\Omega = \begin{bmatrix} (b_1^2 + c_1^2) A_e & (b_1 b_2 + c_1 c_2) A_e & (b_1 b_3 + c_1 c_3) A_e \\ (b_1 b_2 + c_1 c_2) A_e & (b_2^2 + c_2^2) A_e & (b_2 b_3 + c_2 c_3) A_e \\ (b_1 b_3 + c_1 c_3) A_e & (b_2 b_3 + c_2 c_3) A_e & (b_3^2 + c_3^2) A_e \end{bmatrix} \quad (34)$$

Hence from equation (11), the 9 x 9  $[A]_e$  matrix can be evaluated as:

$$[A]_e = \begin{bmatrix} A_{e(1,1)} & A_{e(1,2)} & A_{e(1,3)} & A_{e(1,4)} & A_{e(1,5)} & A_{e(1,6)} & A_{e(1,7)} & A_{e(1,8)} & A_{e(1,9)} \\ A_{e(2,1)} & A_{e(2,2)} & A_{e(2,3)} & A_{e(2,4)} & A_{e(2,5)} & A_{e(2,6)} & A_{e(2,7)} & A_{e(2,8)} & A_{e(2,9)} \\ A_{e(3,1)} & A_{e(3,2)} & A_{e(3,3)} & A_{e(3,4)} & A_{e(3,5)} & A_{e(3,6)} & A_{e(3,7)} & A_{e(3,8)} & A_{e(3,9)} \\ A_{e(4,1)} & A_{e(4,2)} & A_{e(4,3)} & A_{e(4,4)} & A_{e(4,5)} & A_{e(4,6)} & A_{e(4,7)} & A_{e(4,8)} & A_{e(4,9)} \\ A_{e(5,1)} & A_{e(5,2)} & A_{e(5,3)} & A_{e(5,4)} & A_{e(5,5)} & A_{e(5,6)} & A_{e(5,7)} & A_{e(5,8)} & A_{e(5,9)} \\ A_{e(6,1)} & A_{e(6,2)} & A_{e(6,3)} & A_{e(6,4)} & A_{e(6,5)} & A_{e(6,6)} & A_{e(6,7)} & A_{e(6,8)} & A_{e(6,9)} \\ A_{e(7,1)} & A_{e(7,2)} & A_{e(7,3)} & A_{e(7,4)} & A_{e(7,5)} & A_{e(7,6)} & A_{e(7,7)} & A_{e(7,8)} & A_{e(7,9)} \\ A_{e(8,1)} & A_{e(8,2)} & A_{e(8,3)} & A_{e(8,4)} & A_{e(8,5)} & A_{e(8,6)} & A_{e(8,7)} & A_{e(8,8)} & A_{e(8,9)} \\ A_{e(9,1)} & A_{e(9,2)} & A_{e(9,3)} & A_{e(9,4)} & A_{e(9,5)} & A_{e(9,6)} & A_{e(9,7)} & A_{e(9,8)} & A_{e(9,9)} \end{bmatrix} \quad (35)$$

Thus, some of the elements of the 9 x 9  $[A]_e$  matrix can be evaluated as:

$$[A]_{e(1,1)} = \frac{1}{\varepsilon} \left[ \frac{\beta^2 A_e}{6} + c_1^2 A_e \right]$$

$$[A]_{e(1,2)} = \frac{1}{\varepsilon} \left[ \frac{\beta^2 A_e}{12} + c_1 c_2 A_e \right]$$

$$[A]_{e(1,3)} = \frac{1}{\varepsilon} \left[ \frac{\beta^2 A_e}{12} + c_1 c_2 A_e \right]$$

$$[A]_{e(1,4)} = \frac{1}{\varepsilon} [-b_1 c_1 A_e]$$

$$[A]_{e(1,5)} = \frac{1}{\varepsilon} [-b_2 c_1 A_e] \quad (36)$$

$$[A]_{e(1,6)} = \frac{1}{\varepsilon} [-b_3 c_1 A_e]$$

$$[A]_{e(1,7)} = \frac{1}{\varepsilon} \left[ -j\beta b_1 \frac{A_e}{3} \right]$$

$$[A]_{e(1,8)} = \frac{1}{\varepsilon} \left[ -j\beta b_2 \frac{A_e}{3} \right]$$

$$[A]_{e(1,9)} = \frac{1}{\varepsilon} \left[ -j\beta b_3 \frac{A_e}{3} \right]$$

Similarly 72 other elements of the 9 x9 [A]<sub>e</sub> matrix can be evaluated.

## REFERENCES

- Agrawal, A., N. Kejalakshmy, M. Uthman, B. M. A. Rahman and K. T. V. Grattan (2009). "Soft glass equiangular spiral photonic crystal fiber for supercontinuum generation." *IEEE Photonics Technology Letters* **21**(22): 1722-1724.
- Agrawal, A., N. Kejalakshmy, M. Uthman, B. M. A. Rahman and K. T. V. Grattan (2011). *Ultra Low Bending Loss Spiral Photonic Crystal Fibers in Terahertz Regime*. CLEO:2011 Laser Applications to Photonics Applications. Baltimore, Optical Society of America.
- Agrawal, G. P. (2002). *Fiber-Optic Communication Systems*. New York, Wiley.
- Agrawal, G. P. (2008). *Applications of nonlinear fibre optics*. New York, Academic press.
- Almeida, V. R., Q. Xu, C. A. Barrios and M. Lipson (2004). "Guiding and confining light in void nanostructure." *Opt Lett* **29**(11): 1209-1211.
- Atakarmians, S., S. A. Vahid, B. M. Fischer, D. Abbott and T. M. Monro (2008). "Porous fibers: a novel approach to low loss THz waveguides." *Opt Express* **16**(12): 8845-8854.
- Barclay, P. E., K. Srinivasan, M. Borselli and O. Painter (2004). "Efficient input and output fiber coupling to a photonic crystal waveguide." *Opt Lett* **29**(7): 697-699.
- Bennett, P. J., T. M. Monro and D. J. Richardson (1999). "Toward practical holey fiber technology: fabrication, splicing, modeling, and characterization." *Opt Lett* **24**(17): 1203-1205.
- Berenger, J. P. (1994). "A perfectly matched layer for the absorption of electromagnetic waves." *J. Comput. Phys.* **114**(2): 185-200.
- Berenger, J. P. (1996). "Three-dimensional perfectly matched layer for the absorption of electromagnetic waves." *J. Comput. Phys.* **127**(2): 363-379.
- Berk, A. (1956). "Variational principles for electromagnetic resonators and waveguides" *IRE Trans. Antennas Propag.* **4**(2): 104-111.
- Bierwirth, K., N. Shultz and F. Arndt (1986). "Finite difference analysis of rectangular dielectric waveguide structures." *IEEE Trans. Microw. Theory* **MTT-34**(11): 1104-1114.
- Bossavit, A. and I. Mayergoyz (1989). "Edge-elements for scattering problems." *IEEE Trans. Microw. Theory* **25**(4): 2816-2821.
- Bourliaguet, B., C. Pare, F. Emond, A. Croteau, A. Proulx and R. Vallee (2003). "Microstructured fiber splicing." *Opt Express* **11**(25): 3412-3417.
- Bowden, B., J. A. Harrington and O. Mitrofanov (2007). "Silver/polystyrene-coated hollow glass waveguides for the transmission of terahertz radiation." *Opt Lett* **32**(20): 2945-2947.
- Broeng, J., S. E. Barkou, A. Bjarklev, J. C. Knight, T. A. Birks and P. J. S. Russell (1998). "Highly increased photonic band gaps in silica/air structures." *Optics. Comm.* **156**: 240-244.
- Brooke, G. H. and M. M. Z. Kharadly (1976). "Step discontinuities on dielectric waveguides." *Electron. Lett.* **12**(18): 473-475.
- Burke, S. V. (1989). "Spectral index method applied to two nonidentical closely separated rib waveguides." *Electron. Lett.* **25**(9): 605-606.
- Burke, S. V. (1990). "Spectral index method applied to two nonidentical closely separated rib waveguides." *IEE Proc. Pt. J* **137**(5): 289-292.
- Burke, S. V. (1994). "Planar waveguide analysis by the spectral index method: II. Multiple layers, optical gain and loss." *Opt. Quantum Electron.* **26**(2): 63-77.
- Chan, W. L., J. Deibel and D. M. Mittleman (2007). "Imaging with terahertz radiation %U <http://stacks.iop.org/0034-4885/70/i=8/a=R02>." *Reports on Progress in Physics* **70**(8): 1325.

- Chandalia, J. K., B. J. Eggleton, R. S. Windeler, S. G. Kosinski, X. Liu and C. Xu (2001). "Adiabatic coupling in tapered airsilica microstructured optical fiber." *IEEE Photon. Technol. Lett.* **13**(1): 52–54.
- Chen, L. J., H. W. Chen, T. F. Kao, J. Y. Lu and C. K. Sun (2006). "Low-loss subwavelength plastic fiber for terahertz waveguiding." *Opt Lett* **31**(3): 308-310.
- Chiang, K. S. (1986a). "Analysis of optical fibres by the effective-index method." *Appl. Opt.* **25**(3): 348-354.
- Chiang, K. S. (1986b). "Dual effective-index method for the analysis of rectangular dielectric waveguides." *Appl Opt* **25**(13): 2169.
- Chiang, K. S. (1994). "Review of numerical and approximate methods for the modal analysis of general optical dielectric waveguides." *Opt. Quantum Electron.* **26**(3): S113-S134.
- Chiang, K. S., K. M. Lo and K. S. Kwok (1996). "Effective-index method with built-in perturbation correction for integrated optical waveguide." *J. Lightwave Technol.* **14**(2): 223-228.
- Chong, J. H. and M. Rao (2003). "Development of a system for laser splicing photonic crystal fiber." *Opt Express* **11**(12): 1365-1370.
- Chung, Y., N. Dagli and L. Thylen (1991). "Explicit finite difference vectorial beam propagation method." *Electron. Lett.* **37**(23): 2119-2121.
- Cisco. (2012). "Cisco Visual Networking Index: Forecast and Methodology, 2011–2016 ", from [http://www.cisco.com/en/US/solutions/collateral/ns341/ns525/ns537/ns705/ns827/white\\_paper\\_c11-481360.pdf](http://www.cisco.com/en/US/solutions/collateral/ns341/ns525/ns537/ns705/ns827/white_paper_c11-481360.pdf).
- Clarricoats, P. J. B. and A. B. Sharpe (1972). "Modal matching applied to a discontinuity in a planar surface waveguide " *Electron. Lett.* **8**(2): 28-29.
- Crawley, D. A., C. Longbottom, B. E. Cole, C. M. Ciesla, D. Arnone, V. P. Wallace and M. Pepper (2003). "Terahertz pulse imaging: a pilot study of potential applications in dentistry." *Caries Res* **37**(5): 352-359.
- Csendes, Z. and P. Silvester (1970). "Numerical solution of dielectric loaded waveguides: I- finite-element analysis." *IEEE Trans. Microw. Theory* **18**(12): 1124-1131.
- Cullen, A. L., O. Ozkan and L. A. Jackson (1971). "Point-matching technique for rectangular-cross-section dielectric rod." *Electron. Lett.* **7**(17): 497-499.
- Cullen, A. L. and S. P. Yeo (1987). "Using the least-squares boundary residual method to model the symmetrical five-port waveguide junction." *IEE Proc. Pt. H* **134**(2): 116-124.
- Dagli, N. and C. G. Fonstad (1986). "Microwave equivalent circuit representation of rectangular dielectric waveguides." *Appl. Phys. Lett.* **49**(6): 308-310.
- Daly, P. (1984). "Finite element approach to propagation in elliptical and parabolic waveguides." *Int. J. Numer. Methods Eng* **20**(4): 681-688.
- Davies, J. B. (1972). "Review of methods of numerical solution of hollow-waveguide problem." *Proc. IEE* **119**(1): 33-37.
- Davies, J. B. (1973). "A least-squares boundary residual method for the numerical solution of scattering problems." *IEEE Trans. Microw. Theory* **MTT-21**(2): 99-104.
- Davies, J. B. (1989). *Numerical techniques for microwave and millimetre-wave passive structures*. New York, T. Itoh Ed. New York: Wiley.
- Davies, J. B. and C. A. Muilwyk (1966). "Numerical solution of uniform hollow waveguides with boundaries of arbitrary shape." *Proc. IEE* **113**(2): 277-284.
- Desurvire, E., J. R. Simpson and P. C. Becker (1987). "High-gain erbium-doped traveling-wave fiber amplifier." *Opt Lett* **12**(11): 888-890.
- Dupuis, A., J. F. Allard, D. Morris, K. Stoeffer, C. Dubois and M. Skorobogatiy (2009). "Fabrication and THz measurements of porous subwavelength fibers using a directional coupler method." *Opt Express* **17**(10): 8012-8028.

- Eijkelenborg, M. A. v., M. C. J. Large, A. Argyros, J. Zagari, S. Manos, N. A. Issa, I. Bassett, S. Fleming, R. C. McPhedran, C. M. d. Sterke and N. A. P. Nicorovici (2001). "Microstructured polymer optical fibre " *Opt Express* **9**(7): 319-327.
- English, W. and F. Young (1971). "An E vector variational formulation of the maxwell equations for cylindercal waveguide problems." *IEEE Trans. Microw. Theory* **19**(1): 40-46.
- Feit, M. D. and J. A. J. Fleck (1980). "Computation of mode properties in optical fibre waveguides by a propagating beam method." *Appl. Opt.* **19**(7): 1154-1164.
- Fernandez, F. A. and J. B. Davies (1988). "Least-squares boundary residuals solution of microstrip step discontinuities." *Electron. Lett.* **24**(10): 640-641.
- Gallot, G., S. P. Jamison, R. W. McGowan and D. Grischkowsky ( 2000). "Terahertz waveguides." *J. Opt. Soc. Amer. B, Opt. Phys.* **17**(5): 851–863.
- Goell, J. E. and R. D. Standley (1969). "Sputtered glass waveguides for integrated optical circuits." *Bell Syst. Tech. J.* **48**: 3445-3448.
- Goff, D. R. (2002). *Fiber optic reference guide*. Massachusetts, Woburn.
- Goto, M., A. Quema, H. Takahashi, S. Ono and N. Sarukura ( 2004). "Teflon photonic crystal fiber as terahertz waveguide." *Jpn. J. Appl. Phys.* **43** (2B, pt. 2): L317–L319.
- Goure, J. P. and I. Verrier (2002). *Optical fibre devices*. Cornwall, MPG Books Ltd.
- Han, H., H. Park, M. Cho and J. Kim (2002). "Terahertz pulse propagation in a plastic photonic crystal fiber." *Appl. Phys. Lett.* **80**(15): 2634–2636.
- Hano, M. (1984). "Finite-element analysis of dielectric-loaded waveguides" *IEEE Trans. Microw. Theory* **32**(10): 1275-1279.
- Hassani, A., A. Dupuis and M. Skorobogatiy (2008a). "Low loss porous terahertz fibres containing multiple subwavelength holes." *Appl. Phys. Lett.* **92**: 071101.
- Hassani, A., A. Dupuis and M. Skorobogatiy (2008b). "Porous polymer fibers for low-loss Terahertz guiding." *Opt Express* **16**(9): 6340-6351.
- Hecht, J. (1999). *City of light: the story of fiber optics*. New York, Oxford university press.
- Heiblum, M. and J. H. Harris (1975). "Analysis of curved optical waveguides by conformal transformation." *IEEE J. Quantum Electron. Lett.* **QE-11**(2): 75–83.
- Hirayama, K. and M. Koshiba (1989). "Analysis of discontinuities in an open dielectric slab waveguide by combination of finite and boundary elements." *IEEE Trans. Microw. Theory* **MTT-37**(4): 761-767.
- Hockman, G. A. and A. B. Sharpe (1972). "Dielectric-waveguide discontinuities " *Electron. Lett.* **8**(9): 230-231.
- Huang, W. P., C. L. Xu and S. K. Chaudhuri (1992a). "A finite difference vector beam propagation method for three-dimensional waveguide structures." *IEEE Photon. Technol. Lett.* **4**(2): 148-151.
- Huang, W. P., C. L. Xu and S. K. Chaudhuri (1992b). "A wide angle vector beam propagation method." *IEEE Photon. Technol. Lett.* **4**(10): 1118-1120.
- Huang, W. P., C. L. Xu, W. Lui and K. Yokoyama (1996). "The perfectly matched layer (PML) boundary condition for the beam propagation method." *IEEE Photon. Technol. Lett.* **8**(5): 649-651.
- Jacobsen, R. H., D. M. Mittleman and M. C. Nuss (1996). "Chemical recognition of gases and gas mixtures with terahertz waves." *Opt Lett* **21**(24): 2011-2013.
- Jepsen, P. U., D. G. Cooke and B. M. Koch (2011). "Terahertz spectroscopy and imagingVModern techniques and applications." *Laser Photon. Rev.* **5**(1): 124–166.
- Jin, J. M. (1993). *The finite element method in electromagnetics*. New York, Wiley.
- Jin, Y. S., G. J. Kim and S. G. Jeon (2006). "Terahertz dielectric properties of polymers." *J. Korean Phys. Soc.* **49**(2): 513–517.
- John, S. (1987). "Strong localization of photons in certain disordered dielectric superlattices." *Phys Rev Lett* **58**(23): 2486-2489.



- Kagami, S. and I. Fukai (1984). "Application of boundary-element method to electromagnetic field problems." *IEEE Trans. Microw. Theory* **MTT-32**(4): 455-461.
- Kao, K. C. and G. H. Hockman (1966). Dielectric fibre surface waveguides for optical frequencies *Proc. IEE*.
- Karpowicz, N. E., J. Chen, T. Tongue and X. C. Zhang (2008). "Coherent millimetre wave to mid-infrared measurements with continuous bandwidth reaching 40 THz." *Electron. Lett.* **44**(8): 544–545.
- Kawase, K., Y. Ogawa, Y. Watanabe and H. Inoue (2003). "Non-destructive terahertz imaging of illicit drugs using spectral fingerprints." *Opt. Exp.* **11**(20): 2549–2554.
- Keiser, G. (2000). *Optical fiber communications*, McGraw-Hill International Editions.
- Kejalakshmy, N., B. M. A. Rahman, A. Agrawal, H. M. Tanvir and K. T. V. Grattan (2009). "Metal-coated defect-core photonic crystal fiber for THz propagation." *J. Lightwave Technol.* **27**(11): 1631–1637.
- Kejalakshmy, N., B. M. A. Rahman, A. Agrawal, T. Wongcharoen and K. T. V. Grattan (2008a). "Characterisation of single-polarisation single-mode photonic crystal fiber using full-vectorial finite element method." *Appl. Phys. B* **93**: 223-230.
- Kejalakshmy, N., B. M. A. Rahman, A. Agrawal, T. Wongcharoen and K. T. V. Grattan (2008b). "Characterisation of singlepolarization single mode photonic crystal fiber using full-vectorial finite element method " *Appl. Phys. B* **93**(1): 223–230.
- Kendall, P. C., P. W. A. McIlroy and M. S. Stern (1989). "Spectral index method for rib waveguide analysis." *Electron. Lett.* **25**(2): 107-108.
- Kiwa, T., M. Tonouchi, M. Yamashita and K. Kawase (2003). "Laser terahertz-emission microscope for inspecting electrical faults in integrated circuits." *Opt Lett* **28**(21): 2058-2060.
- Knight, J. C., T. A. Birks, P. J. S. Russell and D. M. Atkin (1996a). Pure silica single-mode fibre with hexagonal photonic crystal cladding. *OFC '96*, San Jose.
- Knight, J. C., T. A. Birks, P. J. S. Russell and D. M. Atkins (1996b). "All-silica single-mode optical fibre with photonic crystal cladding." *Opt. Lett.* **21**(19): 1547-1549.
- Knox, R. M. and P. P. Toulous (1970). Integrated circuits for milimeter through optical wave range. *Proc. MRI symposium submillimeter waves*.
- Kohler, R., A. Tredicucci, F. Beltram, H. E. Beere, E. H. Linfield, A. G. Davies, D. A. Ritchie, R. C. Iotti and F. Rossi (2002). "Terahertz semiconductor-heterostructure laser." *Nature* **417**(6885): 156-159.
- Konrad, A. (1977). "High-order triangular finite elements for electromagnetic waves in anisotropic media." *IEEE Trans. Microw. Theory* **25**(5): 353-360.
- Koshiba, M. (1990). *Analysis methods for electromagnetic wave problems*. London, Artech house.
- Koshiba, M., K. Hayata and M. Suzuki (1984). "Approximate scalar finite-element analysis of anisotropic optical waveguides with off-diagonal elements in a permittivity tensor." *IEEE Trans. Microw. Theory* **32**(6): 587-593.
- Koshiba, M., K. Hayata and M. Suzuki (1985a). "Finite-element formulation in terms of the electric-field vector for electromagnetic waveguide problems." *IEEE Trans. Microw. Theory* **33**(10): 900-905.
- Koshiba, M., K. Hayata and M. Suzuki (1985b). "Improved finite-element formulation in terms of the magnetic field vector for dielectric waveguides." *IEEE Trans. Microw. Theory* **33**(3): 227-233.
- Koshiba, M. and K. Inoue (1992). "Simple and efficient finite-element analysis of microwave and optical waveguides." *IEEE Trans. Microw. Theory* **MTT-40**(2): 371-377.
- Koshiba, M. and M. Suzuki (1985). "Vectorial wave analysis of optical waveguides with cross-section using equivalent network approach." *Electron. Lett.* **21**(22): 1026-1028.

- Koshiba, M. and M. Suzuki (1986). "Vectorial wave analysis of dielectric waveguides for optical integrated circuits using equivalent network approach." *J. Lightwave Technol.* **4**(6): 656-664.
- Kristiansen, R. E. (2002). Guiding light with holey fibers. *SPIE's oe magazine*: 25-28.
- Kuhlmey, B. T., R. C. McPhedran and C. Martijn de Sterke (2002). "Modal cutoff in microstructured optical fibers." *Opt Lett* **27**(19): 1684-1686.
- Leon-Saval, S. G., T. A. Birks, W. J. Wadsworth, P. J. S. Russel and M. W. Mason (2004). "Supercontinuum generation in submicron fiber waveguides." *Opt. Exp.* **12**(13): 2864–2869.
- Leung, D. M. H., N. Kejalakshmy, B. M. A. Rahman and K. T. V. Grattan (2012). "Rigorous numerical analysis and characterization of a silicon vertical-slot nano-waveguide." *J. Nonlin. Opt. Phys. Mater.* **21**(1): 125007-125001–125007-125018.
- Li, X. H., R. Song, Y. K. Ee, P. Kumnorkaew, J. F. Gilchrist and N. Tansu (2011). "Light extraction efficiency of III-nitride lightemitting diodes with colloidal microlens array with various aspect ratios." *IEEE Photon. J.* **3**(3): 489–499.
- Lindstrom, A. (2001). "Hole-way to heaven: hollow core fiber could lead the way much lower cost networks", from [www.issueofbroadbandweek.com](http://www.issueofbroadbandweek.com).
- Liu, H. B., Y. Chen, G. J. Bastiaans and X. C. Zhang (2006). "Detection and identification of explosive RDX by THz diffuse reflection spectroscopy." *Opt Express* **14**(1): 415-423.
- Liu, J., T.-H. Cheng, Y.-K. Yeo, Y. Wang, L. Xue, Z. Xu and D. Wang (2009). "Light beam coupling between standard single mode fibers and highly nonlinear photonic crystal fibers based on the fused biconical tapering technique." *Opt. Exp.* **17**(5): 3115–3123.
- Liu, Y., B.M.A.Rahman and K.T.V.Grattan (1994). "Thermal stress-induced birefringence in bow-tie optical fibres" *Appl Opt* **33**(24): 5611-5616.
- Lizawa, K., S. K. Varshney, Y. Tsuchida, K. Saitoh and M. Koshiba (2008). "Bend-insensitive lasing characteristics of singlemode, large-mode area ytterbium-doped photonic crystal fiber." *Opt Express* **16**: 579-591.
- Lu, C. H., C. C. Lan, Y. L. Li and C. P. Liu (2011). "Enhancement of green emission from InGaN/GaN multiple quantum wells via coupling to surface plasmons in a two-dimensional silver array." *Adv. Funct. Mater.* **21**(24): 4719–4723.
- Lu, J. Y., C. P. Yu, H. C. Chang, H. W. Chen, Y. T. Li, C. L. Pan and C. K. Sun (2008). "Terahertz air-core microstructure fiber." *Appl. Phys. Lett.* **92**(6): 064105-064101–064105-064103.
- Mabaya, N., P. Lagasse and P. Vandenbulcke (1981). "Finite element analysis waveguides of optical." *IEEE Trans. Microw. Theory* **29**(6): 600-605.
- Magi, E., P. Steinvurzel and B. Eggleton (2004). "Tapered photonic crystal fibers." *Opt Express* **12**(5): 776-784.
- Mahmoud, S. F. and J. C. Beal (1975). "Scattering of surface waves at a dielectric discontinuity on a planar waveguide." *IEEE Trans. Microw. Theory* **MTT-23**(2): 193-198.
- Marcatili, E. A. J. (1969). "Dielectric rectangular waveguide and directional coupler for integrated optics " *Bell Syst. Tech. J.* **48**: 2071-2102.
- Matsumoto, M., M. Tsutsumi and N. Kumagai (1986). "Bragg reflection characteristics of millimeter waves in a periodically plasma-induced semiconductor waveguide." *IEEE Trans. Microw. Theory* **MTT-34**(4): 406-411.
- Mearz, R. (1995). *Integrated optics: design and modelling*. London, Artech house.
- Morishita, K., S. Inagaki and N. Kumagai (1979). "Analysis of discontinuities in dielectric waveguides by means of the least squares boundary residual method." *IEEE Trans. Microw. Theory* **MTT-27**(4): 310-315.
- Mortensen, N. A. (2002). "Effective area of photonic crystal fibers." *Opt Express* **10**(7): 341-348.

- Myabaev, G. K. and L. L. Scheiner (2002). Fiber-optic communications technology. Singapore, Pearson Education.
- Nagel, M., A. Marchewka and H. Kurz (2006). "Low-index discontinuity terahertz waveguides." *Opt Express* **14**(21): 9944-9954.
- Ng, F. L. (1974). "Tabulation of methods for the numerical solution of the hollow waveguide problem." *IEEE Trans. Microw. Theory* **22**(3): 322-329.
- Nguyen, H. C., B. T. Kuhlmei, E. C. Magi, M. J. Steel, P. Domachuk, C. L. Smith and B. J. Eggleton (2005a). "Tapered photonic crystal fibres: Properties, characterisation and applications." *Appl. Phys. B* **81**(2/3): 377-387.
- Nguyen, H. C., B. T. Kuhlmei, M. J. Steel, C. L. Smith, E. C. Magi, R. C. McPhedran and B. J. Eggleton (2005b). "Leakage of the fundamental mode in photonic crystal fiber tapers." *Opt Lett* **30**(10): 1123-1125.
- Nielsen, K., H. K. Rasmussen, A. J. Adam, P. C. Planken, O. Bang and P. U. Jepsen (2009). "Bendable, low-loss Topas fibers for the terahertz frequency range." *Opt Express* **17**(10): 8592-8601.
- Nielsen, K., H. K. Rasmussen, P. U. Jepsen and O. Bang (2011). "Porous-core honeycomb bandgap THz fiber." *Opt Lett* **36**(5): 666-668.
- NRL, U. N. R. L. (2006). "Photonic crystal fibre from NRL." from [http://www.nrl.navy.mil/techtransfer/fs.php?fs\\_id=97](http://www.nrl.navy.mil/techtransfer/fs.php?fs_id=97).
- Obayya, S. S., B. M. A. Rahman and H. A. El-Mikathi (2000). "New full-vectorial numerically efficient propagation algorithm based on the finite element method." *J. Lightwave Technol.* **18**(3): 409-415.
- Okamoto, K. (2006). Fundamentals of optical waveguides. London, Elsevier.
- Pekel, U. and R. Mittra (1995a). "An application of the perfectly matched layer (PML) concept to the finite element method frequency domain analysis of scattering problems." *IEEE Microwave Guid. Wave Lett.* **5**(8): 258-260.
- Pekel, U. and R. Mittra (1995b). "A finite element method frequency domain application of the perfectly matched layer (PML) concept" *Microwave and Opt. Technolog.* **9**(3): 117-122.
- Peng, S. T. and A. A. Oliner (1981). "Guidance and leakage properties of a call of open dielectric waveguides: Part I - Mathematical formulation." *IEEE Trans. Microw. Theory* **MTT-29**(9): 843-855.
- Photonics, N. (2008). "Crystal-fibre." from <http://www.nktpotonics.com/>.
- Pola, J. R. P., W. Biehlig and F. Lederer (1996). "A generalization of the spectral index method toward multiple rib waveguides." *J. Lightwave Technol.* **14**(3): 454-461.
- Poli, F., A. Cucinotta and S. Seller (2007). Photonic crystal fibres: properties and applications. Dordrecht, Springer.
- Ponseca, C. S., R. Pobre, E. Estacio, N. Sarukur, A. Argyros, M. C. Large and M. A. v. EijkelenborgMay (2008). "Transmission of terahertz radiation using a microstructured polymer optical fiber." *Opt. Lett.*, vol. **33**(9): 902-904.
- Qiao, L. and J. Wang (1992). "A modified ray-optic method for arbitrary dielectric waveguides." *IEEE J. Quantum Electron.* **28**(12): 2721-2727.
- Rahman, B. M. A. and J. B. Davies (1984a). "Finite-element analysis of optical and microwave waveguide problems." *IEEE Trans. Microw. Theory* **MTT-32**(1): 20-28.
- Rahman, B. M. A. and J. B. Davies (1984b). "Finite-element solution of integrated optical waveguide." *J. Lightwave Technol.* **LT-2**(5): 682-688.
- Rahman, B. M. A. and J. B. Davies (1984c). "Penalty function improvement of waveguide solution by finite elements." *IEEE Trans. Microw. Theory* **32**(8): 922-928.
- Rahman, B. M. A. and J. B. Davies (1988). "Analysis of optical waveguide discontinuities." *J. Lighthw. Technol.* **6**(1): 52-57.

- Rahman, B. M. A., A. K. M. S. Kabir, M. Rajarajan, K. T. V. Grattan and V. Rakocevic (2006). "Birefringence study of photonic crystal fibers by using the full-vectorial finite element method." *Appl. Phys. B* **84**(1/2): 75–82.
- Rahman, B. M. A., N. Kejalakshmy, M. Uthman, A. Agrawal, T. Wongcharoen and K. T. V. Grattan (2009). "Mode degeneration in bent photonic crystal fibre study by using the finite element method." *Applied Optics* **48**(31): G131–G138.
- Rahman, B. M. A., M. Uthman, N. Kejalakshmy, A. Agrawal and K. T. V. Grattan (2011). "Design of bent photonic crystal fiber supporting a single polarization." *Appl Opt* **50**(35): 6505–6511.
- Rajarajan, M., S. S. A. Obayya, B. M. A. Rahman, K. T. V. Grattan and H. A. El-Mikathi (2000). "Characterization of low-loss waveguide bends with offset optimisation for compact photonic integrated circuits." *IEE Proc. Optoelectron.* **147**: 382–388.
- Rajarajan, M., B. M. A. Rahman and K. T. V. Grattan (1998). "Numerical study of spot-size expanders for an efficient OEIC to SMF coupling." *IEEE Photon. Technol. Lett.* **10**(8): 1082–1084.
- Russell, P. (2003). "Photonic crystal fibers." *Science* **299**(5605): 358–362.
- Russell, P. J. S. (2006). "Photonic-crystal fibers." *J. Lightwave Technol.* **24**(12): 4729–4749.
- Saad, M. S. (1985). "Review of numerical methods for the analysis of arbitrarily-shaped microwave and optical dielectric waveguides." *IEEE Trans. Microw. Theory* **33**(10): 894–899.
- Saitoh, K. and M. Koshiba (2002). "Full-vectorial imaginary-distance beam propagation method based on a finite element scheme: application to photonic crystal fibers." *IEEE Journal of Quantum Electronics* **38**(927–933).
- Saitoh, K. and M. Koshiba (2003). "Single mode photonic crystal fibres." *IEEE Photonics Technology Letters* **15**(10): 1384–1385.
- Shen, Y. C., T. Lo, P. F. Taday, B. E. Cole, W. R. Tribe and M. C. Kemp (2005). "Detection and identification of explosives using terahertz pulsed spectroscopic imaging." *Appl. Phys. Lett.* **86**(24): 241116–241111–241116–241113.
- Shigesawa, H. and M. Tsuji (1986). "Mode propagation through a step discontinuity in dielectric planar waveguide." *IEEE Trans. Microw. Theory* **MTT-34**(2): 205–212.
- Skorobogatiy, M. and B. A. Dupuis (2007). "Ferroelectric all-polymer hollow Bragg fibers for terahertz guidance." *Appl. Phys. Lett.* **90**(11): 113514–113511–113514–113513.
- Srivastava, R., C. K. Kao and R. V. Ramaswamy (1987). "WKB analysis of planar surface waveguides with truncated index profiles." *J. Lightwave Technol.* **5**(11): 1605–1609.
- Stern, M. S., P. C. Kendall and P. W. A. McIlroy (1990). "Analysis of the spectral index method for the vector modes of rib waveguides." *IEE Proc. Pt. J* **137**(1): 21–26.
- Strachan, C. J., P. F. Taday, D. A. Newnham, K. C. Gordon, J. A. Zeitler, M. Pepper and T. Rades (2005). "Using terahertz pulsed spectroscopy to quantify pharmaceutical polymorphism and crystallinity." *J Pharm. Sci.* **94**(4): 837–846.
- Suzuki, K., H. Kubota, S. Kawanishi, M. Tanaka and M. Fujita (2001). "Optical properties of a low-loss polarization-maintaining photonic crystal fibre." *Opt Express* **9**(13): 676–680.
- Technology, E. o. L. P. a. (2008). "Beam Radius." from [http://www.rp-photonics.com/beam\\_radius.html](http://www.rp-photonics.com/beam_radius.html).
- Temelkuran, B., S. D. Hart, G. Benoit, J. D. Joannopoulos and Y. Fink (2002). "Wavelength-scalable hollow optical fibres with large photonic bandgaps for CO<sub>2</sub> laser transmission." *Nature* **420**(6916): 650–653.
- Themistos, C., B. M. A. Rahman, M. Rajarajan, K. T. V. Grattan, B. Bowden and J. A. Harrington (2007). "Characterization of Silver/Polystyrene (PS)-coated hollow glass waveguides at THz frequency." *J. Lightwave Technol.* **25**(9): 2456–2462.

- Town, G. E. and J. T. Lizier (2001). "Tapered holey fibers for spot-size and numerical-aperture conversion." *Opt Lett* **26**(14): 1042-1044.
- Tsuji, Y. and M. Koshiba (1996). "A finite element beam propagation method for strongly guiding and longitudinally varying optical waveguides." *J. Lightwave Technol.* **14**(2): 217-222.
- Ung, B., A. Mazhorova, A. Dupuis, M. Roze and M. Skorobogatiy (2011). "Polymer microstructured optical fibers for terahertz wave guiding." *Opt Express* **19**(26): B848-861.
- Uthman, M., B. M. A. Rahman, N. Kejalakshmy, A. Agrawal and K. T. V. Grattan (2012). "Stabilized large mode area in tapered photonic crystal fiber for stable coupling." *IEEE Photon. J.* **4**(2): 340-349.
- Van de Velde, K., H. Thienpont and R. Van Green (1988). "Extending the effective index method for arbitrarily shaped inhomogeneous optical waveguides." *J. Lightwave Technol.* **6**(6): 1153-1159.
- Van Der Tol, J. J. G. M. and N. H. G. Baken (1988). "Correction to effective index method for rectangular dielectric waveguides." *Electron. Lett.* **24**(4): 207-208.
- Vassalo, C. (1997). "1993-1995 optical mode solvers." *Opt. Quantum Electron.* **29**(2): 95-114.
- Wang, K. and D. M. Mittleman (2004). "Metal wires for terahertz wave guiding." *Nature* **432**(7015): 376-379.
- Wang, Y., H. Bartelt, S. Brueckner, J. Kobelke, M. Rothhardt, K. Morl, W. Ecke and R. Willsch (2008). "Splicing Ge-doped photonic crystal fibers using commercial fusion splicer with default discharge parameters." *Opt. Exp.* **16**(10): 7258-7263.
- Weirer, J. J., A. David and M. M. Megens (2009). "III-Nitride photonic-crystal light-emitting diodes with high extraction efficiency." *Nat. Photon.* **3**(3): 163-169.
- Williamson, C. (2002). "Holey fibers." *Light reading-Networking the telecom industry*, from [www.lightreading.com](http://www.lightreading.com).
- Wongcharoen, T., B. M. A. Rahman, M. Rajarajan and K. T. V. Grattan (2001). "Spot-size conversion using uniform waveguide sections for efficient laser-fiber coupling." *J. Lightwave Technol.* **19** (5): 708-716.
- Woodward, R. M., V. P. Wallace, D. D. Arnone, E. H. Linfield and M. Pepper (2003). "Terahertz pulsed imaging of skin cancer in the time and frequency domain." *J Biol Phys* **29**(2-3): 257-259.
- Wu, Q., M. Litz and X. C. Zhang (1996). "Broadband detection capability of ZnTe electro-optic field detectors." *Appl. Phys. Lett.* **68**(21): 2924-2926.
- Wu, R. and C. Chen (1986). "A scalar variational conformal mapping technique for weakly guiding dielectric waveguides." *IEEE Journal of Quantum Electronics* **22**(5): 603-609.
- Xiangru, W., X. Caidong, W. Xia, Q. Qi, L. Juanyan, D. Hao and X. Wen (2010). "New side-pump scheme for large mode area fiber lasers by wrapping polished fibers conjugate caustic removed." *Optics Communications* **283**(1): 44-48.
- Yablon, A. D. and R. T. Bise (2005). "Low-loss high-strength microstructured fiber fusion splices using GRIN fiber lenses." *IEEE Photon. Technol. Lett.* **17**(1): 118-120.
- Yablonovitch, E. (1987). "Inhibited spontaneous emission in solid-state physics and electronics." *Phys Rev Lett* **58**(20): 2059-2062.
- Yeh, P., A. Yariv and E. Marom (1978). "Theory of Bragg fiber." *J. Opt. Soc. Am.* **68**(9): 1196-1201.
- Yu, C. P. and H. C. Chang (2004). "Yee-mesh-based finite difference eigenmode solver with PML absorbing boundary conditions for optical waveguides and photonic crystal fibers." *Opt Express* **12**(25): 6165-6177.
- Zhao, G., M. T. Mors, T. Wenckebach and P. C. M. Planken (2002). "Terahertz dielectric properties of polystyrene foam." *J. Opt. Soc. Amer. B, Opt. Phys.* **19**(6): 1476-1479.

- Zhao, H., J. Zhang, G. Liu and N. Tansu ( 2011). "Surface plasmon dispersion engineering via double-metallic Au/Ag layers for III-nitride based light-emitting diodes." *Appl. Phys. Lett.* **98**(15): 151115-151111–151115-151113.